INVESTIGATING MAGNETIC PROPERTIES OF DOT/ANTIDOT STRUCTURES IN MAGNETIC THIN FILMS FOR MICROWAVE DEVICE APPLICATIONS

by
Zeynep Reyhan Öztürk
B.S., Physics Education, Marmara University, 2010
M.S., Physics, Boğaziçi University, 2014

Submitted to the Institute for Graduate Studies in
Science and Engineering in partial fulfillment of
the requirements for the degree of
Doctor of Philosophy

Graduate Program in Physics
Boğaziçi University
2023

ACKNOWLEDGEMENTS

During the journey of accomplishing my Ph.D. study, I have been blessed with great people, without whom I would not have this thesis done. First, I would like to thank my supervisor, Prof. Levent Kurnaz, for his guidance and friendly attitude, he has never hesitated to assist students at all stages, and that was, surely, applied to me. Without his efforts, this work would not have been possible. I thank my co-supervisor, Prof. Fikret Yildizi, for involving me in the subject of this thesis. He shared his experience and knowledge and had effective and beneficial discussions regarding the outcome of this Ph.D. thesis, which opened new perspectives in my life both on scientific and personal improvement. Besides, I would like to thank him for his guidance in evaluating and analyzing the experimental data. Next, I thank Dr. Perihan Aksu for helping me during the experiments. I would like to thank Prof. Numan Akdoğan since he let me know about lithography and gave me the opportunity to learn the lithography technique. Also, I am grateful to Dr. Şafak Gok and Dr. Hasan Pişkin for helping me with the fabrication of the mask and giving me advice to achieve successful lithography. I must thank all members and technicians of the NASAM Spintronic Group for their support and cooperation during my Ph.D. It is a pleasure for me to thank all the people who significantly increased my knowledge about magnetism and helped me in every stage of this work. I would like to thank the committee members who evaluated the reports of this thesis and gave valuable advice about the results of this work. I am especially thankful to my friend, Dr. Ahlam Farhan for her endless support, precious advice, and motivation. I am grateful to her little son, İlyas Kahraman, who always cheered me up in the hard times of my research work. Also, many thanks to my sisters and brother who kept me strong and gave me motivation. Finally, I thank my mother and father for their love, trust, support, and encouragement.

ABSTRACT

INVESTIGATING MAGNETIC PROPERTIES OF DOT/ANTIDOT STRUCTURES IN MAGNETIC THIN FILMS FOR MICROWAVE DEVICE APPLICATIONS

Magnetic insulators with perpendicular magnetic anisotropy enable low-power spin-orbit torque switching, high-frequency oscillation, and fast domain-wall motion [1]. Ferromagnetic insulators with PMA are key for studying skyrmions, magneto-optics, and memory/logic applications [2–4]. Yttrium iron garnet (YIG), with its perpendicular magnetization, revolutionizes current spintronics and magnonics.

This work focuses on growing thin/ultrathin YIG films on Silicon substrates using Pulsed Laser Deposition (PLD) and explores the strain's impact on magnetic anisotropy. We achieved perpendicular magnetic anisotropy without additional layers or doping materials.

Additionally, we studied the magnetic properties of Permalloy (NiFe) thin films with dot/antidot arrays that have the ability to modify the magnetic behavior of magnetic thin films such as the magnetization reversal mechanism, magnetic domains, and control the magnetic anisotropy. The FMR technique determined the magnetization dynamics of the dot/antidot patterned NiFe thin films. The magnetization reversal of various shape, size, and thickness of dot/antidot array were investigated by a micromagnetic simulation, Mumax3 which solves the Landau-Lifshitz-Gilbert (LLG) equation. The remnant magnetization and coercive fields of the structures were extracted from the hysteresis loops. We discovered the excitation of spin-wave modes related to the shape effect from the FMR spectrum and found out different domain wall structures corresponding to different dot/antidot shapes from the simulations.

ÖZET

MANYETİK İNCE FİLMLERDEKİ NOKTA/BOŞLUK YAPILARIN MANYETİK ÖZELLİKLERİNİN MİKRODALGA CİHAZ UYGULAMALARI İÇİN İNCELENMESİ

Dikey manyetik anizotropiye sahip manyetik izolatörler, düşük güç tüketen spin-yörünge tork anahtarlamasına, yüksek frekanslı spin-yörünge tork salınımına, yüksek hızda etki alanı-duvar hareketine olanak sağlar [1]. PMA'lı ferromanyetik yalıtkanlar, skyrmions, manyeto-optik, bellek ve mantık uygulamaları üzerinde çalışmak için kullanılır [2–4]. Dik mıknatıslanmalı Yttrium demir granat (YIG) manyetik izolator, spintronik ve magnonik uygulamalara yenilik getirmektedir.

Bu çalışma, ince/ultra ince YIG filmlerinin darbeli lazer biriktirme (PLD) metodu ile Silikon alttaşa büyütülmesine ve alttaş ile film arasında oluşan gerilimin manyetik anizotropi üzerindeki etkisine odaklanmaktadır. Ek katmanlar veya doping kullanmadan dik manyetik anizotropiyi elde ettik.

Ayrıca nokta/boşluk dizilimli Permalloy (NiFe) ince filmlerin manyetik özellikleri de çalışılmıştır. Nokta ve boşluk dizisi yapıları, mıknatıslanmanın yönünü değiştirme, manyetik bölgeler oluşturma, manyetik ince filmlerin manyetik davranışını değiştirme ve anizotropiyi kontrol etme yeteneğine sahiptir. Nokta/boşluk desenli NiFe ince filmlerin manyetizasyon dinamikleri FMR tekniği ile belirlenmiştir. Çeşitli nokta/ boşluk şekilleri, boyutları ve kalınlıklarında mıknatıslanmayı tersine çevirme, Landau-Lifshitz-Gilbert (LLG) denklemini çözen Mumax3 mikromanyetik simülasyonu ile incelenmiştir. Artık mıknatıslanma ve zorlayıcı alanlar, histerezis döngülerinden çıkarılmıştır. FMR ve simülasyonlardan şekil etkisine bağlı spin dalga modlarının uyarılması ve farklı şekillere karşılık gelen farklı spin bölgeleri bulunmuştur.

TABLE OF CONTENTS

LIST OF FIGURES

LIST OF TABLES

LIST OF SYMBOLS

A	The pinning parameter
$\mathbf{B}$	The magnetic flux density
c	The speed of light
d	The distance
$\mathbf{E}$	The electric field vector
f	The frequency
F	The force
H	Hamiltonian
$\mathbf{H}$	The magnetic field
H_d	The demagnetizing field
$\mathbf{j}$	The current density
J	The exchange constant
K	The cubic anisotropy constant
k	The wave vector
K_u	The uniaxial anisotropy constant
$\mathbf{M}$	The magnetization
p	The magnetic pole
$\mathbf{S}$	The spin angular momentum
T	Temperature
U	The Coulomb energy
V	The volume
ϵ_0	The electric constant
λ	The wavelength
μ	The magnetic moment
μ_0	The magnetic constant
μ_B	Bohr Magnetron
ρ	The electric charge density

$\hbar$	The Planck constant
ϕ	The magnetic flux
χ	The magnetic susceptibility
ψ	The wave function
ω	The resonance frequency

LIST OF ACRONYMS/ABBREVIATIONS

2D	Two Dimensional
3D	Three Dimensional
AFM	Atomic Force Microscopy
BVMSW	Backward Volume Magnetostatic spin wave
ESR	Elektron Spin resonance
FMR	Ferromagnetic Resonance
FWMSW	Forward Volume Magnetostatic spin wave
GGG	Gadolinium Gallium Garnet
IP	In Plane
MOKE	Magnetooptic Kerr Effect
MSSW	Magnetostatic Surface spin wave
NiFe	Permalloy
OOP	Out Of Plane
OM	Optic Microscope
PBC	Periodic Boundary Condition
PLD	Pulsed Laser Deposition
QED	Quantum Electrodynamics
PMA	Perpendicular Magnetic Anisotropy
RF	Radio Frequency
SEM	Scanning Electron Microscopy
UV	Ultraviolet
VSM	Vibrating Sample Magnetometry
XPS	X-Ray Photoelectron Spectroscopy
XRD	X-Ray Diffraction
YIG	Yttrium Iron Garnet

1. INTRODUCTION

High demand for suitable magnetic insulators in spintronics research and device applications has been generated in recent years. Magnetic garnet films have been considered a good alternative material to ferromagnetic conductors in spintronics applications since the beginning of the 1980s. Since garnets are mainly composed of oxides that make them insulators, information losses due to Eddy currents are very low. Insulating garnets are applied in high-frequency applications and are used for fast switching of magnetic properties since their magnetization is very low. Owing to the absence of conduction electrons and Fe^{2+} ions, the ferromagnetic relaxation of magnetic garnets is usually smaller than other ferromagnetic materials. YIG (chemical formula $Y_3Fe_5O_{12}$) is an outstanding material with the lowest relaxation, the lowest intrinsic damping constant of 3×10^{-5} among all materials, especially in microwave device applications as a core material in microwave generators and analyzers [5]. The narrow line width allows the magnon to propagate over distances of centimeters. Owing to this unique property, YIG is used as an essential material for the experimental studies of microwave magnetic dynamics, and microwave magnetic technologies, i.e. magnon transistor and magnon logic gate [6, 7]. and general wave and quasi particle dynamics [8,9]. YIG was synthesized for the first time by Geller and Gilleo in 1957 [10]. Since then, YIG is used as the most suitable ferrite garnet for high-frequency applications [11]. Having a high electric resistivity [12], a high radiation stability [13], a low magnetization [14], narrow ferromagnetic linewidth and thereby, low loss [11], allows YIG material used widely in circulatory, isolators and phase shifters and many microwave applications [15]. The intrinsic constant of YIG is two orders of magnitude smaller than the materials used in spintronics currently, which is mostly preferred for spin-wave-based logic operations. Its low damping makes YIG a suitable material for spin wave studies and magneto-optic applications. As an insulator, the absence of Joule heating is a prominent feature of YIG in the use of electronic devices. In addition to spintronic and microwave applications of YIG, an appreciable interest has occurred in the quantum studies of YIG magnon dynamics. YIG was used in quantum measurement and information processing technologies, cavity-based QED, optomagnonics [16], and optomechanics. It has been realized that a strong coupling between the magnon modes of YIG and a superconducting qubit can be promoted as a tool for quantum information technologies [17]. Magnons are known as bosonic quasiparticles and are the quanta of oscillations of magnetic moments in a magnetic material. Magnonics is the study of the transmission, storage, and information process in spin-wave packets in a magnetic material. In magnon spintronics where the information is carried by spin waves, device applications use mutual conversion between electron spin current and magnon current. In contrast to electronic devices, spintronic devices don't produce joule heating because there are no charges to carriers moving. Recently, there are promising attempts to use the properties of high-frequency ferromagnetic materials for creating spin-wave logic devices and for realizing spin torque oscillators having applications in information processing. Another field, quantum magnonics, is defined as the interaction of magnon spintronics and quantum information. It includes quantum magnonic, spintronic, magnonic, quantum optics, and quantum computing and forms the basis of today's technology. Spin waves in YIG can amplify the oscillating field of a microwave source and can act as quantum buses in long-range qubit interactions. Spin waves can be used in hybrid quantum networks and sensing devices for efficient manipulation and solid-state defect coupling.

Spin waves occur in the microwave frequency range and the wavelength is in the nanometer range. These properties make spin waves used in microwave information processing devices. Spin waves can be obtained in polycrystalline magnetic metals and alloys, but their large intrinsic damping prevents spin wave propagation for long distances. For Iron and Permalloy, the lifetime of a magnon is very short (nanoseconds) and the speed of a magnon is very slow, which results in a 10-micrometer-mean free path of spin waves [18, 19]. For YIG, the magnon lifetime is around a few hundred nanoseconds, and the spin wave propagates over a centimeter distance due to its low damping. That's why YIG is used in microwave devices such as high Q microwave oscillators, microwave filters, microwave generators, and filters [20, 21]. YIG has a cubic crystalline structure. The dimension of the unit cell is 12.37 A° and each cell has 80 atoms. 20 Fe^{3+} ions are shared by the octahedral and tetrahedral sublattices which have antiferromagnetic coupling [22]. The fabrication of good-quality YIG thin films is important for spin wave dynamics. Up to now, the best YIG film was deposited on Gadolinium Gallium Garnet (GGG) substrate by liquid phase epitaxy [23]. The perfect match between YIG and GGG enables high-purity, stress-free, highly homogenous YIG film. The production process, composition, homogeneity, and stoichiometry play a key role in determining the magnetic properties of YIG. YIG is among the most preferred ferromagnetic insulators used in microwave, optical, and magneto-optical applications. Intrinsically low magnetic spin wave damping which is almost 10^{-5} [24] causes exceedingly low losses, especially in microwave device applications such as a resonant element in filtering and tunabling, isolators, phase shifters, etc. is chemically stable, with a high Curie temperature [25]. YIG material is used for high-frequency magnetization dynamics [26]. These properties also have a high effect on electromagnetic properties, e.g., tunable saturation magnetization. YIG has an in-plane anisotropy due to large shape anisotropy and small magneto crystalline anisotropy. Fabrication of YIG thin films with perpendicular magnetic anisotropy is challenging. It is a fact that YIG as a perfect magnetic insulator with perpendicular anisotropy brings novelty to the existing spin-related technologies, magnonic applications, and magnetic memory and logic devices. Perpendicular magnetized YIG is significant for spin-orbit switching, spin transfer torque, and, a reliable and fast response. Controlling magnetic anisotropy in garnets is currently an important and popular subject. Bulk or thick YIG films in the micron range are studied in terms of static and dynamic magnetic properties, and we see their potential applications in many microwave devices as microwave filtering, tuning, insulators, and phase shifters. In addition to those outstanding developments, when the thickness scale of YIG diminishes to a thin/ultrathin regime, it is easier to manipulate magnetic properties, which is crucial for spintronic and magneto-optical applications. Therefore, this thesis covers the structural and magnetic characterization of YIG thin films deposited on Si-100 substrate by pulsed laser deposition. The effect of post-annealing on the crystallization and the effect of thickness on the magnetic properties were studied. Spin wave modes excitation in YIG thin films with PMA is lacking in the literature so far. Thus, spin wave modes were analyzed from the ferromagnetic resonance spectrum of YIG thin films. The findings of these studies provide insight into faster spin wave computing devices and superior magnonic logic device applications.

In addition to YIG, another soft magnetic alloy, Permalloy (NiFe) was the material studied in this thesis. The magnetic properties of confined magnetic nanostructures show significant differences from the pure magnetic thin film. Arrays of NiFe dots in the micron range in lateral dimensions have been fabricated by the lithography technique. Different dot shapes correspond to different magnetic anisotropies, which alter the demagnetization processes. The interaction between the dots leads to different domain configurations. The magnetization reversal of dot arrays in NiFe thin films has been simulated by the Mumax3 program as a function of dot shape, dot size, and separation distance between the dots. The coupling between the dots and the dot shape and array geometry plays a vital role in determining magnetic anisotropy. Another array pattern studied in this thesis is the antidot array in NiFe thin film. Antidot array in magnetic films is interesting from the technological point of view such that these magnetic nanostructures enable the generation of ultra-high-density magnetic storage as well as two-dimensional magnonic crystals and magneto-optic applications. Antidot array, which is an array of holes patterned in ferromagnetic thin films, establishes magnetization pinning centers between the holes. Antidots do not have the superparamagnetic limit as magnetic dots do. The magnetic properties depend on the geometrical parameters, such as the array geometry, hole diameter, hole shape, inter-pattern spacing, and film thickness. The magnetization reversal process is affected by the stray field distribution, which is responsible for the domain nucleation and domain wall motion. The emergence of domains around the hole structures is explained by the intrinsic uniaxial magnetic anisotropy and the demagnetizing fields between the antidots. The antidot structure induces anisotropies which affect the domain wall nucleation and domain wall motion. The coercivity, remnant magnetization, and magnetization reversal process can be controlled by the antidot geometry. Domain walls pass through the area between the antidots and the magnetization is pinned at the boundary of the antidot. This gives rise to an increase in the coercivity with respect to the homogenous thin film. Within the medium between the antidots, memory bits can be captured along the hard magnetic axis of the array structure.

For this thesis, arrays of dots/antidots of different sizes and different shapes in the micron range have been fabricated by using lithography, and further, NiFe thin film with the same thickness has been deposited on the Si substrate with the dot/antidot array pattern. The magnetization dynamics in a ferromagnetic thin film with a dot/ antidot array must be well understood for its implementation in microwave technology. The dynamic response of various shape-Permalloy dot/antidot arrays in a square lattice has been studied as a function of dot/ antidot structure size, and distance between the structures using ferromagnetic resonance measurement at 9.5 GHz.

The first part of this thesis starts with a brief history and the fundamentals of magnetism. Chapter. 1 starts with an introduction to the topics of the thesis. Chapter 2 is dedicated to the theory of magnetism, which outlines the basic terms of magnetism and runs through a classification of magnetic materials. In this chapter, the reason why magnetism cannot be explained in classical mechanics and the electrodynamics approach is discussed. Different types of magnetic order in the solids i.e. diamagnetism, paramagnetism, ferromagnetism, antiferromagnetism, and ferrimagnetism are represented. The definition of magnetic anisotropy and a number of magnetic anisotropy types are given in detail. In the following sections, magnetization dynamics, the damping mechanism, and the ferromagnetic resonance will be explained. Further, the spin wave, magnonics, spin wave excitation, and propagation will be presented. Chapter 3 consists of thin film deposition techniques which are used in this thesis. Pulsed laser deposition and RF sputtering were briefly explained. To fabricate a dot and antidot array on Permalloy film, the photolithography technique was used, so the lithography steps were described. In addition, the structural characterization techniques which are X-ray diffraction (XRD), X-ray Photoemission spectroscopy (XPS), and the magnetization characterization techniques such as vibrating sample magnetometer (VSM) and ferromagnetic resonance (FMR) technique were explained. During the thesis, micromagnetic simulations were performed for the magnetization reversal process. Therefore, I will give some idea about the algorithm of the micromagnetic simulations. In Chapter

4, the structural and magnetic characterization of YIG thin films, in-plane magnetic anisotropy, perpendicular magnetic anisotropy in YIG films grown on Silicon substrate, and the spin wave studies in YIG films with PMA will be discussed comprehensively. In Chapter 5, the magnetization dynamics of NiFe (Permalloy) with dot/antidot array structures will be represented in addition to the preparation of samples by lithography and sputtering. The Ferromagnetic resonance spectrum of dot/antidot arrays shows the spin wave modes excitation due to the shape effect. In Chapter 6, I will show the micromagnetic simulation results for the hysteresis curves of various shape dot and antidot arrays with different inter-pattern spacing. The anisotropy, demagnetization, exchange, Zeeman, and total energies were calculated as a function of the field during the magnetization reversal. Magnetic domains, uniformly magnetized regions in which all magnetic moments are oriented parallel to each other, will be visualized with respect to different dot/antidot shapes. Chapter 7 is devoted to the results of the studies within the thesis. Chapter 8 includes the summary and future works.

The full FMR spectra of pure NiFe thin film, dot, and antidot array patterns in in-plane and out-of-plane measurement geometry are given in the appendices. In this thesis, I make use of the units and definitions of the system international SI. In some figures, the properties are given in the cgs system. This research work has contributed to two publications ([27] and [28]).

2. THEORY OF MAGNETISM

In this chapter, the history of magnetism will be given briefly. The origin of magnetism, magnetic ordering, specifically ferromagnetic materials, magnetic anisotropy, magnetization reversal process, magnetization dynamics, magnonics, and spin waves will be discussed.

2.1. The History of Magnetism

The history of magnetism goes back to earlier than 600 B.C. Magnets have fascinated countless curious souls for two thousand years because of their ability to attract iron and other ferromagnets from far distances. Permanent magnets were quite common in nature and called loadstones which are rocks rich in magnetite (Iron oxide, Fe_3O_4) magnetized by giant electric currents in lightning strikes. People in Sumer, Ancient Greece, and China were acclimated to their natural fascination. The Chinese spoon was an early magnetic device as a South pointer [29]. In 1064, Zheng Gongliang discovered the magnetization of steel needles in the Earth field, thus giving rise to the first artificial permanent magnets. The navigational compass was discovered by Shen Kua in 1088. Owing to the compass, Africa and America were discovered by Cheng Ho in 1433 and Christopher Columbus in 1492, respectively. It is believed that the first scientific content on magnetism was written in William Gilbert's monograph De. Magnete in 1600. Gilbert discovered that the earth itself, not the stars, as previously assumed, is a great magnet. The horseshoe magnet, which has remained a symbol of magnetism to this day, was invented by Daniel Bernoulli in 1743 to make a compact magnet that does not self-destruct in its own demagnetizing field. Carl Friedrich Gauss implemented the first theoretical investigations about the Earth's magnetism (1777-1855). The electromagnetic revolution started with the discovery of the connection between electricity and magnetism. In 1820, Hans-Christian Oersted showed that a current-carrying wire yields a magnetic field around and deflects a compass needle. After a while, Andr´e-Marie Amp‘ere and Dominique-Francois Arago demonstrated that the current-carrying coil behaves like a magnet. Two parallel wires, carrying current, attracted each other if the currents were in the same direction and opposed each other if the currents were in opposite directions. In 1821, Michael Faraday was the initiator of the breakthrough discovery of electromagnetic induction, which states that a change in magnetic intensity produces an electric current. He discovered that if electric currents in a wire produce magnetic fields, magnetic fields can also produce electricity. He demonstrated that when a magnet moves inside a coil of copper wire, a tiny electric current flows through the wire, or when the coil is rotated between the poles of a magnet, a magnetic field causes a current to flow in a coil of wire. Following the link between magnetism and light, the magneto-optic Faraday effect was discovered in 1845. James Clerk Maxwell summarized the unified theory of electricity, magnetism, and light in the four equations called Maxwell's equations (1864) which are given as

$$\nabla \cdot \mathbf{B} = 0, \tag{2.1}$$

$$\epsilon_0 \nabla \cdot \mathbf{E} = \rho, \tag{2.2}$$

$$(1/\mu_0) \times \nabla \cdot \mathbf{B} = \mathbf{J} + \epsilon_0 \partial \mathbf{E}/\partial t, \tag{2.3}$$

$$\nabla \times \partial \mathbf{E} = -\partial \mathbf{B}/\partial t, \tag{2.4}$$

where $\mathbf{E}$ and $\mathbf{B}$ are the electric and magnetic fields, ρ and $\mathbf{J}$ are the electric charge and current densities, respectively, and ϵ_0 and μ_0 are the electric and magnetic constants. Maxwell equations show the relationship between the electric and magnetic fields in free space and the surrounding area's charge and current densities. The solution to Maxwell's equations reveals that the coupled oscillating electric and magnetic fields propagate at the speed of light, c with the value of $2.998 \times 10^8\,\mathrm{s}^{-1}$. The speed of light was derived from the equation $\sqrt{\epsilon_0/\mu_0} = 1/c$ These electromagnetic waves have wavelength λ and frequency f, related by $c = \lambda \cdot f$. Maxwell's equations are not symmetric for the electric and magnetic fields. In theoretical calculations, it is easy to make an analogy between electric and magnetic fields. Similar to Coulomb's positive and negative charge idea, North or south magnetic poles as suggested by Gilbert are not present in nature. Electric charges have no magnetic counterpart. Although magnetic monopoles do not exist, a material's magnetic field is attributed to a magnetic dipole, and the net output of the magnetic field from a closed surface is zero. Magnetic dipoles are represented as current loops. After all, electricity and magnetism are based on electric charges and magnetic dipoles. Lorentz's force on a moving particle with velocity $\mathbf{v}$ and charge q subjected to electric and magnetic fields are $\mathbf{f} = q(\mathbf{E} + \mathbf{v} \times \mathbf{B})$.

In 1824, an iron-cored electromagnet was invented. Electromagnets were more effective than the horseshoe-shaped core temporarily magnetized by the magnetic field produced by current in the windings and used in electric motors and generators efficiently. In 1897, the discovery of electrons brought the facility of communication by telegraph cables distributed over the earth and transmitting messages close to the speed of light. Although the outstanding revolution in electromagnetism, the ferromagnetism concept in materials was still not well explained and understood. Pierre Weiss's molecular field theory (1907) postulates the phase transition at a Curie point, where iron reversibly loses its ferromagnetism. Inside the material, an internal magnetic field aligns in a three-order magnitude greater than and parallel to the magnetization. Maxwell's equation claims that the magnetic field B should be continuous, however, a field that has such a greater magnitude was never observed outside a magnetized iron. Therefore, classical approaches were not enough to explain the nature of ferromagnetism. Only after quantum mechanics and relativity, and the advances in modern physics in the early years of the twentieth century, ferromagnetism started to be understood well. In 1925, it was discovered that Amperian currents are associated with quantized angular momentum and that electrons have quantized spins, and these spins are directed up and down in the magnetic field. Therefore, it turned out that the Ampere current carries a quantized angular momentum due to the quantized spin known as the Bohr magneton $\mu_B = 9.274 \times 10^{-24}\,\mathrm{A\ m^2}$ and magnetic properties originate mainly from the magnetic moments of electrons. In 1929, Werner Heisenberg illustrated that the interactions caused to ferromagnetism are electrostatic and obey the Pauli exclusion principle. Heisenberg represented the Hamiltonian

$$H = -2J\mathbf{S}_i \cdot \mathbf{S}_j, \tag{2.5}$$

where J is the exchange constant. The Hamiltonian gives the interaction between two neighboring atoms, in which the total spins are $\mathbf{S}_i$ and $\mathbf{S}_j$. Atomic magnetic moments and electronic spins are related to each other. When the exchange interaction J is positive, the material is ferromagnetic, which means that the spins align parallel to each other. When the sign of J is negative, the spins at sites i and j tend to align antiparallel. In 1936 and 1948, Louis Neel brought out that this gave rise to antiferromagnetism or ferrimagnetism concerning the crystal lattice structure. At the beginning of the twentieth century, hard and soft magnetic steels were used to understand magnetism. In 1960, major progress in advanced technology was made with the ability to produce new types of alloys, rare earth element-doped materials. Engineering of crystal topology and advancement in chemistry and material science have brought novel approaches and capabilities to do cutting-edge magnetism and quantum-related experiments. In the 1940s and 1950s, the discovery of magnetic resonance methods and the development of spectroscopic and diffraction techniques provided a better understanding of solids' magnetic and electronic structures. Microwave technology was developed during the Second World War. Today, developments in magnetic recording and high-frequency materials establish high improvements in computers, telecommunications, earth sciences, and the internet for the benefit of humanity.

2.2. Magnetic Ordering

This chapter summarizes some basic terms of magnetism. The origin of magnetism basically comes from the orbital and spin angular momentum of electrons and interactions between electrons. The behavior of a material when an external field is applied causes different types of magnetism, i.e. diamagnetism, paramagnetism, ferromagnetism, antiferromagnetism, and ferrimagnetism [30]. In analogy with the interactions between Coulomb charges, the force generated by two magnetic poles is proportional to the dot product of the magnetic pole strengths and is inversely proportional to the square of the distance between the poles, which is defined as

$$F = \frac{p_1 \cdot p_2}{d^2}. \tag{2.6}$$

In the cgs unit system, the proportionality constant is equivalent to 1. In the SI unit system, the force relation can be written as

$$F = \frac{1}{4\pi\mu_0}\frac{p_1 \cdot p_2}{d^2}, \tag{2.7}$$

where μ_0 is the permeability of free space and its value is $4\pi\times 10^{-7}$ weber/ampere meter (Wb/Am) [31]. Assuming one of the poles generates a magnetic field, H, applying a force on the other pole, we can express this force as

$$F = \frac{p_1 \cdot p_2}{d^2} = \mathbf{H}p_2. \tag{2.8}$$

From Equation (2.8), H can be reproduced as

$$\mathbf{H} = \frac{p_1}{d^2}. \tag{2.9}$$

The cgs units for the magnetic field are called Oersteds (Oe). In the SI system, the field is written as

$$\mathbf{H} = \frac{1}{4\pi\mu_0}\frac{p_1}{d^2}. \tag{2.10}$$

In this expression, the units are amperes per meter (A/m). The conversion from the cgs unit system to the SI unit system is 1 Oe =1000/4π A/m. The field strength can be defined as the amount of flux passing through a unit area and is given as

$$\phi = \mathbf{H}A, \tag{2.11}$$

where ϕ is the magnetic flux, $\mathbf{H}$ is the field strength and A is the unit area perpendicular to the field. The flux in the cgs unit system is Oersted.cm^2. In SI unit system, the flux is written as

$$\phi = \mu_0\mathbf{H}A \tag{2.12}$$

with a unit of Weber. Faraday's law states that the change in the flux induces an electric current in a circuit ($\epsilon = -\frac{d\phi}{dt}$). The minus sign shows that the current generates a magnetic field opposite to the magnetic flux. This phenomenon is known as Lenz's law. A current loop in classical electromagnetism explains the magnetic moment μ. A current I flowing around an infinitely small loop which has an area of dA has a magnetic moment $d\mu$ with a relation of

$$d\mu = IdA. \tag{2.13}$$

By summing up the magnetic moments of these "small" loops for a loop of finite size, the net magnetic moment can be expressed as

$$\mu = \int I\,dA. \tag{2.14}$$

The magnetic moment in the cgs unit system is called the emu. In SI units, a magnetic moment unit is given as A m^2. The energy of a magnetic moment is given in the following relation

$$E = \mu_0 \boldsymbol{\mu} \cdot \mathbf{H} = \mu_0 \mu H \cos(\theta), \tag{2.15}$$

where θ is the angle between the magnetic moment, μ and an external magnetic field, H, and μ_0 is the magnetic permeability of the free space. Magnetic induction or magnetic flux density, B, is the response of a material under an external magnetic field, H. The relationship between H and B gives the characteristics of the material. In free space and in some materials, the correlation between B and H is linear, however, it is generally more complicated. B and H may not be the same in magnitude and direction inside the materials due to the magnetization, M. The equation between B and H is (in cgs units)

$$\mathbf{B} = \mathbf{H} + 4\pi\mathbf{M}, \tag{2.16}$$

where $\mathbf{M}$ is the magnetization of the medium. The total magnetic moment per unit volume gives the magnetization, $\mathbf{M}$, and is defined as

$$\mathbf{M} = \frac{\mathbf{m}}{V}. \tag{2.17}$$

In the SI unit system, magnetization is written as

$$\mathbf{B} = \mu_0(\mathbf{H} + \mathbf{M}). \tag{2.18}$$

The units of $\mathbf{M}$ and $\mathbf{H}$ are A/m and the units of μ_0 are weber/A m. So, the units of $\mathbf{B}$ are weber/m^2, or tesla (T); 1 gauss = 10^{-4} Tesla. The magnetic induction, $\mathbf{B}$, and the density of flux, ϕ within the medium are the same. Inside a material, $\mathbf{B} = \phi/A$ is equivalent to $\mathbf{H} = \phi/A$ in free space. Since the flux density differs inside and outside the material, magnetic materials can be classified as follows:

If $\phi_{\text{in}} < \phi_{\text{out}}$, the material is diamagnetic, such as bismuth and helium. These materials have zero magnetic field inside and, therefore, have zero magnetic dipole moment. If $\phi_{\text{in}} > \phi_{\text{out}}$, then there are two situations such that the material is either paramagnetic (Na or AI) or antiferromagnetic (MnO or FeO), in which the atoms or ions have a magnetic dipole moment. Dipole moments in paramagnetic materials are oriented randomly, whereas, in antiferromagnetic materials, dipole moments align antiparallel to each other. In ferromagnetic or ferrimagnetic materials, ϕ inside the material is much greater compared to the ϕ outside. The magnetic dipole moments in ferromagnetic materials align in the same direction. Ferrimagnetic materials show similarity with antiferromagnetic materials since magnetic dipoles are antiparallel to each other, but, the net magnetic moment does not vanish. Some dipole moments are greater than others. Inside ferromagnetic and ferrimagnetic materials, magnetic flux is much more intensive than that of outside.

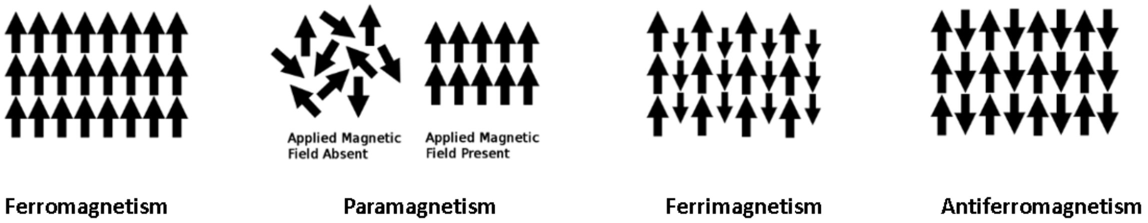

Figure 2.1. Magnetic moment ordering in paramagnetic, antiferromagnetic, ferromagnetic and ferrimagnetic materials [32].

Figure 2.1 refers to the different magnetic orderings. If the magnetization, M aligns parallel to the external magnetic field, H, the relationship between M and H is given in the following

$$\mathbf{M} = \chi \mathbf{H}, \tag{2.19}$$

where χ is the magnetic susceptibility with a unit of emu/cm^{3}Oe. The susceptibility is the response of a magnetic material to an applied magnetic field. The relationship between **B** and **H** is linear, therefore the material is called a linear material. The permeability, $\mu = \mathbf{B}/\mathbf{H}$, shows how permeable a material is to a magnetic field. Using Equation (2.16), permeability and susceptibility are related to each other as

$$\begin{aligned} \mathbf{B} &= (1 + 4\pi\chi)\mathbf{H}, \\ \mu &= 1 + 4\pi\chi. \end{aligned} \tag{2.20}$$

In the SI unit,

$$\begin{aligned} \mathbf{B} &= \mu_0(1 + \chi)\mathbf{H}, \\ &= \mu_0\mu_r\mathbf{H}. \end{aligned} \tag{2.21}$$

Here, μ_r is the relative permeability and is described by the relation $\mu_r = 1 + \chi$. The relative permeability for vacuum is $\mu_r = 1$ and generally inside the material $\mu_r \geq 1$. Magnetic materials can be classified into three regarding relative permeability. In diamagnetic materials, the diamagnetic susceptibility is negative due to the antiparallel orientation of the magnetic dipoles with respect to the external magnetic field, **H**. Therefore, the net magnetic moment is zero. The diamagnetic susceptibility is expressed as

$$\chi^{\text{dia}} = \text{const} < 0. \tag{2.22}$$

Organic materials, metals such as Hg, and superconductors below the critical temperature can be given as examples of diamagnetic materials. The susceptibility for paramagnetic materials is defined as,

$$\chi^{\text{para}} > 0, \tag{2.23}$$

and the temperature dependence of the susceptibility can be represented as

$$\chi^{\text{para}}(T) > 0. \tag{2.24}$$

Each atom in paramagnetic materials has a small magnetic moment that is oriented randomly. When the field is not applied, the net magnetic moment is zero. The magnetic moment in paramagnetic materials is permanent and aligns in an external magnetic field direction, H, with respect to the thermal fluctuations. In Langevin paramagnetism, the magnetic moments of electrons in the inner shell are local due to being partially filled. 4f electrons in rare earth metals and 5f electrons in actinides can be given as examples of localized moments. The equation for the Langevin susceptibility at high temperature is given as

$$\chi^{\text{Langevin}}(T) = \frac{c}{T}, \tag{2.25}$$

which is known as the Curie law. Another type of paramagnetism is Pauli paramagnetism, where nearly free electrons in the valence band have a permanent magnetic moment of 1 μ_B which μ_B is the Bohr magneton. In this case, the susceptibility does not depend on the temperature, which is expressed as

$$\frac{\partial \chi^{\text{Pauli}}(T)}{\partial t} \approx 0. \tag{2.26}$$

The exchange interaction between the permanent magnetic dipoles finds an explanation with quantum mechanics and comprises the origin of the other types of magnetism,i.e., ferromagnetism, ferrimagnetism, and antiferromagnetism. A Critical temperature, T_c which is the Curie temperature, establishes the orientation of magnetic dipoles. Below the Curie temperature, magnetization is spontaneous because of the preferentially oriented magnetic dipoles. At zero temperature, all magnetic moments exhibit parallel orientation with respect to each other. In ferrimagnetism, the lattice has two ferromagnetic sublattices A and B which show different magnetization, $M_A \neq M_B$, the total magnetization is different from zero $(M_A + M_B) \neq 0$ for $T < T_c$. Antiferromagnetism is a kind of ferrimagnetism, but the critical temperature is Neel Temperature, $T_N.M_A = M_B \neq 0$ for $T < T_N$ and $M_A = -M_B$. Therefore, the total magnetization is zero. Above the critical temperature, paramagnetism emerges. The correlation between the temperature and the susceptibility for ferromagnetism, ferrimagnetism, and antiferromagnetism is illustrated in Figure 2.2.

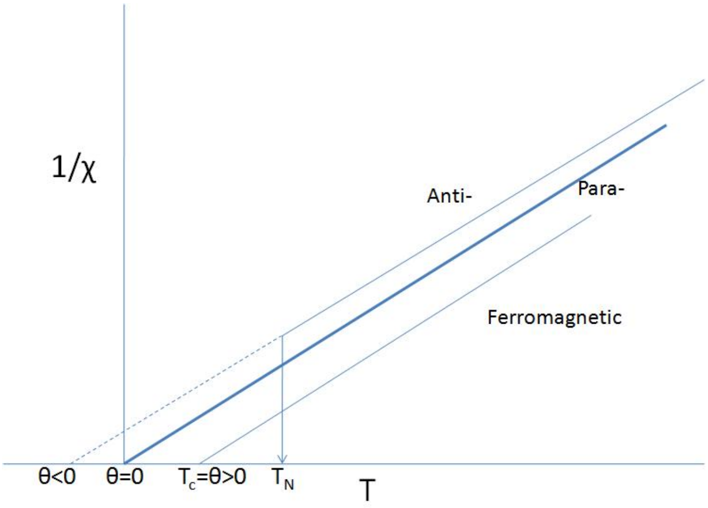

Figure 2.2. Temperature dependence of the magnetic susceptibility χ for (a) diamagnetism and Pauli paramagnetism, and temperature dependence of the inverse magnetic susceptibility χ^{-1} for (b) Langevin paramagnetism, (c) ferromagnetism, antiferromagnetism, and ferrimagnetism. T^* is the critical temperature and θ the paramagnetic Curie temperature [33].

Graphs that show the relation between **M** or **B** and **H** are defined as magnetization curves. Magnetization dependence as a function of the applied field is plotted in Figure 2.3. $\mathbf{M} - \mathbf{H}$ curves are linear for diamagnetic, paramagnetic, and antiferromagnetic materials. Large fields need to be applied to change magnetization slightly. When the field is removed, no magnetization remains. The slope of the M-H curve gives the susceptibility. The susceptibility is small and negative for diamagnetic materials, and the permeability is smaller than one. Paramagnetic and antiferromagnetic materials have a positive slope which means that the susceptibility and permeability are small and positive, and slightly greater than the unity.

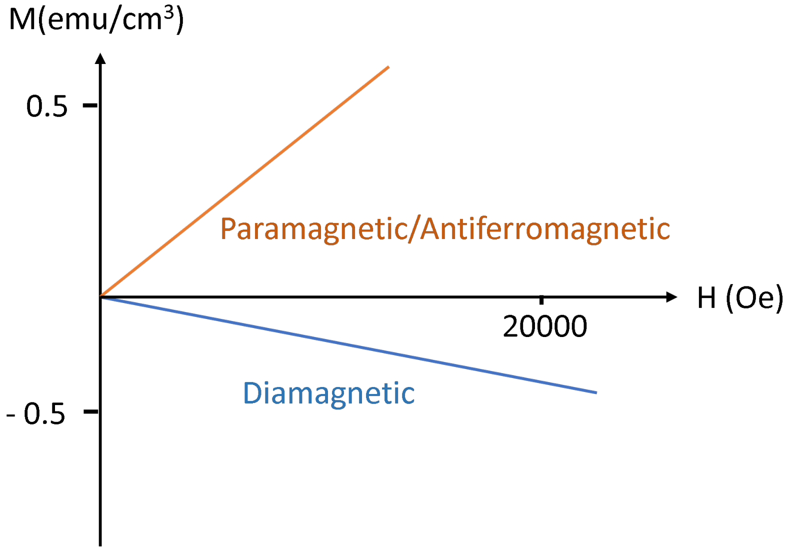

Figure 2.3. Magnetization curve for paramagnetic, antiferromagnetic and diamagnetic materials.

Magnetization curves for ferromagnetic and ferrimagnetic materials are shown in Figure 2.4. The susceptibility and permeability of the ferromagnetic and ferrimagnetic materials are positive and large. Here, the magnetization magnitude is much larger with respect to the other material types. A slightly applied field causes a large amount of change in the magnetization. When the field increases, the magnetization increases as well. After a certain amount of field is applied, the magnetization does not change, which means that magnetization is saturated. When the external field decreases, the magnetization decreases to some extent but does not take the zero value. At zero field, magnetization still exits. When the field is reversed, the graph of $\mathbf{M}$ or $\mathbf{B}$ versus $\mathbf{H}$ curve is known as a hysteresis loop, as shown in Figure 2.5. Permanent magnets are made from ferromagnetic materials owing to their hysteresis behavior. In the beginning, the material is not magnetized. When the field increases in the positive direction, $\mathbf{B}$ increases from 0 to B_s. The magnetization is constant after reaching the saturation, as shown in Figure 2.5. However, $\mathbf{B}$ still increases following the Equation (2.16). Here, $\mathbf{B}_s$ is called the saturation induction, and the curve from zero magnetization to $\mathbf{B}_s$ is defined as the normal induction curve. When H decreases to 0 value, the induction diminishes from $\mathbf{B}_s$ to $\mathbf{B}_r$ which is the residual induction. The reversed field which reduces the induction to zero is called the coercivity, $\mathbf{H}_c$.

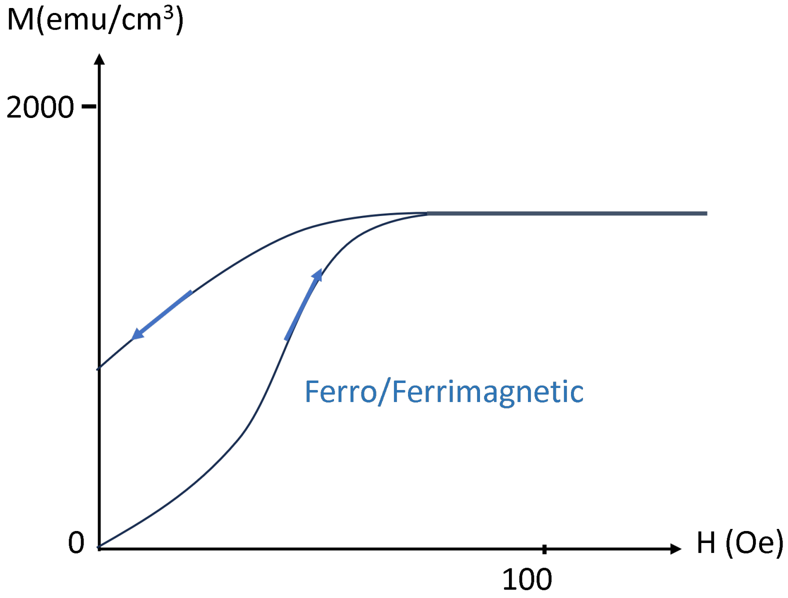

Figure 2.4. Magnetization curve for ferromagnetic and ferrimagnetic materials.

Ferromagnetic materials are either hard or soft with respect to the value of the coercivity. While a hard magnet requires a large field to decrease the induction to 0 value or reach saturation magnetization, a soft magnet can be saturated and demagnetized easily. When the field increases in the reverse direction, saturation is obtained in the reverse direction. There is an inversion symmetry in the hysteresis loop with respect to the origin. Magnetic dipole moments originate from the angular momentum of the electrons. The magnetic moment of a free atom, when there is no magnetic field, includes the orbital angular momenta of the electrons circulating the nucleus and additionally spin angular momentum due to the spin property of the electron. Quantum mechanics clarifies why some isolated atoms have a permanent magnetic dipole moment and other atoms do not. The solution of the Schrodinger equation manifests that the orbital angular momentum of electrons is quantized, and magnetic dipole moments can take only certain values in the presence of an external field.

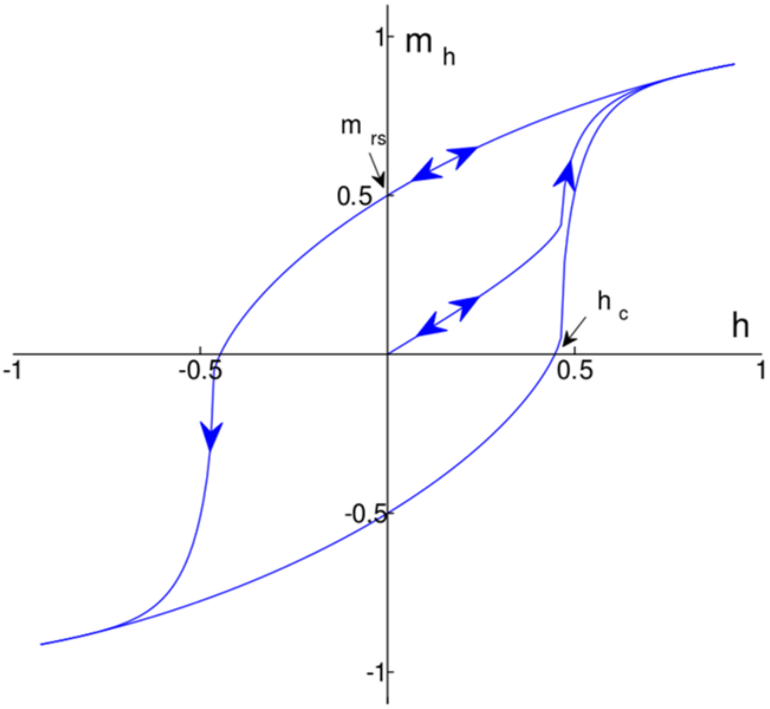

Figure 2.5. Hysteresis loop for the ferromagnetic materials [34].

The Schrodinger equation for the Hydrogen atom is

$$-\frac{\hbar^2}{2m_e}\nabla^2\psi - \frac{e^2}{4\pi\epsilon_0 r} = E\psi, \tag{2.27}$$

where m_e is the electron's mass, e is the electron's charge, and ϵ is the permittivity of the space. The potential is only the coulomb interaction between the electron and the nucleus. The Laplace operator ∇^2 in spherical coordinates is given as

$$\nabla^2 = \frac{1}{r}\frac{\partial^2}{\partial r^2}r + \frac{1}{r^2}(\frac{1}{\sin^2\theta}\frac{\partial^2}{\partial \theta^2} + \frac{1}{\sin\theta}\frac{\partial}{\partial\theta}\sin\theta\frac{\partial}{\partial\theta}). \tag{2.28}$$

The solution to the Schrodinger equation gives the wave function $\psi_{nlm_l}(r,\theta,\phi)$ which consists of both radial and angular parts

$$\psi_{nlm_l}(r,\theta,\phi) = R_{nl}(r)Y_{l,m_l}(\theta,\phi). \tag{2.29}$$

The probability of finding the electron at a point r is the absolute square of the spherical wave function $P = |\psi_{nlm_l}(r,\theta\,\phi)|^2$. The n, I, and m labels are quantum numbers for the permitted solutions of the Schrodinger equation. The n and l labels are the principal and angular momentum quantum numbers, while the label m_l is the magnetic quantum number. Quantum numbers only take the restricted values (n : $1, 2, 3...$, l : $0, 1, 2...(n-1)$, m_l : $-l, (-l+1), ...(l-1), l$). The principal quantum number, n, gives the energy, E_n, of the electron level

$$E_n = -(\frac{m_e e^4}{32\pi^2\epsilon_0^2\hbar^2})\frac{1}{n^2}, \tag{2.30}$$

where $\hbar = \frac{h}{2\pi}$ is the Planck constant. $n = 1$ level has the lowest energy, which is known as the ground state of the hydrogen atom. Electronic shells are formed by the n principal number. The n^{th} shell has n^2 electronic orbitals in which a maximum of two electrons is allowed. The n value affects magnetic properties indirectly since it restricts the allowed values of the l and m_l quantum numbers. The orbital angular momentum, L, is derived from the orbital quantum numbers l as follows:

$$|\mathbf{L}| = \sqrt{l(l+1)}\hbar. \tag{2.31}$$

Labels of l $0, 1, 2, 3, \ldots$ correspond to the atomic orbitals s, p, d, and f. For $l = 0$, there is no contribution from the orbital angular momentum to the magnetic dipole moment. The $n = 1$ level constitutes only s orbitals, the $n = 2$ level contains s and p, and the $n = 3$ level contains s, p, and d orbitals. In the hydrogen atom, orbitals of the same n number have the same energy. The magnetic quantum number,m_l, is for the quantized orientation of the orbital angular momentum with respect to a magnetic field and takes integer values from $-l$ to $+l$. The component of angular momentum along the field direction is calculated as $m_l\hbar$. This value is always less than the magnitude of the total orbital angular momentum. Therefore, the orbital angular momentum vector cannot align along the field direction. It makes a precession in a cone around the field direction. Other than hydrogen, atoms have more electrons interacting with each other and the nucleus. Therefore, the Schrodinger equation can not be solved analytically. The energy of an electron depends on both the principal quantum number and the orbital angular momentum number. Electrons with smaller angular momentum are more stable due to the lower energy. So, they fill the orbits starting from the lowest energy to the highest one. In the periodic table, the order of atomic orbitals is 1s; 2s; 2p; 3s; 3p; 3d; 4s... and so on. The energy of atomic orbital changes in the presence of a magnetic field, H. This change is expressed as

$$E = \mu_0 \mu_B m_l H, \tag{2.32}$$

where $\mu_B = e\hbar/2m_e$ is the Bohr Magneton, the elementary unit of orbital magnetic moment in an atom with a value of 9.274×10^{-24} J/T. In the normal Zeeman effect, the energy is proportional to the orbital angular momentum and the applied field value. The magnetic dipole moment around the field axis is

$$\mathbf{m} = -\mu_B m_l. \tag{2.33}$$

Zeeman splitting between the s and p orbital is shown in Figure 2.6. When there is no field, the s and p orbitals have one energy level. When a magnetic field is applied, the s energy level does not split because the s electron does not have orbital angular momentum. The p energy level splits into three due to the m_l values of -1, 0, and 1. Due to the spin of an electron around its own axis, another quantum number is called the spin quantum number with a value of 1/2. The spin angular momentum is given by the relation

$$|\mathbf{S}| = \sqrt{s(s+1)}\hbar = \frac{\sqrt{3}}{2}\hbar. \tag{2.34}$$

Spin angular momentum is quantized in the vicinity of a magnetic field. Similar to m_l, magnetic spin quantum number, m_s is allowed to take the value of either $+1/2$ or $-1/2$. The spin angular momentum component along the field direction is $m_s\hbar = \pm\hbar/2$. This value is smaller than the magnitude of spin angular momentum. Thus, the spin angular momentum vector makes a precession on a cone around the field axis. A spin magnetic moment along the field direction is given by

$$m = -g_e \mu_B m_s, \tag{2.35}$$

where $g_e = 2.002319$ is the g-factor of the electron. Pauli's exclusion principle implies that electrons with exact quantum numbers (n, l, m_l, m_s) are not allowed to have the same orbit. Therefore, the spin quantum numbers must take the different values of either 1/2 or 1/2. The magnetic moment due to the spin of the electron interacts with the magnetic field originating from the orbital angular momentum of the electron. This interaction is called spin-orbit coupling. The spin-orbit interaction is proportional to Z^4 where Z is the atomic number.

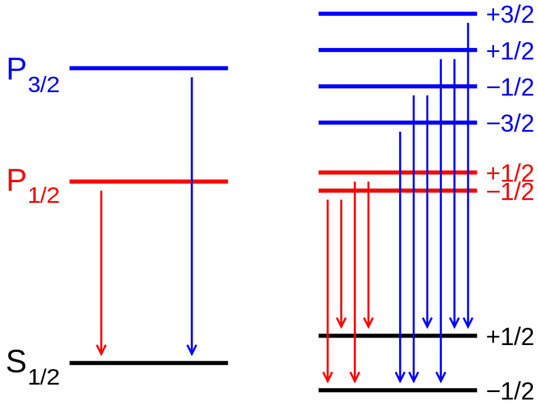

Figure 2.6. The Zeeman effect during a transition between the s and p orbitals [35].

The anomalous Zeeman effect is a result of spin-orbit coupling. The splittings of the upper and lower levels of the transition are not equal due to the anomalous g-factor of the electron with a value of 2. The total angular momentum, J = L + S, and the total magnetic moment, m are not collinear. The value of the atomic magnetic moment in the field axis direction is a function of S, L, and J (rather than just of J as in the normal Zeeman effect) and the relation is given as

$$m = -g \mu_B \mathrm{M}_j. \tag{2.36}$$

In this expression, $\mathrm{M}_J = \mathrm{J}, \mathrm{J}-1, ... -\mathrm{J}$ is the quantum number that shows the projection of the total angular momentum on the field axis. The Lande g-factor is given as

$$g = 1 + \frac{J(J+1) + S(S+1) - L(L+1)}{2J(J+1)}. \tag{2.37}$$

When S is zero, g is equal to one, so, the upper and lower levels in the transition are split by the same amount which is the case in the normal Zeeman effect. When S is not zero, g depends on both L and S. Therefore, the upper and lower levels are split by different amounts. The anomalous Zeeman effect for a transition between the s and p orbitals is shown in Figure 2.7. The allowed transitions are regulated by the selection rules $\Delta\mathrm{M}_J = 0$ or $\Delta\mathrm{M}_J = \pm 1$. If the applied field is very strong, the coupling between S and L can be broken, and each of them directly couples to the magnetic field. S and L further precess about the field axis independently. The electromagnetic field couples only to the orbital angular momentum of the electrons, splitting due to the spin does not occur in the transitions. Thus, the change in the spectrum from the Anomalous Zeeman effect to the normal Zeeman effect is known as the Paschen-Back effect.

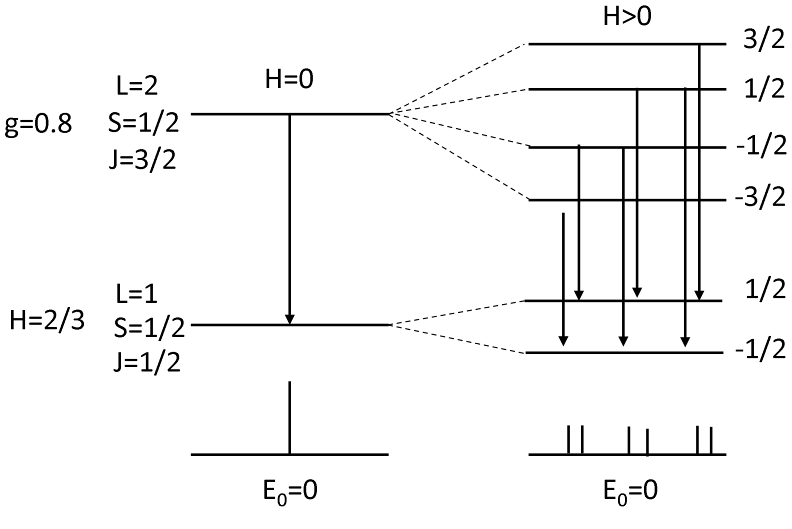

Figure 2.7. Anomalous Zeeman effect transition between the s and p orbitals.

2.3. Ferromagnetism

In this chapter, the concept of ferromagnetism will be detailed. The magnetization of a ferromagnetic material can change from the value of 0 to a saturation value of around 1000 emu/cm^3 applying a magnetic field of only a few Oersteds.

The initial magnetization $M = 0$ can be explained by the domain wall theory, which was postulated by Weiss in 1907 [36]. Weiss molecular field gives an explanation of the Curie-Weiss law, which is $\chi = C/(T - \theta)$ for many paramagnetic materials. Ferromagnetic materials switch to the paramagnetic phase above the Curie temperature, T_c, and the susceptibility follows the Curie-Weiss law. According to Weiss, there is an internal molecular field in the ferromagnetic material below T_c and an internal molecular field occurs for the paramagnetic phase above the T_c. The molecular field magnetizes the material even when a magnetic field is not applied. The magnetization equation in the classical Langevin theory of paramagnetism is given as

$$\mathbf{M} = N\mathbf{m}L(\alpha), \tag{2.38}$$

where $\alpha = mH/k_BT$ and $L(\alpha)$ is the Langevin function. $\mathbf{M}$ versus α is plotted in a solid line in Figure 2.8. In Weiss theory, $\mathbf{M}$ is redefined as $\mathbf{M} = \mathbf{H}_W/\gamma$, where γ is the molecular field constant. Assume that $\mathbf{H}$ only includes the molecular field, since α is proportional to $\mathbf{H}$, $\mathbf{M}$ becomes a linear function of α plotted in the dashed line in Figure 2.8. The only possible physical solutions are the intersection of two curves, either at the origin or at the point $M - spont$, where the material is spontaneously magnetized. The relation between the temperature and the spontaneous magnetization can be explained by replacing H with $H_W = \gamma M$, So, one gets

$$M = (\frac{k_BT}{m\gamma})\alpha. \tag{2.39}$$

Magnetization and α are linearly dependent on each other. The slope of the dashed line increases with the temperature since the slope is dependent on the temperature. The dashed line intersects the Langevin function at a point called M_{spont}. When the dashed line approaches the initial tangent of the Langevin function, the spontaneous magnetization disappears (straight dotted line in Figure 2.8.). The temperature here is the Curie temperature, and for higher temperatures, we have just one solution which has a zero spontaneous magnetization at the origin.

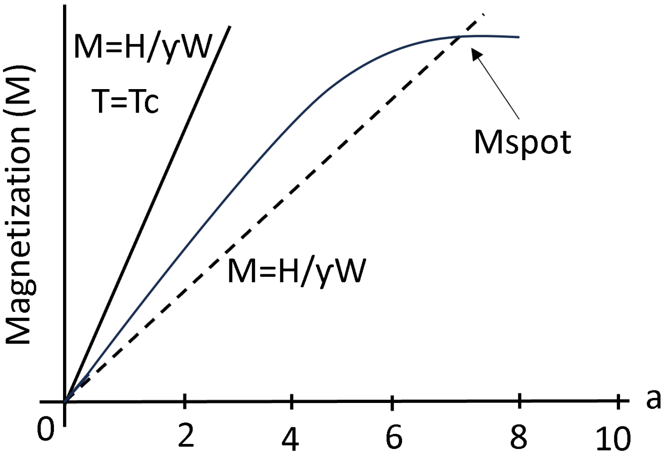

Figure 2.8. Spontaneous magnetization in ferromagnetic materials.

In Figure 2.9, the magnetization decreases smoothly to zero at $T = T_c$. The transition from the ferromagnetic phase to the paramagnetic phase is a second-order phase transition.

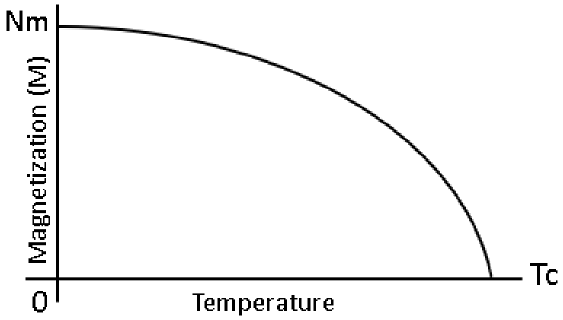

Figure 2.9. Variation of spontaneous magnetization with temperature in ferromagnetic materials [29].

The Curie temperature can be derived from the slope of the Langevin function and the dashed line at the origin as

$$T_c = (\frac{\gamma N m^2}{3k_B}). \tag{2.40}$$

A large molecular field causes a higher Curie temperature, which can be pretended such that strong interaction between magnetic moments needs high thermal energy to rearrange magnetic ordering from the ferromagnetic to the paramagnetic phase. When the Curie temperature is known, the molecular field constant can be determined as well,

$$\gamma = (\frac{3k_B T_c}{Nm^2}). \tag{2.41}$$

Heisenberg explained the Weiss molecular field using quantum mechanics for the many-body problem in 1928. The energy that arises from the electrostatic Coulomb interactions between neighboring atoms forces the electron spins to align parallel to each other. The energy term responsible for the interactions is known as the exchange integral. The exchange interaction is a result of the Pauli exclusion principle. Two electrons with antiparallel spins are permitted to be in the same orbital. The overlap of two electrons gives rise to an increase in the electrostatic Coulomb repulsion between the two. On the contrary, in the case of parallel spins, the electrons must be in different orbitals. As a result, Coulomb's repulsion between electrons is smaller. In fact, it is the spin orientation that determines the Coulomb repulsion between electrons. A rough estimation of the Coulomb energy between two electrons is

$$U = (\frac{e^2}{4\pi\epsilon_0 r}) \approx 2.1 \times 10^{-18}\mathrm{J} \tag{2.42}$$

with r being the average distance between the two electrons, its value is 1 Armstrong. This value is 10^5 times larger than the dipolar interaction between the electrons. The fact that a small change in the electron distribution brings about a large change in total energy reveals the importance of the molecular field.

The helium atom is a good example of a many-body problem, where an electron sits in the 1s atomic orbital and the other electron locates in the 2s orbital. The Hamiltonian, $H = H_1 + H_2 + H_{12}$, includes three terms for the electron and the nucleus interaction separately and for the interaction between each other.

The Hamiltonian terms can be represented such that

$$H_1 = \frac{-\hbar^2}{2m_e}\nabla_1^2 - \frac{Ze^2}{4\pi\epsilon_0 r_1}, \tag{2.43}$$

$$H_2 = \frac{-\hbar^2}{2m_e}\nabla_2^2 - \frac{Ze^2}{4\pi\epsilon_0 r_2}, \tag{2.44}$$

$$H_{12} = -\frac{Ze^2}{4\pi\epsilon_0 r_{12}}. \tag{2.45}$$

In the expressions, H_1 and H_2 constitute the kinetic energy and Coulomb energy term, H_{12} is the Coulomb interaction between electrons. r_{12} is the distance between the atoms, and Z denotes the atom number. Pauli's principle states that the total wave function of a system must be antisymmetric with respect to the interchange of two electrons. The total wave function is the product of spin and spatial parts with the opposite sign. An antisymmetric state for the interchange of spin coordinates is always symmetric for the interchange of spatial coordinates. The wave function of He with the spatial symmetry is expressed as

$$\Psi(\mathbf{r}_1, \mathbf{r}_2) = \frac{1}{\sqrt{2}}[\phi_{1s}(\mathbf{r}_1)\phi_{2s}(\mathbf{r}_2) + \phi_{2s}(\mathbf{r}_1)\phi_{1s}(\mathbf{r}_2)]. \tag{2.46}$$

Similarly, a symmetric state for the interchange of spin coordinates must be antisymmetric for the interchange of spatial coordinates. The spatial antisymmetric wave function is

$$\Psi(\mathbf{r}_1, \mathbf{r}_2) = \frac{1}{\sqrt{2}}[\phi_{1s}(\mathbf{r}_1)\phi_{2s}(\mathbf{r}_2) - \phi_{2s}(\mathbf{r}_1)\phi_{1s}(r_2)], \tag{2.47}$$

where ϕ_{1s} and ϕ_{2s} are the 1s and 2s atomic orbitals and $\mathbf{r}_1$ and $\mathbf{r}_2$ are the electron positions. $1/\sqrt{2}$ is the normalization constant. The energy for the two cases by using the Dirac bra-ket notation is calculated as follows:

$$\begin{aligned}
E &= \langle\Psi(\mathbf{r}_1, \mathbf{r}_2)|H|\Psi(\mathbf{r}_1, \mathbf{r}_2)\rangle \\
&= \frac{1}{2}\langle[\phi_{1s}(\mathbf{r}_1)\phi_{2s}(\mathbf{r}_2) \pm \phi_{2s}(\mathbf{r}_1)\phi_{1s}(\mathbf{r}_2)] \\
&|H_1 + H_2 + H_{12}|[\phi_{1s}(\mathbf{r}_1)\phi_{2s}(\mathbf{r}_2) \pm \phi_{2s}(\mathbf{r}_1)\phi_{1s}(\mathbf{r}_2)]\rangle \\
&= E_1 + E_2 + K \pm J.
\end{aligned} \tag{2.48}$$

It must be noted that the plus sign is for the antiparallel and the minus sign is for the parallel spin orientations. When J is positive, the energy of parallel orientation is smaller than the energy of antiparallel orientation by an amount of 2J. Therefore, a positive J is for parallel spins, which is in the ferromagnetic case. The energy and interactions can be written explicitly such that

$$\begin{aligned}
E_1 &= \langle[\phi_{1s}(\mathbf{r}_1)|H_1|\phi_{1s}(\mathbf{r}_1)\rangle\rangle = \langle[\phi_{1s}(\mathbf{r}_2)|H_2|\phi_{1s}(\mathbf{r}_2)\rangle\rangle,\\
E_2 &= \langle[\phi_{2s}(\mathbf{r}_1)|H_1|\phi_{2s}(\mathbf{r}_1)\rangle\rangle = \langle[\phi_{2s}(\mathbf{r}_2)|H_2|\phi_{2s}(\mathbf{r}_2)\rangle\rangle,\\
K &= \langle[\phi_{1s}(\mathbf{r}_1)\phi_{2s}(\mathbf{r}_2)|H_{12}|\phi_{1s}(\mathbf{r}_1)\phi_{2s}(\mathbf{r}_2)\rangle\rangle\\
&= \langle[\phi_{2s}(\mathbf{r}_1)\phi_{1s}(\mathbf{r}_2)|H_{12}|\phi_{2s}(\mathbf{r}_1)\phi_{1s}(\mathbf{r}_2)\rangle\rangle,\\
J &= \langle[\phi_{1s}(\mathbf{r}_1)\phi_{2s}(\mathbf{r}_2)|H_{12}|\phi_{2s}(\mathbf{r}_1)\phi_{1s}(\mathbf{r}_2)\rangle\rangle\\
&= \langle[\phi_{2s}(\mathbf{r}_1)\phi_{1s}(\mathbf{r}_2)|H_{12}|\phi_{1s}(\mathbf{r}_1)\phi_{2s}(\mathbf{r}_2)\rangle\rangle.
\end{aligned} \tag{2.49}$$

Here, E_1 and E_2 denote the energies of the 1s and 2s orbitals, respectively. K is the Coulomb interaction between the electrons, and J is the exchange interaction. Exchange energy tends to align electron spins and the magnetic dipole moments parallel to each other. The regions where all magnetic dipoles are aligned parallel to each other are called ferromagnetic domains. The demagnetization state of a ferromagnetic material represents the state which composed of many domains with different oriented magnetization vectors, therefore the net magnetization of the material is averaged to zero. The magnetization of the material gives rise to the alignment of all the domains in the same direction. For that reason, ferromagnetic materials are expected to have one single domain in which all magnetic dipole moments point up in the same direction. Domain structures minimize the total magnetic energy of a ferromagnetic material. Specifically, a single domain minimizes the contribution of the exchange energy term to the total magnetic energy. The other energy terms are magnetostatic energy, magnetocrystalline energy, and magnetostrictive energy terms. Magnetostatic energy is responsible for domain formation, and the magnetocrystalline and magnetostrictive energies have an effect on the domain shape and domain size. A ferromagnetic block with a single domain that has a macroscopic magnetization acts as a magnet surrounded by a magnetic field. As seen in Figure 2.10, the associated external field magnetizes the material in the opposite direction rather than its own magnetization. Thus, it is called the demagnetizing field, $\mathbf{H}_d$. The demagnetizing field is the source of the magnetostatic energy that depends on the shape of the material. When the magnetized block separates into two domains with different spin orientations, the demagnetizing field reduces and stores less magnetostatic energy. Since the magnetic moments between the domains are not able to align parallel, the exchange energy of the block increases. For magnetostatic energy with a value of zero, there should not remain any magnetic pole in the block, as shown in Figure 2.10 (c).

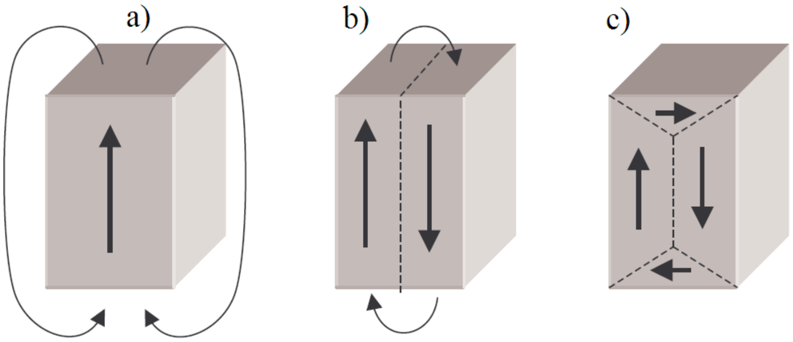

Figure 2.10. Magnetostatic energy and domain configurations in a ferromagnetic material [37].

The magnetization in ferromagnetic crystals prefers to align along certain crystallographic directions, which are defined as the 'easy' axes. When the magnetic field is applied along the easy axis, the crystal reaches saturation magnetization easily. In Figure 2.11, magnetization curves for a ferromagnetic single crystal are plotted for the cases in which the field is applied along the easy and hard axes. When the field is applied along the hard axis, a larger field needs to achieve saturation magnetization.

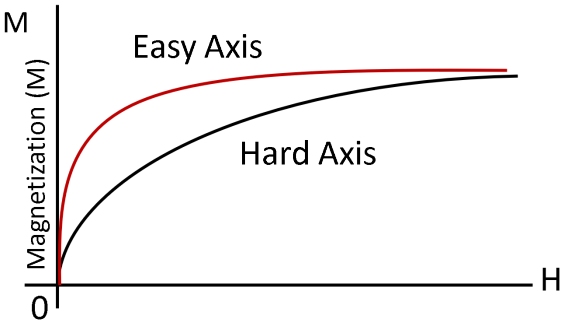

Figure 2.11. Magnetization along the hard and easy axes in a ferromagnetic crystal.

The easy axis of the body-centered cubic (bcc) iron is the (100) direction along the cube edge. Iron is a cubic crystal, so, six edge orientations of (100), (010), (001), (100), (010) and (001) are easy axes. The body diagonal is the hard axis and the face diagonals are the intermediate axis. The unit cell of iron with the easy, intermediate, and hard axes are shown in Figure 2.12. The magnetization aligns along a preferred crystallographic direction due to the magnetocrystalline anisotropy. The crystal energy becomes higher when the magnetization is along the hard axis. The energy difference between magnetization along the easy and hard axes is called the magnetocrystalline anisotropy energy. The area between the hard and easy magnetization curves in Figure 2.11 corresponds to the magnetocrystalline energy of that sample. The magnetocrystalline energy reduces with the domain structures since their magnetization is along the easy axis. In Figure 2.10, the vertical axis is equivalent to a cube edge in bcc iron. Due to the cubic symmetry, the horizontal direction is also an easy axis for the bcc iron. As a result, the domain structures in Figure 2.10 (c) have less magnetocrystalline energy. The horizontal domains at the top and bottom of the crystal are known as 'domains of closure', which emerge when the easy axes are perpendicular to each other. Domain boundaries are the regions where the magnetization direction changes and magnetization does not point along the easy axis. Therefore, domain boundaries are influenced by the magnetocrystalline energy, which prefers large domains with few boundaries.

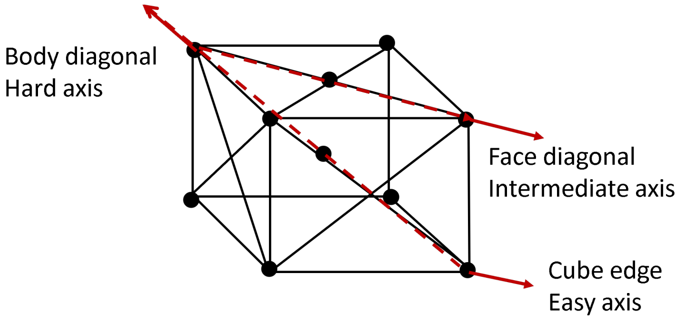

Figure 2.12. Easy, intermediate, and hard axes in a unit cell of bcc iron.

Another term is the magnetostriction energy that is associated with the change in length of a magnetized ferromagnetic material. For example, iron elongates along the magnetization direction, called positive magnetostriction, while Nickel has negative magnetostriction. Although the length changes are small, they affect the domain structure. In Figure 2.13, as a consequence of magnetostriction, the triangular domains of closure tend to elongate horizontally. In contrast, the long vertical domains also try to elongate vertically. Since the elongation in both directions simultaneously is not possible, an elastic strain energy term is introduced to the total magnetic energy. The elastic energy increases when the volume of the domains of closure increases and reduces when the size of the closure domains decreases. This causes smaller primary domains and additional domain walls. Consequently, exchange and magnetostatic energy increase. The reorder of the domain structures can reduce the total energy, as shown in Figure 2.14. The boundaries between neighboring domains in ferromagnetic materials are called domain walls, or Bloch walls, which have a thickness of approximately 10 nm. Magnetization direction changes by either 180° or 90° along the pronounced thickness.

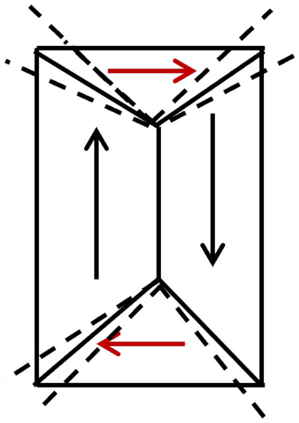

Figure 2.13. Magnetostriction in the triangular domains of closure in bcc iron.

The width of the domain wall is determined by the competition between the energy terms. When the exchange energy is dominant, adjacent magnetic moments are parallel to each other and result in wide domain walls. The change of the angle within the wall is small. On the other hand, the magnetocrystalline anisotropy is dominant if the moments are aligned along the easy axes. This causes narrow domain walls with a sharp transition between the domains. Domain wall does not produce magnetic poles within the material and does not introduce demagnetizing fields to provide minimum energy.

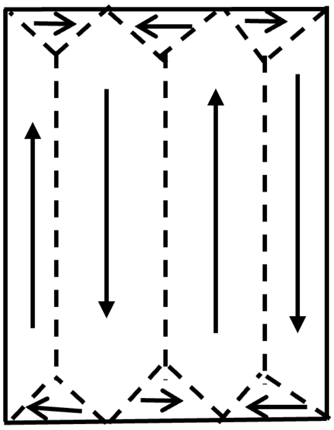

Figure 2.14. Domain reorientation which minimizes the magnetostatic, magnetocrystalline, exchange, and domain wall energy.

A twist boundary is a good example, as shown in Figure 2.15. The magnetization is perpendicular to the boundary and does not change across the wall. Thus, there are no magnetic poles or demagnetizing fields. Another example is 90° tilt boundaries, shown in Figure 2.16. The magnetic moments rotate through the wall by making an angle of 45° with both the wall-normal and the surface.

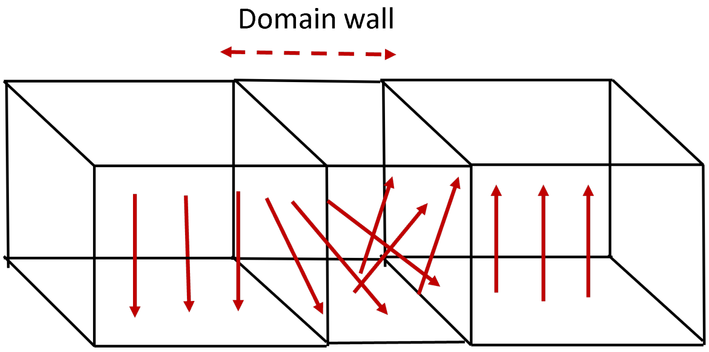

Figure 2.15. A change of 180° in magnetic moment direction within the domain wall.

In magnetic thin films, free poles are formed on the wall surface and cause a decrease in magnetostatic energy. This wall is called the Neel wall, in which the spins rotate around an axis normal to the film surface instead of rotating around an axis normal to the domain wall. The spin rotation in a Neel wall is shown in Figure 2.17.

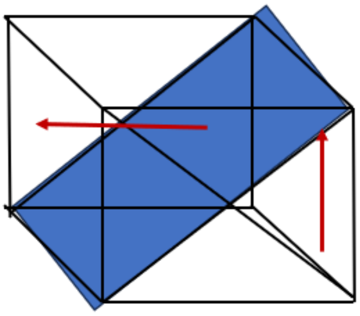

Figure 2.16. A change of 90° in magnetic moment direction within the domain wall.

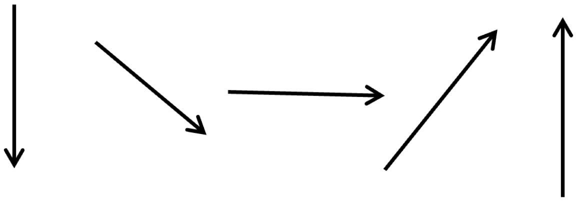

Figure 2.17. Spin rotation in the Neel domain wall.

2.4. Magnetic Anisotropy

Magnetic anisotropy indicates that magnetic properties such as magnetization, and hysteresis curves depend on the direction. The anisotropy is either intrinsic due to the crystal structure or the sample shape, or it is induced by some external mechanism. Spontaneous magnetization arises mainly from the exchange interaction between spins in ferromagnetic and ferrimagnetic materials. Exchange interaction is substantially isotropic, which means that the magnetization can orient itself in any direction inside the crystal with the same energy by the assumption of no other interactions. On the other hand, the existing ferromagnetic materials have spontaneous magnetization which favors lying in a preferred axis or a few axes associated with the crystal structure, the so-called easy axis. To lie the magnetization in another axis rather than the easy axis, one must apply an external field. This phenomenon, called magnetic anisotropy, causes the internal energy to change with the direction of spontaneous magnetization. The energy due to the magnetic anisotropy is defined as magnetic anisotropy energy [38].

2.4.1. Magnetocrystalline Anisotropy

Specifically, magnetocrystalline anisotropy is the magnetic anisotropy energy term that has the same symmetry as the crystal structure of the material. Although the magnetocrystalline anisotropy energy is less than the exchange energy, the anisotropy itself determines the magnetization direction because the exchange interaction is only responsible for the alignment of the magnetic moments parallel to each other without any direction preference. Magnetocrystalline anisotropy is composed of crystal-field interaction and relativistic spin-orbit coupling. Typical anisotropy-energy densities for bcc Fe and for hcp Co are 0.05 $\mathrm{mJ/m^3}$ and 0.5 $\mathrm{mJ/m^3}$, respectively. Rare-earth magnets have higher room-temperature anisotropies of order 10 $\mathrm{mJ/m^3}$. This is due to the large spin-orbit coupling of the rare-earth 4f electrons. Bulk and surface anisotropies, magneto elasticity, and the anisotropic magnetoresistance of metallic ferromagnets are explained by magnetocrystalline anisotropy. As an example, hexagonal cobalt has uniaxial anisotropy with an easy axis parallel to the c-axis of the crystal at room temperature. When the magnetization goes away from the c-axis, the anisotropy energy starts to increase with θ, which is the angle between the c-axis and the magnetization vector, further takes maximum value at $\theta = 90°$, and decreases to the actual value at $\theta = 180°$. The value of anisotropy energy is minimum as long as the magnetization aligns along the $+$ or $-$ direction along the c-axis. The anisotropy energy can be described by a series of powers of $\sin^2\theta$:

$$E_a = K_{u1}\sin^2\theta + K_{u2}\sin^4\theta + K_{u3}\sin^6\theta cos6\phi + ..., \tag{2.50}$$

where K_{ui}'s are the i. uniaxial anisotropy constants and ϕ is the azimuthal angle of the magnetization in a plane perpendicular to the c-axis. Equation (2.50) can be written as well

$$
\begin{aligned}
E_a = & \frac{1}{2}K_{u1}(1-\cos 2\theta) + \frac{1}{8}K_{u2}(3 - 4\cos 2\theta + \cos 4\theta) \\
& + \frac{1}{32}K_{u3}(10 - 15\cos 2\theta + 6\cos 4\theta - \cos 6\theta) \\
& + \frac{1}{32}K_{u4}(10 - 15\cos 2\theta + 6\cos 4\theta - \cos 6\theta)\cos 6\phi + ...
\end{aligned}
\tag{2.51}
$$

The uniaxial anisotropy constants for Co at 15° are $K_{u1} = 4.53 \times 10^5$ J/m^3 and $K_{u2} = 1.44 \times 10^5$ J/m^3 [39]. The higher-order terms can be neglected due to their comparatively too-small values. Since the anisotropy constants are positive, the anisotropy energy increases as the angle increases. At $\theta = 0°$, energy takes the minimum value and the spontaneous magnetization prefers to lie parallel to the c-axis, where the magnetic easy axis is. When the sign of the anisotropy constants is negative, the anisotropy energy reaches the maximum value at the c-axis. The axis in which the energy is unstable is the hard axis of magnetization. In this circumstance, the c-axis becomes the magnetic hard axis. The magnetization is stable in any direction in the c-plane, which means that the c-plane is the easy plane. If $K_{u1} > 0$ and, $K_{u2} < 0$ the direction of stable magnetization makes a cone. In this case, we describe it as the magnetic easy cone. For cubic crystals (Iron and Nickel), the anisotropy energy can be defined by the direction cosines of the magnetization with respect to the three cube edges, which are $\alpha_1 = \sin\theta\cos\phi$, $\alpha_2 = \sin\theta\sin\phi$, and $\alpha_3 = \cos\theta$. The direction cosines are shown in Figure 2.18.

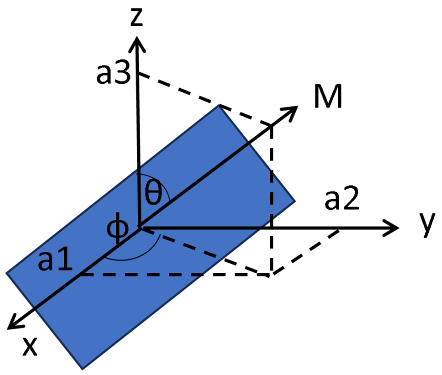

Figure 2.18. The scheme of the direction cosines.

Because of the high symmetry, anisotropy energy is written by expanding in a polynomial series of the direction cosines. The odd powers of α_i should cancel out because the magnetization direction should not change when the sign of α_i changes. Furthermore, when the α_i's interchange, the energy should remain the same. Therefore, the coefficients of the ${\alpha_i}^{2l}{\alpha_j}^{2m}{\alpha_k}^{2n}$ must be the same for the interchange of i, j, k and any combination of l, m, n. The first term must have ${\alpha_1}^2 + {\alpha_2}^2 + {\alpha_3}^2$, which equals 1, and the fourth order terms can be arranged as ${\alpha_1}^4 + {\alpha_2}^4 + {\alpha_3}^4 = 1 - 2({\alpha_1}^2{\alpha_2}^2 + {\alpha_2}^2{\alpha_3}^2 + {\alpha_3}^2{\alpha_1}^2)$. The energy expression becomes

$$\begin{aligned} E_a = K_0 + K_1({\alpha_1}^2{\alpha_2}^2 + {\alpha_2}^2{\alpha_3}^2 + {\alpha_3}^2{\alpha_1}^2) + K_2{\alpha_1}^2{\alpha_2}^2{\alpha_3}^2 \\ + K_3({\alpha_1}^2{\alpha_2}^2 + {\alpha_2}^2{\alpha_3}^2 + {\alpha_3}^2{\alpha_1}^2)^2 + ... \end{aligned} \tag{2.52}$$

Here K_1, K_2, K_3 are the cubic anisotropy constants. For Iron at 20°, $K_1 = 4.72 \times 10^4$ Jm^{-3} and $K_2 = -0.075 \times 10^4$ Jm^{-3} [40]. For Nickel at 23°, $K_1 = -5.7 \times 10^3$ Jm^{-3} and $K_2 = -2.3 \times 10^3$ Jm^{-3} [41]. For [100] direction $(\theta = 90°, \phi = 0°)$, the direction cosines are $\alpha_1 = 1$, $\alpha_2 = \alpha_3 = 0$. Therefore, the energy is equivalent to K_0. For [110] direction $(\theta = 90°, \phi = 45°)$, the direction cosines are $\alpha_1 = 1 = \alpha_2 = 1/\sqrt{2}, \alpha_3 = 0$. The energy is

$$E_a = K_0 + \frac{1}{4}K_1. \tag{2.53}$$

For [111] direction $(\theta = 54.7°, \phi = 45°)$, the direction cosines are $\alpha_1 = \alpha_2 = \alpha_3 = 1/\sqrt{3}$, the magnetocrystalline energy becomes

$$E_a = \frac{1}{3}K_1 + \frac{1}{27}K_2 + \frac{1}{9}K_3 + ... \tag{2.54}$$

If $K_1 > 0$, neglecting K_2 and K_3 terms for iron, the [100] direction is the magnetic easy axis, and the [111] direction is the magnetic hard axis as the energy at [100] direction is less than the energy at [111] direction.

Due to the cubic symmetry, other easy axes are [010] and [001] as shown in the anisotropy energy diagram in Figure 2.19. In the diagram, the vector along the direction of the spontaneous magnetization has a value of the length of $E_a + 2/3K_1$. Concave parts of the surface are along the $[100], [010]$, and $[001]$ directions which are the easy axes where the energy is minimum. If $K_1 < 0$, neglecting K_2 and K_3 terms for nickel, the anisotropy energy is less than zero, and the easy axes are $[111], [\bar{1}11], [1\bar{1}1], [11\bar{1}]$

and the [100] direction is the hard axis since the energy at [111] direction is less than the energy at [100] direction. Figure 2.19 shows the anisotropy energy diagram with an additional $2|K_1|$ term. The surface is convex along the cube axes and concave along the $< 111 >$ axes.

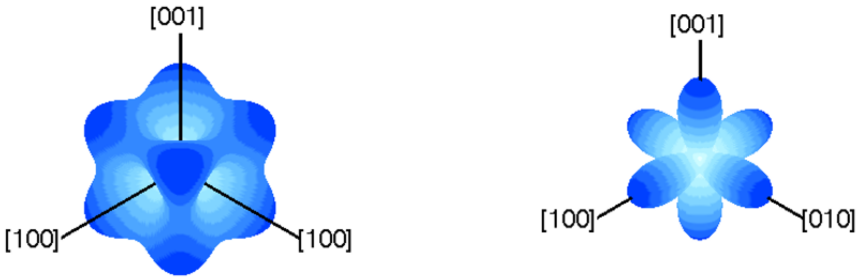

Figure 2.19. The left image: Cubic anisotropy energy diagram of iron for $K_1 > 0$ and $K_2 = 0$. (Radial vector is equal to $E_a + 1/2K_1$.) The right image: Anisotropy energy of nickel for $K_1 < 0$ and $K_2 = 0$ (Radial vector is $E_a + 2|K_1|$) [42].

The corresponding relative magnetization versus external magnetic field is given in Figure 2.20. After applying a small amount of field, the easy magnetization axes are determined to be [100] for bcc-Fe, [111] for fcc- Ni, and [0001]-directions for hcp-Co. In Figure 2.21, anisotropy energy are sketched for the case of $K_1 = K_3 = 0$, $K_2 > 0$ (the left image) and $K_2 < 0$ (the right image). The energy is zero in the x-y, y-z, and x-z planes. However, in $< 111 >$ planes, the energy is maximum when $K_2 > 0$ and is minimum when $K_2 < 0$.

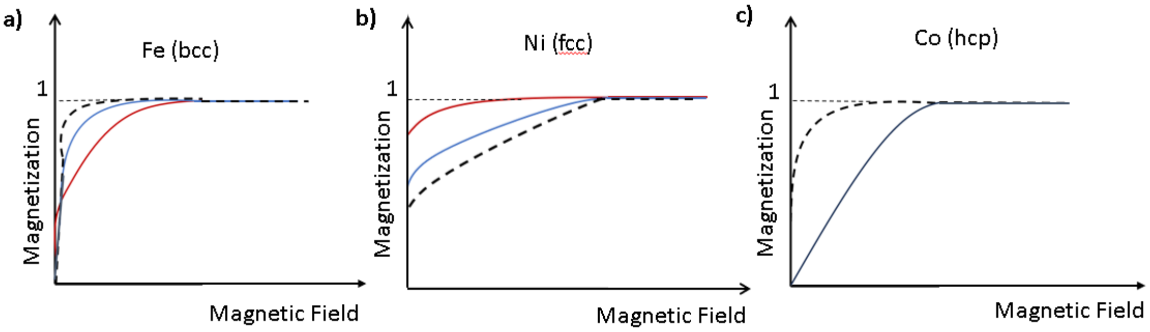

Figure 2.20. Magnetization vs magnetic field graph of (a) bcc-Fe, (b) fcc-Ni, and (c) hcp-Co.

In many ferromagnetic and ferrimagnetic materials, K_1 is higher than K_2, therefore K_2 term is neglected in the anisotropy energy. But, when the magnetization is in the $< 111 >$ plane, the K_2 term can not be neglected. If K_1 and K_2 terms are in the same order, the (110) plane can be an easy or hard axis. The temperature affects the anisotropy constants and the magnetic easy and hard axis. To give an example, for Ni, K_1 is negative below the temperature of 400K and positive above the temperature of 400K. [30].

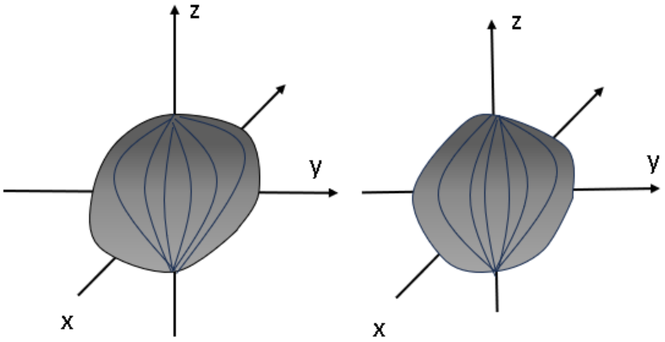

Figure 2.21. The left image: Cubic anisotropy energy diagram of iron for $K_1 = 0$ 0 and $K_2 > 0$. (Radial vector is equal to $E_a + 2/3K_1$.) The right image: Anisotropy energy of nickel for $K_1 = 0$ and $K_2 < 0$ (Radial vector is $E_a + 9/16K_2$) [43].

The magnetocrystalline anisotropy energy per volume for tetragonal and hexagonal materials is given by

$$E_{crys} = K_0 + K_1 \sin^2\theta + K_2 \sin^4\theta + K_3 \sin^6\theta.... \tag{2.55}$$

For positive values of K_1 and K_2, for $\sin\theta = 0$ the energy gets minimum value, and the c-axis [0001] is the easy magnetic axis. If K_1 and K_2 are both negative, the minimum energy is reached at $\sin\theta = 1$. In this case, the easy magnetization axis is along the [0001]-plane, and the [0001]-direction is the hard magnetization axis (see Figure 2.22). If the signs of K_1 and K_2 are different from each other, the easy axis rotates from the c-axis towards the [0001]-plane with $\sin^2\theta = -\frac{K_1}{2K_2}$. The general formula for the anisotropy energy is given as

$$E_a = A_2 cos2\theta + A_4 cos4\theta + A_6 cos6\theta + a_8 cos8\theta + ... \tag{2.56}$$

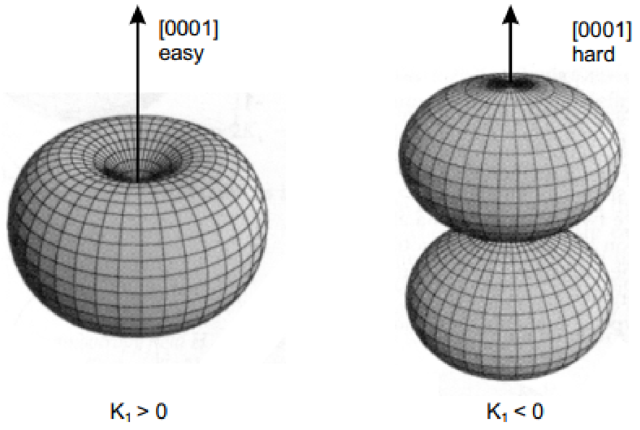

Figure 2.22. The left image: for $K_1 > 0$, the magnetic easy axis is along the [0001] direction.The right image: for $K_1 < 0$, the magnetic hard axis is along the [0001] direction [43].

By comparing Equation (2.54) to (2.51),

$$\begin{aligned} A_2 &= -\frac{1}{2}K_{u1} - \frac{1}{2}K_{u2} - \frac{15}{32}K_{u3}(1+6cos6\phi) + ..., \\ A_4 &= \frac{1}{2}K_{u2} + \frac{3}{16}K_{u3}(1+6cos6\phi) + ..., \\ A_6 &= -\frac{1}{32}K_{u3}(1+6cos6\phi) + ... \end{aligned} \tag{2.57}$$

For the (001) plane of cubic crystal, the constants are

$$\begin{aligned} A_2 &= 0, \\ A_4 &= -\frac{1}{8}K_1 - \frac{1}{32}K_3 + ..., \\ A_6 &= 0, \\ A_8 &= \frac{1}{128}K_3 + ... \end{aligned} \tag{2.58}$$

For the $(1\bar{1}0)$ plane, the constants are

$$\begin{aligned} A_2 &= -\frac{1}{8}K_1 - \frac{1}{128}K_2 - \frac{11}{256}K_3 + ..., \\ A_4 &= -\frac{3}{32}K_1 - \frac{1}{64}K_2 - \frac{17}{512}K_3 - ..., \\ A_6 &= \frac{1}{128}K_2 + \frac{3}{256}K_3 + ..., \\ A_8 &= \frac{9}{2048}K_3 + ... \end{aligned} \tag{2.59}$$

For the (111) plane, the constants are

$$\begin{aligned} A_2 &= 0, \\ A_4 &= 0, \\ A_6 &= -\frac{1}{108}K_2, \\ A_8 &= 0. \end{aligned} \tag{2.60}$$

There is also a contribution from the magnetostatic energy to the magnetic anisotropy energy. The magnetostatic energy is

$$U = \frac{1}{2\mu_0} N I^2 v, \tag{2.61}$$

where N is the demagnetizing factor, I is the intensity and v is the volume of the magnetic material. The demagnetizing factors along the x and y axes of an ellipsoidal magnetic material whose long axis is on the z-axis are given as

$$N_x = N_y = \frac{1}{2}(1 - N_z). \tag{2.62}$$

Equation (2.59) can be written by x, y, and z components

$$\begin{aligned} U &= \frac{1}{2\mu_0} I_s^2 v (N_x sin^2\theta cos^2\phi + N_y sin^2\theta sin^2\phi + N_z cos^2\theta) \\ &= \frac{1}{4\mu_0} I_s^2 v (3N_z - 1) cos^2\theta + \text{const.}. \end{aligned} \tag{2.63}$$

The magnetostatic energy is associated with the magnetization direction, which is called shape anisotropy.

2.4.2. Uniaxial Anisotropy

Figure 2.23 demonstrates some energy landscapes. Isotropic, easy-axis, and easy-plane magnets are shown in the upper row, and the bottom row shows the fourth- and sixth-order energy terms. K_1 term determines two possible equilibrium states, easy-axis, as in Figure 2.23.(b) and easy-plane, as in Figure 2.23.(c). Higher-order uniaxial anisotropies create spin structures with angles $0 < \theta < \pi/2$. Figure 2.23.(d) shows an easy cone magnetism for $K_1 < 0$ and $K_2 > -\frac{K_1}{2}$, where the equilibrium magnetization makes an angle $\theta_c = arcsin(|K_1|/2K_2)$ with the c-axis. Since fourth-order anisotropies are smaller than second-order anisotropies by one or two orders of magnitude, easy-cone magnetism occurs at specific temperatures. Figure 2.24 shows how the energy landscapes take form when non-uniaxial fourth- and sixth-order terms are added. Figure 2.24 (a-d) are the most observed forms [44], but (e) and (f) show exotic magnets with very low symmetry [45].

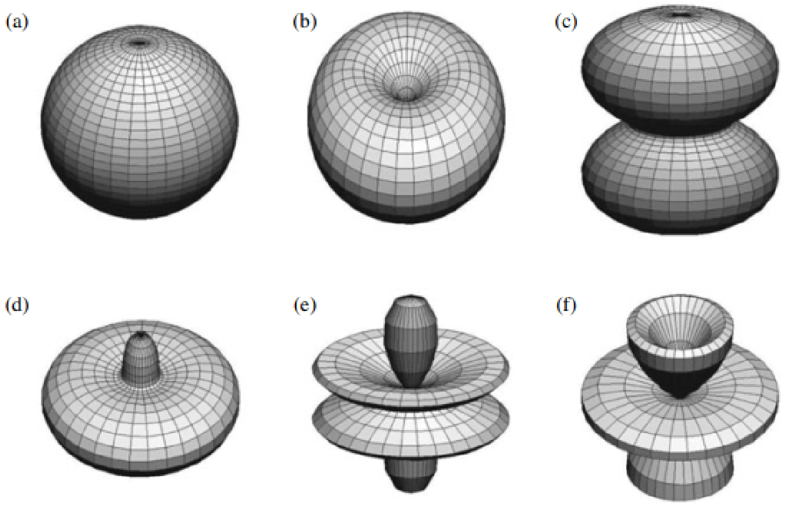

Figure 2.23. Uniaxial anisotropy energy. (a) isotropic, (b) easy axis, (c) easy plane, (d) easy cone, and (e–f) sixth-order landscapes [31].

Dimensional analysis of $K_1/\mu_0 M_s$ has the dimension of a magnetic field. This is a good approach to compare the anisotropies with fields such as the applied field and the coercivity H_c. The anisotropy field of uniaxial magnets can be written as

$$H_a = \frac{2K_1}{\mu_0 M_s}. \tag{2.64}$$

The factor of 2 allows a comparison of H_a with the coercive field. In the Equation (2.55), inserting $\theta = 90°$ and $\theta = 0°$, the anisotropy field becomes

$$H_a = \frac{2(K_1 + K_2 + K_3)}{\mu_0 M_s}. \tag{2.65}$$

The slope of the perpendicular magnetization curve is equivalent to the anisotropy field. The K_2 and K_3 terms do not affect coercivity. In cubic crystals, the anisotropy field of Fe ($K_1 > 0$) is explained as the same as Equation (2.64) while for Ni ($K_1 < 0$), the anisotropy field is $H_a = -4K_1/(3\mu_0 M_s)$. The effect of the anisotropy field of Nickel can be seen in the energy landscape in the (111) direction in Figure 2.24 (b) different from the (001) direction in Figure 2.24 (a).

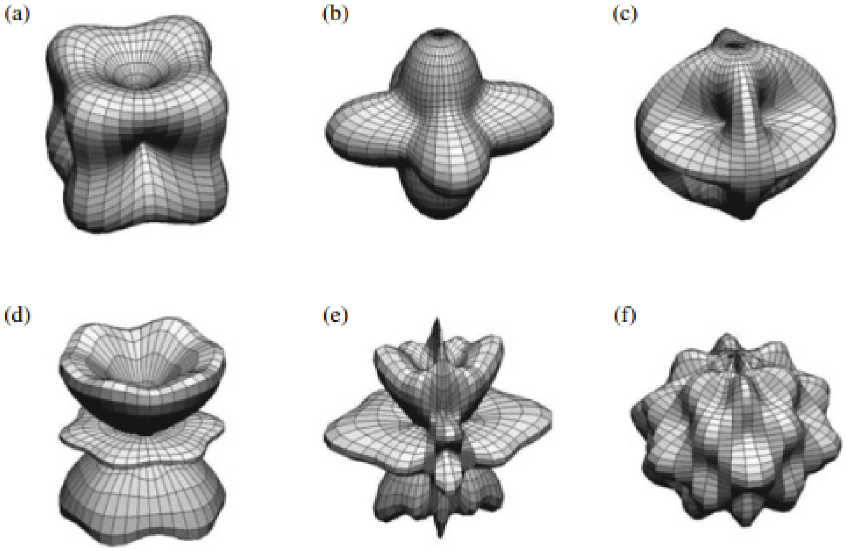

Figure 2.24. Energy surfaces for higher-order anisotropies: (a–c) cubic magnets and (d–f) magnets with low symmetry [31].

2.4.3. Shape Anisotropy

Since the grains are oriented in arbitrary directions, polycrystalline materials do not have magnetocrystalline anisotropy. While the magnetization of the spherical samples is isotropic, it is the shape of the samples that determines the magnetic easy axes for non-spherical samples. This type of anisotropy is called shape anisotropy. At this point, one must consider the stray and demagnetizing field of a sample. The relationship $B = \mu_0(H + M)$ is known to be valid for infinite systems. On the other hand, the stray field that occurs outside the samples with a finite size due to the poles at their surface leads to a demagnetizing field inside the sample. The energy due to the stray field is given

$$E_{str} = -\frac{1}{2}\int \mu_0 M.H_{\text{demag}} dV \tag{2.66}$$

with H_{demag} being the demagnetizing field. For a general shape, the calculation of H_{demag} is highly complicated. For some symmetric objects such as ellipsoids, the relationship that gives H_{demag} is given

$$H_{\text{demag}} = -NM, \tag{2.67}$$

where N is the demagnetizing tensor. If H_{demag} is inserted in the Equation (2.62), one gets

$$\begin{aligned} E_{str} &= \frac{1}{2}\int \mu_0 MNMdV \\ &= \frac{1}{2}V\mu_0 MNM. \end{aligned} \tag{2.68}$$

In this expression, V is the volume of the sample and N is a diagonal tensor with the trace being $trN = 1$ as long as the semiaxes of the ellipsoid (a,b,c) are equivalent to the axes of the coordination system. The magnetization direction with respect to the semiaxes can be written in terms of the direction cosine α_a, α_b, and α_c. Then, the tensor is given as

$$\begin{pmatrix} N_a & 0 & 0 \\ 0 & N_b & 0 \\ 0 & 0 & N_c \end{pmatrix}. \tag{2.69}$$

The stray field energy per volume is given by

$$E_{str} = \frac{1}{2}\mu_0 M^2(N_a\alpha_a^2 + N_b\alpha_b^2 + N_c\alpha_c^2). \tag{2.70}$$

For the sphere, the tensor can be written as

$$\begin{pmatrix} 1/3 & 0 & 0 \\ 0 & 1/3 & 0 \\ 0 & 0 & 1/3 \end{pmatrix}. \tag{2.71}$$

The stray field energy of the sphere is given by

$$E_{str} = \frac{1}{6}\mu_0 M^2. \tag{2.72}$$

Here, the direction cosines are normalized. Following this relationship, one concludes that the energy is isotropic for the sphere samples. In the case of a spheroid, the length of the semiminor axes, a, and b, is the same but is different from the semimajor axis, c. So, the diagonal elements are $N_a = N_b$ and $N_c = 12N_a$. One gets the stray field energy of a spheroid as

$$\begin{aligned} E_{str} &= \frac{1}{2}\mu_0 M^2 (N_a \sin^2\theta \cos^2\phi + N_a \sin^2\theta \sin^2\phi + (1-2N_a)\cos^2\phi), \\ &= \frac{1}{2}\mu_0 M^2 (N_a + (1-3N_a)\cos^2\theta, \end{aligned} \tag{2.73}$$

where θ is the angle between the magnetization and the z-axis for an infinitely long cylinder, $a = b, c = \infty$. By inserting the diagonal elements of the demagnetizing tensor ($N_a = N_b = 1/2$ and $N_c = 0$) in the stray field energy equation, one gets

$$\begin{aligned} E_{str} &= \frac{1}{2}\mu_0 M^2 \frac{1}{2}(\sin^2\theta\cos^2\phi + \sin^2\theta\sin^2\phi), \\ &= \frac{1}{4}\mu_0 M^2 \sin^2\theta. \end{aligned} \tag{2.74}$$

For a thin plate, $a = b = \infty$, and $N_a = N_b = 0$ and $N_c = 1$. The stray field energy of the thin plate is,

$$E_{str} = \frac{1}{2}\mu_0 M^2 \cos^2\theta. \tag{2.75}$$

This relationship holds also for magnetic thin films and multilayers. The energy can be rearranged as

$$E_{str} = K_0 + K^V_{shape} M^2 \sin^2\theta \tag{2.76}$$

with $K^V_{shape} \propto -M^2 < 0$. At the angle of $\theta = 90°$, the energy takes the minimum value, which means that the shape anisotropy causes the magnetic easy axes to lie along the surface of the thin film. In thin films, the magnetization is in-plane if the shape anisotropy dominates the magnetocrystalline energy of the thin film.

2.4.4. Surface Anisotropy

The anisotropy discussed up to now is about the volume, without regard to the surface and interface effects. The effective anisotropy constant due to the broken symmetry at the interface can be written as the sum of both the volume and the surface contributions and can be expressed as

$$K^{eff} = K^V + 2\frac{K^s}{d}. \tag{2.77}$$

K^V and K^s stand for the magnetocrystalline anisotropy constants due to the volume and surface, respectively. The surface-dependent term is inversely proportional to the thickness of the thin film. By multiplying both sides of the Equation (2.73) with thickness, d one gets

$$d \cdot K^{eff} = d \cdot K^V + 2K^s. \tag{2.78}$$

If the relation between $d \cdot K^{eff}$ and d is plotted, the slope gives the volume anisotropy constant with a negative value, and the $2K^s$ term is the zero crossing as seen in the Figure 2.25 for a thin Co layer of different thicknesses, d on a Pd substrate [46]. The K^V takes a negative value due to the shape anisotropy. Thus, the film exhibits an in-plane magnetization. One can notice that the K^s takes a positive value.

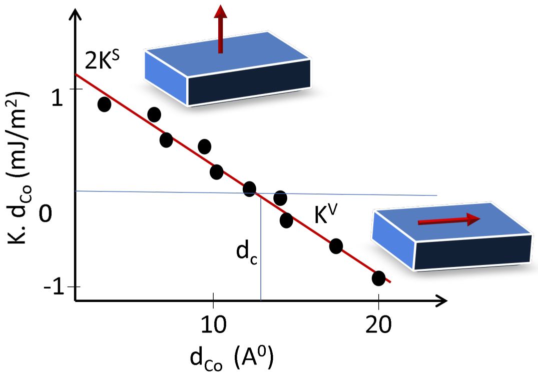

Figure 2.25. Magnetic anisotropy of a Co thin film on a Pd substrate as a function of the Co thickness.

The critical thickness is given by

$$d_c = -\frac{2K^s}{K^v}. \tag{2.79}$$

The change in the sign of the K_{eff} determines the magnetization type and the required thicknesses. If $d < d_c$, the magnetization is out-of-plane, and if $d > d_c$, the magnetization is in-plane. This explains that thick films exhibit in-plane magnetization with the governing volume anisotropy contribution. The surface contribution increases with the decrease in thickness. Below d_c, spin reorientation transition occurs towards the surface normal. The surface anisotropy gives rise to the rotation of the magnetic easy axis within the surface. As an example, the magnetic easy axis of a thin bcc-Fe(110) layer is along the $[1\bar{1}0]$ direction. Above the thickness of $60A^{\circ}$, the easy axis rotates towards the [001] direction as in the bulk samples.

2.4.5. Stress Anisotropy

In the previous sections related to anisotropy, the crystal structure of the magnetic sample was estimated to have a fixed lattice constant. (The distance between atoms in the crystal was constant.) In this chapter, the effect of an elastic degree of freedom on the magnetic properties is presented. Both the crystal elasticity and the magnetic properties of the sample influence each other. This causes magnetoelastic interaction. The magnetocrystalline energy per volume for cubic crystals was

$$E_{crys} = K_1^{cubic} \cdot O(\alpha^4). \tag{2.80}$$

The energy of the tetragonal systems due to the reduced symmetry can be written by

$$\begin{aligned} E_{crys} &= K_1^{tetra} \cdot O(\alpha^2), \\ &= K_1^{tetra} \sin^2\theta, \\ &= K_1^{tetra}(1-\alpha_3^2). \end{aligned} \tag{2.81}$$

The constant terms are omitted to make an easy comparison between the cubic and tetragonal anisotropy constants. The cubic and the tetragonal constants are related to the 4^{th} and 2^{th} order terms, respectively. Therefore, one can assume that K_1^{tetra} is approximately a hundred times bigger than the K_1^{cubic}. A small deformation in the crystal chemistry induces a transition from cubic to tetragonal symmetry and further results in a change in magnetic anisotropy. The deformation from cubic to tetragonal crystalline structure happens below the Curie temperature since the crystal energy is decreased. There is a limitation to this transition. The elasticity energy which is $E_{el} = 1/2C\epsilon^2$ increases during the distortion. The total anisotropy energy with the addition of the elasticity term is given by

$$E_{crys} = K_1(1-\alpha_3^2)\epsilon + 1/2C\epsilon^2. \tag{2.82}$$

Here, ϵ is the deformation parameter. The minimum energy gives the change in length,λ as

$$\lambda = \frac{\delta l}{l} = \frac{-K_1}{C}(1 - \alpha_3^2). \tag{2.83}$$

The value of the magnetostriction is roughly in the order of 10^{-5}. It should be noted that λ depends on the crystalline direction. Therefore, the ϵ parameter turns into the ε tensor. The elastic energy for cubic structure is

$$\begin{aligned} E_{el}^{cubic} &= \frac{1}{2}c_{11}(\varepsilon_{11}^2 + \varepsilon_{22}^2 + \varepsilon_{33}^2) + c_{12}(\varepsilon_{11}\varepsilon_{22} + \varepsilon_{11}\varepsilon_{33} + \varepsilon_{22}\varepsilon_{33}) \\ &+ \frac{1}{2}c_{44}\varepsilon_{12}^2 + \varepsilon_{13}^2 + \varepsilon_{23}^2). \end{aligned} \tag{2.84}$$

In the expression, ε_{ij} is the deformation tensor, and c_{ij} is the elastic constant. For the hexagonal symmetry, the elastic energy is given by

$$\begin{aligned} E_{el}^{hex} &= \frac{1}{2}c_{11}(\varepsilon_{11}^2 + \varepsilon_{22}^2) \\ &+ \frac{1}{2}c_{33}\varepsilon_{33}^2 + c_{12}\varepsilon_{11}\varepsilon_{22} + c_{13}(\varepsilon_{11} + \varepsilon_{22})\varepsilon_{33} \\ &+ \frac{1}{2}c_{44}(\varepsilon_{13}^2 + \varepsilon_{23}^2) + (c_{11} - c_{12})\varepsilon_{12}^2. \end{aligned} \tag{2.85}$$

If the direction of magnetostriction is written in terms of the direction cosines β_i, for cubic crystals, one gets

$$\begin{aligned} \lambda = \frac{\delta l}{l} &= \frac{3}{2} \cdot \lambda_{100}(\alpha_1^2\beta_1^2 + \alpha_2^2\beta_2^2 + \alpha_3^2\beta_3^2 - \frac{1}{3}) \\ &+ 3\lambda_{111}(\alpha_1\alpha_2\beta_1\beta_2 + \alpha_1\alpha_3\beta_1\beta_3 + \alpha_2\alpha_3\beta_2\beta_3), \end{aligned} \tag{2.86}$$

where λ_{100} and λ_{111} are the magnetostriction saturation values. Here, the measurement direction is along the [100] direction, and the spontaneous magnetization axis is along the [111] direction. The relationships between magnetostriction (λ), elastic c_{ij} and magnetoelastic (B_i) constants are

$$\begin{aligned} \lambda_{100} &= -\frac{2}{3}\frac{B_1}{c_{11} - c_{12}}, \\ \lambda_{111} &= -\frac{1}{3}\frac{B_2}{c_{44}}. \end{aligned} \tag{2.87}$$

The magnetostriction λ_{110} can be written by the linear combination of the λ_{100} and λ_{111} as

$$\lambda_{110} = \frac{1}{4}\lambda_{100} + \frac{3}{4}\lambda_{111}. \tag{2.88}$$

In the case of isotropic magnetostriction $\lambda_{100} = \lambda_{111}$, one gets $\lambda_{100} = \lambda_{111} = \lambda_{110} = \lambda_0$. By inserting them in the Equation (2.84), the magnetostriction is obtained as

$$\lambda = \lambda_0(\cos^2\theta - \frac{1}{3}), \tag{2.89}$$

where θ is the angle between the magnetization direction and the measurement direction and given by the means of cosines directions as$\theta =$arccos$(\sum_i \alpha_i\beta_i)$. The magnetostriction is not dependent on the crystallographic direction. The magnetostriction of hexagonal crystalline structures is expressed as

$$\begin{aligned}\lambda = \frac{\delta l}{l} &= \lambda_A((\alpha_1\beta_1 + \alpha_2\beta_2)^2 - (\alpha_1\beta_1 + \alpha_2\beta_2)\alpha_3\beta_3) \\ &+ \lambda_B((1-\alpha_3^2)(1-\beta_3^2) - (\alpha_1\beta_1 + \alpha_2\beta_2)^2) \\ &+ \lambda_C((1-\alpha_3^2)\beta_3^2 - (\alpha_1\beta_1 + \alpha_2\beta_2)\alpha_3\beta_3) \\ &+ \lambda_D(\alpha_1\beta_1 + \alpha_2\beta_2)\alpha_3\beta_3,\end{aligned} \tag{2.90}$$

where the magnetostrictions are labeled as $\lambda_A, \lambda_B, \lambda_C, \lambda_D$ with the relations below

$$\begin{aligned}\lambda_A &= \frac{B_2c_{13} - (2B_3 + B_1)c_{33}}{c_{33}(c_{11} + c_{12}) - 2c_{13}^2} + \frac{B_1}{2(c_{11} - c_{22})}, \\ \lambda_B &= \frac{B_2c_{13} - (2B_3 + B_1)c_{33}}{c_{33}(c_{11} + c_{12}) - 2c_{13}^2} - \frac{B_1}{2(c_{11} - c_{22})}, \\ \lambda_C &= \frac{B_2c_{11} + c_{12}) - (2B_3 + B_1)c_{13}}{c_{33}(c_{11} + c_{12} - 2c_{13}^2)}, \\ \lambda_D &= \frac{1}{4}(\lambda_A + \lambda_B + \lambda_C + \frac{B_4}{c_{44}}).\end{aligned} \tag{2.91}$$

Positive magnetostriction refers to dilatation, while negative magnetostriction represents contraction. For Nickel, $\lambda_{100}, \lambda_{110}$ and λ_{111} are negative. This shows the contraction in all directions. For Fe, λ_{100} is positive while λ_{111} is negative. This means that along the [100] direction which is the easy magnetization axis, there is a dilatation that causes a deformation from a cubic to a tetragonal crystalline structure. For alloys, stoichiometry determines the amount of magnetostriction. Specifically, Permalloy $Ni_{40}Fe_{60}$ has isotropic magnetostriction ($\lambda_{100} = \lambda_{110} = \lambda_{111}$) whereas $Ni_{15}Fe_{85}$ the magnetostriction values in all directions are equal but nearly zero, which is important for technological applications [47]. The magnetic anisotropy up to now is due to the intrinsic nature of the material. The induced magnetic anisotropy can occur through some external treatments, such as thermal annealing. By annealing the sample under a magnetic field applied in different directions, the magnetization curve can change as given in Figure 2.26. Curves A and C are obtained after annealing in a magnetic field which are parallel and perpendicular to the measurement direction.

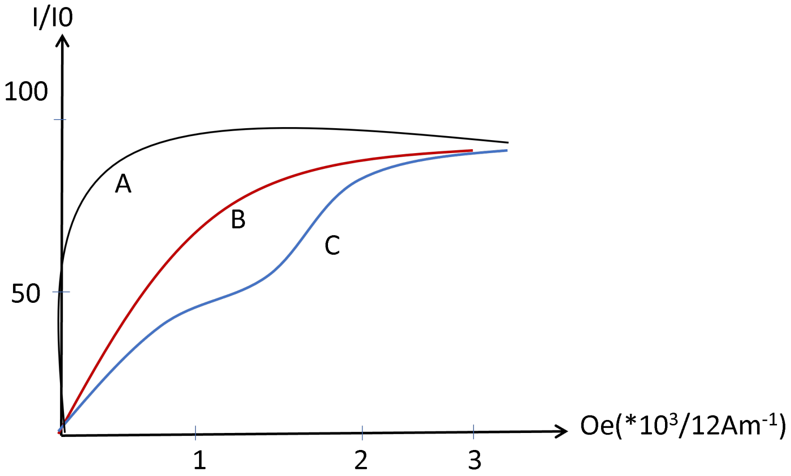

Figure 2.26. Magnetization curves of Permalloy which were cooled from 600° C for the case of A. longitudinal applied magnetic field, B. no magnetic field applied, and C. perpendicular/ circular applied magnetic field [43].

One can conclude that the easy axis of the induced anisotropy is parallel to the direction of the annealing field. Curve B is obtained in the absence of the applied field during annealing, Each magnetic domain has local easy axes that are parallel to the direction of spontaneous magnetization. Another induced magnetic anisotropy is roll anisotropy. For example, $Ni_{50}Fe_{50}$ alloy can be cold-rolled with the (001) plane in the sheet along the [100] rolling direction. After rolling to %50 thickness reduction, a large uniaxial anisotropy occurs. The easy axis is in-sheet plane and perpendicular to the rolling direction. Domain rotation leads to magnetization parallel to the rolling direction with a linear magnetization curve and a constant permeability within a wide range of applied magnetic fields. The magnetization curve is given in Figure 2.27.

Both magnetic annealing and the roll anisotropy lead to directional order. If a NiFe alloy is bombarded with neutrons in a magnetic field applied along the [100] direction, an anisotropy is obtained due to the defects, and the easy axis orients parallel to the [100] direction. Photo-induced magnetic anisotropy is obtained by annealing in electromagnetic radiation. Stress annealing leads to an induced anisotropy.

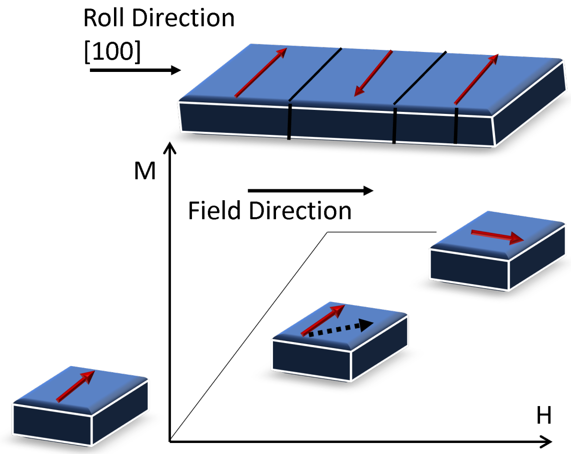

Figure 2.27. Cold rolling mechanism and magnetization curve for $Ni_{50}Fe_{50}$.

2.4.6. Determination of Magnetic Anisotropy

Depending on the Pauli exclusion principle, spins have a totally antisymmetric wave function in the microscopic model for the spins. By excluding the spin-orbit coupling, a symmetric orbital wave function is coupled with an antisymmetric spin wave function or the inverse is true. The symmetric and antisymmetric orbital wave functions for two electrons at the i and j sites of the crystal are given as

$$\begin{aligned}\Psi_{sym} &= \phi_i(\mathbf{r_1})\phi_j(\mathbf{r_2}) + \phi_i(\mathbf{r_2})\phi_j(\mathbf{r_1}),\\ \Psi_{anti} &= \phi_i(\mathbf{r_1})\phi_j(\mathbf{r_2}) - \phi_i(\mathbf{r_2})\phi_j(\mathbf{r_1}),\end{aligned} \tag{2.92}$$

where ϕ's are the wave functions and $\mathbf{r}$'s are the coordinates of the electrons. The energies correspond to

$$\begin{aligned}E_{sym} &= K + J_{ij},\\ E_{anti} &= K - J_{ij}.\end{aligned} \tag{2.93}$$

K stands for the kinetic and potential energy terms and J_{ij} is the exchange energy which is

$$J_{ij} = \langle \phi_i(\mathbf{r_1})\phi_j(\mathbf{r_2}) \mid \frac{e^2}{\mid \mathbf{r_1} - \mathbf{r_2} \mid} \mid \phi_i(\mathbf{r_1})\phi_j(\mathbf{r_2})\rangle. \tag{2.94}$$

The exchange integral is important when the wave functions overlap and the energy levels are split. In insulators, the exchange integral is between the nearest or the next nearest neighbors of the spin system, since the electron wave functions are generally in the atomic sites. For the magnetic oxides, the exchange integral is mediated through an oxygen atom, which is called the superexchange interaction. Let $\mathbf{s_1}$ and $\mathbf{s_2}$ be the spin angular momentum of two individual electrons. Then, the eigenvalues of the total spin angular momentum for symmetric and antisymmetric spin states are 1 and 0, respectively:

$$S^2 = s_1^2 + s_2^2 + 2\mathbf{s_1} \cdot \mathbf{s_2}. \tag{2.95}$$

The eigenvalues are given by the following relation

$$S(S+1) = 2s(s+1) + 2\mathbf{s_1}.\mathbf{s_2}. \tag{2.96}$$

For the value of $s = 1/2$, the operator, $1/2 + \mathbf{s_1}.\mathbf{s_2}$, has the eigenvalues of -1 and $+1$ in the symmetric and antisymmetric spin states. The Hamiltonian relation for this system can be written as

$$H_{ij} = K - (\frac{1}{2} + \mathbf{s_1}.\mathbf{s_2})J_{ij}. \tag{2.97}$$

Here, the interactions between the spins originate from the quantum mechanical Coulomb repulsion. When a magnetic field, $H-0$ is applied to the spin system, the Hamiltonian is expressed in the form

$$H = H_Z + H_E \tag{2.98}$$

with H_Z being the Zeeman energy term and H_E being the exchange energy term. The Zeeman energy is given as

$$H_Z = g\mu_B H_0 \sum_i S_i^z, \tag{2.99}$$

where H_0 is along the z-direction. The Hamiltonian has a positive sign since the spin is assumed to be antiparallel to the magnetic moment. The exchange term is

$$H_E = -2\sum_{i>j} J_{ij}\mathbf{S_i} \cdot \mathbf{S_j}. \tag{2.100}$$

The sum on i is for all lattice and in the exchange term, the sum on $i > j$ is for not counting the same interactions between nearest neighbors twice. The exchange term is positive for the parallel spin alignment and negative for the antiparallel spin alignment. Dipole-dipole interactions which cause magnetostatic demagnetization effects and spin-orbit interactions which cause anisotropy energy can be included in the spin Hamiltonian by replacing the applied field H_0 with the effective field, H_{eff}. The Hamiltonian for an exchange coupled spin assemble is

$$H_E = g\mu_B \sum_i \mathbf{H_i^{eff}} \cdot \mathbf{S_i} - 2\sum_{i>j} J_{ij}\mathbf{S_i} \cdot \mathbf{S_j}. \tag{2.101}$$

If a spin is flipped parallel to the field, while the other spins are aligned antiparallel to the applied field, this state of the spin configuration leads to a large amount of energy of the order $1000k_B$ erg. One can make a comparison with Zeeman energy of $1k_B$ erg if a spin is flipped in the presence of 10 kOe. In order to decrease the large arising exchange energy, numerous spins share one spin flip with small angle deviations between adjacent spins. The exchange energy is proportional to the cosine of the angle between adjacent spins. Therefore, the small angle deviation between adjacent spins allows less exchange energy. At low temperatures, the excited states called spin waves or magnons give information about the thermodynamic behavior of ferromagnets. Bloch was the first to announce that the states around the ground are sinusoidal spin waves [48]. In the mean of raising and lowering operators $S_i^{\pm} = S_i^x \pm S_i^y$ and S_i^z, Equation (2.101) takes the form

$$\begin{aligned} H_E = g\mu_B H^{eff} &\sum_i S_i^z \\ -2\sum_{i,j}&(S_i^z S_j^z + \frac{1}{2}S_i^+ S_j^- + \frac{1}{2}S_i^- S_j^+). \end{aligned} \tag{2.102}$$

The eigenfunction of a spin system with a number of N at the ground state at 0 K can be written by means of the eigenstates of spin-down states, α_i

$$\Psi_0 = \alpha_1\alpha_2\alpha_3...\alpha_N. \tag{2.103}$$

When the temperature increases, the spin system reaches an excited state such that a single spin is flipped. The excited state eigenfunction can be written as

$$\Psi_i = \alpha_1\alpha_2\alpha_3...\alpha_{i-1}\beta_i\alpha_{i+1}...\alpha_N, \tag{2.104}$$

where β_i shows the spin-up state. The linear combination of the eigenfunctions gives the eigenfunction of the Hamiltonian in Equation (2.101) such that

$$\Psi_k = \sum_i C_i^k \Psi_i. \tag{2.105}$$

Since individual spins interact with their nearest neighbors which are $(i-1)^{th}$ and $(i+1)^{th}$ spins by the exchange integral, J, one can follow the relation

$$<\psi_i|H(1/2)|\Psi_k>=<\psi_i|E|\Psi_k> \tag{2.106}$$

and acquire a set of equations

$$E + \frac{1}{2}(N-2)g\mu_B H_0 + \frac{1}{2}(N-5)JC_i^k + J(C_{i+1}^k + C_{i-1}^k) = 0 \tag{2.107}$$

with solutions

$$C_i^k = N^{\frac{1}{2}} e^{ika}, \tag{2.108}$$

where a is the distance between the spins. If periodic boundary conditions are implemented as $C_i^k = C_{i+N}^k$, the wave vector, k, can be found in the following relation as

$$\frac{kaN}{2\pi} = 0, 1, 2, ..., N-1. \tag{2.109}$$

By inserting 2.108 in the Equation (2.107), the energy relation turns into

$$E - E_0 = g\mu_B H^{eff} + 2J(1-\cos k\alpha) = \hbar w_k, \tag{2.110}$$

where E_0 is the ground state energy and $\hbar w_k$ is the energy to excite the spin waves. If the value of the wave vector k is very small, $ka << 1$, then one gets the well-known relation as

$$\hbar w_k = g\mu_B H^{eff} + Dk^2, \tag{2.111}$$

where $D = J\alpha^2$ for $s = 1/2$ linear chain. Spin waves are excited by an effective surface anisotropy field H^{surf} which arises in the first and N^{th} layers. The spins at the surface are not exchange coupled to their nearest neighbor, therefore symmetric surface terms are added to the Hamiltonian to handle this issue

$$H = g\mu_B H^{surf}(S_1^z + S_N^z). \tag{2.112}$$

For $i = 1$ and $i = N$, the energy relation in Equation (2.107) takes the form as

$$\begin{aligned} E + \frac{1}{2}(N-2)g\mu_B H^{eff} + g\mu_B H^{surf}\frac{1}{2}(N-3)JC_1^k + JC_2^k) = 0, \\ E + \frac{1}{2}(N-2)g\mu_B H^{eff} + g\mu_B H^{surf}\frac{1}{2}(N-3)JC_N^k + JC_{N-1}^k) = 0. \end{aligned} \tag{2.113}$$

The solutions are given as

$$C_{i+1}^k = \alpha \cos ki\alpha + \beta \sin ki\alpha \tag{2.114}$$

and the energy relation is given as

$$E = -\frac{1}{2}(N-2)g\mu_B H^{eff} - \frac{1}{2}(N-5)J - 2J\cos k\alpha - g\mu_B H^{surf}. \tag{2.115}$$

The effect of the surface field is just to customize the allowed values of k. The ratio of the coefficients is given as

$$\frac{\alpha}{\beta} = \frac{J\sin k\alpha}{-j(1-\cos k\alpha + g\mu_B H^{surf})}. \tag{2.116}$$

From here, one can conclude that the surface pinning and the spin wave boundary condition depend on the k values. In the case of small k values, the surface anisotropy overcomes the boundary conditions and pins the spins at the surface. When k increases, the exchange interaction increases and dominates the surface anisotropy if $Dk^2 > g\mu_B H^{surf}$. This refers to the presence of a nearly free boundary condition. The allowed values of k can be determined by the relation

$$\cot Nk\alpha = \frac{2(1-g\mu_B H^{surf}/J)}{g\mu_B H^{surf}/J(2-\alpha)}\tan(1/2k\alpha) - \frac{g\mu_B H^{surf}/J}{2-\alpha}\cot(k\alpha). \tag{2.117}$$

If $g\mu_B H^{surf}/J = 1$, nodes are located at $i = 0$ and $i = N+1$. If the value of $g\mu_B H^{surf}/J$ is different rather than 1, then the nodes depend on the k value. In magnetic garnets, the unit cell has up to 32 spins. Lattice sites obey the relation $r_{ij} = r_i + \rho_j$ where ρ_ν represents the intracell vectors for each μ different magnetic site in the unit cell to distinguish the sublattices in the ground state with spins up or down along an axis. The spin deviation operators on the μ distinguished magnetic sites in the magnetic unit cell can explain oscillations apart from the ground state. The normal modes can be attained by expanding the spin wave deviation operators in the spin wave operators [49]. Since magnetic garnets have sites of dodecahedral c, octahedral a, and tetrahedral d symmetry, one must consider the sum of those sites. For Yttrium iron garnet, YIG, the optical and acoustic branches are given as

$$\begin{aligned} \hbar w_0^{op} &\approx -10 J_{ad}, \\ \hbar w_k^{ac} &\approx \frac{5}{16}(8J_{aa} - 5J_{ad} + 3J_{dd})a^2k^2. \end{aligned} \tag{2.118}$$

The nineteen optical modes do not show a strong k dependence [50]. In general, magnetic garnets have acoustic modes with the following relation,

$$\hbar w_k^{ac} \approx \frac{200J_{aa} - 125J_{ad} + 75J_{dd} - 20J_{dc}S_c + 50J_{ac}S_c}{16(-5+6S_c)}a^2k^2. \tag{2.119}$$

Iron ions at the sites of a and d are weakly exchange-coupled to the rare earth ions at the c sites. Therefore, the optical spectra consist of 19 perturbed high-energy YIG modes and 12 low-energy optical modes. The garnet has one acoustic spin wave branch with higher-order optical spin wave branches with high frequencies in the absence of a magnetic field. In this case, the spin wave energy is expressed as Dk^2. The frequency of the optical modes in YIG is in the infrared or visible range in the electromagnetic spectrum. Under the assumption of the two sublattices which consist of two strongly exchange coupled Fe sites as one sublattice and the rare earth (RE) garnet site which is less coupled to the sublattice of iron sites, for specific temperatures at which the magnetization of iron and rare earth garnet are equivalent to each other and for some rare earth ion concentrations, the condition $g_{Fe}M_{Fe} - g_{RE}M_{RE} = 0$ results in zero total angular momentum. Then, the frequency for the optical modes can shift to the microwave regime. Other spin interaction terms can contribute to the Hamiltonian, which has the Zeeman and exchange anisotropy energy terms. Spin-orbit and spin-spin interactions in a tetragonal crystal symmetry with the unit axis in the z direction can induce a second-order crystal field effect in the Hamiltonian given as

$$H_c = D\sum_i (S_z^i)^2 - \frac{1}{3}S(S+1). \tag{2.120}$$

In the expression, D determines the interaction strength. If D is small, this term can be added to the Zeeman term as

$$H_Z = -g_{\parallel}\mu_B H_0^z \sum_i S_z^i - g_{\perp}\mu_B(H_0^x \sum_i S_i^x + H_0^y \sum_i S_i^y). \tag{2.121}$$

The pair Hamiltonian can be written in terms of the spin operators as

$$H_{pair} = \sum_{i>j} \sum_{k,l} J_{ij}^{kl} S_k^i S_l^j, \tag{2.122}$$

where $k, l = x, y, z$. For cylindrical symmetry, the Hamiltonian can be written in the form of $H = H_E + H_d$, where H_E is the exchange energy.H_d is given as

$$H_{pair} = \sum_{i>j} d_{ij}^* \mathbf{S}_I \mathbf{S}_j - 3\mathbf{r}_{ij}^{-2} (\mathbf{S}_i \mathbf{r}_{ij})(\mathbf{S}_j \mathbf{r}_{ij}), \tag{2.123}$$

where $= (d_{ij})^* = d_{ij} + p_{ij}$ and $d_{ij} = g^2(\mu^2)_B(r^{-3})_{ij}$. Here, d_{ij} term is the long-range coupling term related to the magnetic dipolar interactions, and p_{ij} term is the short-range pseudo dipolar exchange interaction. The long-range $(r^{-3})_{ij}$ interactions determine the spin wave dispersion relation and relaxation process. The dispersion relation for a Hamiltonian which has Zeeman, exchange, dipolar, and pseudo-dipolar interactions is given in the following form

$$\hbar w_k = (Dk^2 + g\mu_B H^{eff})(Dk^2 + g\mu_B H^{eff} + g\mu_B 4\pi M \sin^2\theta_k)^{1/2}. \tag{2.124}$$

In the expression, θ_k is the angle between the propagation constant,k, and the magnetization vector, M. H_{eff} can be written as

$$H^{eff} = H_0 - 4\pi N_z M \tag{2.125}$$

with H_0 being the applied field and N_z being the demagnetizing factor along the z-axis. If $4\pi M$ is smaller than H^{eff}, one can get a relation,

$$\hbar w_k \approx Dk^2 + g\mu_B H^{eff} + g\mu_B 2\pi M \sin^2\theta_k. \tag{2.126}$$

This is known as the circular precession approximation. The dispersion relation for $\sin^2\theta_k = 1$ is shown in the broken line in Figure 2.28. The exact dispersion relation is shown by the solid line. The surface anisotropy field establishes boundary conditions and determines the allowed spin wave modes in the ferromagnetic spectrum of a magnetic garnet. The magnetic field orientation and the temperature affect the spectrum, as seen in Figure 2.29 and 2.30.

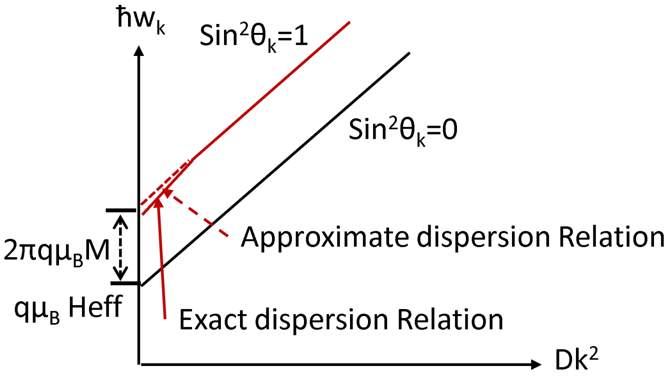

Figure 2.28. Spin wave dispersion relation. The solid line and broken line show Equation (2.124) and Equation (2.126), respectively.

The weak signal at a high field at the parallel orientation is non-propagating surface spin wave mode. The spin wave spectrum does not show only one signal for a critical angle between the magnetic field and the film plane. The pinning is a function of angle due to the isotropic energy and the uniaxial surface anisotropy energy. A non-propagating surface mode emerges depending on the sign of energies between the critical angle and parallel or perpendicular orientation of the magnetic field to the film plane. Different from magnetostatic surface modes in Damon and Esbach [51], the propagation constant of non-propagating surface modes in the film plane is zero. The field at which non-propagating surface modes arise is dependent on the exchange of energy. The angular dependence of the non-propagating surface modes was introduced by Pusskarzki [52]. The surface modes' behavior is determined by mainly the surface anisotropy energies. Assume an uniaxial surface anisotropy field acting on the spin system, and the Hamiltonian includes the nearest neighbor Exchange and the Zeeman energy terms

$$H = -g \sum_{l,j,l+g,j\prime} J_g \mathbf{S}_{lj} \cdot \mathbf{S}_{l+g,j\prime} + g\mu_B \sum_{l,j} H_l^{eff} \cdot \mathbf{S}_{lj}. \tag{2.127}$$

The sum is over j spins located at l sites in the spin system. J_g is the exchange integral between layers l and $l+g$. H_{eff} is the uniform and unidirectional effective magnetic field. The unidirectional surface anisotropy field acts on the spins at the surface and establishes the pinning of surface spins, and determines the allowed k modes by applying a boundary condition.

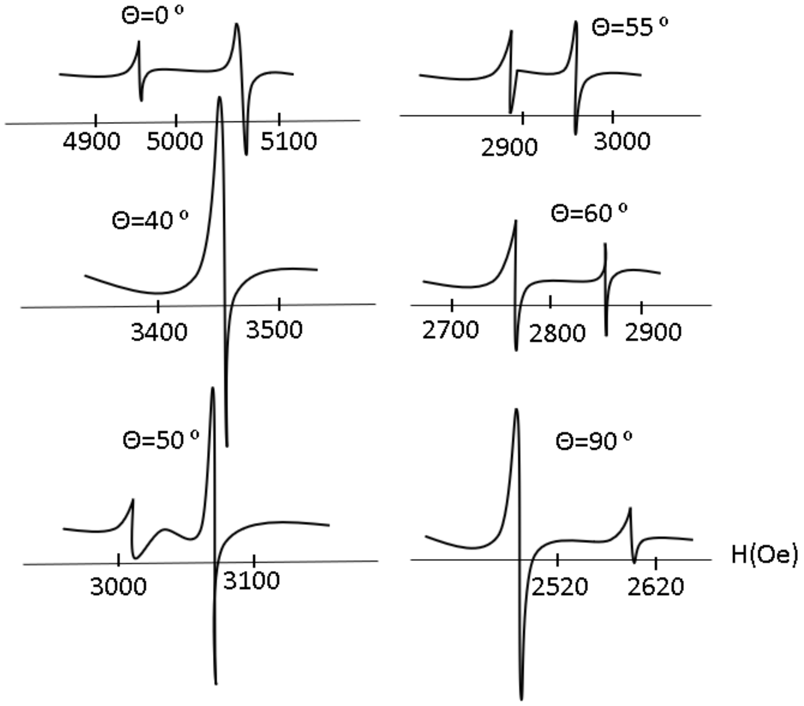

Figure 2.29. Spin wave spectra of YIG film at 9.2 GHz for the different orientations of the magnetic field with respect to the film normal.

The energy of the surface spins are

$$E_{surf} = E_{int} + 2S^2 z_1 J_1 A, \tag{2.128}$$

where the ground state energy of the interior spins are

$$E_{int} = -2S^2 z_0 J_0 - 4S^2 z_1 J_1 - g\mu_B \mathbf{S}_{\hat{r}} \cdot \mathbf{H}^{eff}. \tag{2.129}$$

Here, J_0 is the exchange constant between spins in the l layer, and J_1 is the exchange constant between spins in different layers. The pinning parameter, A is given as,

$$A = 1 - \frac{g\mu_B}{2sz_1J_1}\hat{\mathbf{r}} \cdot \mathbf{H}^{surf}, \tag{2.130}$$

where $\hat{r}$ is the unit vector of spin moments and z_1 is the number of nearest neighbors. The energy of surface spins increases by unpinned boundary conditions or decreases by pinned boundary conditions induced due to the surface anisotropy field.

The energy density is given in the following relation,

$$
\begin{aligned}
E_{surf} &= g\mu_B S a^{-2}\hat{\mathbf{r}} \cdot \mathbf{H}^{surf} \\
&= 2s^2 z_1 J_1 a^{-2}(A-1),
\end{aligned}
\tag{2.131}
$$

where a is the lattice constant. Figure 2.31 illustrates the k values of the spin-wave spectrum. The dashed lines show the antisymmetric and the solid line shows the symmetric state. When the surface pinning parameter goes to minus infinity, the pinned boundary condition $k_n = n\pi/Na$ applies to the lowest order mode. When A goes to unity, the lowest energy mode $k_1 = 0$. The first antisymmetric mode k_2 is equivalent to zero at $A = (N+1)/(N-1)$. For $A > 1$, k_1 is imaginary and a surface acoustic wave occurs. Adding, k_2 is an antisymmetric surface wave at $A = (N+1)/(N-1)$. For $A \leq 1$, the optical surface modes occur. The transverse magnetization component for a few orders of spin-wave modes as a function of the surface parameter, A is given in Figure 2.32.

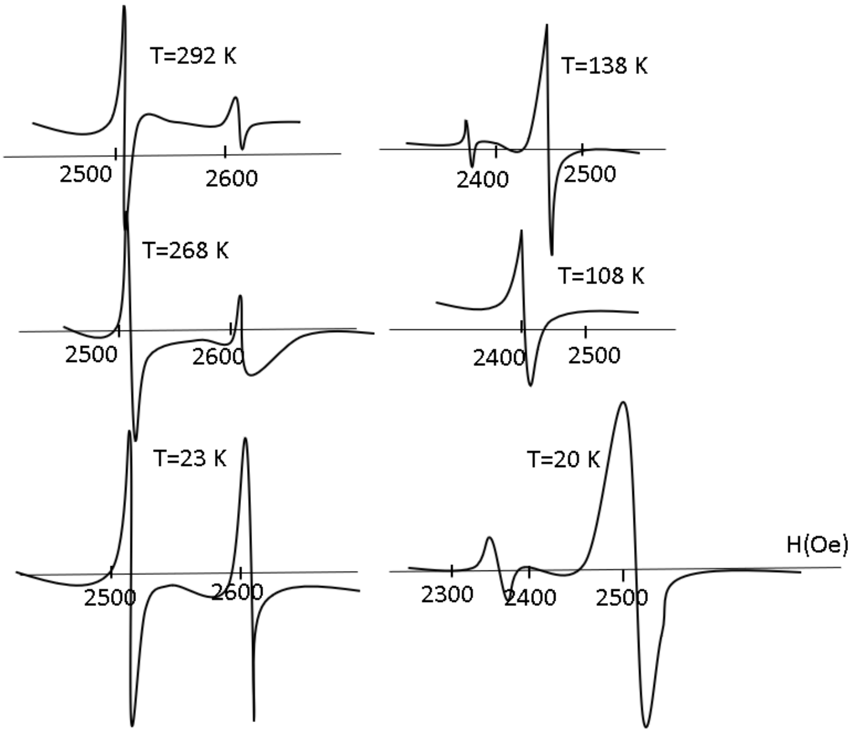

Figure 2.30. Spin wave spectra of YIG film at 9.2 GHz at different temperatures for the parallel orientations of the magnetic field.

The precession amplitude increases as A goes from minus infinity to unity, and at $A = 1$, the precession amplitude becomes zero. When A approaches infinity, the precession increases and returns to the same form as the one $A = -\infty$. The first two modes at $A > 1$ are the surface modes. Their energy shifts to the lower energy and transverse magnitude decrease.

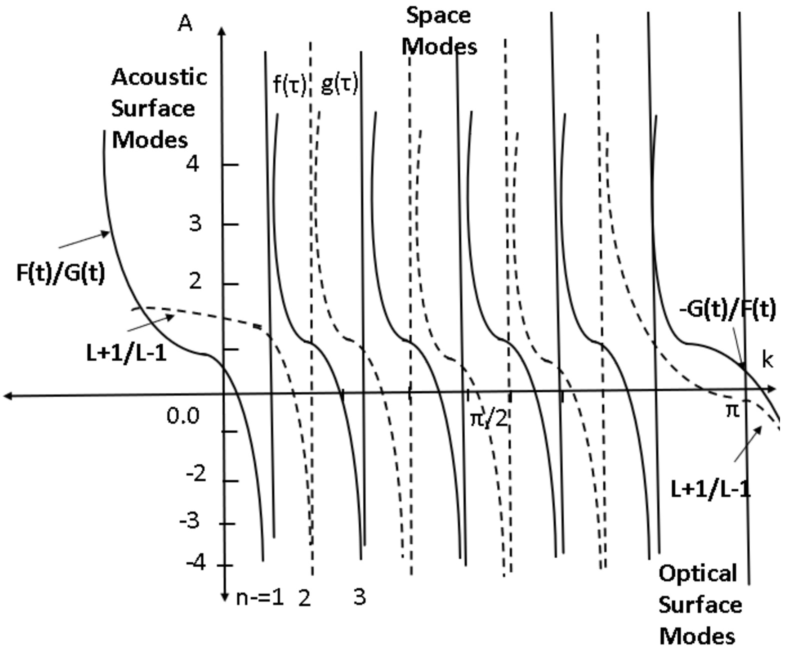

Figure 2.31. Surface anisotropy parameter, A as a function of k.

One can conclude that $A = 1$ or $E_{surf} = 0$ is the natural surface condition. $A > 1$ or $E_{surf} > 0$ gives the surface modes or body modes. $A < 1$ or $E_{surf} < 0$ gives the body modes and $A = 1$ gives the uniform modes ($k = 0$). The angle dependence of the pinning parameter can be shown in the following

$$A = 1 - \frac{g\mu_B}{2sz_1J_1}H^{surf}\cos\theta_0 - \theta, \tag{2.132}$$

where θ_0 is the angle between the z-axis and the unidirectional surface field and θ is the angle between the spin moments' direction and the z-axis. For $|\theta_0 - \theta| < \pi/2$, A becomes smaller than unity, $A < 1$ and for $|\theta_0 - \theta| > \pi/2$, becomes greater than unity, $A > 1$ and for $|\theta_0 - \theta| < \pi/2$, A becomes equal to unity, $A = 1$ where the uniform modes are excited.

The pinning parameter at the substrate (A_s) and the film surface (A_f) are

$$\begin{aligned} A_s &= 1 - \sum a_p^s P_p \cos\theta, \\ A_f &= 1 - \sum a_p^f P_p \cos\theta, \end{aligned} \tag{2.133}$$

where $P_p \cos\theta$ is the Legendre polynomials, which imply the angular dependence of the surface pinning parameter and a_p shows the magnitude of the interaction. In this approach, the precession is isotropic. However, in thin magnetic garnet films, due to the demagnetization factors, the precession is elliptical. To determine the effect of surface in spin wave resonance, the film must be homogenous within the volume. Otherwise, the in homogeneity inside the film gives rise to spin wave spectra, partially or not caused by surface anisotropy. Homogenous 1-micrometer thick YIG films epitaxially grown on gadolinium gallium Garnet (GGG) substrates have higher order spin wave modes with a lower intensity with respect to the principal modes in YIG film grown by liquid phase epitaxy (LPE). The substrate and surface pinning parameters are equal to one. This shows that in LPE-grown films, the surface energy is very small. In the annealed YIG films or YIG films that are grown by chemical vapor deposition (CVD), the surface effect plays an important role in spin wave spectra [53–56].

The non-propagating surface spin wave mode in Figures 2.29 and 2.30 is at the substrate film interface. The mode positions and intensities depend on the angle. The strongest absorption at the lower field is body mode and the weak absorption at the higher field is the surface mode at parallel orientation. As the angle approaches the perpendicular orientation, the surface mode intensity increases, and the body mode intensity decreases. At a critical angle, θ_c, the surface mode and the body mode merge into one uniform mode. As the angle increases to a perpendicular orientation, the surface mode separates from the body mode, and higher-order body modes are observed. As a function of temperature, at parallel orientation, the magnitude of the surface anisotropy energy varies on each surface while no change is observed in the perpendicular orientation. The surface pinning parameters, A_s and A_f, and the surface anisotropy energy at each surface as a function of magnetization direction are given in Figure 2.33.

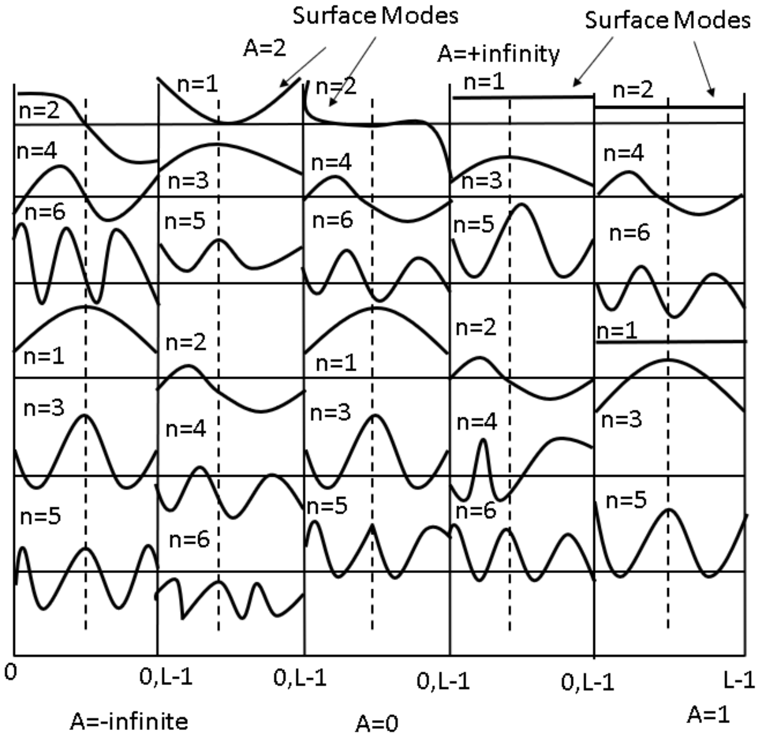

Figure 2.32. Transverse magnetization component for a few orders of spin-wave modes as a function of the surface parameter, A.

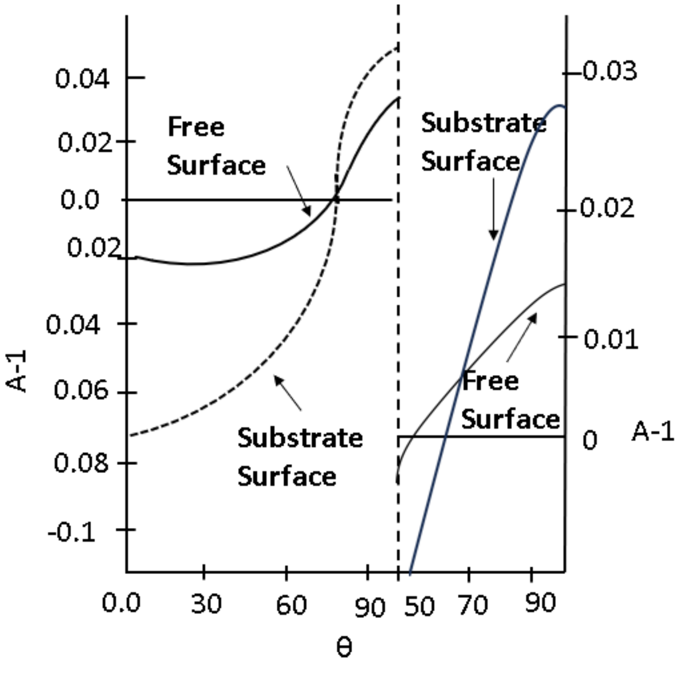

Figure 2.33. Surface pinning parameters at the substrate and free surface of an annealed YIG film.

The curves show the least-square fit of experimental data for YIG[100]/GGG structure with the film thickness of 0.46 micrometer and annealed for 2 hours at 1300° C and the microwave frequency of 23.3 GHz. The pseudosymmetric and pseudoantisymmetric surface modes are at the substrate surface and free surface, respectively. To find the pinning parameters at each angle, asymmetric boundary conditions are applied. After neglecting the odd modes from the Equation (2.132) and by doing the calculation for only p_0 and p_2, the surface pinning parameters are obtained as

$$\begin{aligned} A_s &= 1 - a_0^s - a_2^s \frac{3\cos^2\theta - 1}{2}, \\ A_f &= 1 - a_0^f - a_2^f \frac{3\cos^2\theta - 1}{2}. \end{aligned} \tag{2.134}$$

The surface anisotropy determines the boundary conditions, so the allowed k values can be known and the details of the bulk spin wave spectra can be analyzed.

2.5. Magnetization Dynamics

Magnetic Resonance (MR) is a tool for the investigation of the magnetic properties of materials. Electron paramagnetic resonance (EPR)/electron spin resonance (ESR) and nuclear magnetic resonance (NMR) are related to electrons and nuclei, respectively. In both techniques, the sample is placed in a strong static magnetic field and an orthogonal frequency is applied. In EPR, the frequency is in the range of the microwave regime. In NMR, low radio frequency is used. Energy absorption occurs when the radio frequency is equal to the difference between the two energy levels. The transition between two energy states occurs by obeying the selection rules. The splitting of energy levels occurs at a non-zero total angular momentum. A paramagnetic sample makes a precession motion in a magnetic field. If a microwave field with frequency, M is applied perpendicular to the static field, the power is absorbed when the precession frequency (M_0) is the same as the M frequency.

2.5.1. Ferromagnetic Resonance

When a transverse AC field at the Larmor frequency is applied to a system, the system absorbs energy from the oscillating magnetic field due to spins' split-level energy states. The resonance arises when the natural frequency of the magnetic system coincides with the Larmor frequency. Equation of motion for ferromagnetic resonance can be done by using a classical model in contrast to the spin Hamiltonian equation which has terms with quantum operators. One can transform from the quantum mechanical operators to the classical spin operators by taking time derivation of the expected values of the transverse magnetization moment that are given as

$$\begin{aligned} <\mu_x> &= -g\mu_B S_x, \\ <\mu_y> &= -g\mu_B S_y. \end{aligned} \tag{2.135}$$

By using the Hamiltonian which consists of only the Zeeman term, $H = g\mu_B H_o S_z$, the time derivation of the spin operators is expressed by

$$\begin{aligned} \frac{dS_x}{dt} &= -\gamma H_o S_y, \\ \frac{dS_y}{dt} &= \gamma H_o S_x, \\ \frac{dS_z}{dt} &= 0. \end{aligned} \tag{2.136}$$

The expectation values of the magnetic moment operators,

$$\begin{aligned} \frac{d\mathbf{S}}{dt} &= -\mathbf{S} \times \mathbf{H}_0, \\ \frac{d<\boldsymbol{\mu}>}{dt} &= -<\boldsymbol{\mu}> \times \gamma \mathbf{H}_o, \end{aligned} \tag{2.137}$$

where $\gamma \mathbf{H}_o = \hbar w$ is the energy splitting between the two quantum states. The frequency of the transition between the two states corresponds to the frequency of the RF microwave field in FMR. By adding the exchange energy term in the Hamiltonian, one gets

$$H = g\mu_B \sum_i \mathbf{H^{eff}}_i \cdot \mathbf{S}_i - 2Ja^2 z \sum_i \mathbf{S}_i \cdot \nabla^2 \mathbf{S}_i, \tag{2.138}$$

where a is the lattice constant. The equation of motion for a spin is given by

$$\begin{aligned} i\hbar \frac{d\mathbf{S}_i}{dt} &= [\mathbf{S}_i, H], \\ \hbar \frac{d\mathbf{S}_i}{dt} &= -g\mu_B \mathbf{s} \times \mathbf{H}^{eff} + 2zJa^2 \mathbf{S}_i \times \nabla^2 \mathbf{S}_i. \end{aligned} \tag{2.139}$$

By replacing $\mathbf{S}_i$ with the magnetization $\mathbf{M}$, one gets the expression

$$\frac{1}{\gamma}\frac{d\mathbf{M}}{dt} = -\mathbf{M} \times \mathbf{H}^{eff} + \frac{2A}{M_0^2}\mathbf{M} \times \nabla^2\mathbf{M} \tag{2.140}$$

with $\mathbf{M} = g\mu_B N\mathbf{S}$ and N is the spin number per unit volume. The relation for the exchange constant is $A = zJS^2/a$. The first term is the torque on the magnetization in the effective field, and the second term is the torque caused by the exchange field, $\mathbf{H}_{exc} = -(2A/M_0^2)\nabla^2\mathbf{M}$. The torque due to the effective field can be written as

$$\tau = -\hat{\mathbf{e}}_r \times \nabla\mathbf{E}. \tag{2.141}$$

The magnetization vector in the coordinate system in Figure 2.34 is given by

$$\mathbf{M} = m_0\hat{\mathbf{e}}_r + m_\theta\hat{\mathbf{e}}_\theta + m_\phi\hat{\mathbf{e}}_\phi, \tag{2.142}$$

where $\hat{\mathbf{e}}_r$, $\hat{\mathbf{e}}_\theta$,and $\hat{\mathbf{e}}_\phi$ are the unit vectors in spherical coordinates, $m_\theta = M\delta\theta$, $m_\phi = M\sin\theta\delta\phi$, $\delta\theta$ and $\delta\phi$ are the deviations from the equilibrium. By inserting Equation (2.140) in the Equation (2.139), the equation of motion can be expressed by

$$\frac{1}{\gamma}\frac{d\mathbf{M}}{dt} = \frac{\mathbf{M}}{\mathbf{M_0}} \times \nabla\mathbf{E} + \frac{2A}{M_0^2}\mathbf{M} \times \nabla^2\mathbf{M}. \tag{2.143}$$

Damping terms such as the Landau Lifshitz, Gilbert, and Bloch- Bloembergen can be added to the equation of motion as follows:

$$\frac{\lambda}{M_o^2}\mathbf{M} \times (\mathbf{M} \times \mathbf{H}^{eff}) \tag{2.144}$$

is the Landau Lifshitz damping term,

$$\frac{\alpha}{M_o}\mathbf{M} \times \mathbf{M} \tag{2.145}$$

is the Gilbert damping term, and

$$-\frac{M_{x,y}}{\tau_2} - \frac{M_z - M_0}{\tau_1} \tag{2.146}$$

is the Bloch- Bloembergen damping term. In the equilibrium, the net torque on the system is zero. Therefore, the left-hand side of the Equation (2.142) is zero and the second term on the right-hand side is zero. The first term can be written as

$$\frac{\mathbf{M}}{\mathbf{M_0}} \times \nabla\mathbf{E} = E_\theta\hat{\mathbf{e}}_\phi - E_\phi\csc\theta\hat{\mathbf{e}}_\theta = 0 \tag{2.147}$$

with $E_\theta = \frac{\partial}{\partial\theta}$ and $E_\phi = \frac{\partial}{\partial\phi}$. By expanding the equation of motion in Equation (2.142) around the equilibrium,

$$\begin{aligned}\frac{1}{\gamma}\delta(\frac{d\mathbf{M}}{dt}) &= \delta(\frac{\mathbf{M}}{\mathbf{M_0}} \times \nabla\mathbf{E}) + \frac{2A}{M_0^2}\delta(\mathbf{M} \times \nabla^2\mathbf{M}) \\ &= \frac{1}{\mathbf{M_0}}\delta\mathbf{M} \times \nabla\mathbf{E} + \frac{\mathbf{M}}{M_0} \times \delta\mathbf{E} + \frac{2A}{M_0^2}\delta(\mathbf{M} \times \nabla^2\mathbf{M}).\end{aligned} \tag{2.148}$$

The first term on the right-hand side is zero. The second term can be expanded by

$$\frac{\mathbf{M}}{M_0} \times \delta\mathbf{E} = -\frac{\csc\theta}{M_0}(E_{\theta\phi}m_\theta + E_{\phi\phi}\csc\theta m_\phi)\hat{\mathbf{e}}_\theta + \frac{1}{M_0}(E_{\theta\theta}m_\theta + E_{\theta\phi}\csc\theta m_\phi)\hat{\mathbf{e}}_\phi. \tag{2.149}$$

A set of coupled equations is expressed by

$$\begin{aligned}\frac{1}{\gamma}\frac{dm_\theta}{dt} &= \frac{\csc\theta}{M_0}(E_{\theta\phi}m_\theta + E_{\phi\phi}\csc\theta m_\phi) - \frac{2A}{M_0^2}\delta(\mathbf{M} \times \nabla^2 m_\phi), \\ \frac{1}{\gamma}\frac{dm_\theta}{dt} &= -\frac{1}{M_0}(E_{\theta\theta}m_\theta + E_{\theta\phi}\csc\theta m_\phi) + \frac{2A}{M_0^2}\delta(\mathbf{M} \times \nabla^2 m_\theta).\end{aligned} \tag{2.150}$$

The solutions are

$$\begin{aligned}m_\theta &= (\alpha_1 \sin k_1 y + \beta_1 \cos k_1 y + \gamma_1 \exp -k_2 y) \exp -iwt, \\ m_\phi &= (\alpha_2 \sin k_1 y + \beta_2 \cos k_1 y + \gamma_2 \exp -k_2 y) \exp -iwt,\end{aligned} \tag{2.151}$$

where k_2 is the surface mode at $y = 0$ surface. The relations between the amplitudes are

$$\begin{aligned}\frac{\alpha_2}{\alpha_1} = \frac{\beta_2}{\beta_1} &= \frac{E_{\theta\theta}/M_0 + Dk_1^2}{iw/\gamma - E_{\theta\phi}/M_0}, \\ \frac{\gamma_2}{\gamma_1} &= \frac{E_{\theta\theta}/M_0 - Dk_2^2}{iw/\gamma - E_{\theta\phi}/M_0}.\end{aligned} \tag{2.152}$$

The dispersion relation is given in the following:

$$(\frac{w}{\gamma})^2 = (E_{\theta\theta} \pm Dk_{1,2})(E_{\phi\phi} \pm Dk_{1,2}^2) - E_{\theta\phi}^2. \tag{2.153}$$

In the assumption of a uniaxial anisotropy constant, K_u with a perpendicular magnetic easy axis to the film plane, the derivatives are

$$E_{\theta\theta} = E_{\phi\phi} = M(H_0 + H_u) \tag{2.154}$$

with H_0 as the applied field and $H_u = \frac{2K_u}{M_0}$ is the effective uniaxial anisotropy. By substituting the derivatives in Equation (2.152), the dispersion relation takes the form as

$$\frac{w}{\gamma} = H_0 + H_u - Dk_1^2, \tag{2.155}$$

which gives a circular precession. The k values are acquired by the boundary conditions. The torque due to the surface anisotropy energy is

$$\mathbf{T}^s = -\frac{\mathbf{M}}{M_0} \times \nabla E^s. \tag{2.156}$$

The exchange torque, which is $\mathbf{T}^s = \frac{2A}{M_0^2}\mathbf{M} \times \frac{\partial \mathbf{M}}{\partial y}$ is equivalent to the surface torque.

$$\begin{aligned} \delta\mathbf{T}^s &= \delta\left(-\frac{\mathbf{M}}{M_0} \times \nabla E^s\right) \\ &= \frac{1}{M_0}\left(E^s_{\theta\phi}\csc\theta m_\theta - E^s_\phi \cot\theta\csc\theta m_\theta + E^s_{\phi\phi}\csc^2\theta m_\phi\right)\hat{\mathbf{e}}_\theta \\ &- \frac{1}{M_0}\left(E^s_{\theta\theta} m_\theta + E^s_{\theta\phi}\csc\theta m_\phi\right)\hat{\mathbf{e}}_\phi. \end{aligned} \tag{2.157}$$

The variation of the exchange-related torque is

$$\delta\mathbf{T}^s = \frac{2A}{M_0}\left(\frac{\partial m_\theta}{\partial y}\hat{\mathbf{e}}_\phi - \frac{\partial m_\phi}{\partial y}\hat{\mathbf{e}}_\theta\right). \tag{2.158}$$

By equating the variations in Equations (2.156) and (2.157), one can have the following matrix relation,

$$\begin{bmatrix} \frac{\partial m_\theta}{\partial y} \\ \frac{\partial m_\phi}{\partial y} \end{bmatrix} = -\begin{bmatrix} \eta^s_{\theta\theta} & \eta^s_{\theta\phi}\csc\theta \\ \eta^s_{\theta\phi}\csc\theta - \epsilon^s_\phi\cot\theta\csc\theta & \eta^s_{\phi\phi}csc^2\theta \end{bmatrix} \cdot \begin{bmatrix} m_\theta \\ m_\phi \end{bmatrix}, \tag{2.159}$$

where $\eta_{ij} = E_{ij}/2A$. For $\theta_0 = \pi/2$,

$$\begin{bmatrix} \frac{\partial m_\theta}{\partial y} \\ \frac{\partial m_\phi}{\partial y} \end{bmatrix} = -\begin{bmatrix} \eta^s_{\theta\theta} & \eta^s_{\theta\phi} \\ \eta^s_{\theta\phi} & \eta^s_{\phi\phi} \end{bmatrix} \cdot \begin{bmatrix} m_\theta \\ m_\phi \end{bmatrix}. \tag{2.160}$$

The spin wave shift is given with the expression $\tan\delta = -\alpha_1/\beta_1$. By applying the boundary condition given in Equation (2.160) [56], k_1 can be obtained from the relation

$$k_1 \tan\delta = \frac{k_2 K_+ \eta^s_{\theta\theta}\eta^s_{\phi\phi}}{k_2 + K_-}, \tag{2.161}$$

where $K_\pm = 1/2(\eta^s_{\theta\theta}(1 \pm \sigma) + \eta^s_{\phi\phi}(1 \pm \sigma))$ with $\sigma = (1 - \zeta^+\zeta^-)^{-1/2}$ and

$$\zeta^\pm = \frac{iw/\gamma \pm E^b_{\theta\phi} M_0}{(E^b_{\theta\theta} - E^b_{\phi\phi})/2M_0}, \tag{2.162}$$

where E^b is the energy in the interior of the film.

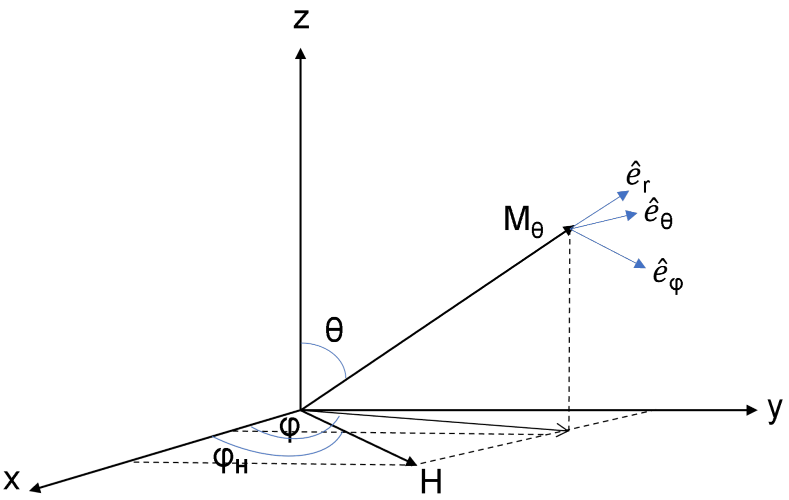

Figure 2.34. The FMR coordinate system.

The surface energy density is represented as

$$E^s = -\mathbf{M}_0 \cdot \mathbf{H}^{surf} = M_0 H^{surf} \sin\theta \cos\phi_s - \phi \tag{2.163}$$

with ϕ_s being the uniaxial anisotropy energy direction. Puszkarzki's microscopic model in the presence of surface anisotropy yields that

$$\begin{aligned} E^s_{\theta\theta} &= E^s_{\phi\phi} = H^{surf} M_0 \sin\theta \cos\phi_s - \phi, \\ E^s_{\theta\phi} &= 0, \\ \sigma &= 0. \end{aligned} \tag{2.164}$$

$K_\pm$ is obtained as

$$\begin{aligned} K_\pm &= \frac{H^{surf} M_0}{2A} \sin\theta \cos{(\phi_s - \phi)}, \\ k_1 \tan\delta &= \frac{H^{surf} M_0}{2} \sin\theta_H \cos{(\phi_H - \phi_s)}. \end{aligned} \tag{2.165}$$

For the uniaxial surface anisotropy energy, $E^s = K^s \sin^2\theta \sin^2\phi$. At $\theta = \pi/2$, one obtains

$$\begin{aligned} E^s_{\theta\theta} &= -2K^s \sin^2\phi, \\ E^s_{\phi\phi} &= -2K^s (\sin^2\phi - \cos^2\phi), \\ E^s_{\theta\phi} &= 0. \end{aligned} \tag{2.166}$$

$K_\pm$ is obtained as

$$K_\pm = -\frac{K^s}{2A}(3\cos^2\beta - 1 \pm \sigma \sin^2\beta), \tag{2.167}$$

where $\beta = \pi/2 - \phi$ is the angle between the magnetization and the film plane. The boundary condition is $k_1 \tan\delta \approx K_\pm$. The total energy density includes Zeeman, demagnetization, magnetostatic, uniaxial, and crystalline anisotropy energy. The Zeeman energy density is given

$$\begin{aligned} E_z &= -\mathbf{M}\cdot\mathbf{H}_0 \\ &= M_0 H_0 \sin\theta \cos(\phi - \phi_H). \end{aligned} \tag{2.168}$$

Here, the applied magnetic field, H_0 is along the xy plane. The magnetostatic energy is represented as

$$E_m = 2\pi \mathbf{M}\cdot\mathbf{N}\cdot\mathbf{M} \tag{2.169}$$

with $\mathbf{N}$ as the demagnetization tensor. For thin films, the demagnetization energy can be written by

$$E_m = 2\pi M_y^2 = 2\pi M_0^2 \sin^2\theta \sin^2\phi. \tag{2.170}$$

The uniaxial anisotropy perpendicular to the film plane is written as

$$E_u = -K_u \sin^2\theta \sin^2\phi. \tag{2.171}$$

Magnetostatic and uniaxial anisotropies have the same form in FMR. Therefore, one can neglect the uniaxial term and instead, can use the magnetostatic energy term as an effective uniaxial anisotropy energy term as $2\pi M^2 - K_u$. The crystalline energy for cubic crystals is

$$E_c = \frac{K_1}{M^4}(M_i^2 M_j^2 + M_j^2 M_k^2 + M_k^2 M_i^2), \tag{2.172}$$

where i, j, and k stand for the crystal direction axis [100], [010], and [001]. Here, the second-order terms are not included. For (111) thin film, E_c takes the form as

$$\begin{aligned} E_c &= \frac{K_1}{M^4}(\frac{1}{4}M_x^4 + \frac{1}{3}M_y^4 + \frac{1}{4}M_z^4 + \frac{1}{2}M_x^2 M_y^2 + \frac{\sqrt{2}}{3}M_x^3 M_y - \sqrt{2}M_x M_y M_z^2) \\ &= K_1(\frac{\sin^4\theta\cos^4\phi}{4} + \frac{\sin^4\theta\sin^4\phi}{3} + \frac{\cos^4\theta}{4} + \frac{\sin^2 2\theta\cos^2\phi}{8} \\ &+ \frac{\sqrt{2}}{3}\sin^4\theta\sin\phi\cos^3\phi - \frac{\sqrt{2}}{8}\sin^2 2\theta \sin 2\phi. \end{aligned} \tag{2.173}$$

The equilibrium can be obtained with $E_\theta = 0$ and $\csc\theta E_\phi = 0$. This can be done by putting the angle $\theta = \pi/2$ and $E_\phi = 0$. After substituting the values, one gets

$$\begin{aligned} &M_0H_0(\sin\phi - \phi_H) + 2\pi M_0^2 \sin 2\phi + K_1\left(1/12 \sin 2\phi(1 - 7\cos 2\phi)\right. \\ &+ 2/3\cos^2\phi(2\cos 2\phi - 1) = 0. \end{aligned} \tag{2.174}$$

This relation does not have analytical solutions. The second derivative of the energy lets the dispersion relation be solved. By setting $E_{\theta\phi} = 0$, and $\alpha = \pi/2 - \phi_H$ and $\beta = \pi/2 - \phi$ where α and β are the angles between **H** and **M** and the film normal. For a [111] film with the **H** and **M** are on the (110) plane, the dispersion relation becomes

$$\begin{aligned} (\frac{w}{\gamma})^2 &= (H_0\cos\alpha - \beta - 4\pi M_0\cos 2\beta + \varUpsilon_1(\beta) + Dk^2) \\ &\times (H_0\cos\alpha - \beta - 4\pi M_0\cos^2\beta + \varUpsilon_2(\beta) + Dk^2). \end{aligned} \tag{2.175}$$

The equilibrium of **M** is

$$H_0\sin(\alpha - \beta) + 2\pi M_0\sin 2\beta + \varUpsilon_3(\beta) = 0. \tag{2.176}$$

$\varUpsilon_1(\beta)$, $\varUpsilon_2(\beta)$, and $\varUpsilon_3(\beta)$ are expressed as

$$\begin{aligned} \varUpsilon_1(\beta) &= H_k(\frac{1}{8}\sin^2(2\beta) - \frac{2}{3}\cos^4\beta - \frac{\sqrt{2}}{2}\sin(2\beta)(1 + \frac{2}{3}\sin^2\beta), \\ \varUpsilon_2(\beta) &= -H_k(\frac{1}{12}\cos(2\beta) + \frac{7}{12}\cos 4\beta + \frac{\sqrt{2}}{6}(\sin(2\beta) - 2\sin(4\beta)), \\ \varUpsilon_3(\beta) &= H_k(\frac{1}{24}\sin(2\beta)(1 + 7\cos(2\beta)) - \frac{\sqrt{2}}{6}\sin^2\beta(1 + 2\cos(2\beta)), \end{aligned} \tag{2.177}$$

where $H_k = 2K_1/M$ is the effective anisotropy field. At $k = 0$, one gets the resonance field at the frequency of w as

$$\begin{aligned} H_u\cos(\alpha - \beta) = 2\pi M_0 &\left(\cos^2\beta + \cos(2\beta) - \frac{1}{2}(\varUpsilon_1(\beta) + \varUpsilon_2(\beta))\right) \\ &+ \frac{1}{2}\left(4\pi M_0(\cos^2\beta - \cos(2\beta)) + \varUpsilon_2(\beta) - \varUpsilon_1(\beta)^2\right. \\ &\left. + 4(\frac{w}{\gamma})^2\right)^{1/2}. \end{aligned} \tag{2.178}$$

From the dispersion relation in Equation (2.175), the energy of the spin wave mode with k_n can be obtained by

$$H_n = H_u - \frac{Dk_n^2}{\cos(\alpha - \beta)}. \tag{2.179}$$

For the case of an in-plane applied magnetic field which corresponds to $\alpha = \beta = 0$, Equation (2.179) turns out to be

$$\begin{aligned} H_{n\perp} &= H_{u\perp} - Dk_n^2 \\ &= \frac{w}{\gamma} + 4\pi M_{eff} + \frac{2}{3}H_k - Dk_n^2. \end{aligned} \tag{2.180}$$

Here, D, M_{eff}, H_k, and γ can be found by the dispersion relation and equilibrium condition. The surface anisotropy energy can be obtained by the angular-dependent spin wave spectra. If one goes back to the Landau-Lifshitz -Gilbert equation of motion, which is

$$\frac{d\mathbf{M}}{dt} = \gamma\left(\mathbf{M} \times \mathbf{H} \times \mathbf{H_{eff}}\right) + \frac{G}{\gamma M^2}\left(\mathbf{M} \times \frac{\partial \mathbf{M}}{\partial t}\right). \tag{2.181}$$

H_{eff} includes RF microwave field, $h(t)$ with a frequency of $w/2\pi$, demagnetizing field, and magnetocrystalline anisotropy field. The gyromagnetic ratio is $\gamma = g\mu_b\hbar^{-1}$ with g being the splitting factor,$\hbar$ being the Planck constant, and G is the Gilbert damping term. The splitting factor of a free electron is 2.0023 and the Gilbert damping is 1.758810^7 Hz Oe^{-1} [57]. To find the resonance frequency, and the FMR linewidth from the Equation (2.181), coupled differential equations of the magnetization components are studied in [58, 59]. Another approach to determine the resonance frequency is to take the second derivative of the magnetic free energy density, F with respect to the angular components [60]

$$w_{res} = \frac{\gamma}{M \sin\theta}(F_{\theta\theta}F_{\phi\phi} - F_{\theta\phi}^2)^{1/2}. \tag{2.182}$$

Here, the damping parameter, α is not included. The minimum of the free energy density yields the crystallographic easy axis. The resonance frequency for the tetragonal symmetry and the magnetic field applied at θ_H and ϕ_H in Figure 2.35. At $\theta_H = \theta = 0°$, the dispersion relation is

$$\frac{w}{\gamma} = H_{R\perp} - 4\pi M + \frac{2(K_2 + K_{4\perp})}{M}. \tag{2.183}$$

At $\theta_H = \theta = 90°$, and $\phi_H = 45°$, the dispersion relation is

$$(\frac{w}{\gamma})^2 = (H_{R\parallel} - \frac{2K_{4\parallel}}{M})(H_{R\parallel} + 4\pi M - \frac{2K_2}{M} + \frac{K_{4\parallel}}{M}). \tag{2.184}$$

The dispersion relation for $\phi_H = \phi = 45°$ is written as

$$\begin{aligned}(\frac{w}{\gamma})^2 &= H_R \cos(\theta_H - \theta) + (-4\pi M + \frac{2K_2}{M} + \frac{K_{4\perp}}{M} - \frac{K_{4\parallel}}{2M}) \cos(2\theta) \\ &+ (\frac{K_{4\perp}}{M} + \frac{K_{4\parallel}}{2M}) \cos(4\theta) \times H_R \cos(\theta_H - \theta) \\ &+ (-4\pi M + \frac{2K_2}{M} + \frac{K_{4\parallel}}{2M}) \cos^2\theta \\ &+ (\frac{2K_{4\perp}}{M} + \frac{K_{4\parallel}}{2M})) \cos^4\theta - \frac{2K_{4\parallel}}{M}.\end{aligned} \tag{2.185}$$

At $\theta_H = \theta = 90°$, and $\phi_H = 0°$, the dispersion relation is

$$(\frac{w}{\gamma})^2 = (H_{R\parallel} + \frac{2K_{4\parallel}}{M})(H_{R\parallel} + 4\pi M - \frac{2K_2}{M} + 2\frac{K_{4\parallel}}{M}). \tag{2.186}$$

At $\theta_H = \theta = 90°$, the dispersion relation is

$$\begin{aligned}(\frac{w}{\gamma})^2 &= (H_{R\parallel} \cos(\phi - \phi_H) + \frac{2K_{4\parallel}}{M} \cos(4\phi)) \\ &\times (H_{R\parallel} + 4\pi M - \frac{2K_2}{M} + \frac{K_{4\parallel}}{2M}(3 + 4\cos\phi)).\end{aligned} \tag{2.187}$$

Here, K_2, $K_{4\perp}$, and $K_{4\parallel}$ are the second and fourth anisotropy energy constants. H_R is the resonance field determined by θ, ϕ, θ_H, ϕ_H, and the frequency of $w/2\pi$. The effect of the magnetic anisotropy on the resonance frequency (Equation (2.184) and (2.185)) is shown in Figure 2.36. The magnetic field is parallel or perpendicular to the film plane. The fourth-order anisotropy constants are not included in the plot. When there is no applied field, the magnetization is perpendicular to the film plane. The microwave absorption occurs at the intersections of the microwave frequencies with the w/γ curves. The broken curve shows the paramagnetic condition when both magnetization and K_2 are zero. When the applied field is perpendicular to the film plane, the resonance field is 0.03 T at 9.3 GHz, shown in a dotted curve ($K_2 = 1.7 \times 10^5$ J m^{-3}). In the case of larger K_2, there is no perpendicular resonance below 9.3 GHz.

When the magnetic field is parallel to the film plane, the microwave frequency is 9.3 GHz and $K_2 = 1.8 \times 10^5$ J m^{-3}, resonances occur at 0.001 T and 0.54 T. The magnetization at 0.001 T is perpendicular both to the film plane and the applied field and the resonance absorption is less. The magnetization aligns parallel to the field for the larger amount of the magnetic field. The transverse microwave field (h_y) absorption is observed. For 4 GHz frequency, the excitation of resonance modes occurs where M is not parallel to H at 0.3 T, the signal intensity is small. Another resonance mode at the same frequency appears at around 0.4 T where M and H are parallel to each other.

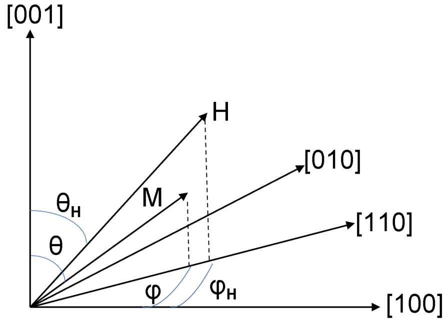

Figure 2.35. The angles of the applied field, H, and the magnetization, M. The microwave field is in the film plane.

At 9.3 GHz, one resonance mode is obtained at the value of $K_2 < 1.8 \times 10^5$ J m^3. For the larger value of K_2, two resonant modes occur at the $H_{r\|}$. As K_2 increases, the resonant mode at the low field goes to the high-field range, and the intensity of the signal increases. Meanwhile, resonant modes at high fields go towards a higher field range, but the intensity does not change. The resonance fields for the spontaneous magnetization, which is in plane or perpendicular to the film plane, are depicted in Figure 2.37. For the value of $K_2 = 1.5 \times 10^5$ J m^{-3}, the magnetic easy axis is perpendicular to the film plane. At 9.3 GHz, the perpendicular resonance field is less than the parallel resonance field and paramagnetic resonance in the broken curve shown in Figure 2.36.

The magnetic easy axis is in the film plane for Copy code $K_2 = 1.1 \times 10^5\,\mathrm{J\,m^{-3}}$. The parallel resonance field is less than the perpendicular resonance field. From all these findings, one can conclude that the value of the resonance field is the lowest when the field is applied along the easy axis. In FMR, the rf susceptibility $\chi(w)$ is the response of the magnetization to a time-dependent magnetic excitation $h(t) = (h_\theta + h_\phi)e^{iwt}$. At a constant frequency $w/2\pi$, the second derivative of the complex susceptibility $\chi(w)''$ is measured as a function of the applied field.

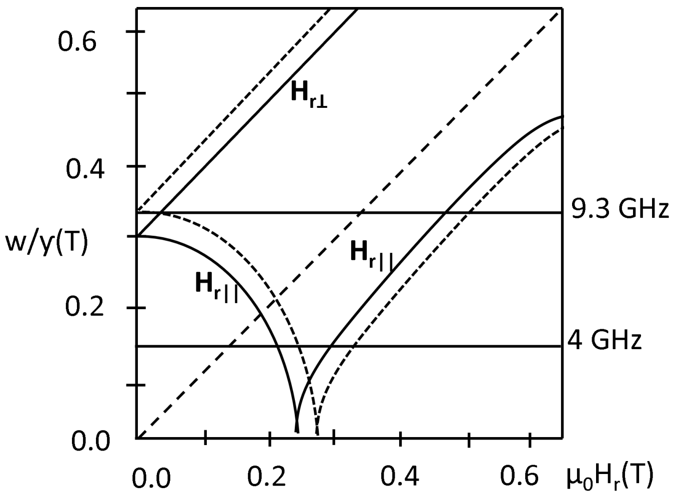

Figure 2.36. w/γ for a thin film with $\mu_0 M = 0.528$ T. Dotted curve shows that $K_4 = 0$ and $K_2 = 1.7 \times 10^5$ J m^{-3}. Full curve shows $K_2 = 1.8 \times 10^5$ J m^{-3}. The magnetic easy axis is perpendicular to the film plane when there is no applied field. The intersections of the 9.3 GHz and 4 GHz lines with the H_r lines give the resonance frequency. The broken line shows the paramagnetic resonance.

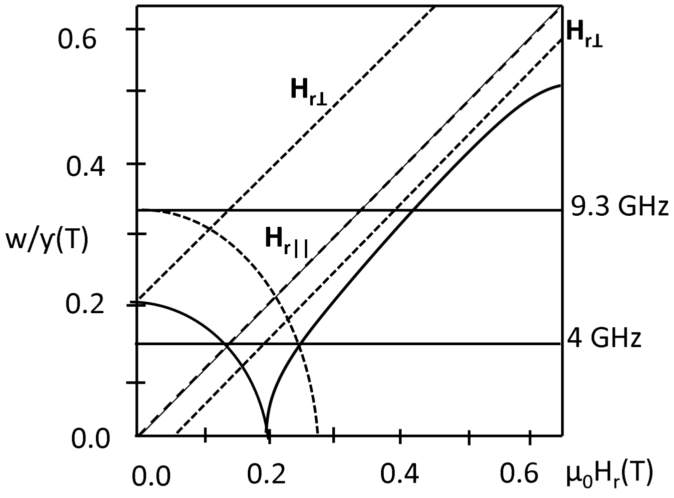

Figure 2.37. w/γ for a thin film with $\mu_0 M = 0.528$ T. Dotted line shows that $K_4 = 0$ and $K_2 = 1.5 \times 10^5$ J m^3. The broken line shows $K_2 = 1.0 \times 10^5$ J m^3. The magnetic easy axis is perpendicular to the film plane for the larger K_2.

Landau Lifshitz equation of motion and Maxwell equations for the rf electric and magnetic fields are both taken into account to evaluate the absorption part. In bulk samples or thick films, the boundary condition and the orientation of **h**, **H**, and **M** with respect to the sample gives rise to a set of equations that are numerically soluble. One must also consider the surface anisotropy due to the boundary condition [61, 62]. In the ultrathin film, calculations are much easier. The complex susceptibility for a bcc film with transverse microwave field, $h_y(t)$, and the applied field in the film plane is

$$\begin{aligned}\chi_y &= \chi_y' + \chi_y'' - \frac{M_y(t)}{h_y} \\ &= \left\{ M(H,T)d\left[H + 4\pi(N_\perp - N_\parallel)M(H,T) - \frac{2K_2}{M} - \frac{iw}{\gamma}\left(\frac{G}{\gamma M(H,T)}\right)\right]\right\} \\ &\quad\times \left\{\left[H + 4\pi(N_\perp - N_\parallel)M(H,T) - \frac{2K_2}{M} - \frac{iw}{\gamma}\left(\frac{G}{\gamma M(H,T)}\right)\right]\right. \\ &\quad\times \left.\left[H + \frac{2K_4}{M}\cos^4\phi - \frac{iw}{\gamma}\left(\frac{G}{\gamma M(H,T)}\right) - \left(\frac{w}{\gamma}\right)^2\right]\right\}^{-1}.\end{aligned} \tag{2.188}$$

The power of the absorbed microwave is $P(H) = 0.5w\text{Im}(\chi_y)|h_y|^2$ where the $Im(\chi_y) = \chi(w)''$. The maximum absorption is when the value of the $\chi(w)''$ is the maximum. The shape of the signal, the intensity, and the half width at half maximum (HWHM) can be determined by following the Equation (2.188). The peak-to-peak resonance linewidth $\mathit{\Delta} H_{pp}$ indicates the relaxation rate of the magnetization. The magnetic inhomogeneities, the Gilbert damping, and the line broadening caused by the exchange conductivity determine the $\mathit{\Delta} H_{pp}$. Intrinsic damping is a measure of the viscous damping of the magnetization precession and low-energy spin waves, and the dissipation of the absorbed microwave energy from the spins to the lattice vibrations. Intrinsic damping is related to the Gilbert damping term in the Equation (2.181) which depends on the temperature, and the wave vector, k [63]. The resonance linewidth and the frequency dependence are given in the following relation as

$$\mathit{\Delta} H_{pp} = \mathit{\Delta} H_{inhom} + 1.16\frac{G}{\gamma^2 M(T,H)}w. \tag{2.189}$$

$\mathit{\Delta} H_{inhom}$ does not depend on the frequency. Inhomogeneous linewidth broadening arises from magnetic inhomogeneities. The intrinsic damping of the magnetization motion is given by the Gilbert damping term. The friction is linear-dependent on the frequency. As the frequency increases, the linewidth increases, as well. The homogenous linewidth broadening is angle-dependent [64] and given by

$$\varDelta H_{hom}(\theta,\phi)=\frac{2}{\sqrt{3}}\frac{1}{|\frac{\partial w}{\partial H_{res}}|}\frac{G}{M^2}(\frac{\partial^2 F}{\partial\theta^2}+\frac{1}{\sin^2\theta}\frac{\partial^2 F}{\partial\phi^2}). \tag{2.190}$$

The Gilbert damping along the easy axis is larger than the hard axis. The viscous damping of the magnetization precession along the easy axis is larger because of the shift into the hard axis. When the magnetic field is applied along the hard axis, the precession is towards the easy axis, therefore damping is less. $\varDelta H_{inhom}$ is caused by the magnetic imperfections within the sample, and it might be very large due to the coupling of the uniform resonance mode ($k = 0$) with spin waves $k \neq 0$. The susceptibility is given by the relation

$$\chi^n = I_n\frac{4\pi M_0(Dk_n^2+\frac{1}{M_0}\frac{\partial^2 E}{\partial\theta^2})((\frac{w_0}{\gamma})^2-(\frac{w}{\gamma})^2+\frac{2iw}{\gamma^2 T_2}}{[(\frac{w_0}{\gamma})^2-(\frac{w}{\gamma})^2]^2-\frac{4w^2}{\gamma^4 T_2^2}}, \tag{2.191}$$

where I_n is the amplitude coefficient. The absorption is the complex part of the susceptibility relation, which is given by

$$\chi_2^n = I_n\frac{4\pi M_0(Dk_n^2+\frac{1}{M_0}\frac{\partial^2 E}{\partial\theta^2})\frac{2w}{\gamma^2 T_2}}{[(\frac{w_0}{\gamma})^2-(\frac{w}{\gamma})^2]^2-\frac{4w^2}{\gamma^4 T_2^2}}, \tag{2.192}$$

where D is the exchange stiffness, T_2 is the spin-spin relaxation time, w_0 is the Larmor frequency and found by the relation [65, 66]:

$$(\frac{w_0}{\gamma})^2=(Dk_n^2+\frac{1}{M_0}\frac{\partial^2 E}{\partial\theta^2})(Dk_n^2+\frac{1}{M_0\sin^2\theta}\frac{\partial^2 E}{\partial\phi^2})-(\frac{1}{M_0\sin\theta}\frac{\partial^2 E}{\partial\theta\partial\phi})^2+\frac{1}{\gamma^2 T_2^2}. \tag{2.193}$$

At the surface of a thin film, $\nabla_n M = 0$ due to the exchange interaction between spins. Spins must have the same magnetization and the same precession frequency at the surface, and below the surface, if the internal field is uniform within the film. If the magnetization is not the same, additional torque will be implemented on the spin at the surface. The varying magnetization and surface anisotropy energy along the surface region gives rise to unpinned modes. This model is known as the volume inhomogeneity model [67]. According to the model, the surface magnetization magnitude gets a lower value than the bulk magnetization within a thickness, ε below the surface. Figure

2.38 shows the change in magnetization in the surface and bulk region as a function of thickness. M_0 is the saturation magnetization. For ε is not zero, the spins at the surface do not come to resonance while the spins in bulk are in resonance. Since the spins at the surface and in bulk are exchange-coupled with each other, it leads to a phase difference in the spin wave around the surface.

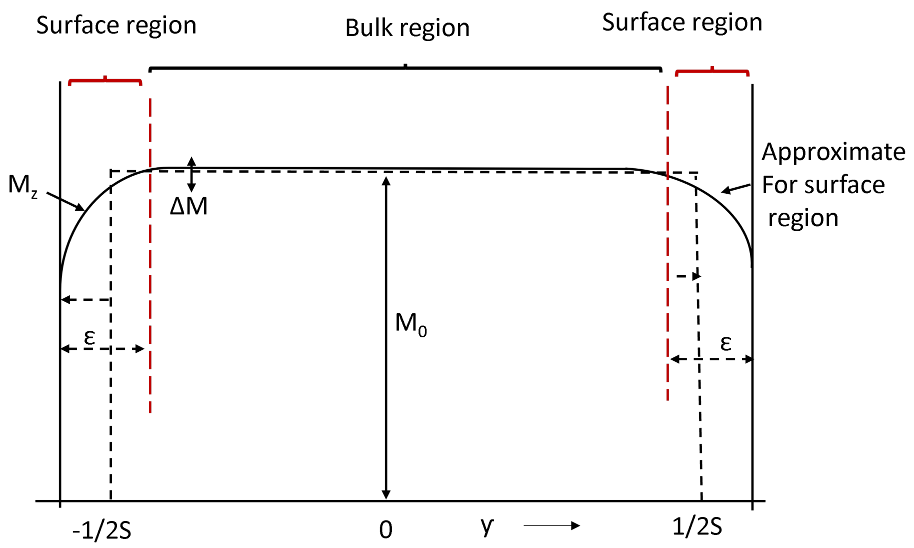

Figure 2.38. Saturation magnetization as a function of the film thickness.

.

If one assumes that a thickness of $\varepsilon/2$ below the surface results in half of the magnetization, $M_0/2$, this corresponds to a phase difference of 90° at a critical thickness ε_{cr} proportional to $(A/M_0^2)^{1/2}$. The surface spins are unpinned for the thickness below the critical thickness ($\varepsilon << \varepsilon_{cr}$). Otherwise, $\nabla M = 0$ at the surface can not be maintained, yielding partially pinned low-order spin waves. For the circular precession, the equation of motion for magnetization is

$$\frac{2A}{M_0}\frac{\partial^2 m}{\partial y^2} + \kappa^2 m = 0, \tag{2.194}$$

where κ^2 is given by the relation

$$\kappa^2 = \left((\frac{w}{\gamma})^2 + (2\pi M_0 \sin^2\theta)^2 \right)^{\frac{1}{2}} - H_{eff} - \frac{2A}{M_0^2}\frac{\partial^2 M_y}{\partial y^2} - 2\pi M_0 \sin^2\theta. \tag{2.195}$$

For the perpendicular resonance, $\sin^2\theta = 0$,

$$\kappa_{\perp}^2 = \frac{w}{\gamma} - H_{eff} - \frac{2A}{M_0^2}\frac{\partial^2 M_y}{\partial y^2}. \tag{2.196}$$

For the parallel resonance, $\sin^2\theta = 1$,

$$\kappa_{\|}^2 = \left((\frac{w}{\gamma})^2 + 42\pi^2 M_0^2\right)^{\frac{1}{2}} - H_{eff} - \frac{2A}{M_0^2}\frac{\partial^2 M_y}{\partial y^2} - 2\pi M_0. \tag{2.197}$$

The term with the $\frac{\partial^2 M_y}{\partial y^2}$ overcomes the other terms when the surface layers are very thin, so Equation (2.194) can be rewritten as

$$\frac{\partial^2 m}{\partial y^2} + \frac{\partial^2 M_y}{\partial y^2} m = 0. \tag{2.198}$$

By integrating once and applying the condition $M_0 = m = 0$ at the film surface, one can find

$$\frac{\partial m}{\partial y} + \frac{\partial M_y}{\partial y} m = 0, \tag{2.199}$$

which is valid for the bulk edge in addition to the surface. The spins are unpinned since $\nabla = 0$. Inserting the dispersion relation of the bulk region which is $w/\gamma = H_b^{eff} + Dk_n^2$, the perpendicular resonance in Equation (2.196) is

$$\kappa_{\perp}^2 = H_b^{eff} + Dk_n^2 - H_s^{eff} - \frac{2A}{M_0^2}\frac{\partial^2 M_y}{\partial y^2} \tag{2.200}$$

with H_b^{eff} and H_s^{eff} being the bulk and surface effective field,respectively. The difference between the bulk and surface effective fields can be up to $4\pi M_0$. The term $\frac{2A}{M_0^2}\frac{\partial^2 M_y}{\partial y^2}$ dominates the other terms for $Dk_n^2 << 4\pi M$, $\varepsilon^2 << 2A/\pi M_0^2$ and $Dk_n^2 << 4\pi M_0$. For $Dk_n^2 >> 4\pi M$, the term $\frac{2A}{M_0^2}\frac{\partial^2 M_y}{\partial y^2}$ dominates the other terms if $\varepsilon^2 << \lambda_n/\pi$ and $Dk_n^2 >> 4\pi M_0$. The relation which holds the two conditions is $\varepsilon^2 << \varepsilon_{cr}^2$ with

$$\varepsilon_{cr}^2 = \frac{2A}{M_0^2\pi}(1 + \frac{Dk_n^2}{4\pi M_0})^{-1}. \tag{2.201}$$

2.6. Magnonics

Magnetostatic modes are magnetic excitations in a magnetic specimen. For garnet films more than 5 μm, one can ignore the exchange interaction due to the very small value. Magnetostatic modes are normal modes of vibration of magnetization, $M(r,t)$, and obey the Maxwell equations:

$$\begin{aligned} \nabla \times \mathbf{H} &= 0, \\ \nabla \cdot \mathbf{H} &= -4\pi \nabla \cdot \mathbf{M} \end{aligned} \tag{2.202}$$

and the torque equation

$$\begin{aligned} \frac{1}{\gamma}\frac{\partial \mathbf{M}}{\partial t} &= \mathbf{M} \times \mathbf{H}_{eff} \\ &= \mathbf{M} \times (\nabla E - \mathbf{h}e^{-iwt}), \end{aligned} \tag{2.203}$$

where the effective field is

$$\mathbf{H}_{eff} = \mathbf{H}_0 - \mathbf{H}_u - 4\pi \mathbf{N} \cdot \mathbf{M}_0 + \mathbf{h}e^{-iwt} \tag{2.204}$$

with $\mathbf{H}_0$ being the applied field, $\mathbf{H}_u$ being the uniaxial anisotropy field, $\mathbf{N}$ being the demagnetization tensor and $\mathbf{h}$ being the transverse r.f. field. The magnetization in the case of low-intensity signal is

$$\mathbf{M} = M_o \hat{\mathbf{n}} + \mathbf{m}e^{-iwt}, \tag{2.205}$$

where $\hat{\mathbf{n}}$ is in the direction of H_{eff} and $\mathbf{m}$ is the rf microwave field component perpendicular to $\hat{\mathbf{n}}$. Equation (2.203) establishes a relation between $\mathbf{m}$ and $\mathbf{h}$ via the susceptibility tensor, χ which is

$$\mathbf{m} = \boldsymbol{\chi} \cdot \mathbf{h}. \tag{2.206}$$

The relationship between susceptibility and permeability is

$$\boldsymbol{\mu} = 1 + 4\pi \boldsymbol{\chi}. \tag{2.207}$$

When the applied field, $\mathbf{H}_0$ is along the $\hat{\mathbf{x}}$ direction and the higher order terms are excluded, Equation (2.203) can be written by means of the components as

$$\begin{aligned} iwm_z &= -\gamma((H_0 - H_u)m_y - M_0 h_y), \\ iwm_y &= -\gamma((H_0 m_z + M_0 h_z). \end{aligned} \tag{2.208}$$

The permeability tensor becomes

$$\begin{pmatrix} 1 & 0 & 0 \\ 0 & 1+4\pi M_0\frac{H_0}{H_0(H_0-H_u)-w^2/\gamma^2} & -i4\pi M_0\frac{w/\gamma}{H_0(H_0-H_u)/M_0^2-w^2/\gamma^2} \\ 0 & i4\pi M_0\frac{w/\gamma}{H_0(H_0-H_u)-w^2/\gamma^2} & 1+4\pi\frac{H_0-H_u}{H_0(H_0-H_u)-w^2/\gamma^2} \end{pmatrix}. \tag{2.209}$$

When the applied field, $\mathbf{H}_0$ is along the $\hat{\mathbf{y}}$ direction, the permeability tensor takes the form as

$$\begin{pmatrix} 1+4\pi M_0\frac{H_0-4\pi M+H_u}{(H_0-4\pi M+H_u)^2-(w\gamma)^2} & 0 & i4\pi M_0\frac{w/\gamma}{(H_0-4\pi M+H_u)^2-(w\gamma)^2} \\ 0 & 1 & 0 \\ -i4\pi M_0\frac{w/\gamma}{(H_0-4\pi M+H_u)^2-(w\gamma)^2} & 0 & 1+4\pi M_0\frac{H_0-4\pi M+H_u}{(H_0-4\pi M+H_u)^2-(w\gamma)^2} \end{pmatrix}. \tag{2.210}$$

Applying the Maxwell equations, the dispersion relation can be evaluated as

$$\begin{gathered} \nabla\times\mathbf{h}=0, \\ \nabla\cdot(\mathbf{h}+4\pi\mathbf{m})=0, \\ \nabla\cdot(\boldsymbol{\mu}\cdot\mathbf{h})=0. \end{gathered} \tag{2.211}$$

A scalar potential, ζ can be defined, which gives $\mathbf{h}=\nabla\zeta$. After substituting $\mathbf{h}$ in Equation (2.210), one obtains

$$\nabla\cdot(\boldsymbol{\mu}\cdot\nabla\zeta)=0. \tag{2.212}$$

The normal modes in a rectangular film are defined by the in-plane wave vector, $\mathbf{K}_{\text{in-plane}}=(k_x,k_z)$ and the perpendicular wave number, k_y, and the frequency, w. The interior solution of 2.212 is given as

$$\zeta_{int}=(a\text{exp}(ik_yy)+b\text{exp}(-ik_yy))\text{exp}(i(k_xx+k_zz))\text{exp}(-iwt). \tag{2.213}$$

By replacing Equation (2.213) in Equation (2.212), for the parallel orientation, one gets

$$k_x^2+\mu_{yy}k_y^2-\mu_{zz}k_z^2=0, \tag{2.214}$$

and for the perpendicular orientation, the following relation is valid

$$\mu_{zz}(k_x^2+k_z^2)+k_y^2-=0. \tag{2.215}$$

The external solution of Equation (2.212) for $y > d/2$ or $y < -d/2$ is such that

$$\zeta_{ext} = C_{1,2}\text{exp}(\pm k_y y)\text{exp}(i(k_x x + k_z z))\text{exp}(-iwt). \tag{2.216}$$

Then, Equation (2.212) becomes

$$\kappa_y^2 = k_x^2 + k_z^2 = 0. \tag{2.217}$$

For an in-plane wave vector, k_y can be either real or imaginary. The real one is volume mode and the imaginary one is surface mode. According to the boundary conditions, the normal components of bulk and the tangential components of **h** must be continuous such that

$$\partial_y \zeta_{ext} = (\mu_{yx}\partial_x + \mu_{yy}\partial_y + \mu_{yz}\partial_z)\zeta_{int}. \tag{2.218}$$

Here, $\zeta_{ext} = \zeta_{int}$ for $y = \pm d/2$. The resulting characteristic equation is

$$(\kappa_y^2 + (k_x\mu_{yx} + k_z\mu_{yz})^2 - (k_y\mu_{yy})^2)\sin k_y d - 2\kappa_y k_y \mu_{yy}\cos k_y d = 0. \tag{2.219}$$

The dispersion relation divides into bulk and surface modes in the case of parallel orientation. Bulk and surface modes are separated from each other at a boundary with a critical ratio of k_z/k_x. The dispersion relation of volume modes with $k_y^2 > 0$ is

$$tan(k_x d\alpha^1/2 + n\pi) = \frac{2\mu_{yy}\alpha^{1/2}(1+\eta^2)^1/2}{1+\eta^2 - |\mu_{yz}|^2\eta^2 - \alpha\mu_{yy}^2}. \tag{2.220}$$

The dispersion relation of surface modes with $k_y^2 < 0$ is

$$tanh(k_x d|\alpha|^1/2) = \frac{2\mu_{yy}|\alpha|^{1/2}(1+\eta^2)^1/2}{1+\eta^2 - |\mu_{xz}|^2\eta^2 + \alpha\mu_{yy}^2} \tag{2.221}$$

with $\eta = k_z/k_x$, $\alpha = \mu_{zz}/\mu_{yy}(\eta_c^2 - \eta^2)$, $\eta_c^2 = -\mu_{zz}^{-1}$ and $k_y = k_x\alpha^{1/2}$. Magnetostatic surface and bulk modes for a parallel magnetized film with $K_u = 0$ are sketched in Figure 2.39. According to Equation (2.220) for n layers, the volume modes are between the frequencies of $w = \gamma H_0$ and $w = \gamma(H_0(H_0 + 4\pi M))^1/2$. The surface modes occur above the $w = \gamma(H_0(H_0 + 4\pi M))^1/2$ at a critical angle of η_c. The surface mode is limited to the upper boundary of $w = \gamma(H_0 + 2\pi M)$.

In uniaxial anisotropy, the volume modes at $k_x - w$ plane shift to the $w = \gamma(H_0(H_0 - H_u))^{1/2}$. At $k_x = k_y = 0$, $w = \gamma(H_0(H_0 - H_u + 4\pi M))^{1/2}$. The effect of the uniaxial anisotropy on the surface modes is to change some surface modes to the volume modes. In perpendicular orientation, the only allowed modes are volume modes. The dispersion relation is

$$tan(\mu_{xx}^{1/2}(k_x^2+k_y^2)^{1/2}d+n\pi)=\frac{2(-\mu_{xx})^{1/2}}{1+\mu_{xx}}. \tag{2.222}$$

The uniaxial anisotropy shifts the magnetostatic modes by $\delta w=\gamma H_u$. For a finite dimension of magnetic samples, the quantized wave vectors are defined as $k_x=n_x\pi/l_x$ and $k_z=n_z\pi/l_z$, where n_x and n_z are positive integers and l_x and l_z are dimensions.

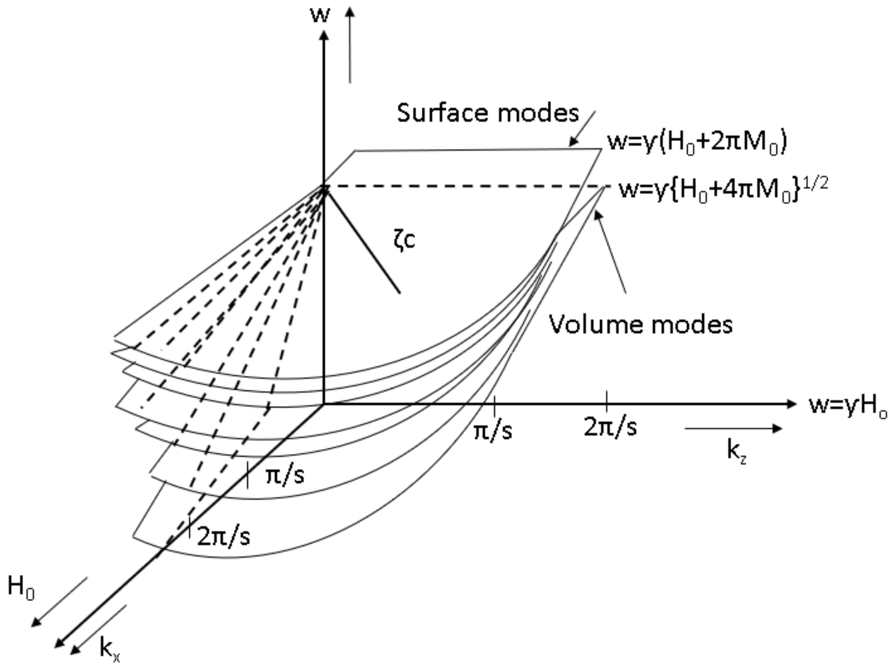

Figure 2.39. Magnetostatic bulk and surface modes in a ferromagnetic material [57].

The absorption that arises due to the excitation by the microwave field **h** is proportional to $\mathbf{m}\cdot\mathbf{h}$. In the case of parallel orientation, magnetization is written in the form $(0, m_y(\mathbf{r})\text{exp(-iwt)}, m_z(\mathbf{r})\text{exp(-iwt)})$ where

$$\begin{aligned} m_z&=(\mu_{zz}-1)\frac{\partial\zeta}{\partial z}+(\mu_{zy})\frac{\partial\zeta}{\partial y},\\ m_y&=(\mu_{yz})\frac{\partial\zeta}{\partial z}+(\mu_{yy}-1)\frac{\partial\zeta}{\partial y}.\end{aligned} \tag{2.223}$$

The microwave field, $\mathbf{h}$ can be written such that (h_x, h_y, h_z)exp(-iwt). The absorption power for the mode $(n_x\pi/l_x, n_z\pi/l_z)$ is

$$\mathbf{m} \cdot \mathbf{h} = 1/2\mathrm{Re}(\mathbf{m} \cdot \mathbf{h}^*) \tag{2.224}$$

and

$$\begin{aligned} \zeta &= X(x)Y(y)Z(z) \\ &= (a\mathrm{exp}(ik_y y)) + b\mathrm{exp}(ik_y y))\mathrm{exp}(i(k_x x + k_z z))\mathrm{exp}(-iwt). \end{aligned} \tag{2.225}$$

By taking the integral overall volume, the allowed resonance conditions can be determined by

$$\langle \mathbf{m} \cdot \mathbf{h} \rangle = (\frac{I_z A}{n_z \pi}[Y(y)]_{-d/2}^{d/2} + B\int_{-d/2}^{d/2} Y(y)dy) \sin{(n_z\pi/l_x)}(l_x n_x/\pi) \sin{(n_x\pi/l_x)} \tag{2.226}$$

with A and B being functions of $\mathbf{h}$, h_i, w, and M_0. Following Equation (2.226), one can draw a conclusion such that there is no absorption once one of n_x or n_z is even. If both n_x and n_z are odd, the absorption intensity is higher for the low modes, n_x, and is less for the higher modes for which the applied field is along the x-direction. Figure 2.40 displays the magnetostatic spectrum of a 12 μm YIG film. The uniaxial anisotropy is not taken into account in the spectrum. $(n, 1)$ labelled modes are surface modes where $\eta > \eta_{cr}$ and $(1, n)$ refers to the volume mode that holds the condition $\eta < \eta_{cr}$. In thin/ultrathin YIG films, the magnetostatic energies are not large compared to the exchange energy. Figure 2.41 shows the magneto exchange spectrum branch for a 480 nm YIG film. High field exchange modes occur at $n = 1$ branch, while at $n = 3$, the low field magneto exchange modes are observed. An easy plane anisotropy energy yields excitation of bulk modes within the surface modes. If the excitation is interrupted by an inhomogeneous anisotropy, a considerable separation distance occurs between the surface modes in the spectrum.

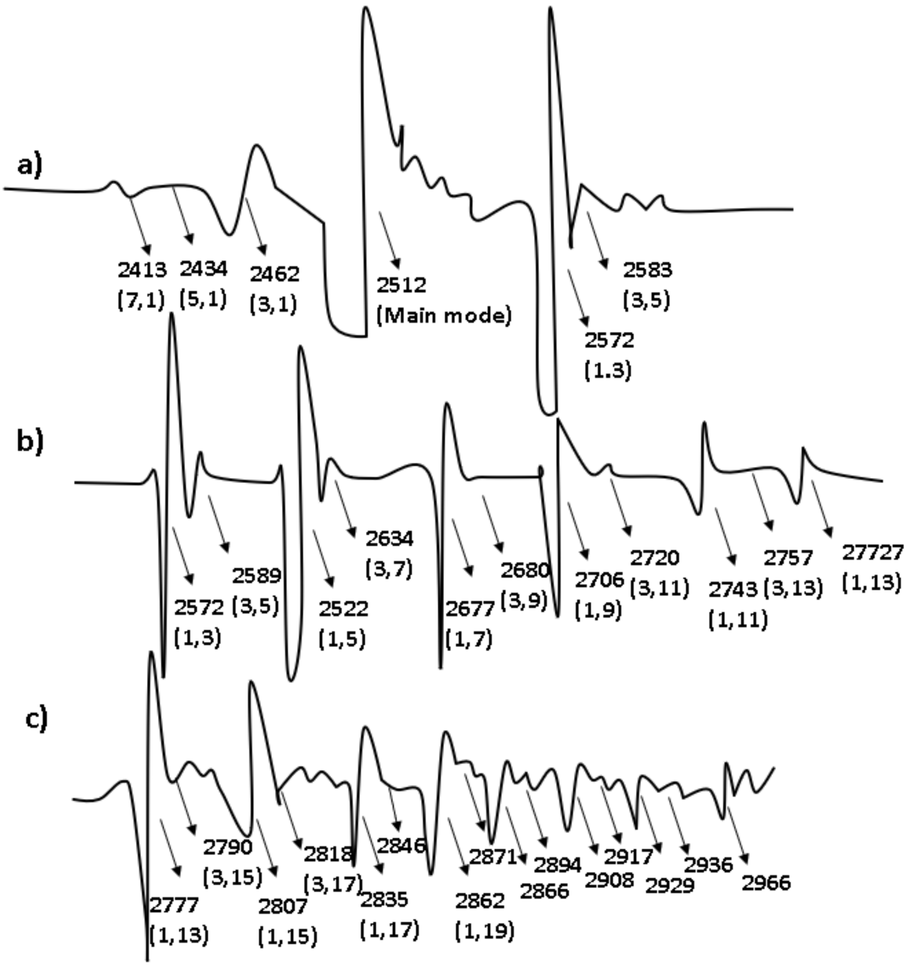

Figure 2.40. Magnetostatic mode spectrum of a 12 μm YIG film at the parallel orientation.

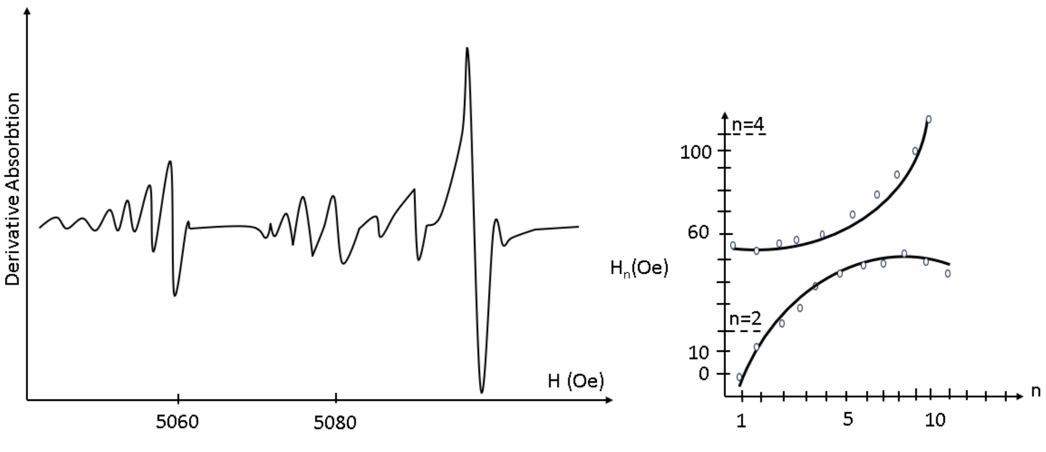

Figure 2.41. The left. High field magneto exchange modes at $n = 1$ and low field exchange modes at $n = 3$. The right. The resonance field versus n modes. $n = 1$ and $n = 3$ branches come closer.

2.6.1. Spin Wave Propagation

Magnetostatic waves are produced at high frequencies and their velocity depends on the frequency, which makes them suitable for microwave delay lines. Magnetostatic wave wavelength is between the micron and millimeter range. For YIG, the frequency of magnetostatic waves is between 1 and 40 GHz [51,68]. Three types of magnetostatic waves can be generated in a device geometry, depending on the orientation between the applied field and spin-wave propagation. In the case of surface spin waves, H_0 and M_0 are parallel to $\hat{\mathbf{x}}$ while $\hat{\mathbf{k}}$ is parallel to $\hat{\mathbf{z}}$. For forward volume modes, H_0 and M_0 are parallel to $\hat{\mathbf{y}}$ while $\hat{\mathbf{k}}$ is in the xz plane. For backward volume modes, H_0 and M_0 are parallel to $\hat{\mathbf{x}}$ while $\hat{\mathbf{k}}$ is parallel to $\hat{\mathbf{x}}$. In the assumption of zero uniaxial anisotropy, the frequency of the magnetostatic surface modes are

$$(H_0^2 + H_0 4\pi M_0)^{1/2} < \varOmega < H_0 + 2\pi M_0 \tag{2.227}$$

and for volume modes are

$$(H_0)^{1/2} < \varOmega < (H_0^2 + H_0 4\pi M_0)^{1/2}. \tag{2.228}$$

The volume modes are in the spin wave band range and the surface modes are above the spin wave band as shown in Figure 2.42. The group velocity is $\partial w/\partial k$. The group delay is inversely proportional to the group velocity and the film thickness. The relation between the group velocity and the frequency is not linear. There needs to be modifications for a non-dispersive delay line generation. The excitation and dispersion relations of spin waves are studied in detail by Damon and Escbach [51,68]. When the wave number, k goes to zero, the frequency of the forward volume magnetostatic waves goes to $f_H = \gamma H_0$ with an internal field, H_0. When k increases, the frequency goes to $f_1 = \sqrt{f_H(f_H + f_M)}$ with $f_M = 4\pi\gamma M_0$ and M_0 is the saturation magnetization. The dispersion relation does not change with the change in the propagation direction in the film plane, since the propagation direction is perpendicular to the applied field direction. The dispersion relation for the forward volume modes in Figure 2.43 is given as [69–71]

$$f_{\text{FVMSW}} = \sqrt{f_H(f_H + f_M(1 - \frac{1 - \exp(-kd_0)}{kd_0}))}. \tag{2.229}$$

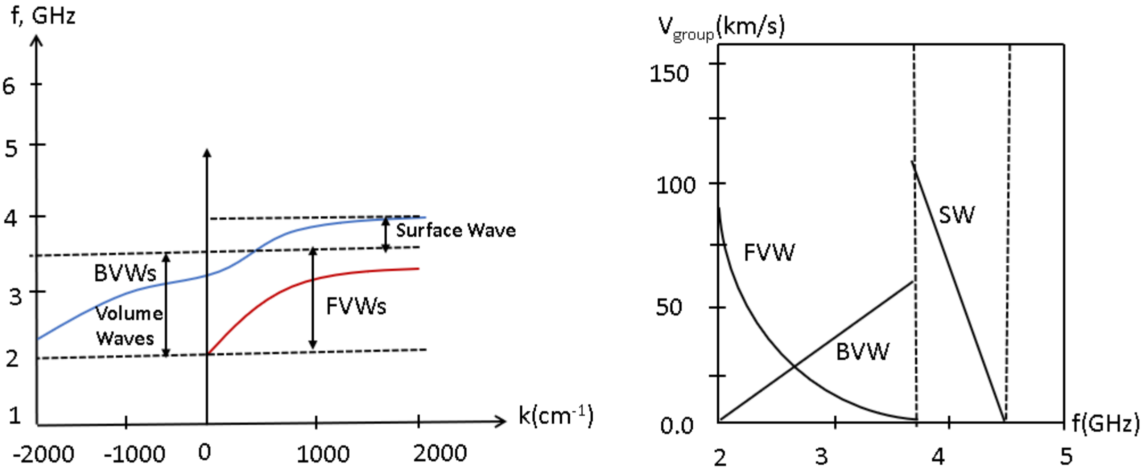

Figure 2.42. The left. The dispersion relation for the magnetostatic wave modes in the y direction for YIG films at a field of 710 eV. The right. Group velocity versus frequency for magnetostatic modes.

In in-plane magnetized films, backward volume magnetostatic modes and magnetostatic surface modes can be excited. The dispersion curve for the backward volume modes is calculated depending on the relation

$$f_{\mathrm{BVMSW}} = \sqrt{f_H(f_H + f_M\frac{(1-\exp(-kd_0))}{kd_0}))}. \tag{2.230}$$

The slope of the dispersion curve of the backward volume modes is negative, which means that their group velocity is negative. The phase and group velocity propagate oppositely. One can conclude from the dispersion curve that the frequency decreases when the wave number increases. Different from the volume modes in which the magnetization precession is sinusoidal within the thickness of the film, the precession of the surface spin waves is exponential along the thickness and has a maximum value at one surface depending on the direction of the applied field or propagation direction. The dispersion relation for magnetostatic surface spin waves is given by

$$f_{\mathrm{MSSW}} = \sqrt{(f_H + f_M/2)^2 - (f_M/2)^2\exp(-2kd_0)}. \tag{2.231}$$

For the small k values, the frequency of surface modes has the same value as one of the backward volume modes, f_1 which is the FMR frequency of the in-plane magnetized films. When k increases, the frequency of the surface spin wave modes becomes $f_H + f_M/2$ [51, 72]. In Figure 2.43, the lowest-order uniform modes are shown. For higher-order modes, the dispersion is not uniform and can be explained by other dispersion laws [24,51,69]. The magnetostatic volume and surface modes can be excited by a waveguide with a microstrip antenna. From all, the excitation of surface spin waves is very efficient and non-reciprocal. In practice, the film thickness is much smaller than the magnetostatic spin wave wavelength ($kd_0 << 1$). For this reason, the magnetization precession is uniform across the thickness. The non-reciprocality in excitation arises from the spin wave interference caused by the parallel and perpendicular components of the microwave field. MSSW and FWMSW s are the most studied ones for applications. Recently, BVMSSWs have been under investigation for their unique dispersion properties from a technical point of view. Another type of spin wave which taken interest lately is dipolar exchange spin waves with short wavelengths formerly studied by [70, 71].

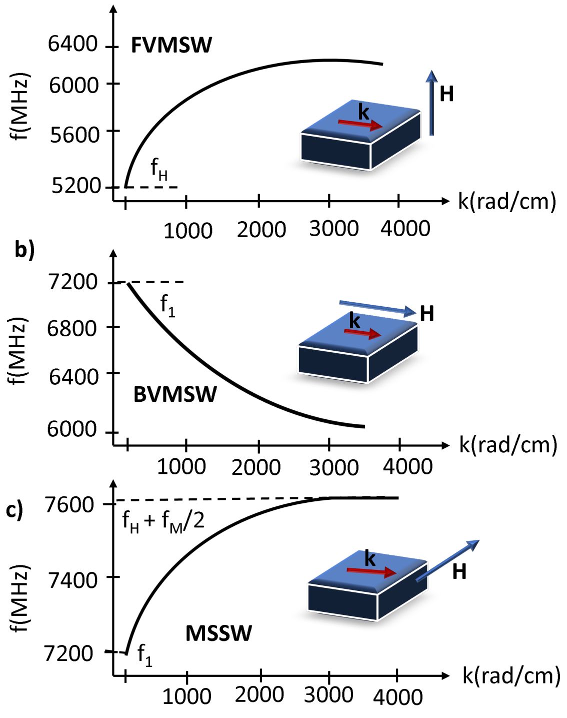

Figure 2.43. Dispersion curves for the forward volume magnetostatic modes, backward volume magnetostatic modes, and magnetostatic surface modes in a 5 μm film with a saturation magnetization of 1750 Gauss at an applied field of 1850 Oe.

3. THIN FILM DEPOSITION AND CHARACTERIZATION TECHNIQUES

In the scope of this thesis, thin film deposition techniques such as sputtering and pulsed laser deposition techniques were used. To produce the dot/antidot array structures, the photolithography technique was used. The chemical and crystal structure analysis of the produced thin films was done by X-ray photoemission spectrum (XPS) and X-ray diffraction (XRD) measurement techniques. The magnetic analysis was done by using a vibrating sample magnetometer (VSM) and ferromagnetic resonance (FMR) measurement. The magnetization curves of the array structures were simulated by using a micromagnetic simulation, Mumax3. Therefore, a short description of the techniques used in this work is given in the following sections.

3.1. Pulsed Laser Deposition (PLD)

Pulsed laser deposition (PLD) is a technique that uses ultra-short and high-energy laser pulses from energy sources such as Nd: YAG, krypton fluoride (KrF), or argon fluoride (ArF) excimer lasers with a wavelength of 355 nm, 248 nm, or 193 nm, respectively [73]. Excimer lasers supply high power and stability of energy during ablation. A scheme that shows the pulsed laser deposition is given in Figure 3.1. To deposit a thin film on a substrate, the target surface is ablated with short laser pulses at a repetition rate. The target surface vaporizes due to superheating, ionizes, and finally turns into a high-energy plume spreading towards the substrate. The ejected specimen condenses on the substrate surface, which stands opposite to the target. In PLD, the ejected plume from the target surface is due to the photon interaction and has the same stoichiometry as the target material, in contrast to the thermal evaporation technique in which the resulting stoichiometry depends on the vapor pressure of each element of the heated target. PLD is a suitable technique to obtain the stoichiometry of multi-element targets on the deposited thin film. The kinetic energies of the ablated particles can determine the surface diffusion, but the energy is not high enough to produce bulk samples. Therefore, only thin/ultrathin films of metals, insulators, and semiconductors can be produced by using PLD. It is possible to have the same stoichiometry of the target in the thin film by arranging the suitable growth conditions such as laser energy, pulse duration time, repetition rate, the distance between the target and the substrate, deposition temperature, and oxygen pressure.

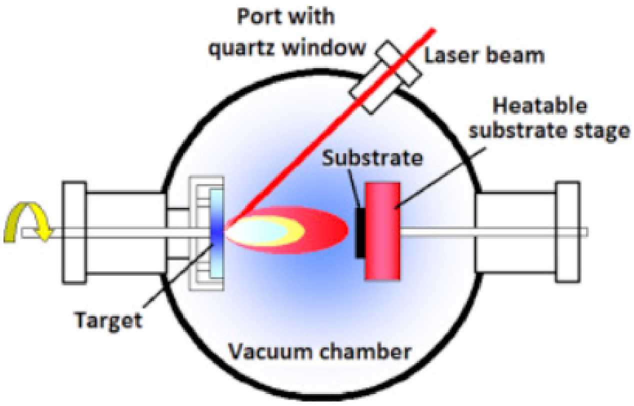

Figure 3.1. The scheme of the pulsed laser deposition [74].

3.2. RF Sputtering

Sputtering is a common technique to deposit thin films on substrates. The ejection of atoms from a target surface occurs by bombarding them with high-energy ions. The momentum of the ions striking the target surface is transferred to the ejecting atoms from the cathode/target and the sputtered atoms move toward the substrate. The ions are generated due to the glow discharge caused by the electric field between two electrodes in a gas at low pressure. At a low voltage, the gas ionizes and becomes conductive, called plasma. To form a plasma, a moderate vacuum pressure is needed between the range of 10^{-1} to 10^{-3} Torr. In sputtering, an inert gas, usually Argon (Ar) gas, is used since it does not react with materials. Positive Ar ions are accelerated by a high electric field and move to the cathode (negative electrode) and hit the target. Particles eject from the target surface to the plasma and travel to the substrate. The sputtering process is schematically shown in Figure 3.2. During sputtering, momentum transfer does not cause heat on the target, so there is no decomposition of the target or substrate. This type of sputtering is called DC sputtering. Plasma ions become neutral after striking the target. If the target is an insulator, the electrical charge of the target becomes positive after the plasma bombarding. The charge on the target may repel the bombarding ions and cause to terminate the sputtering process. For continuous sputtering, more electrons must be attracted from the plasma, which requires the reversal of the polarity. By applying radio frequency RF voltage on the target, the polarity can be reversed periodically. This type of sputtering is called RF sputtering. RF sputtering is used in either conductors or isolators. The sputtering can be more efficient by using a magnetron source. A magnetic field spirals the electrons, which enables more ionization and higher density in plasma. Positive ions in the plasma which is produced by magnetic glow discharge bombard the target. This type of sputtering is described as magnetron sputtering. By sputtering, it is possible to deposit thin films which have the same stoichiometry as the target. The thin film of elements such as metals, semiconductors, alloys, and compounds is produced by the sputtering technique [75, 76].

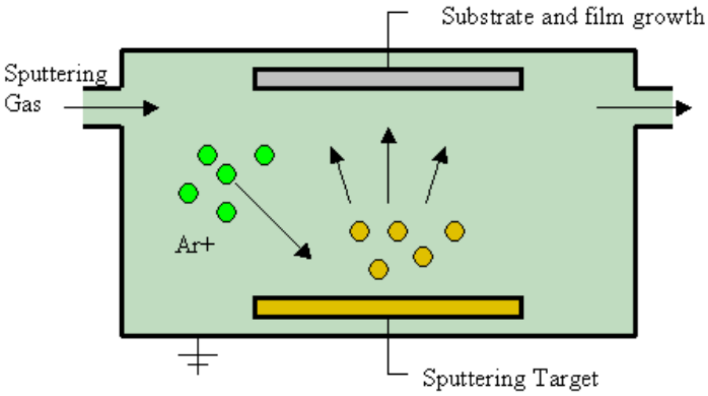

Figure 3.2. A scheme of the sputtering process [77].

3.3. X-Ray Diffraction(XRD)

XRD is an analytical technique that gives information about the crystal structure of the materials and thin films such as crystal phase, unit cell, and atomic spacing. By using this technique, chemical analysis, stress measurement, and texture analysis of the materials can be performed [78]. XRD shows the atomic structure of the material. The elastic scattering intensity of an X-ray beam from the electron clouds of the individual atoms, when it hits a sample, depends on the angle of the incidence and scattering, polarization, and wavelength. Max von Laue found out that X-rays reflect from crystalline materials like three-dimensional diffraction gratings (1912). In Xray diffraction, monochromatic Xrays and a crystalline sample make constructive interference. An incident beam of X-ray interferes with another at the atomic planes of the crystal when they leave the crystal. Bragg's law explains the X-ray beam's reflection from a crystal surface at certain angles of incidence, θ, such that

$$n\lambda = 2d \sin\theta, \tag{3.1}$$

where d is the distance between atomic layers in a crystal, λ is the wavelength of the incident X-ray and n is an integer as shown in Figure 3.3.

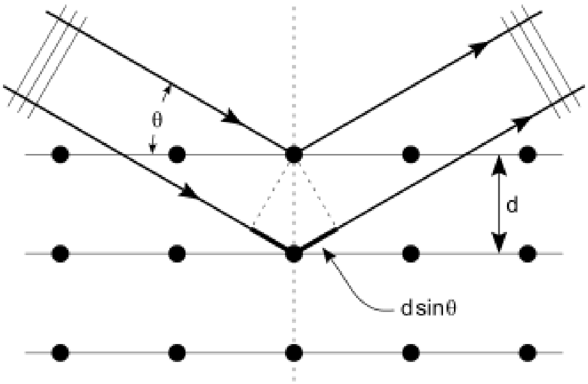

Figure 3.3. Bragg's law [79].

According to Bragg's law, the wavelength of electromagnetic radiation is related to the diffraction angle and the lattice spacing. The incoming beam gives rise to radiation of scattered ones as a spherical wave. If the scattered ways are symmetrically separated from each other with a distance of d, the spherical waves make constructive interference in directions in which the difference in path length is equivalent to an integer multiple of the wavelength. The incoming beam is deflected by an angle 2θ and generates a reflection spot in the diffraction pattern. Xrays are produced by a cathode ray tube by heating a filament, which generates electrons. The accelerated electrons under a voltage bombard the target. If the energy is high enough for the inner shell electrons of the target, X-rays are produced. Constructive interference and a diffracted ray arise in certain conditions based on Bragg's Law.

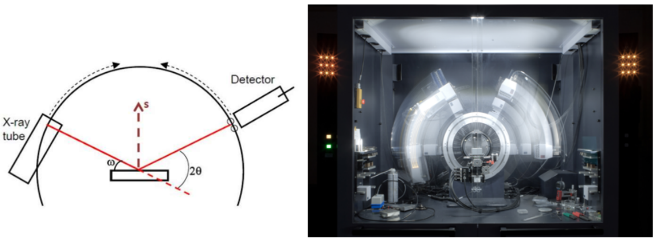

Figure 3.4. X-ray Diffraction measurement scheme [79].

Diffracted rays are detected. The crystalline sample is scanned through a range of 2θ angles and all diffraction directions of the lattice are obtained. XRD spectra consist of K_α which has two subcomponents $K_{\alpha1}$ and $K_{\alpha2}$, and K_β. The wavelength of $K_{\alpha1}$ is shorter, and the intensity is twice the intensity of $K_{\alpha2}$. Specific wavelengths are enhanced depending on the target materials such as Cu, Fe, Mo, and Cr. Monochromatic X-rays are obtained by filtering with foils or crystal monochromators. As a target, Cu is generally used for single-crystal diffraction (CuKα radiation = $1.5418A°$). Figure 3.4 shows an XRD measurement scheme. X-rays are collimated and directed to the sample. The intensity of the reflected X-rays is saved as the sample and detector are rotated. As long as the geometry of the incident X-rays satisfies the Bragg condition, constructive interference and a peak intensity arise. The sample rotates in the collimated X-ray beam path at an angle θ in an X-ray diffractometer. The X-ray detector is placed on an arm and records the diffracted X-rays by rotating at an angle of 2θ using a goniometer. XRD satisfies information about the compounds in nanoparticles, calculating or comparing with the standard value of lattice parameters and crystallinity of the sample. Diffraction peaks corresponding to dspacings, let us identify the material, since the dspacings of each material are unique. For identification, d-spacings are compared with the standard reference patterns.

3.4. X-Ray Photoemission Spectroscopy (XPS)

X-ray photoelectron spectroscopy (XPS) is a quantitative spectroscopic technique. XPS is a powerful analytic method due to the surface sensitivity and the identification of the chemical state of the elemental compounds in the material. XPS can provide information about the elements inside a material, the elemental composition, chemical state, empirical formula, and electronic state. Except for hydrogen and helium, XPS detects all elements. The underlying principle of this technique is the photoelectric effect.

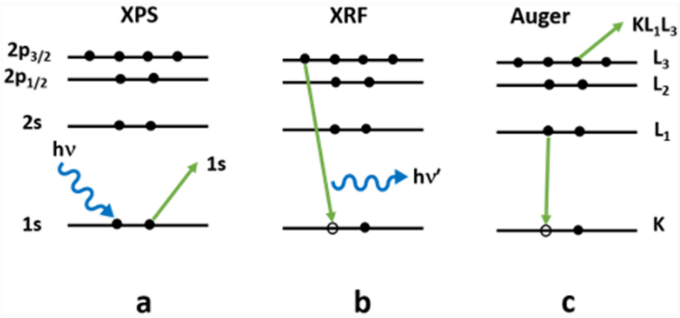

Figure 3.5. X-ray bombarding the material surface. (a) emission of a photoelectron, (b) x-ray fluorescence, and (c) emission of an Auger electron [80].

By bombarding the material surface with soft X-rays whose energies are lower than 6 keV, electrons are emitted from the surface, and the kinetic energy of the emitted electrons is measured by an electron Energy Analyzer. The x-ray energy transfer to a core-level electron is shown in Figure 3.5 (a). The energy of the X-ray ($h\nu$) is equal to the total of the binding energy (BE), kinetic energy (KE), and the work function of the spectrometer, (ϕ_s) such that

$$h\nu = \mathrm{BE} + \mathrm{KE} + \phi_s. \tag{3.2}$$

The binding energy of the electron is material-specific and can be determined from the Equation (2.224). Any electron that has a lower BE than the X-ray source energy is emitted from the material and detected by a detector. Due to the emitted electron, a hole occurs at the core level. To relax the ionization state, an electron from the valance band fills the hole by releasing energy in two processes described as X-ray

Fluorescence and Auger electron emission, as shown in Figure 3.5b and c. The Auger electron is used in XPS qualitative analysis. An XPS instrument is composed of an X-ray source, an ion gun, a stage, extraction lenses, and a detector in an ultra-high vacuum environment. A diagram of an XPS system is illustrated in Figure 3.6.

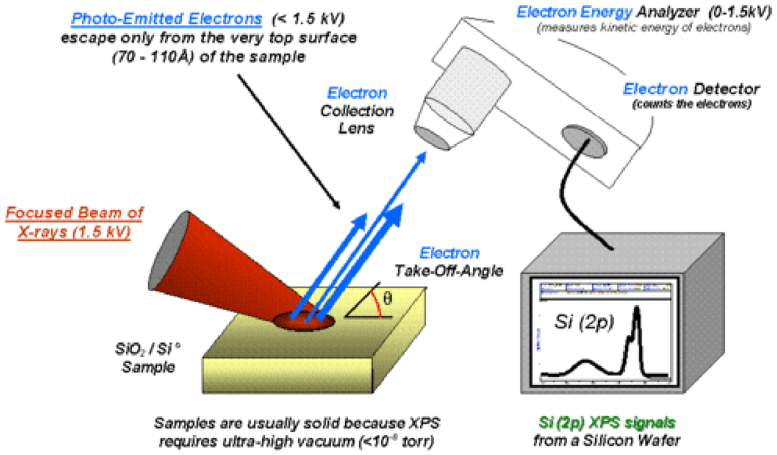

Figure 3.6. An X-ray Photoemission spectroscopy (XPS) scheme [81].

The binding energies can be obtained from the positions of the peak and the elements inside the sample. An XPS spectrum is plotted by the number of electrons at a specific binding energy. Each element has characteristic XPS peaks which give the electron configuration such as 1s, 2s, 2p, 3s, and so on. The number of detected electrons in each peak determines the amount of the element in the sample. For the values of atomic percentage, the intensity of each raw XPS signal is divided by a relative sensitivity factor (RSF) and is normalized over all the detected elements.

3.5. Photolithography

Lithography is a widely used technique in integrated circuits (IC), microsystems (MEMS) fabrication, and the semiconductor industry. Several layers with different patterns constitute the components of a device. Lithography enables the transfer of different patterns on each respective layer. The principle is imaging a pattern from a mask onto a photosensitive layer. There are many lithography techniques such as photolithography, x-ray lithography, electron beam lithography, micro-contact lithography, and nano-imprint lithography. Among all, photolithography is a classic and conventional technique. The steps of the process are depicted in Figure 3.7. Photolithography copies the pattern on a lithographic mask onto a photoresist-coated substrate via an optic system. Photoresists have a photo-sensitive compound, a polymeric backbone, and a solvent. Resists are classified into positive and negative resists according to the solubility after radiation exposure. When a positive photoresist is illuminated by radiation, the exposed areas are more soluble. When a negative photoresist is under-exposure, the exposed area hardens. As shown in Figure 3.7, the first step is the resist coating on a substrate. The substrate must be cleaned with alcohol and must be baked to remove water on the surface. Usually, the surface is covered with Hexamethyldisalizane or HMDS to determine the adhesion between the resist and the wafer. After the primer is applied, the substrate must be cooled to room temperature.

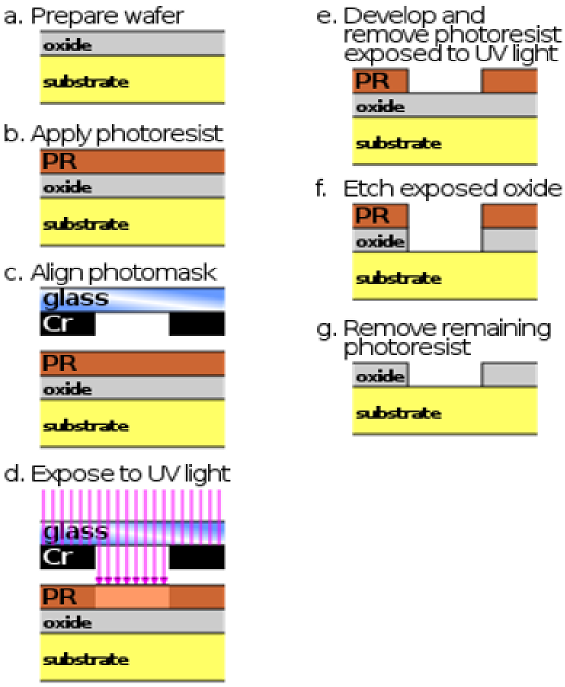

Figure 3.7. The steps of the lithography process [82].

A photoresist is coated homogeneously on the surface by spin coating until the desired thickness is achieved. A soft bake is done to remove the solvents in the resist and cool down to room temperature. By using a mask aligner, the resist-coated substrate is exposed to ultraviolet light through a Cr mask. After a chemical reaction with the resist and light, the areas illuminated become soluble. The resist is removed by using a developer. The resist on the exposed areas is removed, while the resist on the region that is not exposed to UV light remains on the substrate. The structure is etched based on the pattern and finally, the remaining photoresist is cleared away. The exposure of the resist types and the final structure is shown in Figure 3.8.

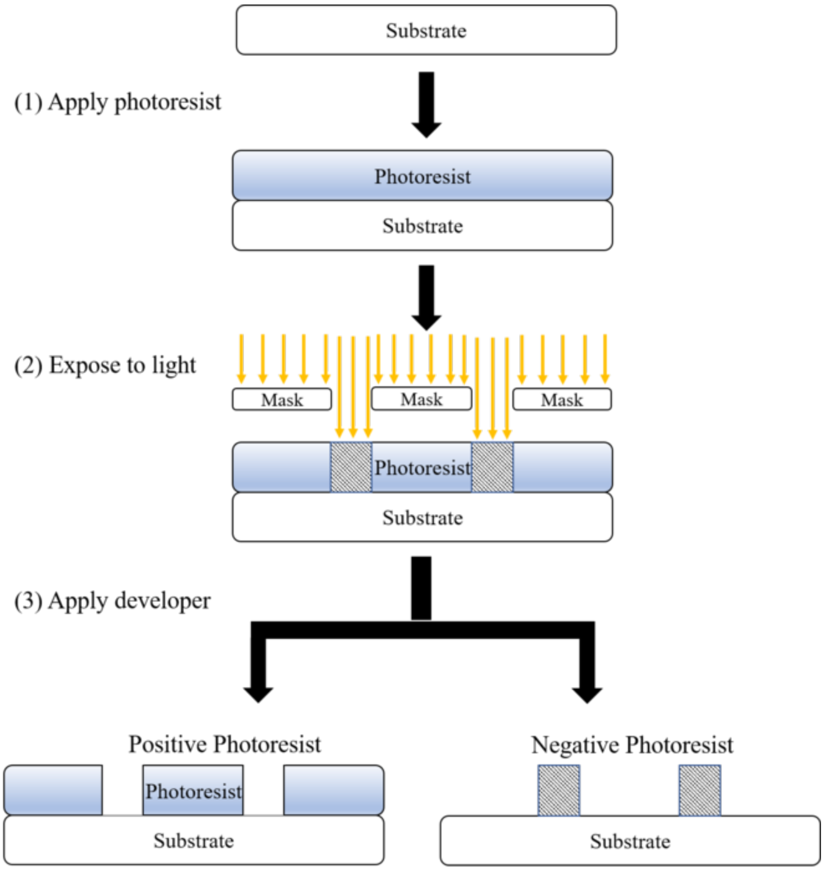

Figure 3.8. The patterns obtained using positive and negative photoresist when exposed to UV light [83].

3.6. Vibrating Sample Magnetometer (VSM)

Vibrating-Sample Magnetometer measures the flux change in a coil when a magnetized sample is vibrated near it [84]. The sample is attached to the end of a non-magnetic rod that oscillates between the pickup coils. The other end is connected to a loudspeaker cone or a mechanical vibrator. The stray magnetic field of the magnetized sample moves with the sample, resulting in a changing magnetic flux in the coils. An alternating electromotive force (emf) is enhanced in coils due to the oscillating magnetic field of the vibrating sample. The magnitude of the alternating emf and the magnetic moment of the sample are proportional to each other. The induced electric field in the pickup coils generates current which is proportional to the magnetization of the sample. By using a lock-in amplifier sensitive to the signals at the vibration frequency, the small emf is amplified. Depending on the voltage generated by this varying magnetic flux in the coils, a hysteresis curve is recorded. The VSM scheme is shown in Figure 3.9.

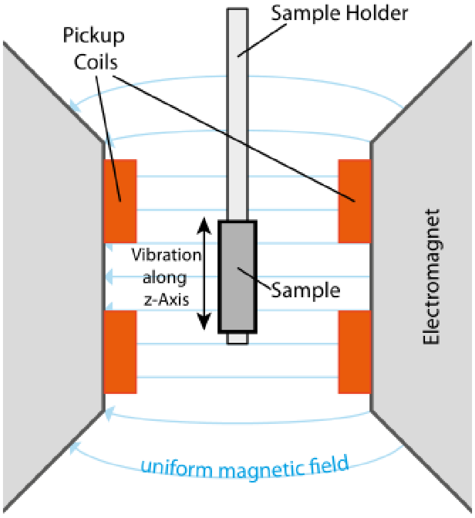

Figure 3.9. Vibrating sample magnetometer scheme [85].

3.7. Ferromagnetic Resonance (FMR)

FMR is a technique for measuring both magnetostatic properties such as anisotropies and exchange coupling, as well as spin dynamics, which includes damping constant, g factor, and spin relaxation. FMR spectrometer records the electromagnetic wave that is absorbed by the sample in the presence of an external DC magnetic field. The spectrometer involves a detector, electromagnetic wave excitation source, and transmission line which links the sample and electromagnetic source. Since the precession frequency of ferromagnetic materials is at the microwave regime, which ranges from 0.1 GHz to 100 GHz, FMR absorption is obtained at the microwave range. Other components of the FMR spectrometer are the resonator and electromagnet. The magnetic field produced by the electromagnet changes the magnetization of the sample along the measurement. The sample placed inside the cavity absorbs energy from the microwave source. The change in the reflectance or transmittance of the microwave is recorded by the detector, the Schottky barrier diode when the magnetic field is swept. The reflectance is measured at a fixed band frequency. A Klystron going through a waveguide into a metallic cavity produces a microwave. The signal is reflected from the cavity to a detector. Metallic cavities are TE mode with a very high Q-factor. The excitation magnetic field is maximum at the cavity center where the sample is mounted. A circulator is used to prevent the microwave to return to the generator after going to the detector. A microwave bridge is described as the combination of the microwave source, detector, circulator, etc. in a box. A ferromagnetic resonance spectrometer is shown in Figure 3.10. The microwave frequency is matched with the eigen resonance of the cavity. By increasing the magnetic field, resonance absorption of the spin system is enhanced. Ideally, the cavity stores all microwave energy and there is no microwave power reflected. Resonance characteristics change with small changes in the dielectricity and permeability in the cavity. The absorption of ferromagnetic resonance in the spin system is enhanced. Microwave power is reflected from the cavity and detected at a diode. The absorption spectrum is recorded according to the difference between the incident and reflected signals. For field swept FMR detection, TE102 cavity is used with unload Q of $9,000$ at X-band, and FMR signal is recorded through the measurement of reflectance, and therefore one vector network analyzer (VNA) port for S11 is used. One can differentiate the original data for the derivative spectrum that determines the peak position and line width. [57,86].

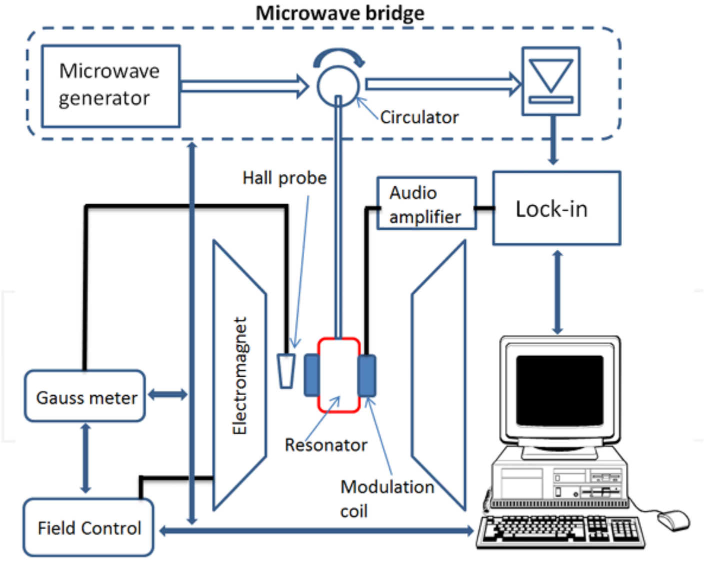

Figure 3.10. Ferromagnetic resonance spectrometer [86].

3.8. Micromagnetic Simulations

Mumax3 is a GPU-accelerated micromagnetic simulation program that calculates the space and time-dependent magnetization dynamics in ferromagnets using a finite-difference discretization [87]. Open-source programs OOMMF (CPU) [88] and MicroMagnum (GPU) [87], and the commercial GpMagnet (GPU) [89] uses a similar technique. Mumax3 is open-source software written in Go programming language and uses Nvidia's CUDA platform as a compiler to do the computation in GPU. The software is run by an Nvidia GPU driver and a Linux, Windows, or Mac platform. Mumax3 uses a finite difference (FD) discretization of space and comprises a 2D or 3D grid of orthorhombic cells. Volumetric quantities, such as the magnetization and effective field, are assumed at the center of each cell. However, coupling quantities, such as the exchange strength, act between the face of the cells. Each cell corresponds to a region index from 0 to 256. Materials are represented by different region indices.

Coupling parameters such as exchange strength are indicated by the region indices of the two interacting cells. In addition to space dependence, Mumax3 allows material parameters in each region to be time-dependent. Externally applied field or electrical current density can be assigned region and time-dependent, such that an antenna's RF field or an AC electrical current are functions of time. Mumax3 calculates the reduced magnetization $\mathbf{m}(\mathbf{r}, t)$ evolution. The time derivative of magnetization, torque, has three contributions: Landau-Lifshitz torque, Zhang-Li spin transfer torque, and Slonczewski spin transfer torque. The Landau-Lifshitz torque used in Mumax3 is

$$\mathbf{ø_{LL}} = \gamma_{LL} \frac{1}{1+a^2} (\mathbf{m} \times \mathbf{B}_{\text{eff}} + \alpha(\mathbf{m} \times (\mathbf{m} \cdot \mathbf{B}_{\text{eff}}))), \tag{3.3}$$

where γ_{LL} is the gyromagnetic ratio (rad/Ts), which can be altered by the user, and α is the damping parameter. The effective field includes the external applied field $\mathbf{B}_{ext}$, magnetostatic field $\mathbf{B}_{\text{demag}}$, Heisenberg exchange field, $\mathbf{B}_{\text{exch}}$, Dzyaloshinskii-Moriya exchange field $\mathbf{B}_{\text{dm}}$, magnetocrystalline anisotropy field $\mathbf{B}_{\text{anis}}$, and thermal field $\mathbf{B}_{\text{therm}}$. Figure 3.11 shows the damping in magnetization precession.

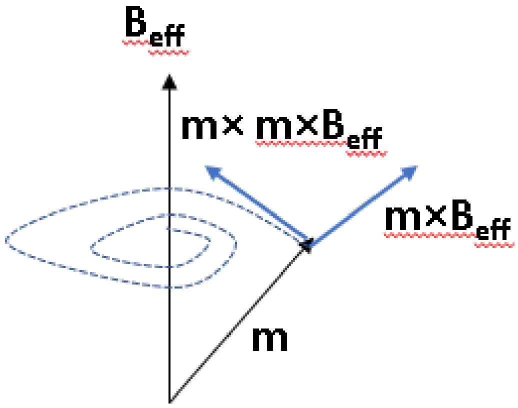

Figure 3.11. Damping of the precession of a magnetic moment. Due to the torque $(\mathbf{m} \times \mathbf{B}_{\text{eff}})$, the magnetic moment rotates around the effective field direction. The damping term $\alpha(\mathbf{m} \times (\mathbf{m} \cdot \mathbf{B}_{\text{eff}}))$ makes the precessional motion slow down.

Mumax3 brings a bunch of Runge Kutta methods. RK45 which is known as the Dormand Prince method is used for dynamical simulations. It provides a 5^{th} order convergence and a 4^{th} order error estimate for adaptive time step control. RK32 is the

Bogacki Shampine method. This method offers 3^{th} order convergence and a 2^{nd} order error estimate for adaptive time step control. It is used when the magnetization relaxes to the ground state, yielding a better performance than RK45. RK12 is Heun's method and is used for finite temperature simulations with 2^{nd}-order convergence and 1^{st} order error estimate. RK1, which is known as Euler's method, is for academic use. A relax() function is used in mumax3 to find the system's minimum energy. With this function, the precession term in Equation 3.3 is disabled, and the effective field decreases the energy. Relax function runs in time until the total energy reaches the numerical noise level. Meanwhile, the state is close to equilibrium and the torque magnitude will be monitored rather than energy since the torque decreases monotonically and is less noisy compared to the energy. After the relax function is implemented, the residual torque is reduced to the order of 10^4–$10^7\gamma_{LL}$ T, which shows that the system is in fact close to the equilibrium. In the relax function, the RK23 solver shows better performance than RK45. Both solvers have similar large-time steps near equilibrium, but torque evaluation per step for RK23 is half of the RK45. relax() function is suitable when the initial magnetization state is random and then the ground state is obtained, or when the change in energy is very large. By using another function, minimize, the minimum energy state is enhanced by the conjugate gradient method. For cases of small changes in energy, the minimize function is a better alternative. When sudden energy changes are present in the system, the minimize function can bring the system to a local minimum, but not to the real minimum energy state. Therefore, the minimum function is used for the evaluation of the hysteresis loop. However, this method is not suitable for high-energy initial states like random magnetization, where the relax() function is more powerful. For a physically correct simulation and efficient computing time and memory, parameters like mesh geometry, and material specifications such as the saturation magnetization, damping parameter, and exchange stiffness constant must be defined well. Foremost, the simulation mesh which is the size of the box around the magnetic object should be set. The simulation size should be larger than the object size, since the stray field should be included and exclude the edge effect. The number of cells should be powers of 2, or small prime factors 2, 3, 5, 7. The cell size is arranged such that the exchange coupling between the magnetic moments in the neighboring cells is determined. Therefore, the cell edge length should be smaller than the exchange length, which is represented as

$$l_{exch} = \sqrt{\frac{A_{exc}}{1/2\mu_0 M_{sat}}}. \tag{3.4}$$

So, the magnetization from one cell to another does not change rapidly. Setting a periodic boundary condition (PBC) value in a direction allows wrap-around exchange interaction along that direction. PBC value is the number of repetitions that the demagnetization field acts. The scheme for the hysteresis loop calculation in the Mumax3 simulation program is given in Figure 3.12.

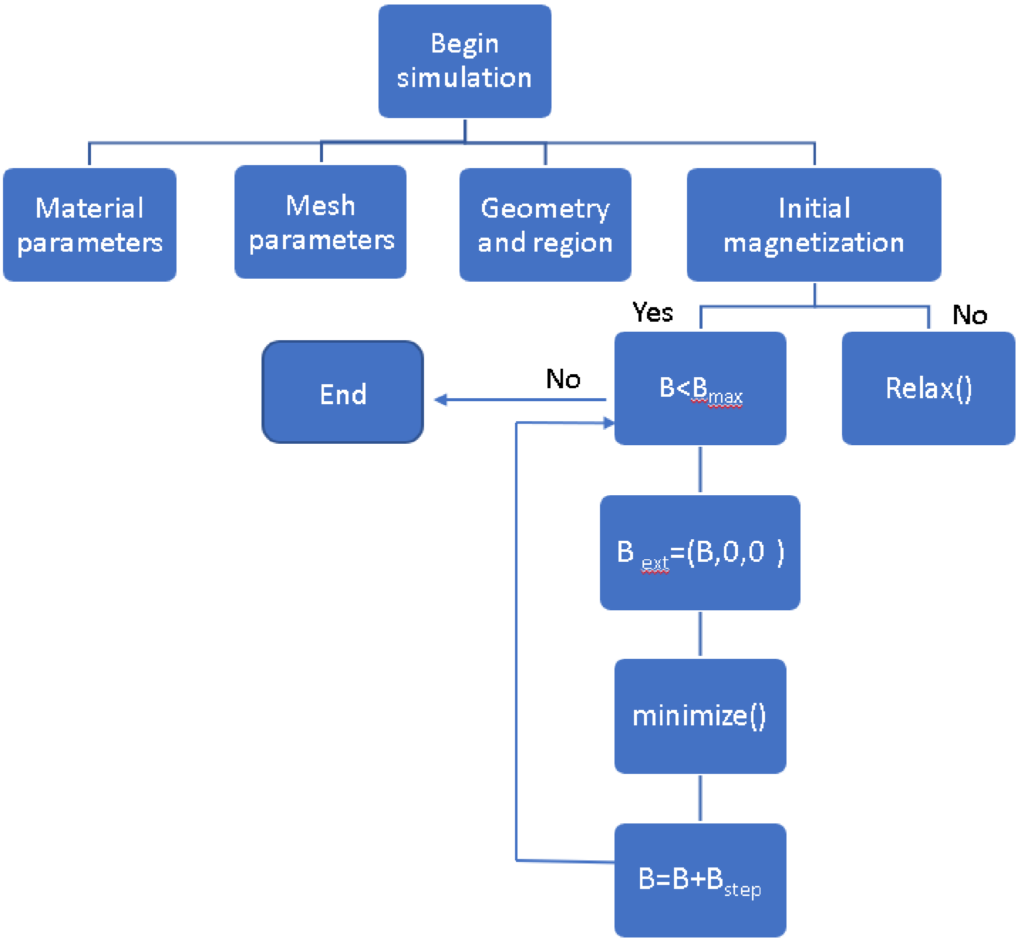

Figure 3.12. The algorithm for the magnetization loop simulation.

4. STRUCTURAL AND MAGNETIC ANALYSES OF YIG THIN FILMS

Yttrium iron garnet (YIG) is a ferrimagnetic oxide with a chemical formula $Y_3Fe_5O_{12}$. The crystal structure possesses a cubic symmetry. The lattice parameter of a cubic unit cell of YIG is 12.376± 0.004 A°. Each unit cell has eight chemical formulas which yield twenty-four Y^{3+} ions, forty Fe^{3+} ions, and ninety-six O^{2-} ions. YIG owns three sublattices. Figure 4.1 shows the schematic diagram for the d, a, and c sites occupied by the iron ions Fe^{3+}, Yttrium ions (Y^{3+}), and oxygen ions O^{2-} surrounding them, respectively.

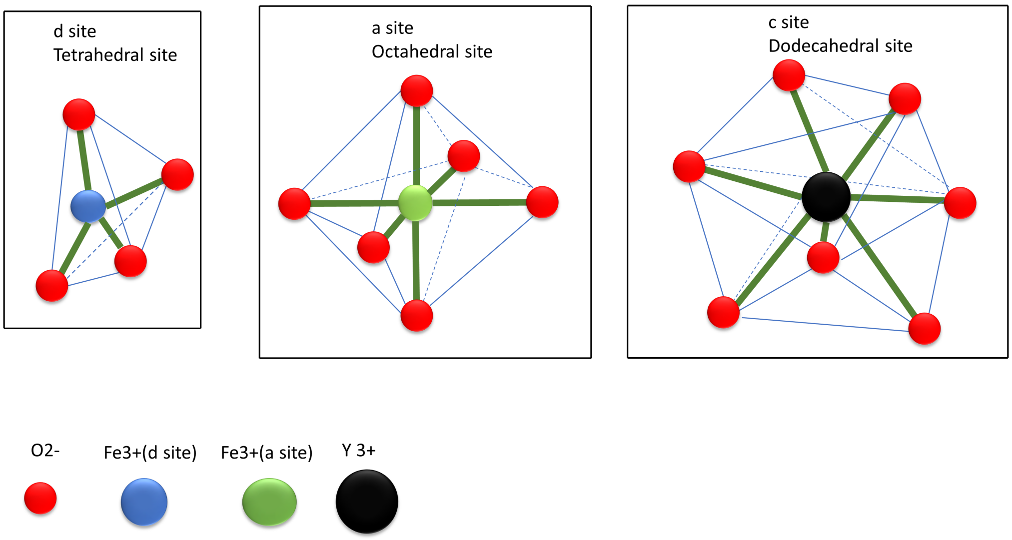

Figure 4.1. The sublattices of the crystalline structure of YIG are named tetrahedral, octahedral, and dodecahedral sites. The black spheres are yttrium, the blue sphere is iron in the d site, the green sphere is iron in the site and the red spheres are oxygen ions.

The Y^{3+} ions are located on the c sites (dodecahedra), and each site is surrounded by eight O^{2-} ions, which constructs a twelve-sided polyhedron with eight corners. Sixteen Fe^{3+} ions are on the site which are named octahedral sites surrounded by six

O^{2-} ions in octahedral symmetry, and twenty-four Fe^{3+} ions are on the d sites which are named tetrahedral sites surrounded by four O^{2-} ions in the tetrahedral symmetry. The O^{2-} ions are positioned on the h sites, the meeting point of the corners of one octahedron, one tetrahedron, and two polyhedrons as shown in Figure 4.1. Therefore, each O^{2-} ion is surrounded by one a site Fe^{3+} ion, one d site Fe^{3+} ion, and two c site Y^{3+} ions. The Y^{3+} and Fe^{3+} ions in the sites make YIG a significant material for magnetic studies. The cell cites connection and exchange interaction paths are shown in Figure 4.2.

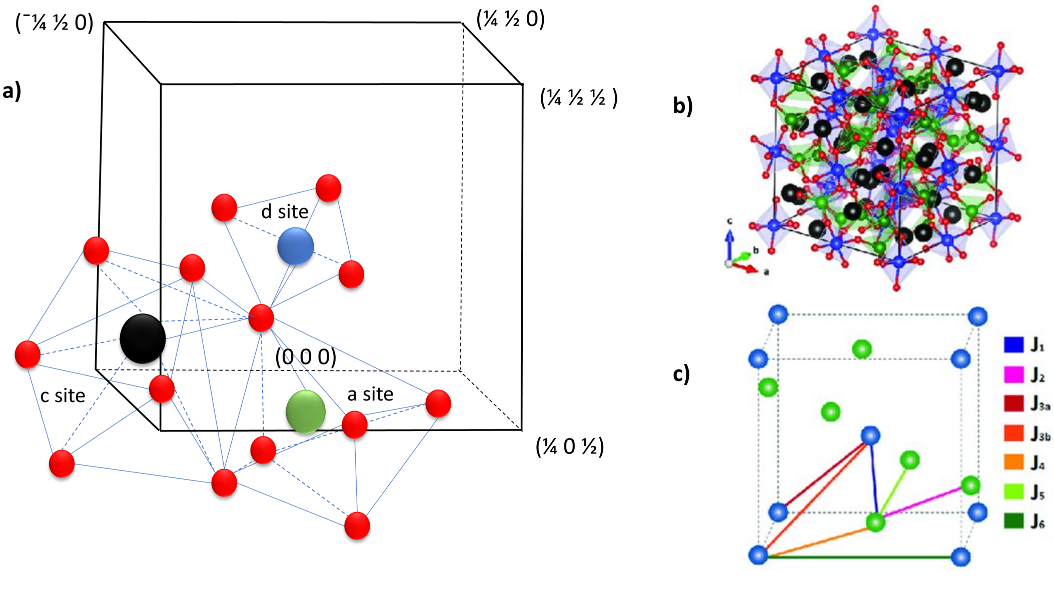

Figure 4.2. The combination of the cell sites and magnetic exchange paths in YIG. a) First octant of the unit cell of YIG. Fe^{3+} ions in green are in the tetrahedral sites, and Fe^{3+} ions in blue are in the octahedral sites. b) Unit cell of YIG. The tetrahedral sites are more major than the octahedral sites. c) Exchange interactions between the iron ions are labeled.

The Y^{3+} ions don't have a permanent magnetic moment. The magnetization in Yttrium iron garnet originally comes from the super-exchange interactions between the a-site Fe^{3+} ions and the d-site Fe^{3+} ions, which are antiparallel oriented to each other. Magnetic moments of the Fe^{3+} ions in d and a-sites cancel each other. The angle between the magnetic ion, oxygen ion, and magnetic ion bond determines the strength of the super-exchange interactions. The strongest interactions take place at the angle of 180 °, whereas the weakest interactions occur at the angle of 90 °. In YIG, the strongest super-exchange interaction is observed in the bond of a-site Fe^{3+}, O^{2-}, and d-site Fe^{3+} ions which makes the largest angle of 126.6 °. Therefore, an antiparallel alignment occurs between the magnetic moments of the a-site and the d-site Fe^{3+} ions. The magnetic moment of a Fe^{3+} ion is equivalent to five Bohr magnetrons (5 μ_B). Thus, the net magnetic moment of each unit is 40 μ_B. The saturation magnetization value ($4\pi M_s$) of YIG at room temperature, is reported as 1750 G.

In this thesis, the phase formation and crystallization of YIG thin film on a Si (100) substrate were studied. Obtaining a YIG phase on a Si substrate is considerably challenging due to the lattice mismatch between the substrate and the film. After the achievement of the YIG phase formation on the Si substrate, magnetic characteristics were measured and analyzed by VSM and FMR techniques as a function of thickness. In the following sections, the deposition process and structural analyses of the YIG thin films and the magnetic properties as a function of thickness are studied.

4.1. YIG Thin Films with In-Plane Anisotropy (IPA)

Pulsed laser deposition is a useful technique to deposit thin films which contain multi-component oxides. YIG thin films with various thicknesses were grown on Si (100) substrate by PLD deposition at a deposition temperature of 400 °C in an Oxygen atmosphere. Prior to the thin film deposition, the oxide layer was etched from the surface of Si (100) substrates with diluted Hydrofluoric (HF) acid. The substrates were further immersed in acetone, methanol, and Isopropyl alcohol for a few minutes by shaking them in an ultrasonic bath. Then, the substrates were spray-dried by blowing Nitrogen gas on the surface. After the cleaning procedure, the substrates were placed into a high vacuum PLD chamber, which was previously evacuated to a base pressure of 1.0×10^{-9} mbar, and were annealed at 500 °C for an hour to remove any contamination. PLD with a KrF excimer laser, a Coherent COMPex Pro 205F operating at $\lambda = 248$ nm, was carried out to obtain the stoichiometric YIG thin films by adjusting the oxygen pressure and deposition temperature. The commercial polycrystalline sintered YIG target was ablated with a pulse duration of 20 ns. The distance between the target and substrate was adjusted to 60 mm. The YIG thin films were fabricated using laser energy of 220 mJ with a pulse repetition rate of 10 Hz by keeping the oxygen atmosphere at 1.0×10^{-5} mbar. The substrates were being annealed at 400°C during ablation. The deposition rate was determined as about 0.96 nm per minute. After the deposition finished, the YIG films were cooled at a rate of 9.6 °C/min inside the chamber. For the chemical analysis, XPS measurement was employed as seen in Figure 4.11. To characterize the crystalline structure of the produced films, XRD $\theta - 2\theta$ scans were performed.

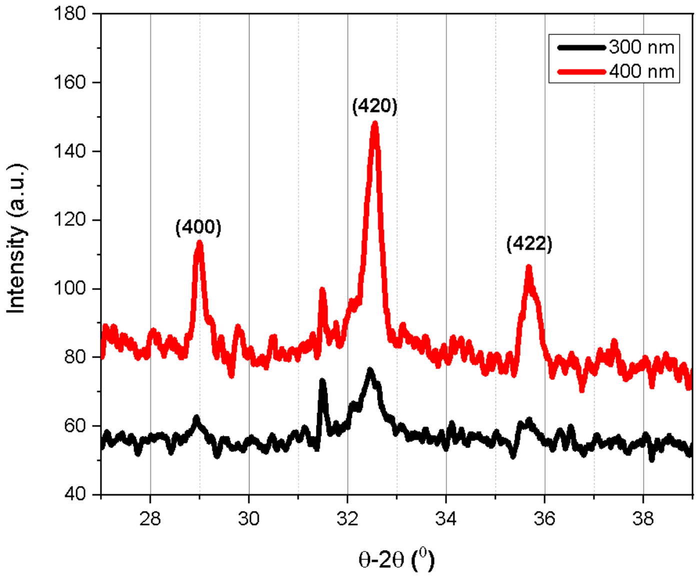

Figure 4.3. XRD spectrum of 300 and 400 nm YIG films.

As-grown YIG thin films did not show any diffraction peaks of the characteristic YIG phase. Therefore, a post-deposition annealing process is required to obtain a proper crystal structure of the YIG film. The effect of the annealing temperature on the crystal formation of the YIG phase on the Si substrate was studied. The as-grown films were annealed at 750 °C, 800 °C, and 850 °C for two hours in an air atmosphere. The cooling of substrates down to room temperature was slower than the heating process, which is at a rate of 1.2 °C/min, to prevent any damage to the YIG films.

After annealing at 850 °C, typical XRD peak(s) of the YIG phase were obtained. One can conclude that annealing allows a reorientation of the ions inside the YIG crystal lattices and improves the quality of the crystal. The film thicknesses were determined by a DEKTAK profilometer as 200, 300, and 400 nm. After annealing, polycrystalline YIG thin films are acquired, which show typical YIG XRD peaks. Figure 4.3 shows the characteristic (400), (420), and (422) peaks for 300 and 400 nm YIG films annealed at 850 °C. The intensity of the peaks for 400 nm film is higher than the peak intensity for the 300 nm film.

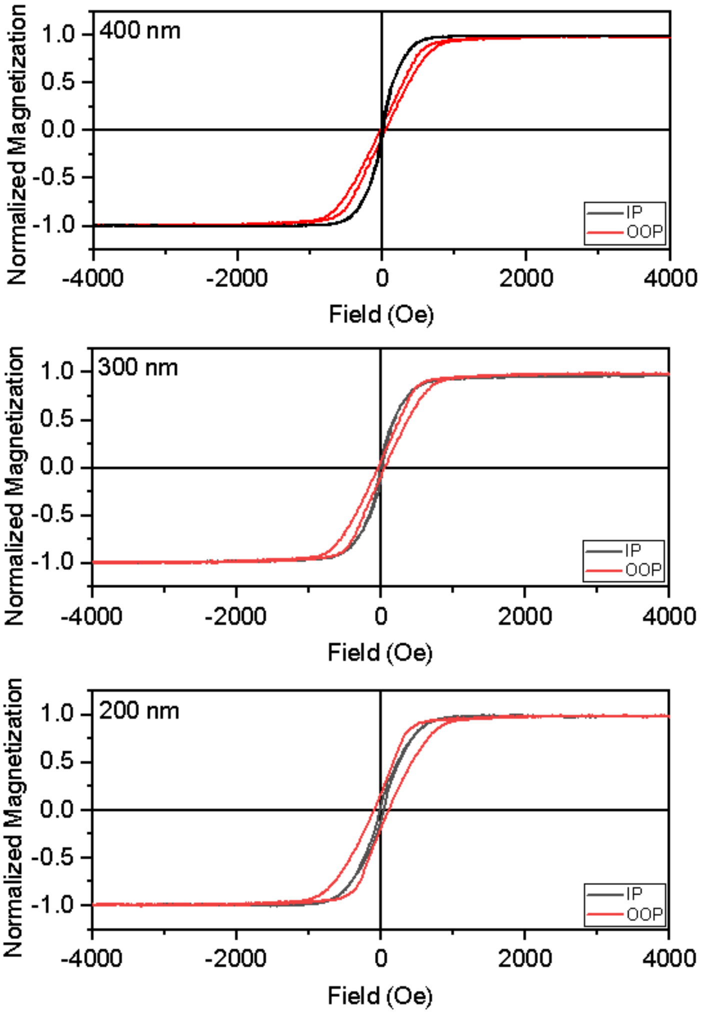

Figure 4.4. The hysteresis curves of 200,300, and 400 nm YIG films at in-plane (IP) and out-of-plane (OOP) measurement geometries.

The hysteresis loops of the annealed films were measured by using Quantum Design vibrating sample magnetometer (VSM). In Figure 4.4, all the films are in-plane magnetized. The coercivity value in out-of-plane (OOP) geometry decreases as the thickness increases from 200 nm to 400 nm.

FMR measurement was carried out at 9.1 GHz by applying a magnetic field (H) in parallel and perpendicular directions to the film plane. Both ferromagnetic resonance mode and spin wave modes were observed in the OOP geometry measurement as shown in Figure 4.5a), where the direction of the H changed from the sample plane (0°) to the sample normal (90°).

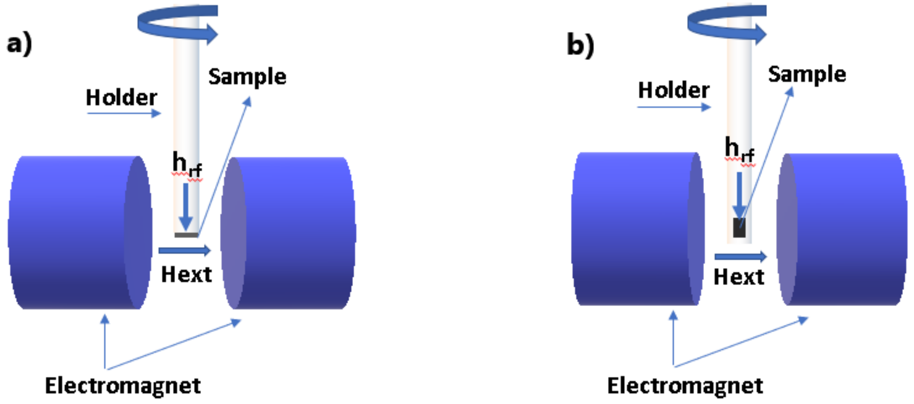

Figure 4.5. The out-of-plane (OOP) and in-plane (IP) FMR measurement geometries.

When the annealing temperature increases from 750 ° to 850 ° for the 400 nm film, the number of spin-wave modes increases at the perpendicular orientation, as shown in Figure 4.6. When the applied field was perpendicular to the film plane (90°), the main peak shifted towards the higher magnetic field region, as shown in Figure 4.7. This shows the presence of in-plane magnetic anisotropy that originates from the demagnetization field. When the angle increases towards 90 °, the number of spin wave modes increases. In addition, as the film thickness increases, the splitting of spin-wave modes increases.

In the in-plane measurement geometry (Figure 4.5 b)), there is no significant difference in the resonance spectrum as the film thickness increases. Unlike the out-of-plane FMR measurement, no magnetic anisotropy was observed in in-plane geometry where the magnetic field lies in the film plane. Shape anisotropy and magnetocrystalline anisotropy are the most common anisotropies in thin garnet films. For films with 200 nm, 300 nm, and 400 nm thicknesses, in-plane anisotropy occurs due to the dominance of shape anisotropy in YIG thin films.

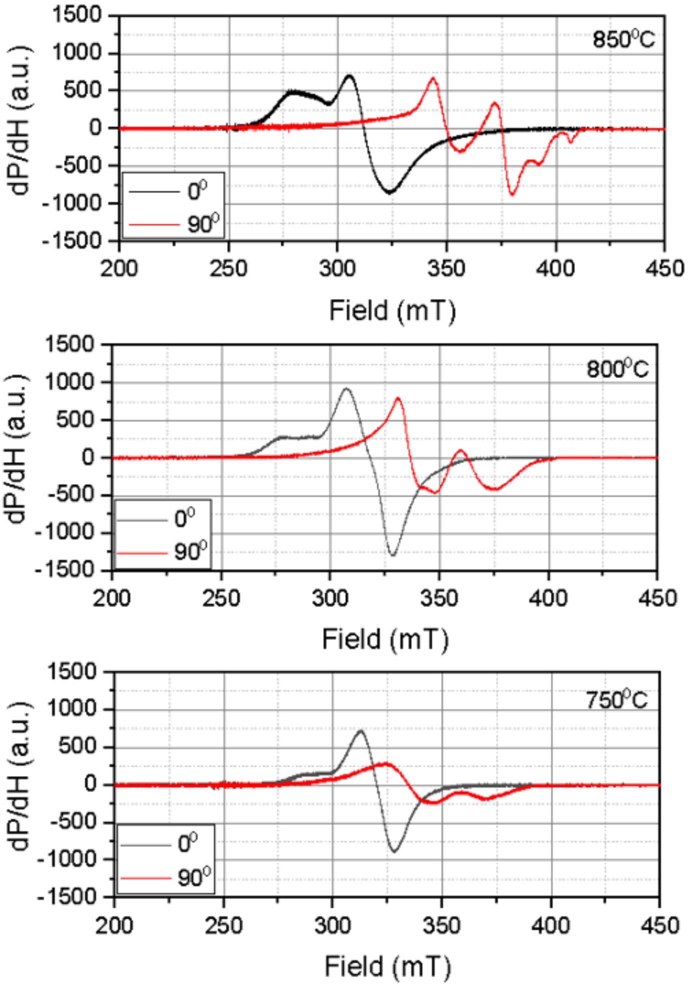

Figure 4.6. OOP FMR spectrum of a 400 nm YIG film at 850°C, 800°C and 750°C annealing temperature.

The angular variation of resonance and magnetostatic spin wave resonance fields for 400, 300, and 200 nm YIG films are shown in Figure 4.9. The splitting of the uniform resonance modes into three and four can be seen around the angle of 90 °. The 400 nm film has more spin wave modes than 300 and 200 nm films around 90 °.

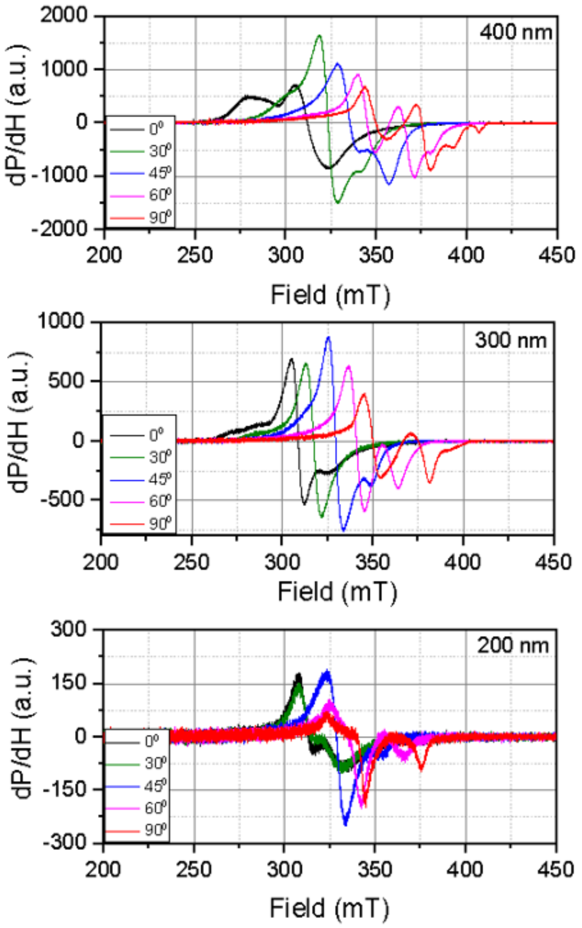

Figure 4.7. OOP FMR spectrum of 400, 300, and 200 nm YIG thin films as the angle ranges from 0° to 90° by a step of 30°.

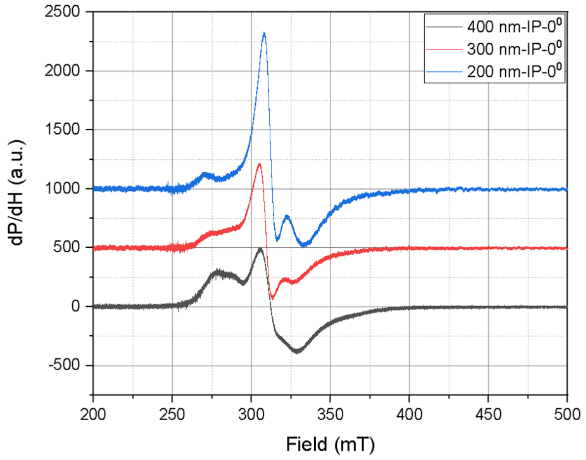

Figure 4.8. FMR spectrum for IP measurement of 400 nm, 300 nm, and 200 nm YIG thin films.

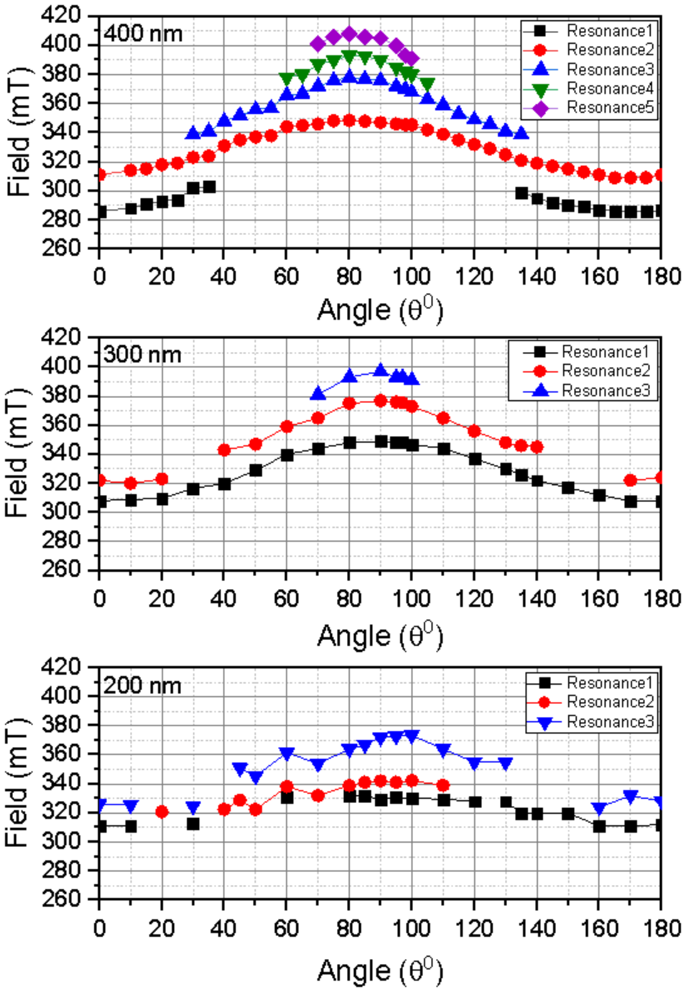

Figure 4.9. Resonance field as a function of angle for 400, 300, and 200 nm film thicknesses.

4.2. YIG Thin Films with Perpendicular Magnetic Anisotropy (PMA)

Magnetic garnet films have replaced the conducting ferromagnetic materials in spintronic applications since the insulator garnets do not carry the disadvantages of eddy currents and do not have information loss in many applications [90]. High interest in garnet films comes from the use of these materials in high-frequency applications and the ability to switch magnetic properties easily [91]. Particularly, perpendicular magnetization in garnet films is important for spintronics applications such as spin–orbit switching, spin-transfer torque (STT), and a reliable and fast response [92]. YIG is one of the most essential magnetic insulators. Static and dynamic magnetic properties of bulk YIG crystal or micrometer-thick YIG films have been studied and used in microwave applications i.e. microwave filtering, tunable, isolators, and phase shifters [93, 94]. In addition, thin/ultrathin YIG films are used in many spintronics [95–97] and magneto-optical applications [98–100]. An adjustment of the orientation and magnitude of the magnetic anisotropy is necessary for spintronic applications [101,102]. Perpendicular magnetic anisotropy (PMA) has given rise to a crucial advancement in technology. The high-density magnetoresistive random-access memory devices (MRAM) are good examples of the use of PMA. Tuning of the magnetic anisotropy enables the increased data storage capacity in magnetic recording media, improvement in magnon transistors [103], and logic devices [102]. PMA in metal thin films is well studied and applied [104,105], however obtaining PMA in insulating materials such as YIG is a challenge. Ferromagnetic insulators with PMA have been particularly significant for fundamental scientific research and technology. As an example, YIG with PMA has found wide use in spin–orbit torque (SOT) applications [106]. The magnetic anisotropy in YIG films is the in-plane anisotropy (IPA) due to the strong shape anisotropy. If the magnetocrystalline anisotropy dominates the shape anisotropy, the magnetic easy axis switches from in-plane to out of the film plane, yielding PMA. Control of magnetic anisotropy in YIG thin films has been researched using different substrates, applying different temperatures, and changing the thicknesses [107,108]. In some studies, PMA in YIG films was obtained by adding a buffer layer [23] and doping with rare earth elements [109,110]. It is possible to grow epitaxial YIG thin films on garnet substrates such as yttrium aluminum garnet (YAG) [111] and gadolinium gallium garnet (GGG) due to their similar crystalline structure with YIG [112]. The lattice constants of YIG film and GGG substrate are $a_{\mathrm{YIG}} = 12.376$ A° and $a_{\mathrm{GGG}} = 12.383 A^{\circ}$ [113]. The perfect lattice match between YIG and GGG opens a way to produce high-quality crystallized YIG thin films [114]. While so, GGG usage has some limitations and is costly for industrial applications. Besides, silicon (Si) as a substrate is cost-effective and widely used in electronic devices and integrated circuits. Si has an fcc diamond cubic crystal with a 5.43 A° lattice constant. The nearest neighbor distance of two Si atoms is 2.35 A° [115]. The cubic structure of YIG includes Y^{3+} ions in dodecahedra (c) sites, Fe^{3+} ions in tetrahedral (d), and octahedral

(a) sites in polyhedrons of oxygen ions [116]. The nearest inter-ionic distance in the YIG crystal structure is between Y^{3+} and O^{2-} , determined as 2.37 A° [116]. It seems that the atomic distances in YIG and Si are comparable to each other. Therefore, one can deposit crystalline/texture YIG films on Si (100). In this study, PMA is obtained in YIG thin films deposited on Si substrates by the PLD technique. Parameters such as oxygen pressure, growth temperature, laser power, and pulse duration time, post-annealing temperatures were adjusted to obtain the stoichiometry and crystallinity of the YIG films. YIG films with different thicknesses were produced and annealed to improve the crystallization and reduce the substrate-film lattice mismatch. The effect of the thickness on the magnetic anisotropy was studied. The thickness that PMA is observed is reported as 10-20 nm for YIG [117]. Our finding is that the lattice distortion/texture in YIG films causes PMA in 15–50 nm thickness. This study aims at fundamental understanding and the application of YIG thin films with PMA in technology.

Firstly, Si substrates were put in acetone, methanol, and Isopropyl alcohol using an ultrasonic bath for 15 minutes, and then were mounted to the ultra-high vacuum PLD chamber. The substrates were annealed at 500 °C for an hour in a vacuum base pressure of 1.0×10^{-9} mbar. PLD with a KrF excimer laser with lambda 248 nm, pulse energy of 220 mJ, frequency of 20 Hz, and duration time of 20 ns was carried out to deposit YIG film on Si substrate. The distance between the Si substrate and the polycrystalline YIG target was kept at 60 mm. The oxygen pressure was 1.0 $\times10^{-5}$ mbar. The deposition temperature was 500°C. After deposition, the films were cooled to room temperature inside the chamber at a cooling rate of 10 °C/ min, ex-situ annealed in the atmosphere at 850 °C for 3 hours and cooled down at a rate of 1.2 °C/min. Film thicknesses were 40, 90, and 120 nm. The surface morphology and roughness of the films were investigated by Atomic Force Microscopy (AFM). Figure 4.10 shows an AFM image of the annealed YIG film with a root-mean-square (RMS) roughness of 0.8 nm. The crystal structure of the annealed films was characterized by XRD measurement using a Rigaku 2000 DMAX meter with a wavelength of 154 nm. A typical (420) peak of the YIG phase was obtained for the annealed films, as seen in the XRD scan in Figure 4.10. The signal detected at 44° is from the sample plate. The other peaks around the (400) plane of the Si are the K_β, L_1, L_2, K_1, and K_2 lines of the incident x-ray.

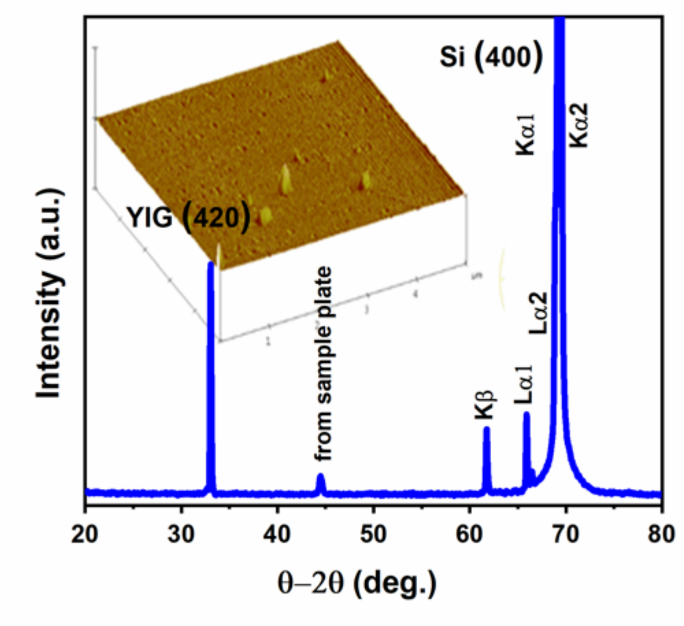

Figure 4.10. XRD $\theta - 2\theta$ scan, which indicates the (420) peak of a YIG thin film. Inset is the AFM image of a 20 nm YIG thin film.

The chemical analysis was carried out by an XPS measurement. The XPS survey spectrum shows the presence of Y, Fe, and O elements on the surface of the YIG thin film in Figure 4.11 (a). The fittings of the spectral ranges to find the composition ratio of the elements are given in Figures 4.11 (b)-(d). The valance state of the Fe ions is shown in the XPS spectrum of the Fe 2p region, Figure 4.11 (c). The compositional ratio, Y/Fe, and Fe/O were 0.59 and 0.44, respectively, which are very close to the bulk YIG compositional ratios, Y/Fe = 0.6 and Fe/O = 0.42 [97]. Ferromagnetic resonance (FMR) measurements were employed for the annealed YIG films by an X-Band (9.1 GHz) JEOL series ESR spectrometer at room temperature. FMR is a classical technique, in which from the analysis of the spectra, the anisotropy constants can be deduced [33-35]. The field (H) derivative of the absorbed RF power (P) dP/dH gives the resonance spectrum as a function of the applied magnetic field. The measured sample dimension was 3×3 mm^2. The FMR spectra were recorded by sweeping the angle at which the field applied between the film plane and the film normal.

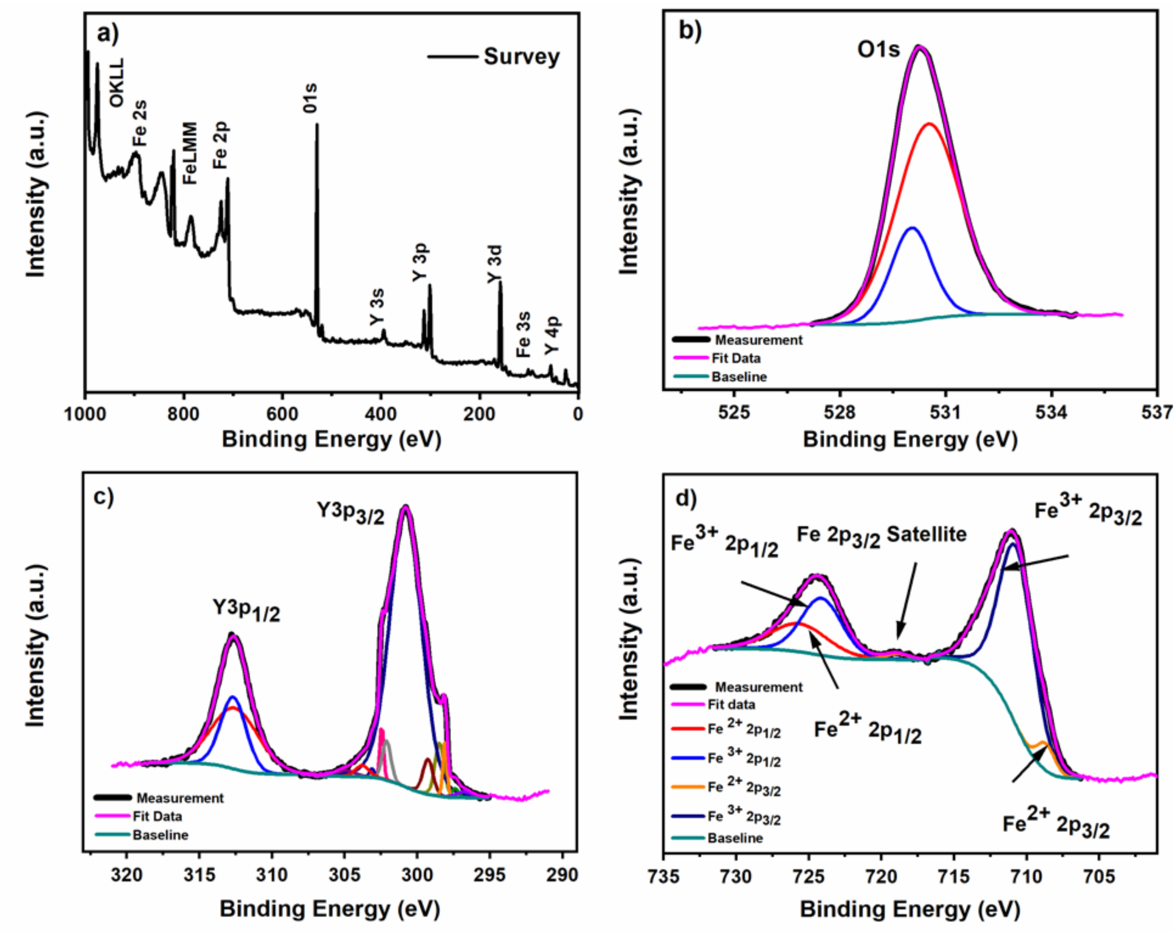

Figure 4.11. The XPS spectrum of the YIG thin film grown on a Si (100) substrate. (a) The survey scan. The fitted XPS spectrum of each element in YIG i.e. (b) O 1s, (c) Y 3p, and (d) Fe 2p.

In in-plane measurement, the magnetic component of the microwave field is in the film plane, and the external magnetic field is applied from the film plane towards the film normal. In out-of-plane measurement, the magnetic component of the microwave field is perpendicular to the film plane and the external magnetic field rotates in the film plane. The FMR spectra in the out-of-plane measurement were represented in Figure 4.13 (c). Figures 4.12 (a) and (b) show the applied field direction parallel to the film normal and in the film plane. When the field was applied parallel to the film normal, the spectrum was at a low field range in the red curve, then it shifted to the high field range in the black curve for the field parallel to the film plane.

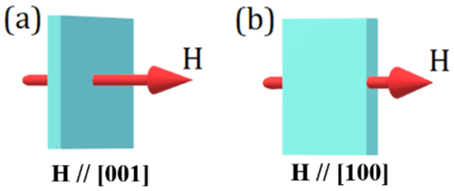

Figure 4.12. FMR measurement geometry. (a) The field was applied parallel to the film normal (H//[001]), (b) the field is parallel to the film plane (H//[100]).

This can be explained in such that the magnetic easy axis is perpendicular to the film plane. According to the spectrum measured in in-plane geometry, there was no anisotropic behavior due to the fact that thin films with PMA do not have any anisotropic behavior in the film plane [118]. The intrinsic magnetic properties of the system are analyzed by angular FMR measurements and numerical calculations. Based on the energy Hamiltonian in Equation (4.1), the micromagnetic parameters of YIG/Si (100) were numerically solved. The magnetic behavior of the systems was described by the two energy terms in the Hamiltonian [119], where (θ, θ_H) and (ϕ, ϕ_H) are the polar and azimuthal angles for magnetization vector **M** and external DC magnetic field vector **H** with respect to the film plane. The first term of the Hamiltonian is the Zeeman energy term. Effective magnetic anisotropy energy includes the demagnetization energy, the interface energy, and the first-order term of magnetocrystalline energy. The second term is the second-order magnetocrystalline energy. The expression for the energy is

$$\begin{aligned} E = &-\sum_{i=1}^{N} M_{\text{eff}} H[\cos\theta_H \cos\theta_i + \sin\theta_i \cos(\phi_H - \phi_i)] \\ &+ \sum_{i=1}^{N} [K_{\text{eff}} \cos^2\theta_i + K_{\text{eff}_{-q}} \cos^4\theta_i], \end{aligned} \tag{4.1}$$

where M_{eff}, K_{eff}, and $\mathrm{K}_{\text{eff}_{-q}}$ are the effective magnetization, effective magnetic anisotropy energy density, and the second order magneto crystalline energy density, respectively.

The DC magnetic field was scanned from 0 to 1 T to determine the field that gives the maximum dynamic susceptibility value. This field is called the resonance field (H_{res}).

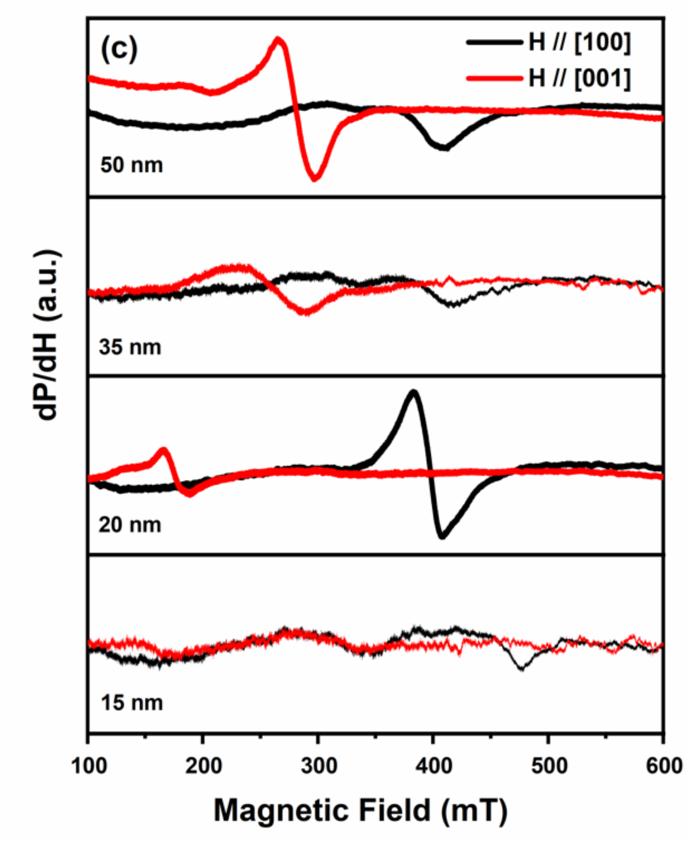

Figure 4.13. FMR spectra of all the YIG films in OOP measurement geometry. (c) The curves in black and red colors refer to the FMR spectrum for the case in (a) and (b), respectively.

The resonance fields in the out-of-plane geometry were obtained by analyzing the dynamic susceptibility spectra, which were recorded using the Boohoo formulation for ferromagnetic resonance in multi-layer thin films [65, 66]. Employing the same procedure for different angles between the magnetic field and the film plane, the experimental data can be simulated at room temperature. The simulation model yielded M_{eff}, K_{eff}, and K_{eff-q} for all samples. The magnetic parameters which give the minimum total energy are listed in the Table. Figure 4.14 represents the angular dependence of the resonance field for different thicknesses. The table shows the result of the numerical calculations. The sign of the effective anisotropy energy density is positive, which proves that the magnetic easy axis is perpendicular to the plane. The value of the effective magnetization is smaller compared to the bulk YIG value, which might originate from crystal vacancies/deficiencies, diffusion between the substrate and the film, and the variation of Fe ions in the film. In general, shape anisotropy lies in the film plane. When the thickness increases, shape anisotropy increases and induces in-plane magnetic anisotropy. The strain relaxation between the substrate-film causes the effective perpendicular magnetic anisotropy to decrease, as shown in Table 4.1.

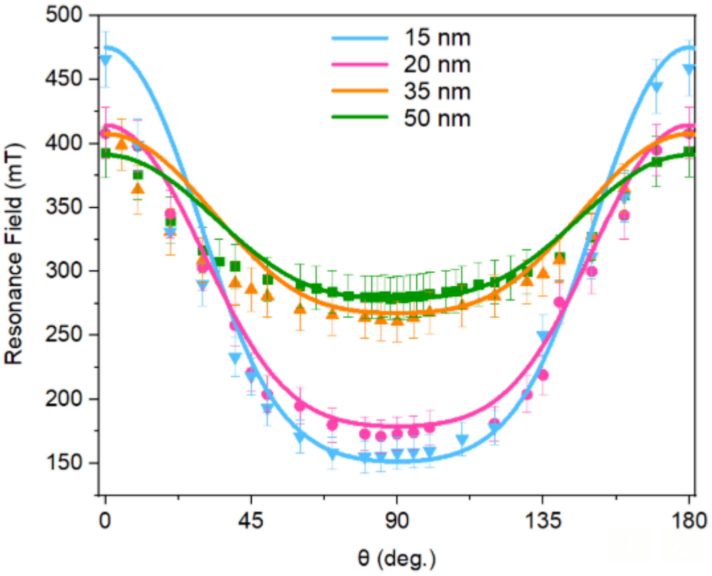

Figure 4.14. Angular variation of the resonance fields. Experimental and theoretical results are shown by symbols and solid lines, respectively.

The discussion about the structural and magnetic characterization of YIG films grown on Si (100) is given in the following. XPS analysis gives information about the composition and electronic state of the Y-Fe-O elements on the film surface. For the stoichiometry of the YIG film, the percentages of O 1s, Fe 2p, and Y 3p peak areas in Figures 2(b)-2(d) were found using relative sensitivity factors in CasaXPS software. The stoichiometry was calculated as Y : 3.06, Fe : 5.17, and O : 11.7. These values are close to the ideal stoichiometry, which is Y : Fe : O of 3 : 5 : 12. The Fe percentage in the YIG thin film was found to be 20.6%, which is similar to the percentage in bulk

YIG, 20% [11]. Figure 4.11 d) illustrates the core level of Fe 2p spectra in which both Fe^{3+} and Fe^{2+} are observed in the film [120]. The binding energies of the 2p3/2 and 2p1/2 peaks of Fe^{3+} and Fe^{2+} are 711.1 eV and 724.4 eV. The peaks located at 710.9 eV and 725.8 eV belong to Fe^{3+} 2p3/2 and Fe^{3+} 2p1/2, and the binding energies of 708.86 eV and 724.16 eV correspond to Fe^{2+} 2p3/2 and Fe^{2+} 2p1/2, respectively. The satellite structure of Fe 2p3/2 was seen at 718.8 eV, which is higher than 710.9 eV. This implies that the Fe ions are in +3 valance states in the spectrum and at tetrahedral sites of the YIG lattice [121,122].

Table 4.1. The simulation results for YIG thin films with PMA.

	$K_{\mathbf{eff}}$ ($\mathbf{J}/m^3$)	$K_{\mathbf{eff}-q}$ ($\mathbf{J}/m^3$)	$M_{\mathbf{eff}}$ ($\mathbf{kA}/m$)
15 nm	1773	320	105
20 nm	1456	250	105
35 nm	1260	150	105
50 nm	1180	120	105

The crystallization of the as-grown and annealed films was analyzed by XRD measurements. No characteristic XRD peaks were present in as-grown films. A post-annealing was employed to have the characteristic diffraction peaks of the YIG phase. The films were annealed at the temperature of 850° C for two hours, and the (420) peak of the YIG phase was observed from the XRD scan in Figure 4.10. Polycrystalline YIG thin film grown on quartz is reported to have three characteristic peaks [117]. There seems to be preferential crystalline ordering or texture in the relevant samples in this study. By annealing the films, the YIG lattice is placed on the Si substrate by making an angle of 26.6° between the (400) plane of Si and the (420) plane. Figure 4.15 shows that the film lattice has two different crystallographic orientations, repeating with respect to the c symmetry axis. The lattice mismatch is calculated as 1.94%. The lattice constant of YIG is larger than that of the Si substrate. Therefore, a small compressive strain at the interface gives rise to a tetragonal distorted YIG crystalline structure. FMR spectra of the samples when the external magnetic field was applied parallel to the film normal and film plane are shown in Figure 4.13. The resonance field takes the minimum value when it is applied along the magnetic easy axis. The spectra prove the presence of PMA for all thicknesses.

The FMR spectrum for the external field parallel to the film normal shifts to a higher field range with the increasing film thickness. On the contrary, in the case of H parallel to the film plane, the FMR spectrum goes to a low field range with increasing thickness. One can conclude that the uniaxial PMA reduces as the thickness increases. Thickness, substrate, temperature, interfacial energy, and strain are some of the factors that affect magnetic properties.

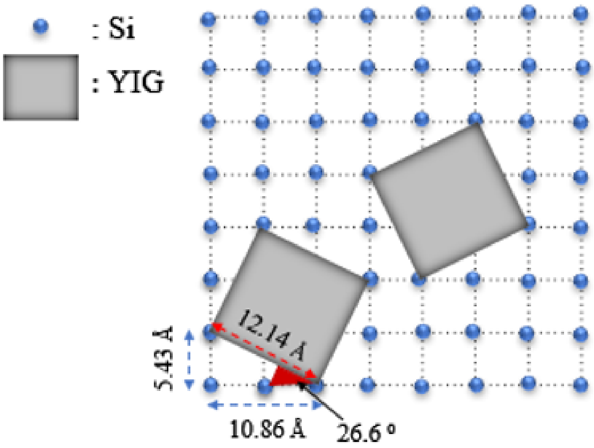

Figure 4.15. The two preferential crystalline orderings/texturing in the annealed YIG thin film.

In this work, especially, the strain effect is the main factor that can control the magnetic anisotropy of the samples. The strain between the film and the substrate is tensile by 0.65% when YIG film is grown on the GGG substrate. The strain is compressive by an amount of 1.9% when YIG film is deposited on Si (100). The films experience much greater strain originating from the high lattice mismatch between Si and YIG. With the use of Si substrate, the thickness in which PMA was observed, magnetic anisotropy values, and FMR linewidth were different from studies that use lattice-matched substrates in the YIG thin film fabrication. From the FMR spectra of the films, a single uniform ferromagnetic resonance peak was detected as shown in Figure 4.13. Thickness, crystal quality, and magnetic homogeneity of films affect the shape and intensity of the FMR spectra. The FMR linewidth broadens inhomogeneously originating from imperfections in the film like defects, symmetry breaking in the film surface and interface between substrate and film, oxygen vacancies, and ion diffusion between the layers [112].

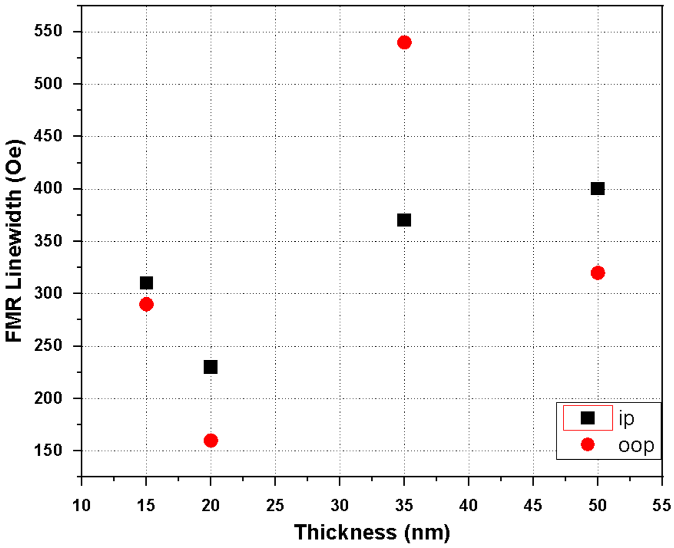

Figure 4.16. FMR linewidth versus thickness in the in-plane (IP) and out-of-plane (OOP) geometry.

The intensity of the FMR peak is low and the linewidth is larger for the thinnest film. When the thickness increases, more spins interact with the microwave field, therefore the spectra have higher intensity. Uncontrollable parameters during deposition might cause an unsystematic change in the shape and intensity of the FMR peaks when the thickness increases. Nevertheless, PMA was still observed in the pronounced thicknesses. Figure 4.16 shows the in-plane and out-of-plane FMR linewidths for the corresponding thicknesses. The linewidth of the 20 nm YIG film was found to be 230 Oe when the field is applied parallel to the film plane. The linewidth was 160 Oe when the field is perpendicular to the film plane. Both linewidths are larger than the FMR linewidth of YIG grown on GGG substrate [123]. Similar linewidth values with our findings are reported in a few studies for the case in which YIG is grown on quartz [108, 112]. As an example, the FMR linewidth of 12 nm YIG film was found as 250 Oe. According to another study, the linewidths were between 70 Oe and 340 Oe for the films between 100 nm and 290 nm. The increase in the FMR linewidth might be due to defects related to surface roughness, Fe deficiency, and magnon scatterings [124].

Typically, most of the thin films exhibit in-plane anisotropy due to the effect of shape/dipolar anisotropy. To overcome the shape anisotropy, there need additional treatments that will change the easy axis from the film plane to the film normal. One way for that is to increase the magnetocrystalline/surface anisotropy or introduce texture that is able to induce a perpendicular magnetic anisotropy [105]. In this study, the lattice mismatch between Si and YIG formed a compressive strain at the interface and led to a lattice distortion [125]. The compressive strain in the film plane gave rise to an expansion along the c-axis. By so, the easy axis switched from the film plane to the film normal [96]. In some studies, PMA was obtained in YIG deposited on various substrates for the film thicknesses between 10 nm-20 nm [117]. However, in this study, PMA was observed up to 50 nm film thickness because of texture and the lattice distortion of YIG. Also, in the literature, PMA in YIG films was obtained in YIG grown on the buffer layer except for GGG [126]. This study shows that PMA was achieved in YIG films grown on a non-garnet substrate with no additional buffer layer or doping with other materials.

The lattice mismatch causes the lattice constant to be compressed along the film plane. From the XRD profile in Figure 4.17, one can observe that (420) peak shifts to a higher angle with increasing thickness, which refers to the compression of the crystalline lattice. Since the unit cell volume of YIG is preserved during the growth, the c lattice constant elongates at the out-of-film plane, while the in-plane lattice constant a is compressed due to the Si substrate. The expansion of the c-axis leads to a strong tetragonal lattice distortion for 15, 20, 35, and 50 nm films. When the thickness increases, the compressed film begins to relax. The a and c lattice constants approach each other and finally, the crystal lattice takes cubic form as shown in Figure 4.18.

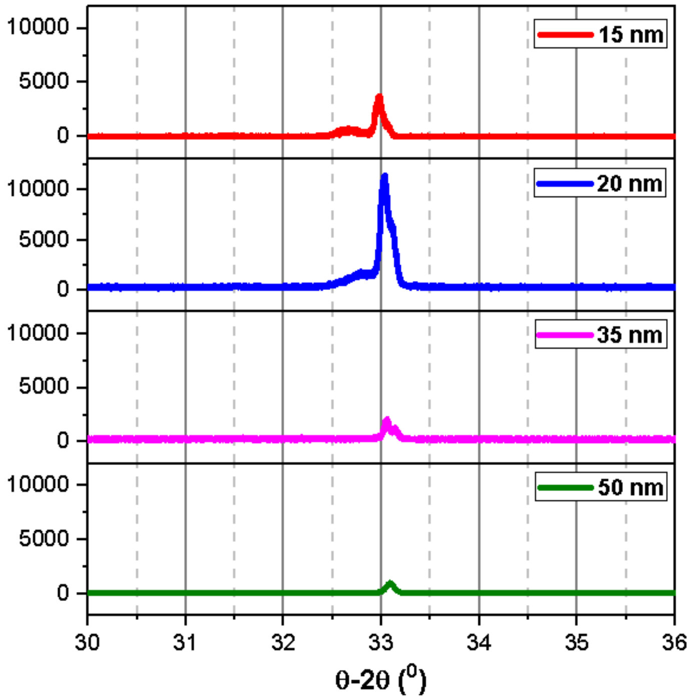

Figure 4.17. The position of the (420) peak with respect to the thickness.

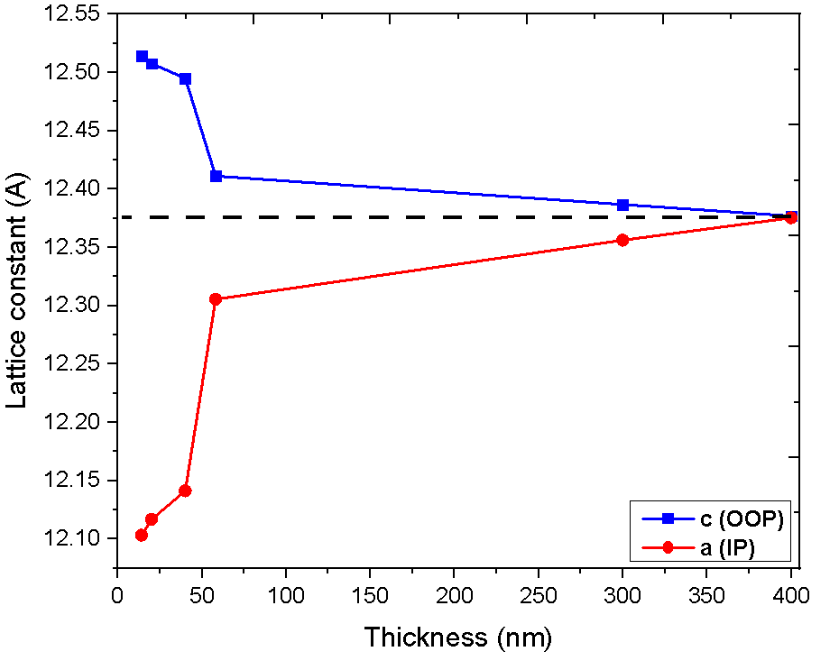

Figure 4.18. Thickness dependence of the in-plane (red circles) lattice constant a and out-of-plane (blue squares) lattice constant c of the YIG thin films on Si substrate for a thickness range between 15 nm and 400 nm.

We observed that the lattice constants of 300 and 400 nm thick film which are 12.356 nm and 12.375 nm are close to the bulk YIG value, 12.376A° [40]. We have obtained three intense peaks of YIG films at (400), (420), and (410) planes indicating the polycrystalline structure for the films with thicknesses of 200 nm and 400 nm as shown in Figure 4.3. The relaxed films have a cubic lattice structure. The Scherrer formula was applied to calculate the crystalline size and found as 15.6 nm for 400 nm YIG thin film and 344.8 nm for 15 nm YIG film annealed at 850°. When the crystallite size increases, the XRD peak broadens. The increase in grain size leads to a decrease in the domain wall energy of the YIG thin film.

With this work, we demonstrated the tune of the magnetic anisotropy from in-plane to perpendicular magnetization by decreasing the film thickness and introducing the strain due to the lattice mismatch. For the films with a thickness of 200, 300, and 400 nm, the resonance field shifted to the higher fields with increasing angles. This refers to the magnetic easy axis being in the film plane. In-plane anisotropy occurred due to the dominance of shape anisotropy in YIG films. However, when the film thickness was reduced, we observed a gradual change in the anisotropy direction. The magnetic anisotropy was perpendicular to the film plane for a thickness range of 15 nm to 50 nm. In conclusion, in thinner films, magnetocrystalline anisotropy gets stronger than the shape anisotropy and forces the easy axis to align perpendicular to the film plane. For thicker films, the shape anisotropy is more dominant than the magnetocrystalline anisotropy, yielding in-plane anisotropy. The anisotropy transition from in-plane to out-of-plane mainly originates from the lattice tetragonal distortion. Due to the compressive tension, the expansion along the c-axis causes the easy axis to extend perpendicular to the film plane, which results in PMA.

4.3. Spin Wave Modes in YIG Thin Films with PMA

The investigation of spin wave (SW) propagation in thin and ultrathin YIG films has received great attention after high-quality ultrathin YIG films can be produced by some deposition techniques such as liquid phase epitaxy (LPE) [127, 128] pulsed layer deposition (PLD) [124, 125, 129, 130], and sputter deposition [131–133]. The study of spin waves is crucial to processing information and spin-wave logic devices. Isotropic excitation and propagation of spin waves are used for SW logic devices, such as the SW interferometer. Damon-Eschbach spin wave modes and Magnetostatic spin wave modes propagate in different ways in the material. MSFVM spin waves propagate through the volume of the material without a non-reciprocal effect and lower energy losses. The applications of MSFVM spin waves are limited, as a large magnetic field must be applied to saturate the film out of plane [134–138]. However, PMA films allow the investigation of MSFVM spin waves with small or even zero applied area [139].

Spin wave devices, where spin waves are information carriers, are considered to be potential candidates for technology that is not based on post-semiconductor and electron charge. In a spin wave device, isotropic coherent spin waves (magnons) with out-of-plane magnetization and in-plane propagation are desired, However, due to the absence of low-damping perpendicular magnetic material, in-plane ferrimagnet yttrium iron garnet (YIG) is used with a large out-of-plane bias magnetic field; negating the benefits of isotropic spin waves. Magnonics is a study of the control of spin wave propagation in magnetic materials. Magnonics uses the spin angular momentum, amplitude, and phase of spin waves to transmit store, and process information, unlike the electric charge. Spin wave (SW) emerges as a result of the excitation of magnetic moments of a stationary spin system by external parameters such as thermal, optic, and magnetic excitation parameters. Due to the nanometer wavelength and gigahertz frequencies of spin waves, microelectronic devices have been fabricated. In addition to these properties, low power consumption let spin wave be a new generation data carrier [140] and therefore, spin wave-based spintronic applications. A promising magnetic insulator, yttrium iron garnet (YIG), has a high interest in magnonics and spintronics due to its long spin-wave lifetime. The spin wave propagation distance of YIG is in the centimeter range. The very low damping and narrow FMR linewidth are some of the unique features which belong to YIG material. These properties are appealing for microwave information processing [141], quantum technologies [16, 142, 143], quantum computing [144], phase separators [145], magnonic logic devices, and magnon transistors [8, 146]. Spin wave interferometers and logic devices depend on spin waves' isotropic excitation and propagation. A low-loss spin-wave propagation is possible with the use of YIG material. YIG enables fast switching of magnetization from in-plane to out-of-plane under a moderate external field owing to its small saturation magnetization [147].

The control of magnetic anisotropy of YIG is crucial for low-power consumption magnetic memory and logic applications. The magnetization of YIG thin film is, in general, in the film plane since the magnetocrystalline anisotropy is not strong enough to overcome the shape anisotropy, therefore anisotropy favors in-plane orientation. In the 1980s, spin wave resonance was studied in bulk or micron-thick YIG that have an in-plane anisotropy (IPA) [148]. For a few decades, ultrathin/thin YIG films have attracted more interest because they allow the control of magnetic anisotropy, fabrication of micro/nanodevice, and use of them in the spintronic/magnonics technology today. PMA in YIG thin films is significant for spin transfer torque magnetic random-access memory (STT)- (MRAM) applications [149,150]. But, the achievement of PMA in YIG thin film is not easy and challenging. Some special treatments are required. For instance, decreasing the film thickness down to an ultrathin regime, adding a buffer layer, doping, and strain effect at the interface or the film surface. PMA can be obtained due to the substrate/film lattice mismatch and single crystalline or texture structure of thin/ultrathin YIG films grown on Si (100) substrate [27]. Determination of perpendicular magnetic anisotropy (PMA) in relatively thick YIG films with much faster spin texture dynamics and terahertz switching frequency, is still a major challenge because of the dominant shape anisotropy.

The magnetostatics spin wave (MSSW) modes in Permalloy (NiFe), and CoFeAl ferromagnetic thin films [151], dipole-exchange spin wave modes in Fe-N thin films [152], and spin-wave resonance in half-metallic ferromagnets [153] can be given as examples for the magnetic materials used in spin wave studies which have an in-plane anisotropy. Another example is the characterization of spin wave propagation in ultrathin YIG films with in-plane anisotropy (IPA) [154,155]. The excitation of perpendicular standing spin wave (PSSW) modes in YIG / CoFeB layers is another study reported in [150]. PSSW modes were excited due to the exchange coupling in the YIG/CoFeB layers. Another excitation of PSSW modes was determined due to the interfacial spin transfer torque in YIG /Cobalt (Co) heterostructures [156]. However, spin wave modes in pure YIG thin films with PMA need further investigation. The out-of-plane magnetization enables efficient excitation of spin waves, propagation in arbitrary directions, high spin-wave transmission, and computing free of non-reciprocity in the spin wave interferometer [157,158]. The out-of-plane magnetized majority gate is used mostly in spin wave logic devices and integrated devices. However, the in-plane magnetized majority gate shows limited performance [147].

In this study, multiple spin wave modes were observed in YIG thin films with PMA whose thicknesses are in the 40-120 nm range. Obtaining PMA in relatively thick YIG films is attractive for many technological applications. The garnet-type substrates which have lattice match with YIG find wide use in producing epitaxial YIG thin film. But, their complex lattice structure, higher growth temperature, and small PMA values are some of the disadvantages in spintronics applications. In this research, the use of Si substrate in YIG thin film fabrication is cost-effective and is compatible with many spintronic and magnonic applications. Our finding is promising for advanced spin wave-based technology.

YIG thin films were deposited on Si (100) substrates by the PLD technique. Si substrates were cleaned using acetone, methanol, and Isopropyl alcohol in an ultrasonic bath. Then, substrates were put inside the ultra-high vacuum chamber and annealed at 500° C for an hour at a base pressure of 1.0×10^{9}mbar. The distance between the Si substrate and the YIG target was adjusted to 60 mm. The oxygen pressure was 1.0×10^{5} mbar. The substrate temperature was 500° C. The parameters for the KrF excimer laser used in PLD are $\lambda = 248$ nm, an energy of 220 mJ pulses with 20 Hz pulse rate and 20 ns pulse duration time. After the deposition ended, the films were cooled to RT inside the chamber at a cooling rate of 10° C /min. Following the same procedure as the previous work, the films were ex-situ annealed at 850° C for 3 hours and cooled down to RT at a cooling rate of 1.2° C /min. All the films were grown under the same conditions. Based on a deposition rate of 2 nm/min, by changing only the time, 40, 90, and 120 nm YIG films were produced. For the surface morphology, SEM and AFM were employed on the annealed films. The XRD $\theta - 2\theta$ scans were carried out for the crystallization of the annealed films using a Rigaku 2000 DMAX diffractometer. The hysteresis loops of the films were obtained by using Quantum Design VSM. Ferromagnetic resonance is a powerful technique to analyze spin waves. FMR operating at a frequency of 9.1 GHz was used to analyze the magnetic anisotropy.

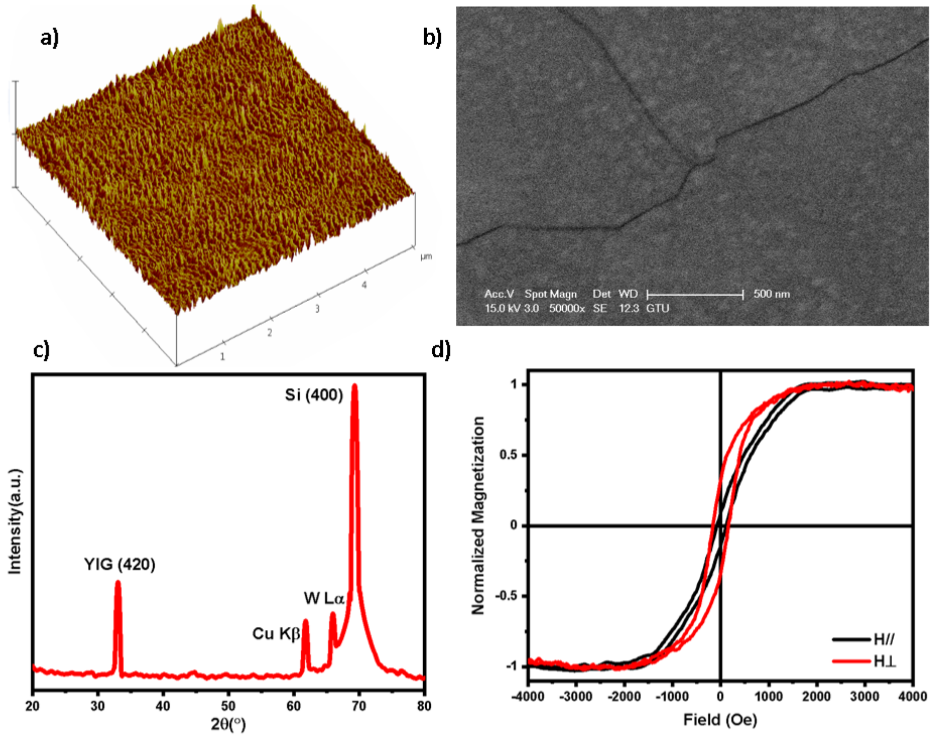

Figure 4.19. The surface morphology, crystalline structure, and magnetization curves of the annealed 90 nm YIG thin film. Images of a) AFM and b) SEM. c) XRD scan, which shows (420) and (400) diffraction peaks of the YIG film and Si substrate. d) Hysteresis loops of the YIG film when the external field, H is parallel to the film plane (H $\parallel$) and perpendicular to the film plane (H $\perp$).

SEM and AFM images of the film surface are shown in Figure 4.19. A 5 × 5 microns-surface profile of the annealed YIG film was imaged by AFM. The root-mean-square surface roughness (RSM) was found to be 1.4 nm. Inhomogeneous crack profiles that are larger than grain size were present on the annealed film surface in the SEM image (Figure 4.19 b)). The cracks might be caused by the difference between the thermal expansion coefficients of Si, 4.7 $\times 10^{-6}$ °C^{-1} [12], and YIG, 9.2 $\times 10^{-6}$ °C^{-1} [159]. Another possible reason is the strain due to the lattice mismatch of the substrate and the film. When the film thickness increases, the film lattice relaxes on the substrate, whose lattice constant is smaller. The strain gave rise to the randomly distributed cracks at the film surface. From the out-of-plane XRD pattern, a (420) characteristic peak of an annealed YIG thin film was obtained, as seen in Figure 4.19 c). The hysteresis curves in Figure 4.19 d) indicate that the magnetic susceptibility at the film normal is larger compared to the measured susceptibility at the film plane. The comparison of the out-of-plane hysteresis loop in red and the in-plane hysteresis loop in black shows that the magnetic easy axis is in the film normal.

The saturation magnetization values are between 1249.72 and 1733.28 G for the film thickness from 40 nm to 120 nm. This shows that saturation magnetization increases when the thickness increases. Possible reasons are stoichiometry, Oxygen and Fe vacancies/defects, crystalline structure, and strain effect. A less saturation magnetization value than the bulk crystal originates from the point defects, inhomogeneous magnetic anisotropy, stress, dislocations, inter diffusion, and voids as reported in [160, 161]. 120 nm film has a saturation magnetization value close to the bulk YIG (1750 G) [162]. The magnetization, magnetic anisotropy, and spin waves were analyzed by FMR measurement at RT. FMR spectrum can yield information about the crystalline structure and magnetic homogeneity of the films. The FMR spectra as a function of angle were obtained in in-plane (IP) and out-of-plane (OOP) measurement geometry. In the IP geometry, the microwave magnetic field is perpendicular to the film plane and the external field is in the film plane. In the OOP geometry, the microwave field is in the film plane and the external field is applied from the film plane to the film normal. Figure 4.20 shows that while the IP FMR spectra have no magnetic anisotropy, the OOP FMR spectra represent magnetic anisotropy for all film thicknesses. Resonance modes shift to a lower field value when the angle rotates from 0° to 90° between the applied field and the sample plane. The resonance field value at the angle of 90° is smaller than the resonance field at the angle of 0°. This behavior of the spectrum proves PMA in YIG films. Several splittings of the spin waves accompany the uniform FMR mode when the magnetic field is parallel and perpendicular to the film plane. The superposition of spin waves and the main resonance mode causes a relatively larger linewidth compared to the few Oe FMR linewidth of YIG film grown on a garnet substrate. Inhomogeneous magnetic regions, magnon scatterings, and strain anisotropy in the film cause a large FMR linewidth.

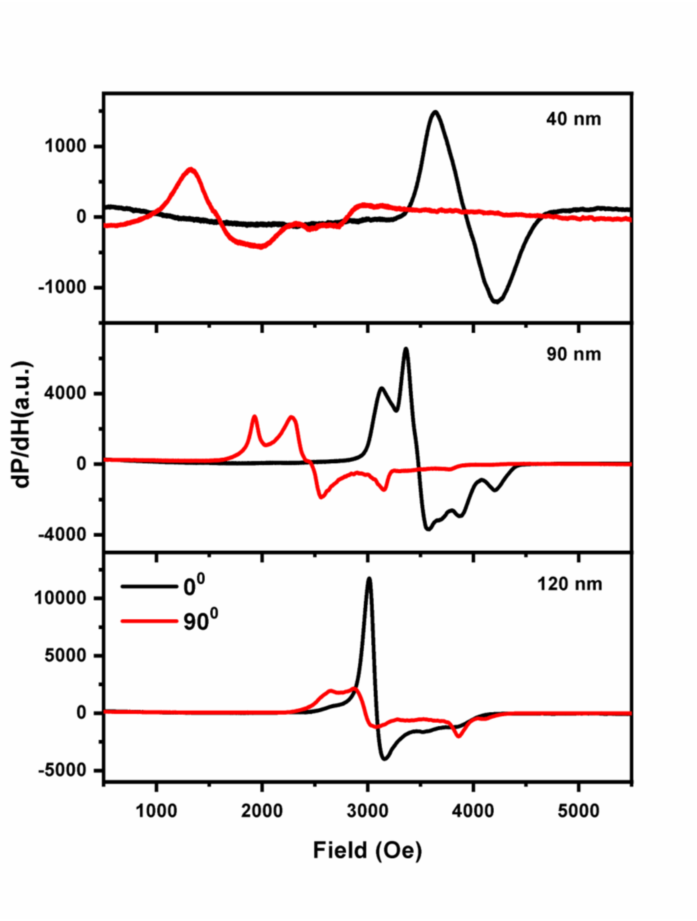

Figure 4.20. Spin wave resonance spectra of YIG thin films in the OOP FMR measurement when the field is applied parallel to the film plane (0°) and perpendicular to the film plane (90°).

In this study, 40 nm film has a broadened spin wave mode profile that indicates a higher magnetic inhomogeneity in the film. The uniform ad spin wave modes were excited by the microwave field at 9.1 GHz. The modes are standing spin wave modes or arbitrary modes related to the nonuniform magnetization and inhomogeneous volume/surface effects. Standing spin waves are determined by the change in the resonance field and mode intensity when the thickness changes [35]. Figure 4.20 shows the increase in the mode intensity and the shift of the modes as the thickness increases from 40 nm to 120 nm. This proves that the additional resonance modes are standing spin wave modes and some come from surface inhomogeneity. The effective anisotropy values are derived from the FMR spectrum by employing Kittel's formulation for the field applied parallel and perpendicular to the film plane [163]. The FMR mode enables enough information about the anisotropy and the effective magnetization. Therefore, all calculations were made taking into account the FMR mode. The anisotropy field is determined using the relation of $4\pi \mathrm{M_{eff}} = 4\pi \mathrm{M_s} - 2\mathrm{K}_{\perp}/\mathrm{M}_s$ with $\mathrm{K}_{\perp}$ being the perpendicular anisotropy constant. Table 4.2 shows the results for the saturation and effective magnetization, anisotropy field (H_a), shape anisotropy, Lande factor (g), and exchange stiffness (D). The sign of effective magnetization is minus, which refers to perpendicular magnetic anisotropy in YIG films. The effective magnetization increases with the increasing thickness, as shown in Table 4.2. The positive perpendicular anisotropy constant implies that the favored magnetic easy axis is perpendicular to the film plane. g values are between 1.91 and 2.10 in Table 4.2. Saturation and effective magnetization, effective anisotropy values, and g values of different thicknesses.

Table 4.2. The results for the magnetic parameters of YIG thin films.

Magnetic Parameters	**40 nm**	**90 nm**	**120 nm**
$4\pi M_s(\mathbf{G})$	1249.72	1331.36	1733.28
$4\pi M_{\mathbf{eff}}(\mathbf{G})$	-1528.38	-1405.29	-701.31
H_a (**Oe**)	-2778.17	-2736.65	-2434.59
$K_{\perp} \times 10^2$ (**erg/cm^{-3}**)	1382.14	1450.42	1679.86
$K_{\mathbf{shape}} \times 10^2$ (**erg/cm^{-3}**)	621.73	705.62	1195.96
g	2.10	1.92	1.91
D$\times 10^{-9}$ (**Oe.cm^2**)	1.02	3.72	5.12

The resonance field at parallel and perpendicular orientations of the magnetic field with respect to the film plane approaches each other when the thickness increases. 120 nm film does not have a strong anisotropy because the crystalline anisotropy is smaller than the shape anisotropy. A comparison of shape and strain anisotropies allows knowing about the anisotropy type that the YIG film possesses. Shape anisotropy in thick YIG films induces an in-plane anisotropy since the magnetoelastic effects decrease due to the relaxation of the lattice. For that reason, PMA in thick films is challenging [16]. In this study, the perpendicular magnetic easy axis in YIG films is due to the compressive strain between the substrate and the film $(a_{\mathrm{YIG}} = 12.376A^{\circ})$[30], $(a_{\mathrm{Si}} = 5.43A^{\circ})$ [37]. The volume of YIG must be conserved during the growth, a compression at the film plane gives rise to an extension along the crystal c-axis. The magnetic easy axis shifts from in-plane to out-of-plane according to the lattice distortion along the c-axis. The FMR spectra show that the lattice strain does not relax completely because of the spin wave modes in regions with different effective magnetic anisotropies. Nonuniform strain distributions within the films cause inhomogeneous effective anisotropy. One can say that tetragonal lattice distortion due to the substrate/ film lattice mismatch results in strain-induced perpendicular magnetic anisotropy [104].

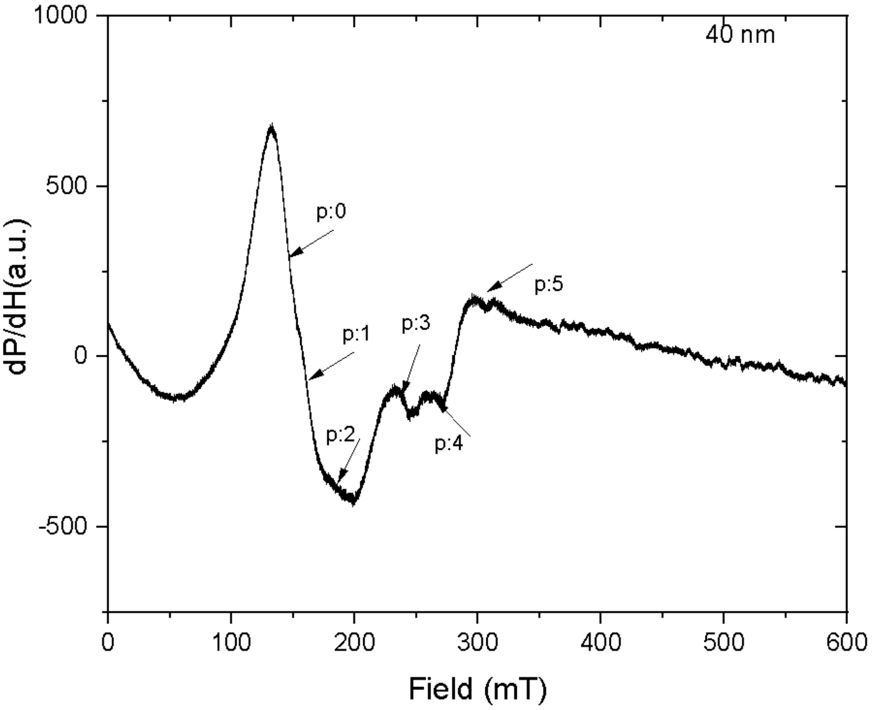

Figure 4.21. The odd and even modes for 40 nm YIG film.

Ferromagnetic resonance mode is the uniform magnetization precession around an effective magnetic field. Spin waves are non-uniform modes of precession that are excited by an effective surface anisotropy. Surface anisotropy allows the pinning of spins on the interface or surface of the film. When the surface magnetization is nonuniform or anisotropy energy is inhomogeneous in the film surface, it causes the generation of unpinned modes. Surface boundary conditions determine the allowed spin wave modes, which are quantized by the pinning condition [54]. The surface boundary condition might depend on the angle, and annealing temperature can change the effective surface anisotropy field. The pinning of magnetization at the interface or surface enables spin wave occurrence [20].

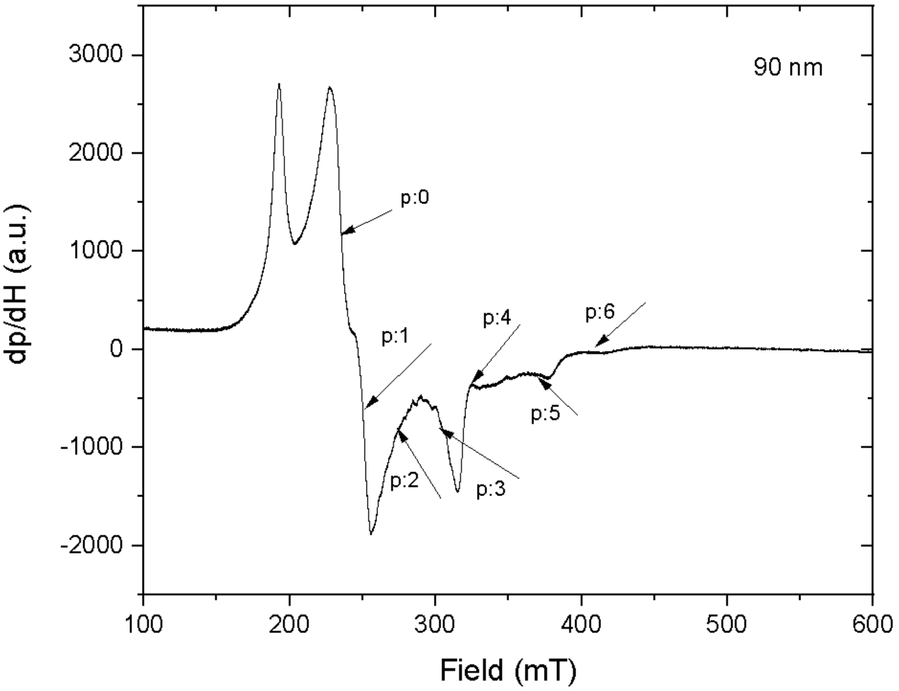

Figure 4.22. The odd and even modes for 90 nm YIG film.

The quantum number of these modes is determined by pinned and unpinned boundary conditions. While Odd modes correspond to the unpinned surface, even modes are ascribed to the pinned surfaces. In the samples subject to this study, asymmetrical boundary conditions caused the spins to be unpinned at the free surface and pinned at the interface of the YIG film and Si substrate. The spin wave modes were excited up to the 6th order by the microwave field. It is possible to understand how strong the exchange interaction, which is the short-range interaction between two adjacent spins, is by knowing the exchange stiffness of the material. The methods to measure the exchange stiffness are given in the studies [164, 165]. In this study which uses the dipole-exchange interaction approach, the exchange stiffness was obtained by employing the quadratic dispersion relation in the case of the applied field being normal to the film plane [166]:

$$H_{res} = H_0 + Dk^2 \tag{4.2}$$

with H being the resonance field of FMR mode and D being the exchange stiffness constant. $k = n\pi/d$ is the spin wave vector, where n is the quantized number and d is the film thickness. The exchange stiffness was found via the slope of the quadratic relation between H and n^2, as given in Figure 4.24. The weaker modes along the main FMR resonance mode of 90 nm and 120 nm, films arise at the lower fields in Figures 4.22 and 4.23. These modes are considered surface spin waves that might emerge from the cracks on the film surface annealed at high temperatures.

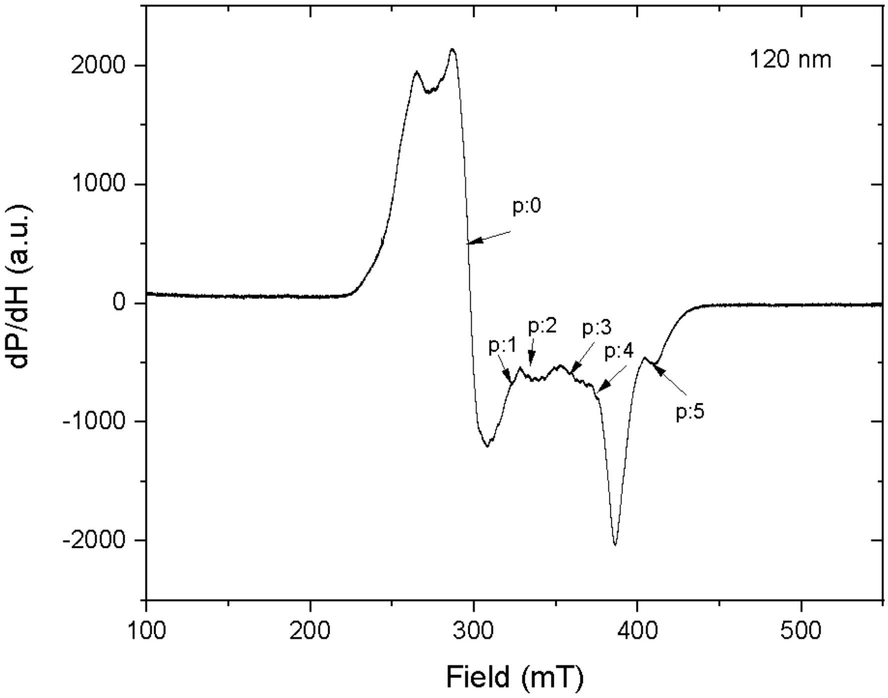

Figure 4.23. The odd and even modes for 120 nm YIG film.

Another possible reason is that when the thickness increases, the relaxation of the film on the Si substrate forms randomly distributed cracks on the film surface, which cause inhomogeneous magnetic regions that respond to the applied field individually. The excitations of spins in these regions due to the microwave RF field are different. The cracks confine spin waves along the lateral, leading to the reflection of spin waves from the domain walls. In Figure 4.24, the deviations from the fitted line were due to the surface anisotropy, the partial pinning of surface spins, and the inhomogeneous volume magnetization within the films as explained in the Portis model [55]. The high deviation for the 40 nm YIG film can be expressed by the high volume inhomogeneity and the large resonance linewidth.

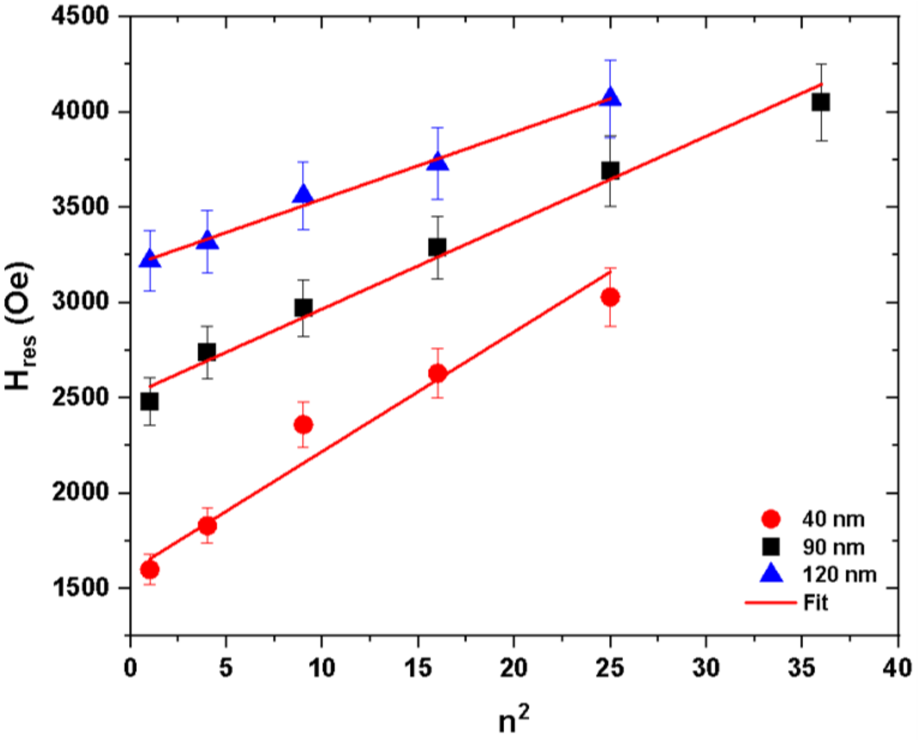

Figure 4.24. The relation between the n^2 versus H_n.

The exchange stiffness was between 1.02×10^{-9} and 5.12×10^{-9} Oe cm^2 as seen in Table 4.2, which is comparable with the bulk YIG [165]. When the film relaxes, spin wave modes, called the thickness modes, and surface modes emerge within the volume. When the exchange interactions are strong within the thin film, standing spin wave modes are likely to occur. The modes that establish a linear relationship between $H_n - n^2$ prove that the modes around the main mode at the higher fields in the spectrum are standing spin wave modes.

5. MAGNETIZATION DYNAMICS OF NiFe DOT/ANTIDOT ARRAYS

Investigation of the magnetic properties of ferromagnetic nano/microstructures has high interest recently due to their potential applications such as high-density storage devices, logic devices, and magnetic field sensors. The reversal mechanism of magnetic nanostructure array must be understood well to produce robust magnetic devices. The fabrication of nano/micro patterns on magnetic structures has become easier with the advancements in lithography techniques. Dot and Antidot array structures have the ability to modify the magnetic behavior of magnetic thin films i.e. the magnetization reversal mechanism, formation of various magnetic domain structures, and control the magnetic anisotropy. Such nano/microstructures on thin films are used as spin-wave waveguides, magnonic crystals, magnonic transistors, magnonic phase shifters, microwave filters, spin-wave logic devices, and high-density magnetic data storage technology. The shape itself, the size of the structure, and the array geometry enable the reorientation of the magnetic characteristics of the material.

In this thesis, dot, and antidot array structures were produced by a lithography technique, and an RF sputtering technique was employed for the NiFe thin film deposition. A reference uniform NiFe thin film was deposited by following the same growth condition with the patterned films to make a comparison between the patterned and pure films by means of the shape effect on the magnetic properties. The effects of the dot/antidot array on the magnetic anisotropy were investigated by the FMR technique. The FMR measurements were performed at 9.1 GHz at room temperature, both in the film plane and out-of-the-film plane geometry.

5.1. Material and Methods

The fabrication of a dot array of magnetic nanostructures on Si substrate by lithography is schematically represented in Figure 5.1. Foremost, a soda lime mask of the pattern design with different diameters and inter-pattern spacing was created using a Heidelberg mask writer in a clean room environment. Silicon (Si) substrates were cleaned using acetone and Isopropyl alcohol (IPA) in an ultrasonic bath, followed by spray drying with N_2 gas. Substrates were baked for a few minutes to prevent any contamination on the surface. A positive photoresist was spin-coated on the substrates based on the datasheet of the resist. After spin coating, substrates were soft-baked on a hot plate. The resist-coated substrates were exposed to a 365 nm Ultraviolet (UV) light using the soda lime mask via a mask aligner. The areas that see the UV light were dissolved in a developer solution and the areas that are not exposed remained, the final patterns on the substrates were expected to be the ones transferred from the mask onto the substrate. By checking the array pattern by using an optical microscope, the antidot structures were successfully confirmed to be on the Si substrate.

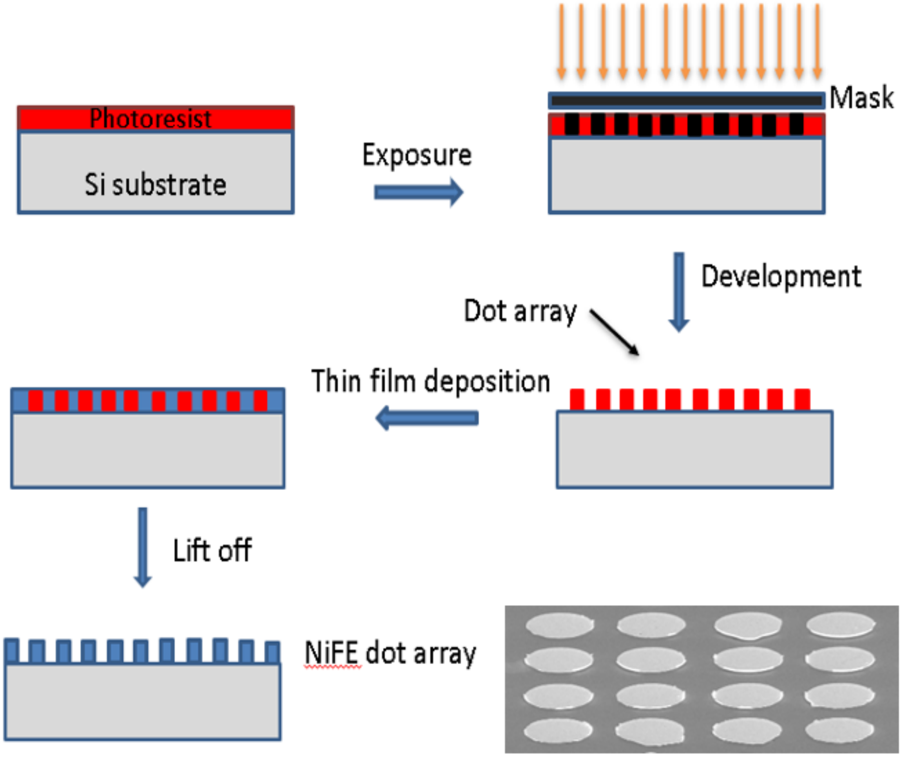

Figure 5.1. Lithography steps.

A 20 nm ferromagnetic NiFe (Permalloy) thin film was grown onto Si substrates with an array structure by RF sputtering. Another pure NiFe thin film was deposited under the same condition, as well. The base pressure of the vacuum chamber was 2×10^{-9} mbar. After a lift-off process with acetone and Isopropyl alcohol on the deposited films, the patterned films have been imaged by Philips XL-30 FEG scanning electron microscope (SEM) and Nikon ECLIPSE LV150 optical microscope (OM) to confirm the sizes and shapes of the structures. Figure 5.2 shows the SEM images of the NiFe dot and antidot array structure after the lift-off process. The film thicknesses were determined to be 20 nm by XRR measurement.

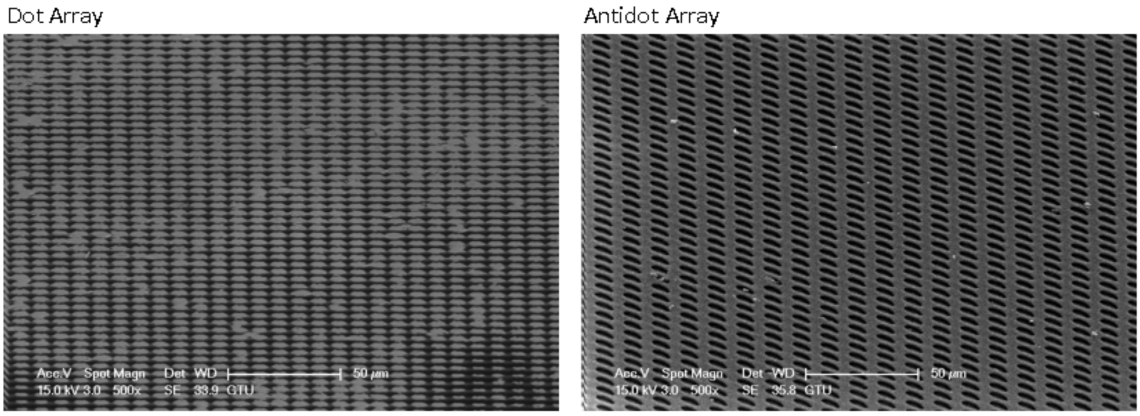

Figure 5.2. SEM images of a dot and antidot array.

The effects of the dot/antidot array on the magnetic anisotropy were investigated by the FMR technique. The room temperature FMR measurement was performed at 9.1 GHz microwave frequency by an X-band Jeol JES-FA300 electron spin resonance (ESR) spectrometer. The angular variation of FMR spectra was analyzed in in-plane and out-of-plane geometries by rotating the sample inside the cavity. During the in-plane measurement, the microwave magnetic field was perpendicular to the film plane and an external DC magnetic field was applied in the film plane. In the out-of-plane geometry, the microwave field was in the film plane, and the applied field was swept from the film plane ($H \perp n$, n is the film normal) towards the film normal ($H \parallel n$).

5.2. FMR of NiFe Dot Array

Circular dot arrays of NiFe with different diameters and separation distances were manufactured by the lithography and sputtering technique. The in-plane and out-of-plane FMR measurements of 20 nm pure thin film and the dot arrays with a diameter of 4 μm and 6 μm and separation distance of 2.50 μm between the adjacent dots as a function of angle gives the resonance field profile as shown in Figure 5.3. The full spectrum of pure thin film and dot arrays is given in the Appendix section (A1-A6).

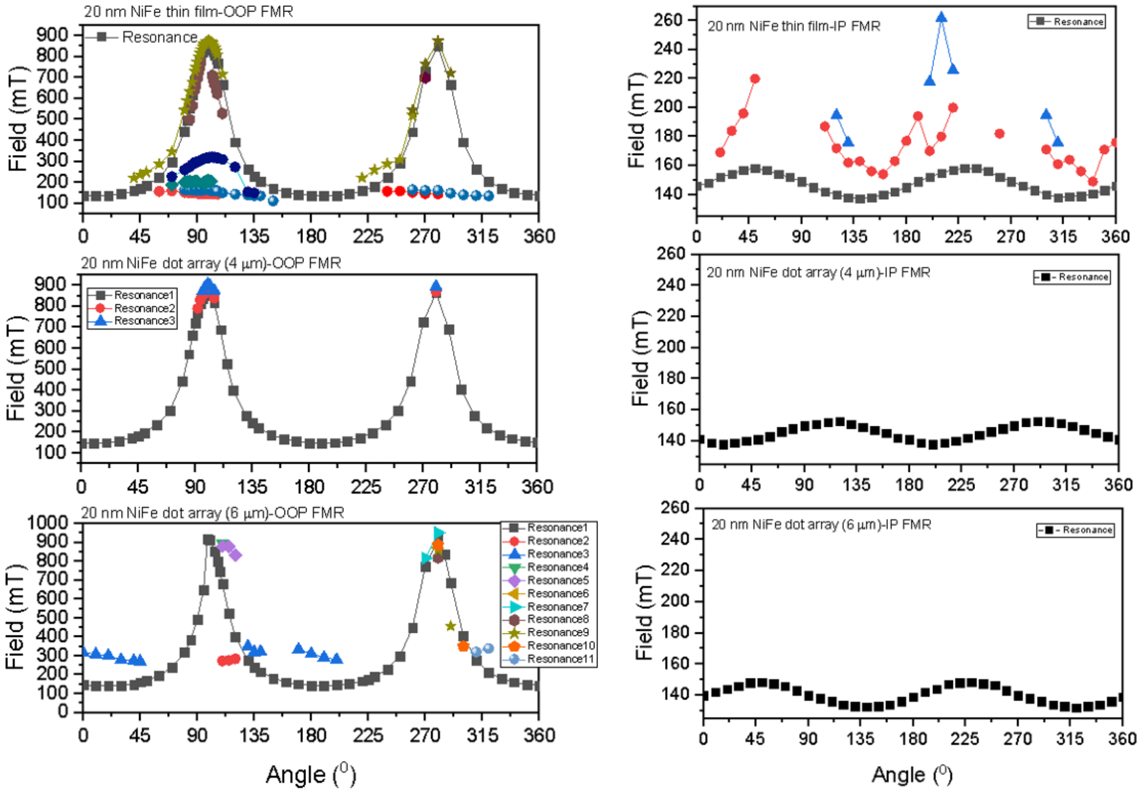

Figure 5.3. Angular variation of the resonance field of 20 nm NiFe dot arrays for OOP and IP FMR measurement.

Another thickness of 40 nm was deposited for the circle and half-circle dot array with a diameter of 15 μm and separation distance of 6 μm and the size of the half-circular dot was 8 μm and separation distance of 2.5 μm. The FMR spectrum of 40 nm pure thin film, circle, and half-circle dot array in the OOP and IP measurement convention was illustrated in Figure 5.4. The black and red spectrum corresponds to the spectrum obtained when the magnetic field is applied along the film plane and applied perpendicular to the film plane, respectively.

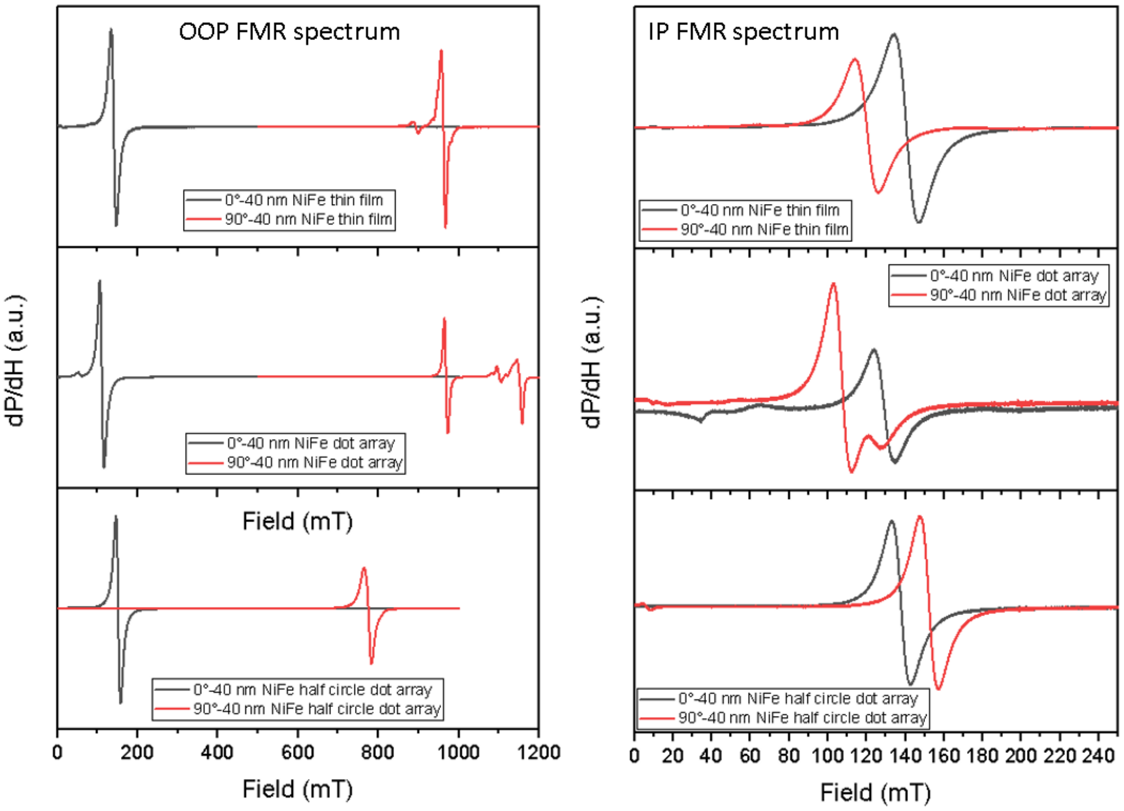

Figure 5.4. FMR spectra at the angle of 0° and 90° for the 40 nm NiFe circular and half-circular dot array at the IP and OOP measurement geometries.

In the OOP FMR spectrum, the FMR peak intensity decreases when the field value increases to 1000 mT, and spin wave modes occur around the main resonance peak for the pure thin film. In the circular dot array spectrum, the FMR peak is sharper with respect to the pure thin film and the number of spin waves increases and spin waves are located far from the main peak at a larger field than 1000 mT. In the half-circular dot array spectrum, the anisotropy is less, since the FMR signal at the angle of 90° was obtained at a lower value of 800 mT field. Besides, the spin wave modes are within the main FMR signal, which causes a larger FMR linewidth. The absorption of the pure film takes place at a field of 150 mT at 0° and 115 mT at 90°. The circular dot array has a resonance peak at 130 mT at 0° and 105 mT at 90°, with spin wave mode at 130°. The angular variation of the field in OOP measurement geometry for the pure thin film shows that spin wave modes are likely to occur when the field is applied perpendicular to the film plane.

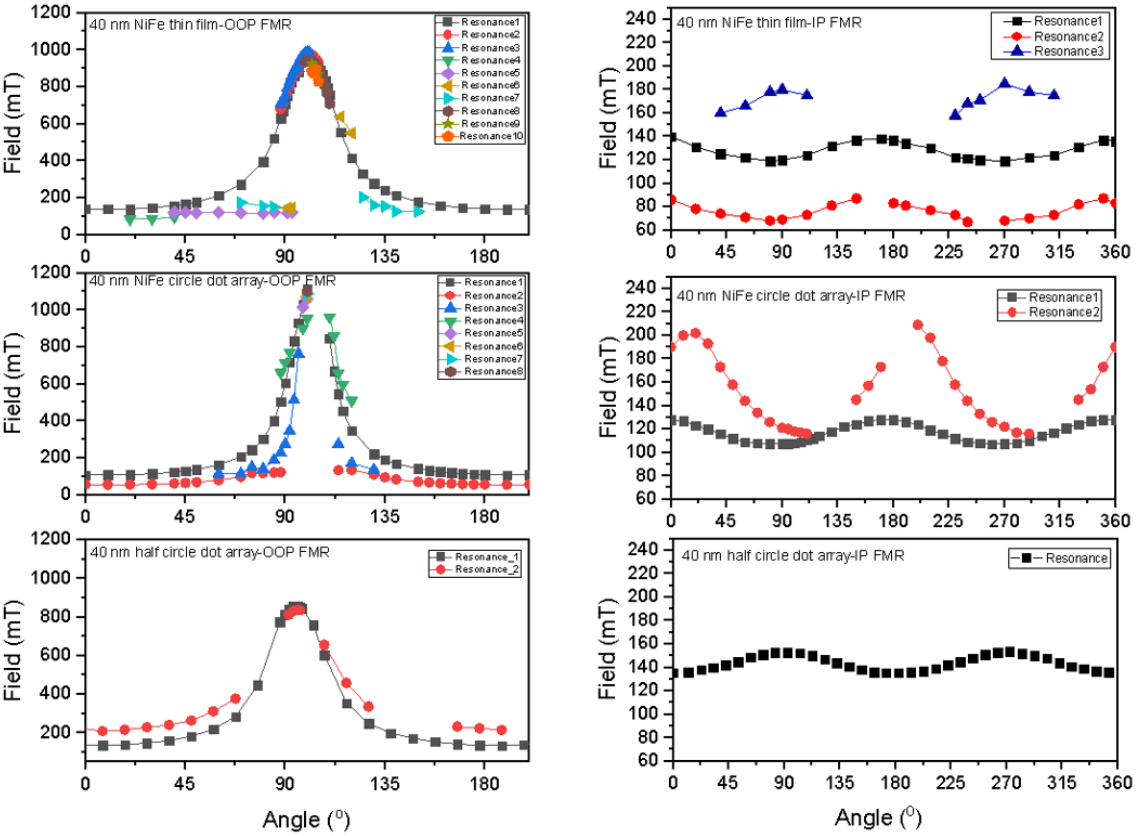

Figure 5.5. Resonance field as a function of angle for OOP and IP FMR measurement of 40 nm NiFe circular and half-circular dot array.

In the half-circular dot array, there are two spin wave modes following the main FMR mode due to the shape effect. In the half-circular dot array, only one spin wave mode was observed. In the IP measurement geometry, two-fold magnetic anisotropy was observed in all the films. The spin wave modes are in pure and dot array patterned film, while half-circle dot array film has only uniform mode. Both the uniaxial anisotropy and the shape anisotropy are present in the films. The ring dot array was produced to see the difference between the circular dot and the ring structure. The SEM image of the ring array is shown in Figure 5.6.

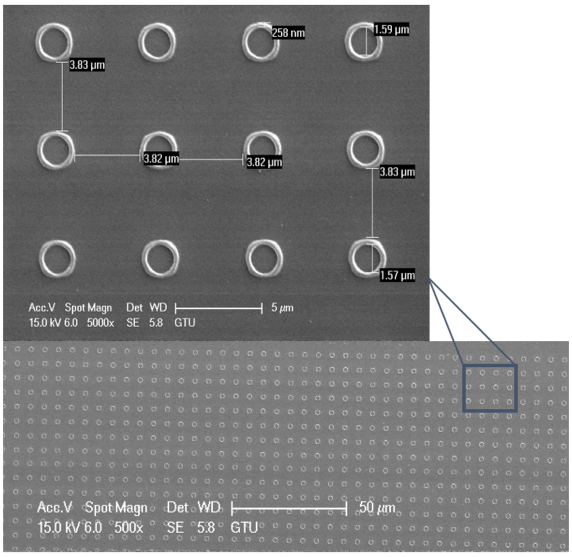

Figure 5.6. The SEM images of the ring dot array.

From the OOP and IP FMR measurements, the angular variation of the resonance field of different sized-ring arrays was obtained. Z25 is a label of the 20 nm pure thin film. Z23 denotes the ring dot array with a diameter of 4.75 μm, a width of 1.55 μm, edge-to-edge separation distance along the x direction is 3.20 μm and along the y direction is 3.70 μm. Z24 and Z17 are the labels of the other ring arrays, with the sizes shown in the parentheses in Figure 5.7. When one compares the width values of 1.55 and 0.50 μm array, the thinner ring array has a clear shape effect in the variation of the resonance field with angle. Z17 has spin wave modes excited at different angles from the main FMR peak. However, in Z23, spin wave modes follow the same trend as the main resonance peak when the angle changes and additional peaks arise at lower fields at the perpendicular orientation. In Z24, the distance between the rings is less than in Z23. Spin wave modes appear at an angle of 90 degrees. Figure 5.8 shows that the magnetic anisotropy of the patterned films is less than the pure thin film in the IP measurement geometry. Especially, the Z17 ring array has no IP anisotropy. While the peak position of the dot array with a diameter of 4 μm is at 950 mT, it is 870 mT for the dot array with a diameter of 6 μm. For the antidot array, we observe a much more shift to a lower field value, 600 mT. The anisotropy in the antidot array spectrum is less than the dot array. The IP anisotropy of the dot array is less than the pure film. The IP anisotropy of the antidot array is more than the 4 μm size dot array structure.

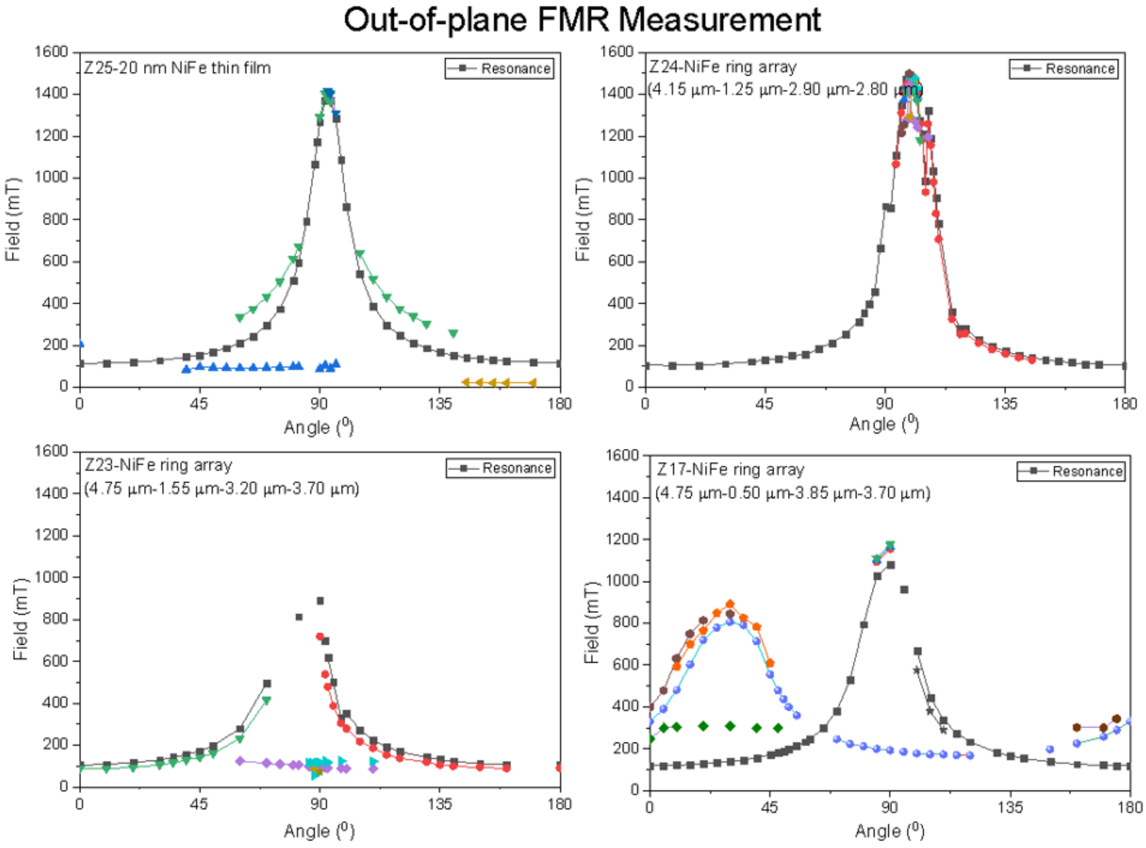

Figure 5.7. The angular variation of the resonance field for the OOP FMR measurement of the ring dot array.

The OOP and IP FMR spectrum of the dot and antidot array thin films were shown in Figure 5.9. The full spectrum of the antidot array is given in the Appendix section (A7 and A8). One can see that the peak shifts as a function of the dot size. Figure 5.10 shows the angular variation of the resonance field of pure, dot, and antidot array thin films. The pure thin film possesses more spin wave modes around the uniform resonance mode, while the number decreases in the dot array pattern and spin wave modes collected near the main mode at the perpendicular field. In the antidot array pattern, there is a spin wave mode whose resonance field changes with the angle. In the IP orientation, while the pure film has two additional spin wave modes, the dot and antidot array patterns have only uniform resonance peaks, and the anisotropy does not show a significant change in all the films.

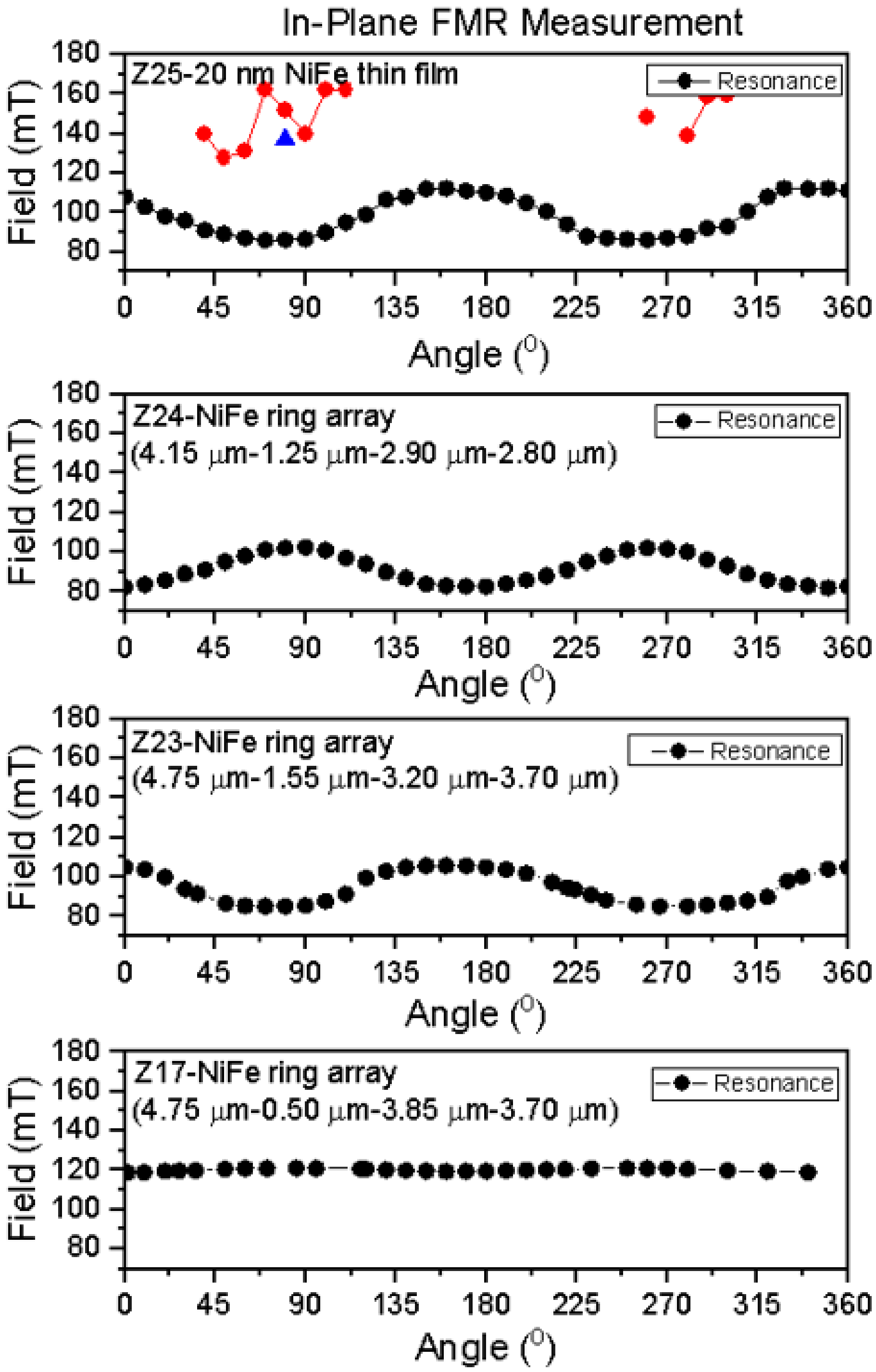

Figure 5.8. The angular variation of the resonance field for the IP FMR measurement of ring shape dot array.

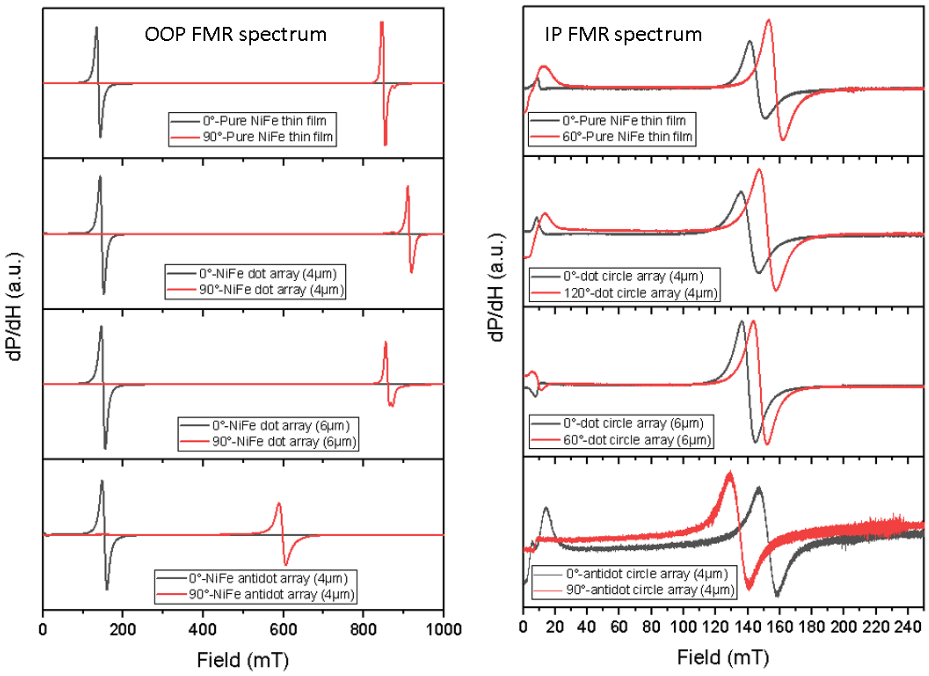

Figure 5.9. FMR spectrum for OOP and IP measurement geometry of 20 nm NiFe dot and antidot array.

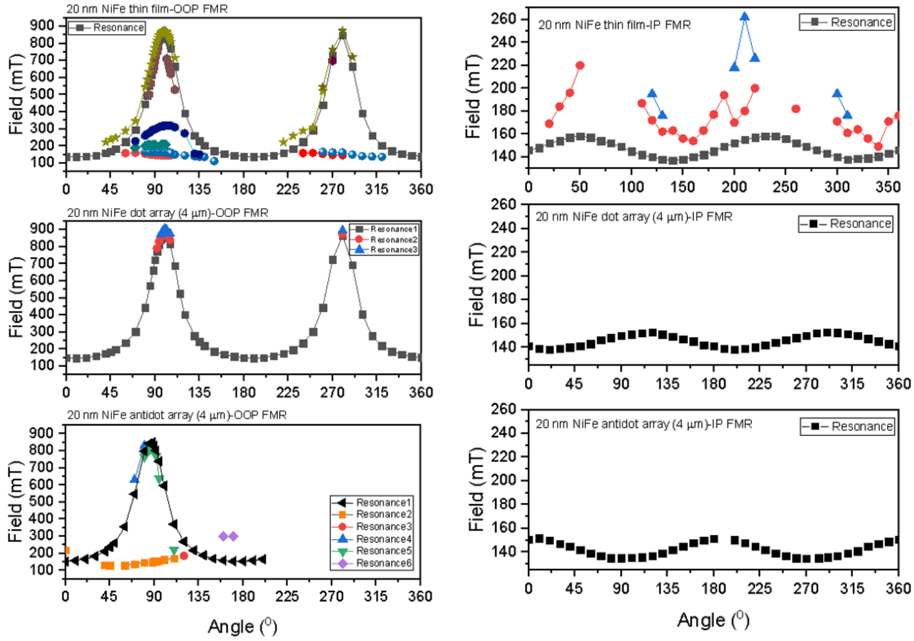

Figure 5.10. Resonance field as a function of the angle for the OOP and IP FMR measurement of 20 nm NiFe dot and antidot array.

5.3. FMR of Antidot Array

Another type of magnetic nanostructure is an antidot structure in which holes are embedded into the continuous magnetic films. Antidots are artificial nano/microscale defects introduced to the continuous film. The size and distribution of the antidots affect the magnetic properties of the continuous film such as the magnetic anisotropy, magnetization reversal, and coercive field, and changes the intrinsic magnetic anisotropy locally with periodic domain structures around the holes. The magnetization reversal process of the antidot arrays is interesting from a fundamental point of view. Antidots introduce locally distributed shape anisotropy fields and perform as pinning centers, which inhibits the domain wall movement during magnetization reversal. The magnetization reversal mechanism is strongly influenced by the shape, size, and distance between the holes. These defects provide for applications such as waveguides, filters, and data storage in technology.

For the fabrication process of an antidot array of magnetic nanostructures on a Si substrate, a soda lime mask of the pattern design was created using a Heidelberg mask writer in a clean room environment. After that, Silicon (Si) substrates were rinsed subsequently with acetone and Isopropyl alcohol (IPA) in an ultrasonic bath followed by spray drying with N2 gas to remove dust from the surface. A heat treatment at 95°C was applied for a few minutes to prevent contamination on substrates prior to coating of resist. A positive AZ1505 photoresist was spin-coated on the surface of the cleaned substrates following the recipe in the photoresist datasheet. Then, resist-coated substrates were soft-baked on a hot plate. The thickness of the photoresist on the Si substrate was approximately 500 nm based on the datasheet. Photolithography at a 365 nm Ultraviolet (UV) wavelength was performed on resist-coated substrates using the soda lime mask via a mask aligner. Thereafter, a post-bake was applied for a few minutes. The areas exposed to UV light were dissolved in a developer solution. So, the pattern on the mask was transferred onto the substrate. After checking the array by using an optical microscope, the antidot structures were successfully confirmed to be on the Si substrate. The SEM images of the circle, pacman, and half-circle antidot array are shown in Figure 5.11. The AFM image of the pacman antidot array is shown in Figure 5.12.

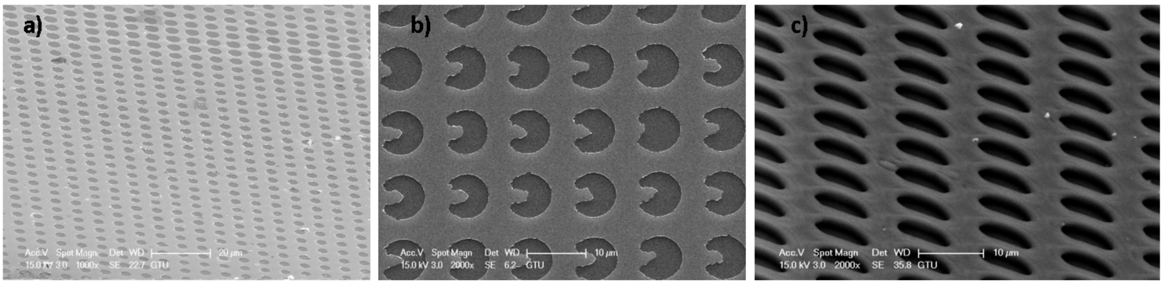

Figure 5.11. SEM images of the a) circle, b) pacman, and c) half-circle antidot array.

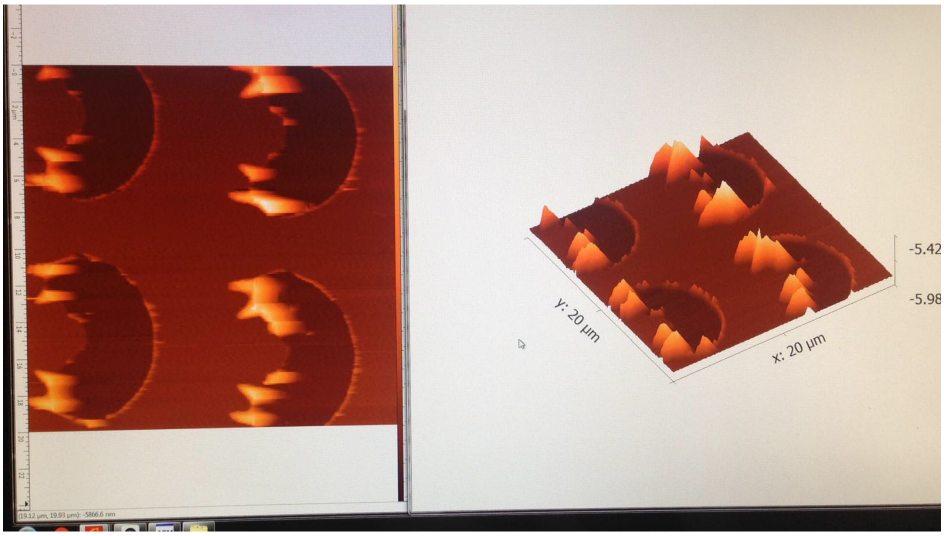

Figure 5.12. AFM image of the Pacman antidot array.

In the OOP and IP FMR measurement geometry, the angular variation of the resonance fields of the pure, circular antidot, and large and narrow size Pacman antidot array thin films were shown in Figure 5.14.

The sizes of the holes were depicted in Figure 5.13. The resonance field takes the maximum value at the angle of 90° which is the case for the pure and Z2 labeled antidot array pattern. However, the maximum resonance field is observed at an angle larger than 90°.

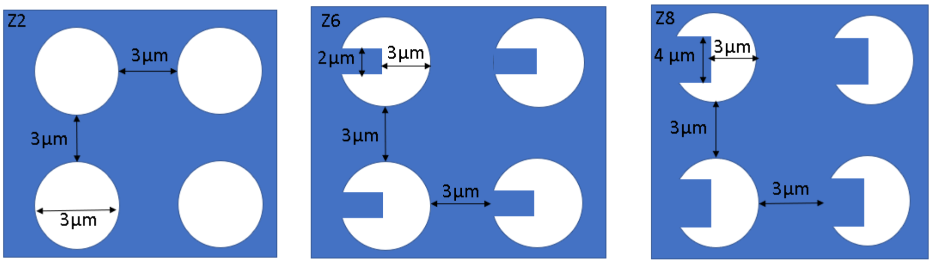

Figure 5.13. A scheme that shows the edge-to-edge separation distance and the sizes of the antidot structures which are labeled as Z2, Z8, and Z6.

This might be due to the initial angle that was not adjusted exactly at 0° so the shift of 10° in each angle was encountered. The Z6 antidot array does not have a proper resonance field profile as a function of angle. In the IP orientation, Z2 has a larger variation of the resonance field, while Z8 has the least change in the resonance field. However, Z6 has the largest change in the resonance field among all the others.

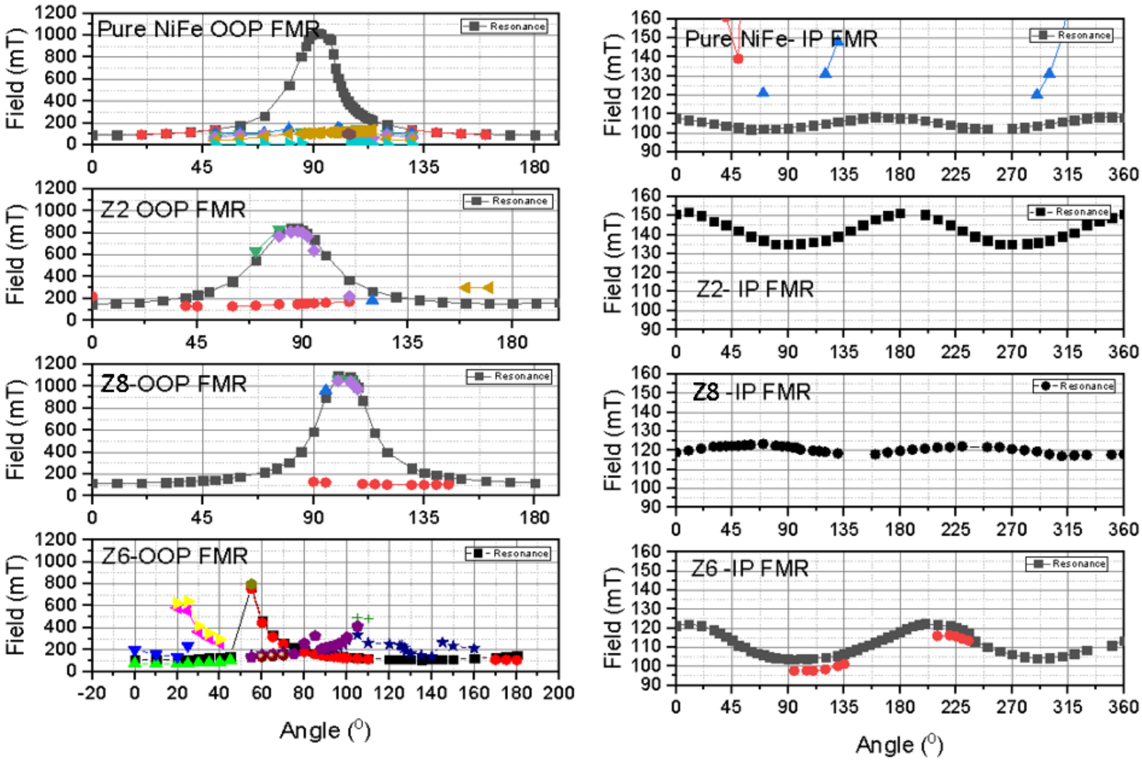

Figure 5.14. The angular variation of the resonance field of Z2, Z8 and Z6 in OOP and IP FMR measurement.

The angular variation of the resonance field in the OOP measurement was shown in Figure 5.15. For the half-circular antidot structures, the size and separation distance of Z21 labeled patterned film was defined as the radius is 7 μm, the edge-to-edge distances between the holes are 6.5 μm and 6 μm. The same convention was used for the other half-circular antidot arrays. One realizes that Z21 requires a larger resonance field at an angle of 90° than the pure and patterned films. However, a number of spin-wave modes appear in Z22 and Z4 due to the shape effect. The angular variation of the resonance field of the half-circular antidot arrays in the IP measurement was shown in Figures 5.16. Z21 and the pure thin film have similar magnetic anisotropy. However, Z22 and Z4 have smaller magnetic anisotropy, but spin wave modes have additional anisotropies. The angular variation of the resonance field at OOP and IP geometries for the pacman shape antidot array structures were shown in Figures 5.17 and 5.18.

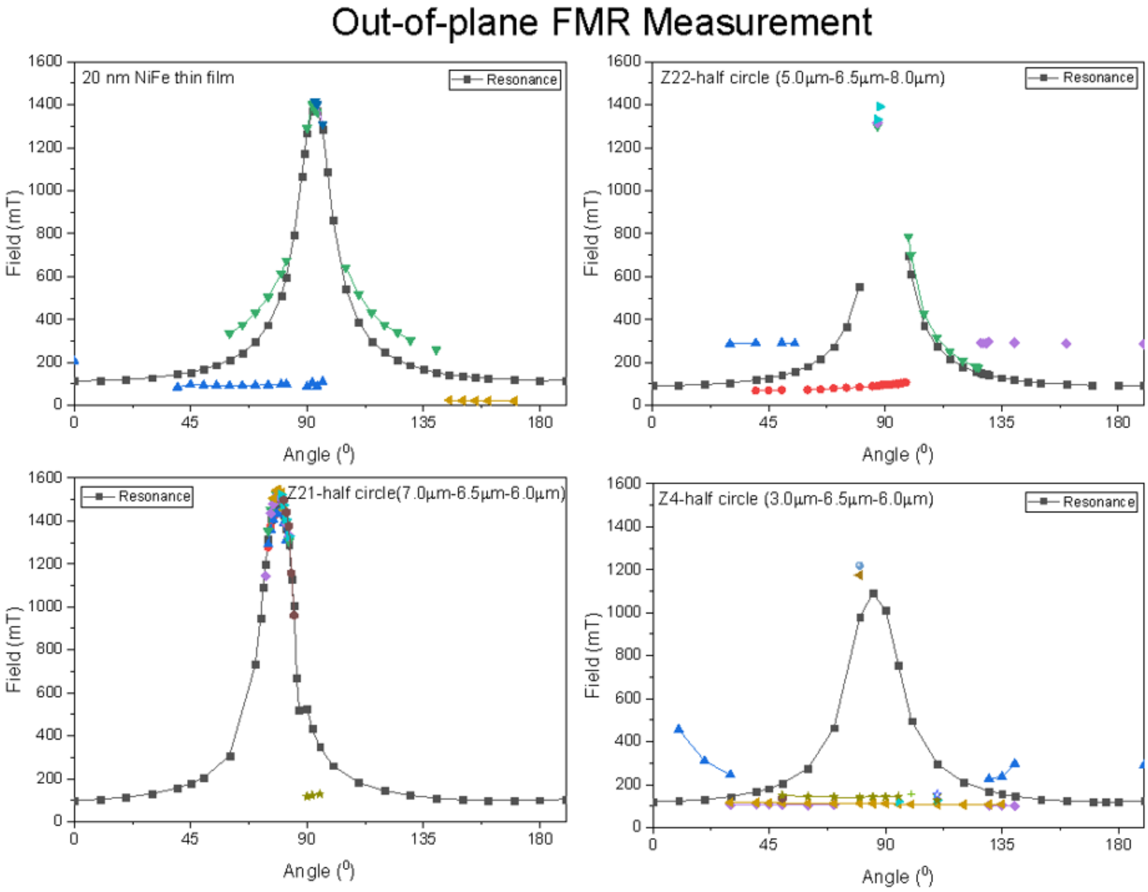

Figure 5.15. The angular variation of the resonance field in OOP FMR measurement of half-circle shape antidot array.

When the separation distance increases along the y directions, the number of spin-wave modes increases. Z26 labeled film does not have spin-wave modes, only uniform resonance mode exists. The IP geometry measurements show that the anisotropy intensity in antidot arrays is less than the pure thin film. When the size of the pacman increases, as in the case of Z17 and Z3 films, the number of spin waves that accompany the uniform resonance increases. However, the IP anisotropy of the large Pacman antidot array is less than the pure and narrow pacman array.

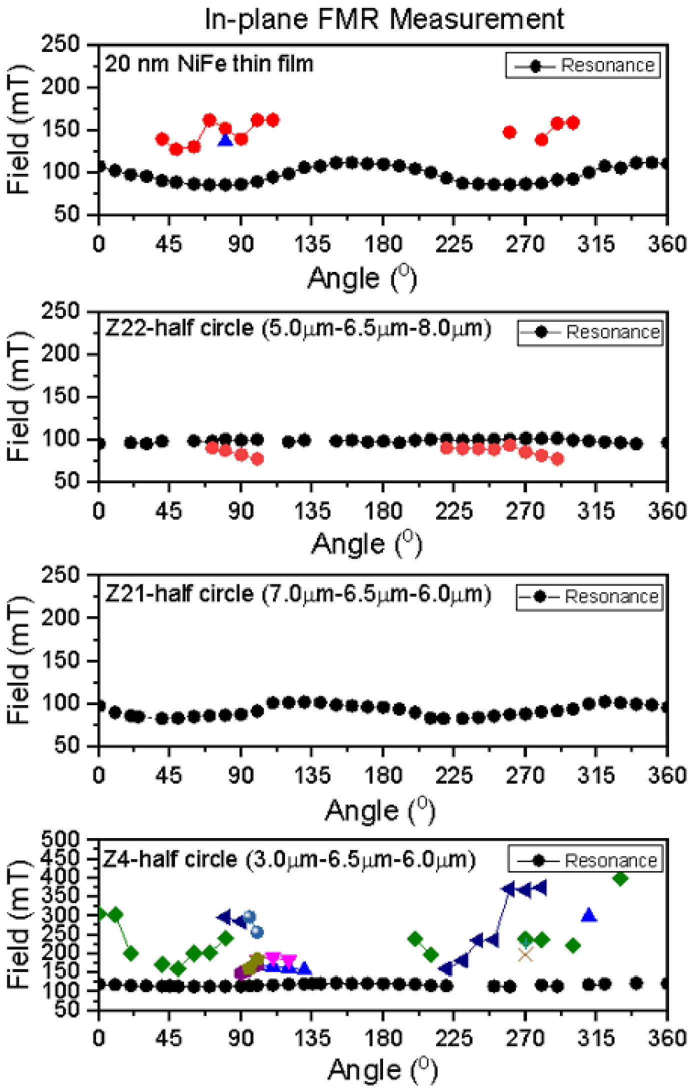

Figure 5.16. The angular variation of the resonance field in IP FMR measurement of half-circle shape antidot array.

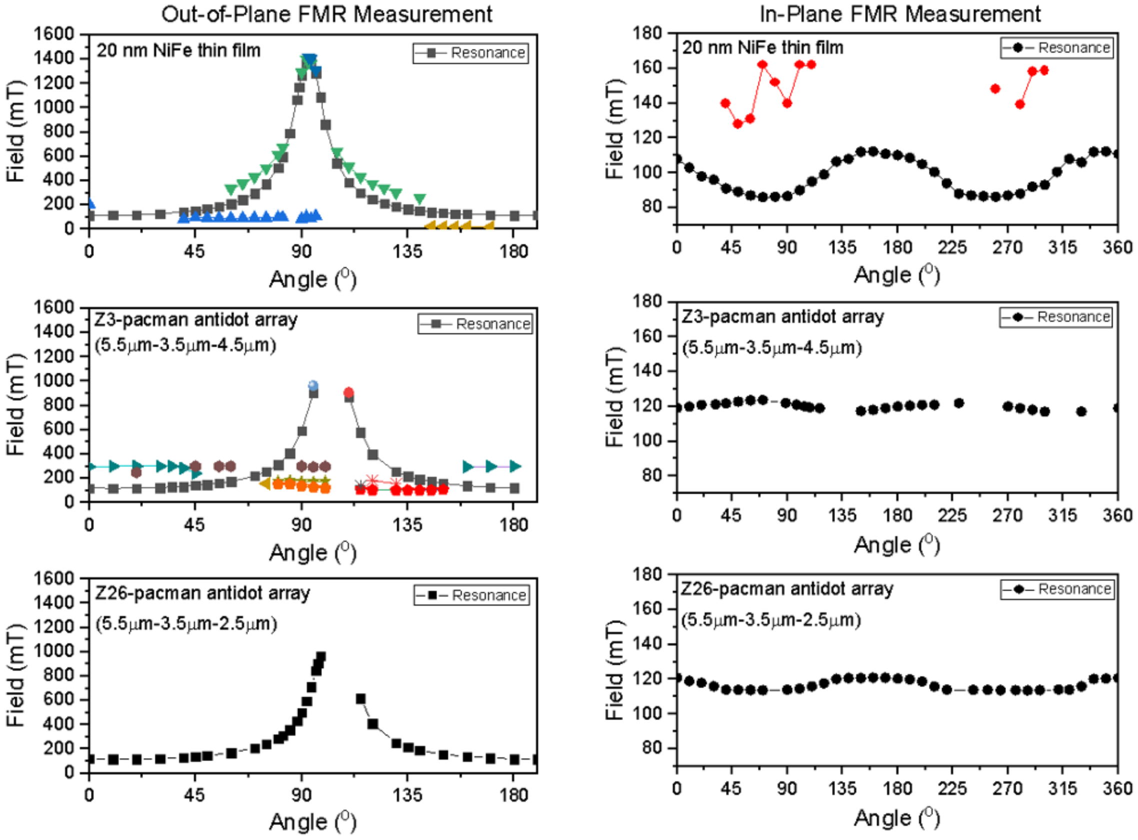

Figure 5.17. The angular variation of the resonance field in IP and OOP FMR measurement of the pacman shape antidot array with dimensions of 5.5 μm width, edge to edge distances of 3.5 μm along the x direction, 4.5 μm and 2.5 μm along the y direction.

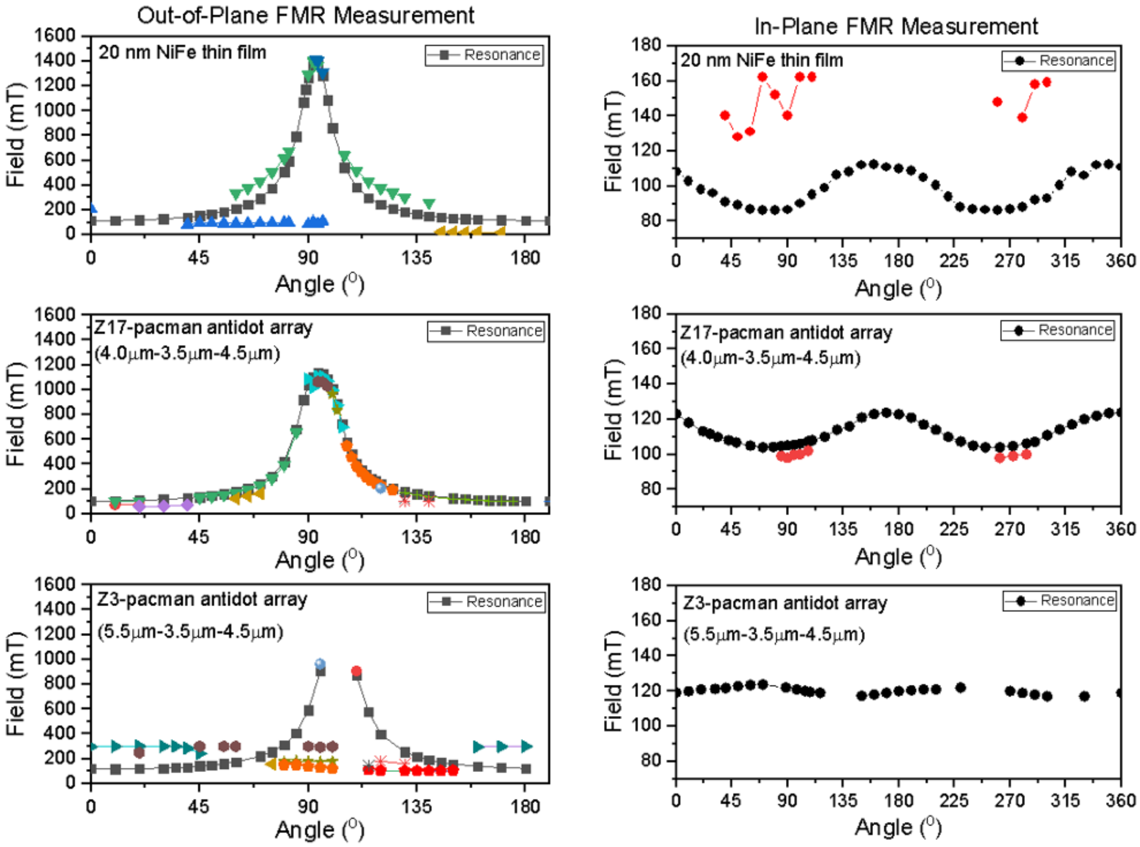

Figure 5.18. The angular variation of the resonance field in IP and OOP FMR measurement of the pacman shape antidot array with dimensions of 4 μm and 5.5 μm widths, edge to edge distances of 3.5 μm and 4.5 μm along the x and y directions.

6. MICROMAGNETIC SIMULATIONS OF NiFe DOT/ANTIDOT ARRAYS

As the dimension of materials diminishes down to the nanometer scale, the nano-size structure possesses different and new characteristics since quantum size effects start to exhibit on the surface of the sample. Simulations help to understand and choose which material and geometry are suitable for the aim of an experiment. Micromagnetics is based on the continuum theory and calculates the magnetization distribution corresponding to the change in an external field. The study of confined magnetic structures with nano/micro size yields new insight into the fundamental science, data storage applications, etc. Magnetization curves of the Permalloy (NiFe) circular dot and antidot array were investigated by means of the micromagnetic simulation program, Mumax3 [167].

6.1. Micromagnetic Simulations of NiFe Dot Arrays

The principal approach is to divide the magnetic sample into cells described by the LLG equation and the interaction with neighboring cells. According to the finite difference method used in the micromagnetic simulation, the sample geometry is divided into $N = N_x N_y N_z$ cubic cells. The cell size must be in the exchange length order of 5.7 nm for Permalloy material. The grid size and cell size were chosen in the following: The grid size was (1024, 1024, 1) and the cell size was (5×10^{-9}m, 5×10^{-9}m, 20×10^{-9}m). The radius of the dot is 3 μm. The demagnetizing field is affected by the boundaries of the pattern structure. To minimize the effect of the demagnetizing field, periodic boundary conditions were implemented in the x and y-direction, which is repeated 5 times at each side of the sample in the x and y-direction. The saturation magnetization was chosen as 8.6 $\times 10^5$ A/m and the exchange stiffness was 13 $\times 10^{-12}$ J/m, both typical values for Permalloy. The magnetization was applied uniformly along the x direction. The uniaxial anisotropy with a value of 8 $\times 10^2$ J/m^2 was defined along the x direction. The maximum applied field was 100 $\times 10^{-3}$ T with a step field of 1 $\times 10^{-3}$ T. The anisotropy, demagnetization, exchange, Zeeman, and total energy were saved when the field was applied from 0.1 T to -0.1 T and from -0.1 T to 0.1 T with a step field of 0.001 T. The hysteresis loops of the circular, pacman, and half-circular dots were shown in Figure 6.1. The coercive fields of the circle, pacman, and half-circular dots are 0.001 T, 0.002 T, and 0.008 T, respectively. This can be explained such that when the size of the dot decreases, the coercivity increases. The remnant magnetization values (M/M_s) of the circle, pacman, and half-circular dots are 0.55, 0.25, and 0.38. The field that saturates the magnetization increases from 0.012 T, 0.026 T, and 0.03 T for the circle, pacman, and half-circular dots, respectively.

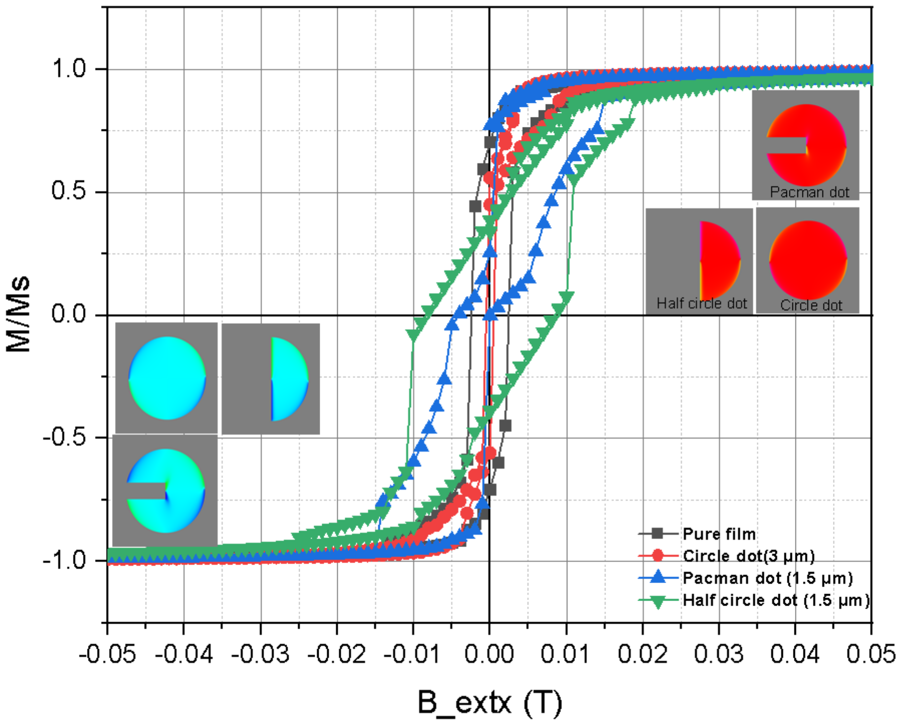

Figure 6.1. In-plane hysteresis loops of the circular dot (radius, r=1.5 μm), pacman dot (r=1.5 μm) and half-circular dot (r=1.5 μm).

The demagnetizing fields at the saturation field of 0.1 T for the pure thin film, circular, pacman, and half-circular dots are calculated as -0.008 T, -8.4×10^{-4} T, -7.12×10^{-4} T, and -4.2×10^{-4} T. When the value of the applied field decreases to zero, the demagnetizing fields for the pure thin film, circular, pacman, and half-circular dots are -0.0026 T, -3.93×10^{-4} T, -1.75×10^{-4} T, and -1.5×10^{-4} T.

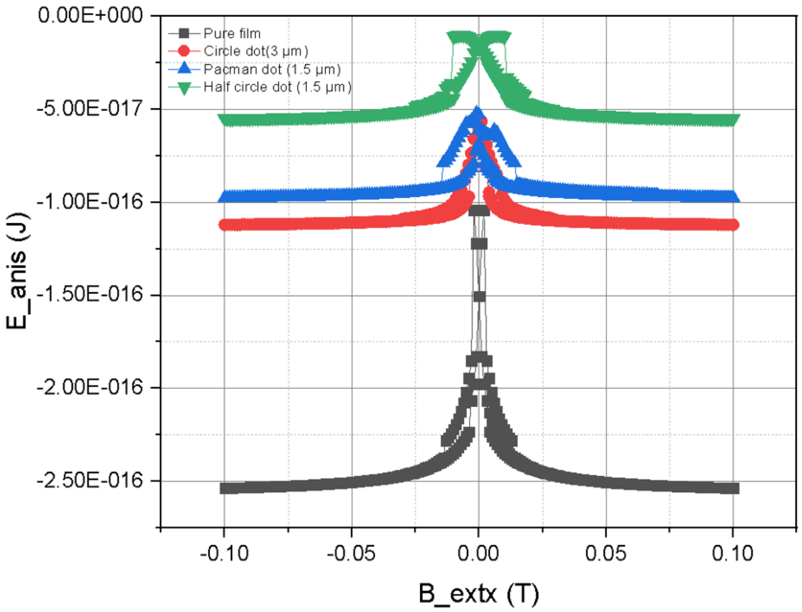

Figure 6.2. The anisotropy energies of circular dot (radius, r=1.5 μm), pacman dot (r=1.5 μm) and half-circular dot (r=1.5 μm).

The anisotropy energies of the pure thin film, circular, half-circular, and pacman dots during the reversal of the external field are shown in Figure 6.2. The anisotropy energies at the saturation field of 0.1 T for the pure thin film, circular, pacman, and half-circular dots are -2.53×10^{-16} J, -1.12×10^{-16} J, -9.76×10^{-17} J, and -5.51×10^{-17} J. In the case of zero applied field, the anisotropy energies of the pure thin film, circular, pacman, and alf-circular dots are -1.5×10^{-16} J, -5.77×10^{-17} J, -5.28×10^{-17} J, and -1.5×10^{-17} J. The demagnetizing energies of pure thin film, circular, half-circular, and pacman dots during the reversal of the external field are shown in Figure 6.3. The demagnetizing energies at the saturation field of 0.1 T for the pure thin film, circular, pacman, and half-circular dots are 1.02×10^{-15} J, 5.83×10^{-16} J, 5.19×10^{-16} J, and 6.18×10^{-16} J.

When the applied field is zero, the demagnetizing energies of the pure thin film, circular, pacman, and half-circular dots are 3.4×10^{-16} J, 2.52×10^{-16} J, 8×10^{-17} J, and 1.6×10^{-16} J.

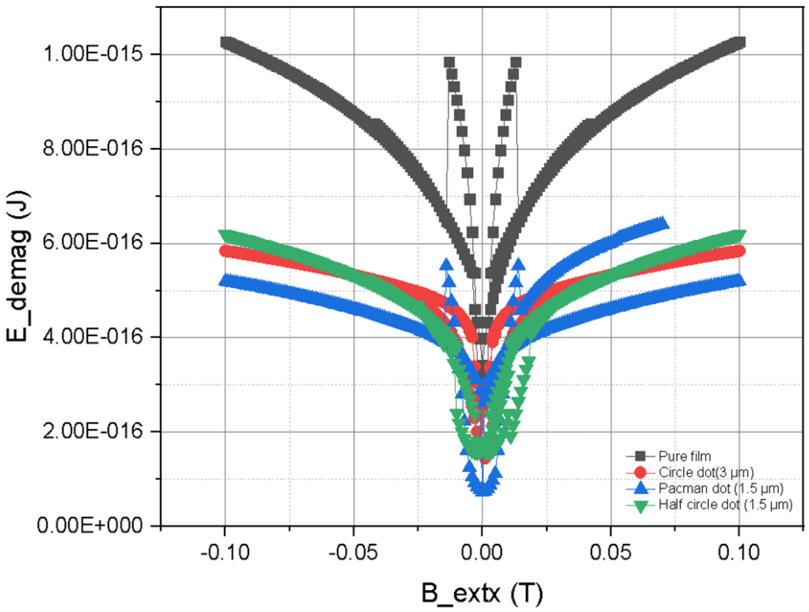

Figure 6.3. The demagnetization energies of circular dot (radius, r=1.5 μm), pacman dot (r=1.5 μm) and half-circular dot (r=1.5 μm).

The exchange energies of pure thin film, circular, half-circular, and pacman dots during the reversal of the external field are shown in Figure 6.4. The exchange energies at the saturation field of 0.1 T for the pure thin film, circular, pacman, and half-circular dots are 2.01×10^{-17} J, 3.97×10^{-18} J, 5.26×10^{-18} J, and 9.53×10^{-18} J. When the applied field is zero, the exchange energies of the pure thin film, circular, pacman, and half-circular dots are 3.1×10^{-17} J, 4.97×10^{-17} J, 2.22×10^{-17} J, and 3.97×10^{-17} J.

The Zeeman energies of pure thin film, circular, half-circular, and pacman dots during the reversal of the external field are shown in Figure 6.5. The Zeeman energies at the saturation field of 0.1 T for the pure thin film, circular, pacman, and half-circular dots are -2.73×10^{-14} J, -1.21×10^{-14} J, -1.05×10^{-14} J, and -5.9×10^{-15} J. When the applied field is zero, the Zeeman energies of the pure thin film, circular, pacman, and half-circular dots are 1.47×10^{-29} J, 5.18×10^{-30} J, 2.0×10^{-30} J, and 1.79×10^{-30} J.

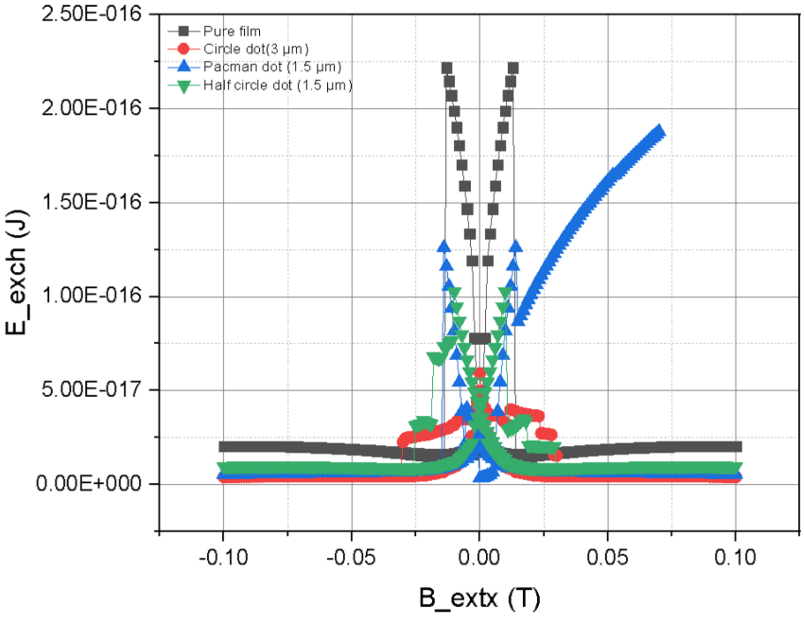

Figure 6.4. The exchange energies of circular dot (radius, r=1.5 μm), pacman dot (r=1.5 μm) and half-circular dot (r=1.5 μm).

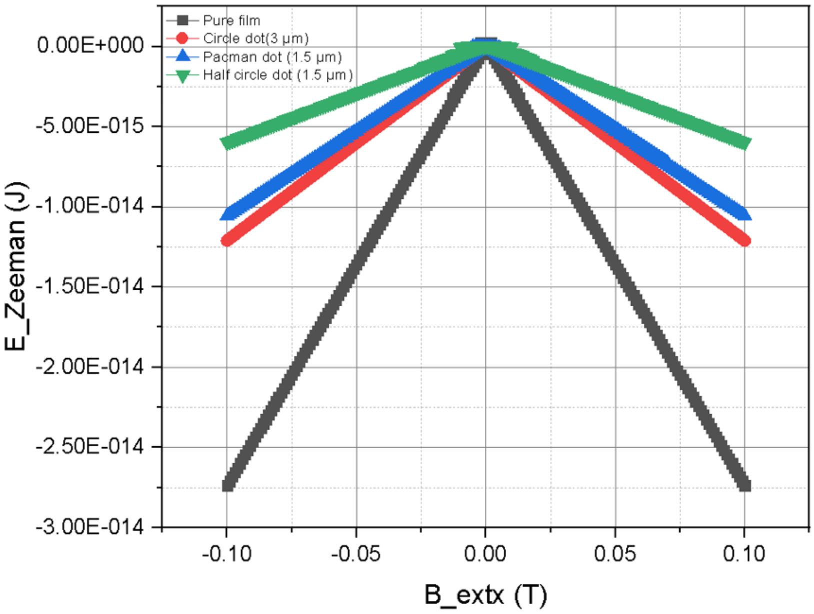

Figure 6.5. The Zeeman energies of circular dot (radius, r=1.5 μm), pacman dot (r=1.5 μm) and half-circular dot (r=1.5 μm).

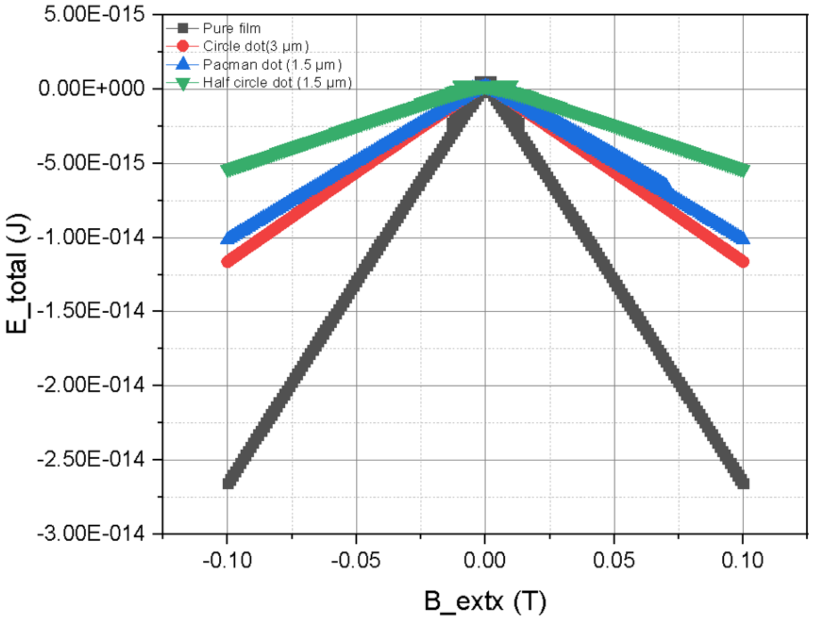

Figure 6.6. Total energies of circular dot (radius, r=1.5 μm), pacman dot (r=1.5 μm) and half-circular dot (r=1.5 μm).

The total energies of pure thin film, circular, half-circular, and pacman dots during the reversal of the external field are shown in Figure 6.6. The total energies at the saturation field of 0.1 T for the pure thin film, circular, pacman, and half-circular dots are -2.65×10^{-14} J, -1.16×10^{-14} J, -1.01×10^{-14} J, and -5.0×10^{-15} J. When the applied field is zero, the total energies of the pure thin film, circular, pacman, and half-circular dots are 2.21×10^{-16} J, 2.44×10^{-16} J, 4.9×10^{-17} J, and 1.87×10^{-16} J.

The previous simulations are performed for the single dot structures. Now, the hysteresis loops of dot array structures with a radius of 2 μm and separation distances of 2, 2.5, and 3 μm are shown in Figure 6.7. When the separation distance increases, the coercivity decreases. The coercivity for the array of the circular dots with a separation distance $(2 \times 10^{-6}\text{m}, 2 \times 10^{-6}\text{m}, 0)$ is 0.005 T, the coercivity for the array of the circular dots with a separation distance $(2.5 \times 10^{-6}\text{m}, 2.5 \times 10^{-6}\text{m}, 0)$ is 0.004 T, and the coercivity for the array of the circular dots with a separation distance $(3 \times 10^{-6}\text{m}, 3 \times 10^{-6}\text{m}, 0)$ is 0.002 T. The remnant magnetizations (M/M$_s$) are 0.85, 0.39, and 0.61 for the separation distance of $(2 \times 10^{-6}\text{m}, 2 \times 10^{-6}\text{m}, 0)$, $(2.5 \times 10^{-6}\text{m}, 2.5 \times 10^{-6}\text{m}, 0)$, and

$(3\times10^{-6}\text{m}, 3\times10^{-6}\text{m}, 0)$, respectively. The field that needs to saturate the dot array with an inter-distance of 2.5 μm is the largest. The saturation fields are 0.007, 0.04, and 0.015 for the separation distance of $(2\times10^{-6}\text{m}, 2\times10^{-6}\text{m}, 0)$, $(2.5\times10^{-6}\text{m}, 2.5\times10^{-6}\text{m}, 0)$, and $(3\times10^{-6}\text{m}, 3\times10^{-6}\text{m}, 0)$, respectively.

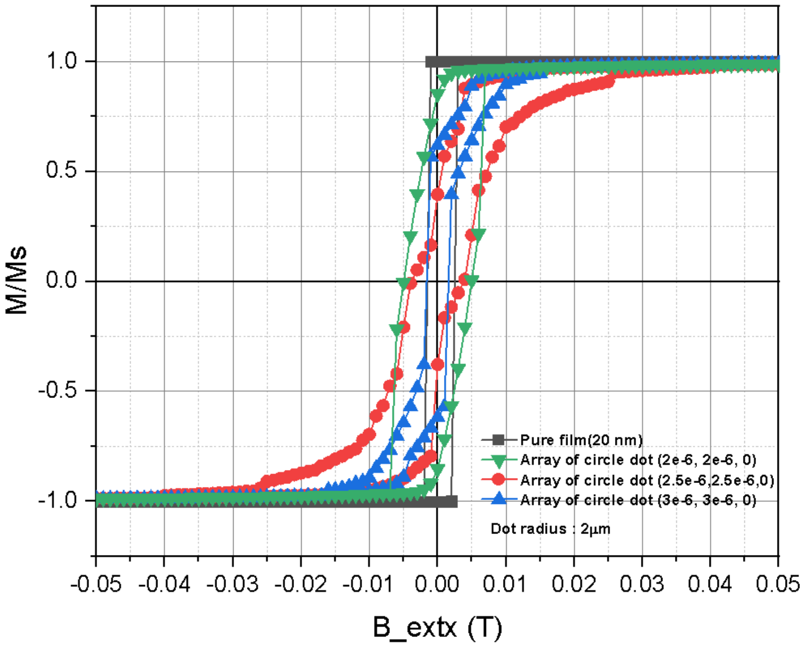

Figure 6.7. In-plane hysteresis loops of 20 nm pure NiFe thin film, an array of circular dots with a radius of 2 μm and separation distances of 2, 2.5, and 3 μm.

The anisotropy energies of the corresponding structures during the reversal process are simulated as illustrated in Figure 6.8.The anisotropy energies of the pure thin film and circular dot arrays with a radius of 2 μm and separation distances of 2, 2.5, and 3 μm at the saturation field of 0.1 T are -2.5×10^{-16} J, -1.99×10^{-16} J, -9.34×10^{-17} J, and -5.0×10^{-17} J. When the applied field is zero, the anisotropy energies of the pure thin film and circular dot arrays with a radius of 2 μm and separation distances of 2, 2.5, and 3 μm are -2.5×10^{-16} J, -1.7×10^{-16} J, -5.4×10^{-17} J, and -2.72×10^{-16} J.

The demagnetization energies of the related structures are shown in Figure 6.9. The demagnetization energies of the pure thin film and circular dot arrays with a radius of 2 μm and separation distances of 2, 2.5, and 3 μm at the saturation field of 0.1 T are 4.86×10^{-17} J, 7.93×10^{-16} J, 9×10^{-16} J, and 4×10^{-16} J. When the applied field is zero, the demagnetization energies of the pure thin film and circular dot arrays with a radius of 2 μm and separation distances of 2, 2.5, and 3 μm are 4×10^{-17} J, 5×10^{-16} J, 4×10^{-16} J, and 2.2×10^{-16} J.

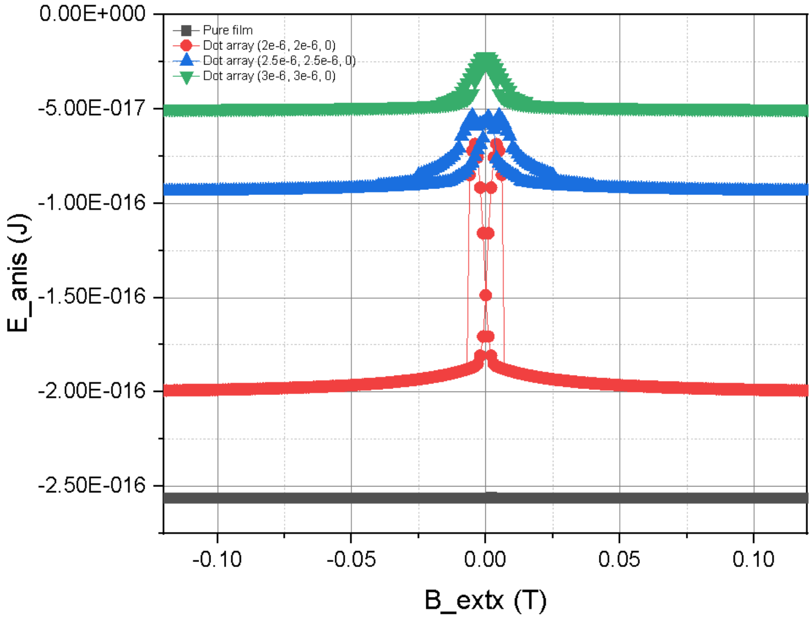

Figure 6.8. The anisotropy energies of 20 nm pure NiFe thin film, an array of circular dots with a radius of 2 μm and separation distances of 2, 2.5 and 3 μm.

The exchange energies of the related structures are shown in Figure 6.10. The exchange energies of the pure thin film and circular dot arrays with a radius of 2 μm and separation distances of 2, 2.5, and 3 μm at the saturation field of 0.1 T are 1.72×10^{-32} J, 1.33×10^{-17} J, 1.22×10^{-17} J, and 4.6×10^{-18} J. When the applied field is zero, the exchange energies of the pure thin film and circular dot arrays with a radius of 2 μm and separation distances of 2, 2.5, and 3 μm are 9×10^{-29} J, 1.6×10^{-17} J, 7×10^{-17} J, and 3.26×10^{-17} J. The Zeeman energies of the related structures are shown in Figure 6.11. The Zeeman energies of the pure thin film and circular dot arrays with a radius of 2 μm and separation distances of 2, 2.5, and 3 μm at the saturation field of 0.1 T are -2.75×10^{-14} J, -2.14×10^{-14} J, -1.0×10^{-14} J, and -5.3×10^{-15} J. When the applied field is zero, the Zeeman energies of the pure thin film and circular dot arrays with a radius of 2 μm and separation distances of 2, 2.5, and 3 μm are -2.7×10^{-16} J, -1.9×10^{-16} J, -5.7×10^{-17} J, and -3.6×10^{-17} J.

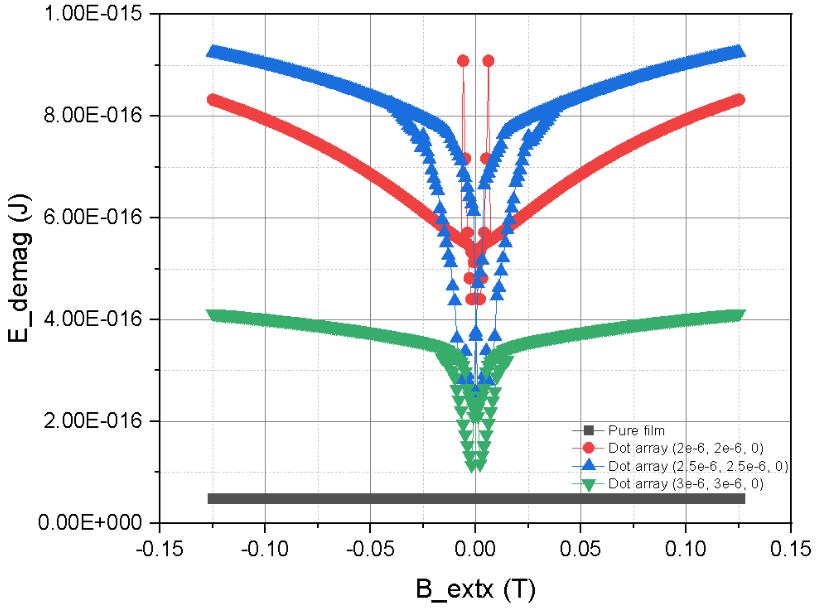

Figure 6.9. The demagnetization energies of 20 nm pure NiFe thin film, an array of circular dots with a radius of 2 μm and separation distances of 2, 2.5 and 3 μm.

The total energies of the related structures are shown in Figure 6.12. The total energies of the pure thin film and circular dot arrays with a radius of 2 μm and separation distances of 2, 2.5, and 3 μm at the saturation field of 0.1 T are -2.77×10^{-14} J, -2.08×10^{-14} J, -9×10^{-15} J, and -5.0×10^{-15} J. When the applied field is zero, the total energies of the pure thin film and circular dot arrays with a radius of 2 μm and separation distances of 2, 2.5, and 3 μm are -4×10^{-16} J, 1.6×10^{-16} J, 4×10^{-16} J, and 1.96×10^{-16} J.

Next, the simulation results for the circular NiFe dot array and circular antidot array will be discussed. The hysteresis loops for the pure thin film, circular dot array, and circular antidot array with the same radius size of 2 μm are given in Figure 6.13. The antidot structure causes the coercivity increases due to the domain formations between the antidots.

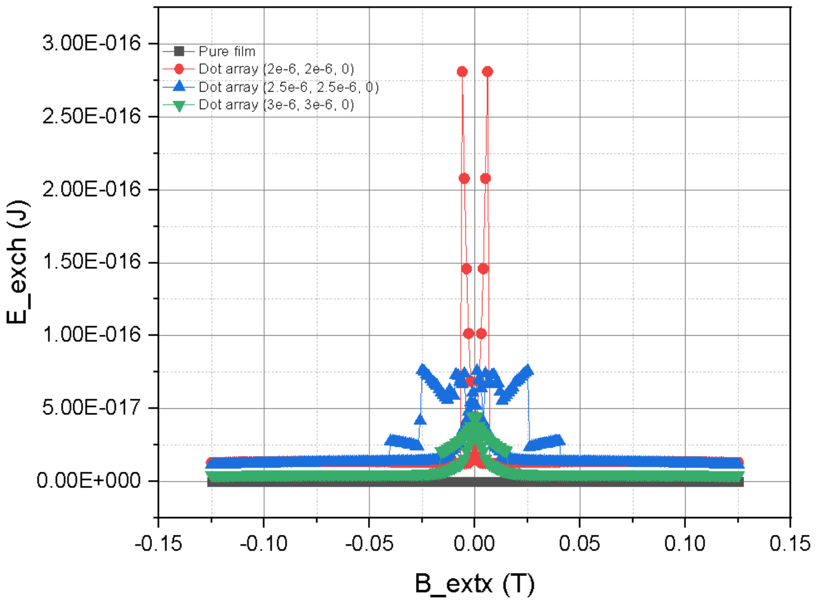

Figure 6.10. The exchange energies of 20 nm pure NiFe thin film, an array of circular dots with a radius of 2 μm and separation distances of 2, 2.5, and 3 μm.

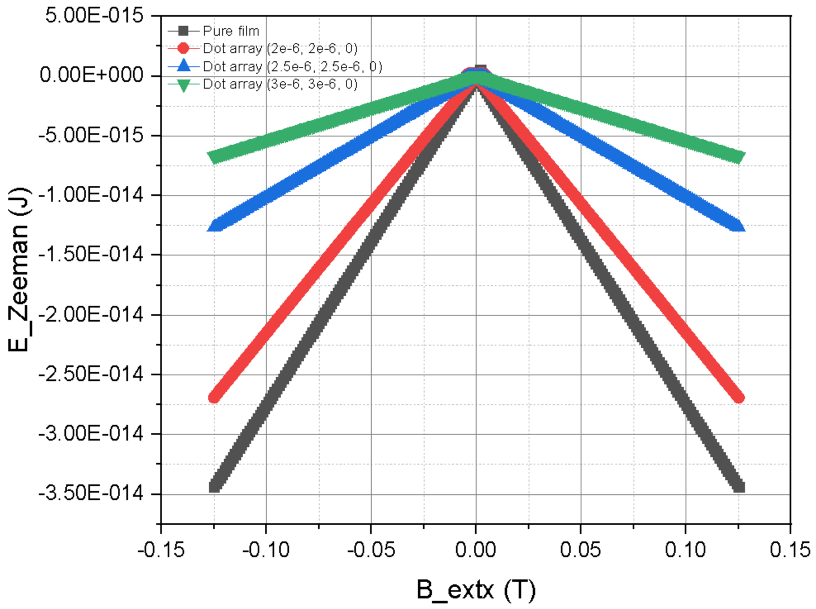

Figure 6.11. The Zeeman energies of 20 nm pure NiFe thin film, an array of circular dots with a radius of 2 μm and separation distances of 2, 2.5 and 3 μm.

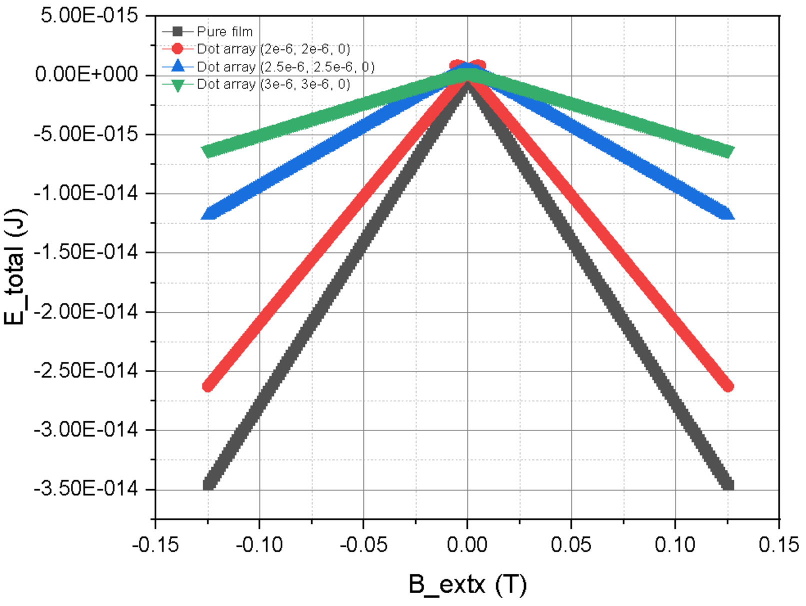

Figure 6.12. The total energies of 20 nm pure NiFe thin film, an array of circular dots with a radius of 2 μm and separation distances of 2, 2.5 and 3 μm.

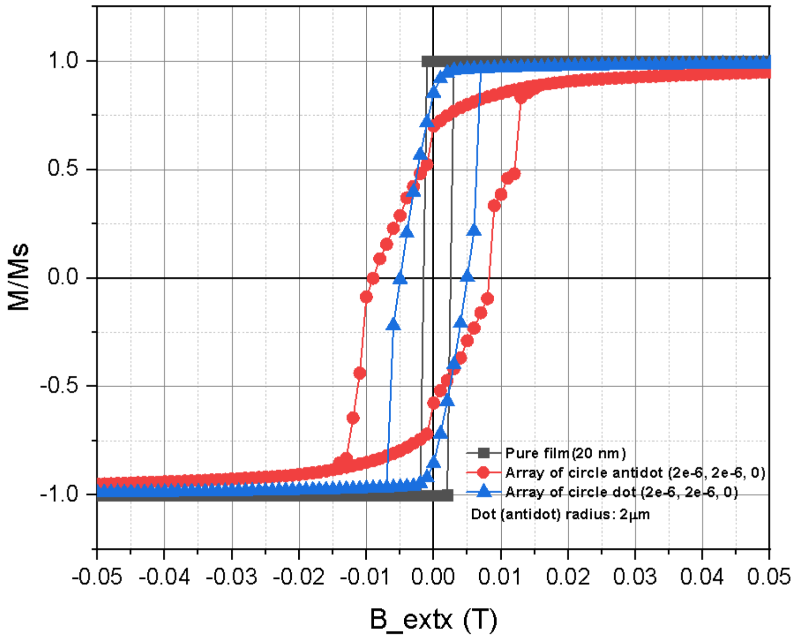

Figure 6.13. In-plane hysteresis loops of 20 nm pure NiFe thin film, an array of circular dots (radius, r=2 μm), and an array of circular antidots (r=2 μm).

The coercive fields for the circular dot and antidot arrays are 0.0049 T and 0.009 T, respectively. The remnant magnetization of the antidot array decreases with respect to the dot array and the pure film. The remnant magnetizations are 0.85 and 0.70 for the circular dot and antidot arrays. The saturation fields are 0.85 T and 0.70 T for the circular dot and antidot arrays.

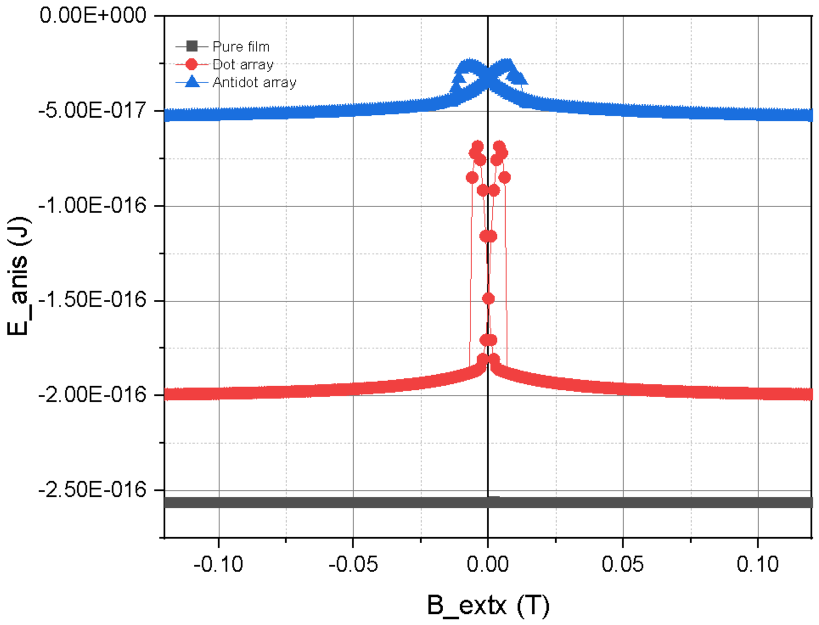

Figure 6.14. The anisotropy energies of 20 nm pure NiFe thin film, an array of circular dots (radius, r=2 μm), and an array of circular antidots (r=2 μm).

The anisotropy energy of the pure thin film, circular dot array, and circular antidot array are shown in Figure 6.14. The anisotropy energies of the pure thin film, circular dot array, and circular antidot array with the same radius size of 2 μm at the saturation field of 0.1 T are -2.56×10^{-16} J, -1.98×10^{-16} J, and -5.24×10^{-17} J. When the applied field is zero, the anisotropy energies of the pure thin film, circular dot array, and circular antidot array with the same radius size of 2 μm are -2.56×10^{-16} J, -1.48×10^{-16} J, -3.26$\times 10^{-17}$ J. The demagnetization energy of the pure film, circular dot array, and circular antidot array are shown in Figure 6.15. The demagnetization energies of the pure thin film, circular dot array, and circular antidot array with the same radius size of 2 μm at the saturation field of 0.1 T are 4.86×10^{-17} J, 7.93×10^{-16}

J, 7.3×10^{-16} J. When the applied field is zero, the demagnetization energies of the pure thin film, circular dot array, and circular antidot array with the same radius size of 2 μm are 4.8×10^{-17} J, 5.12×10^{-16} J, 3.93×10^{-16} J. The exchange energy of the pure film, circular dot array, and circular antidot array are shown in Figure 6.16.

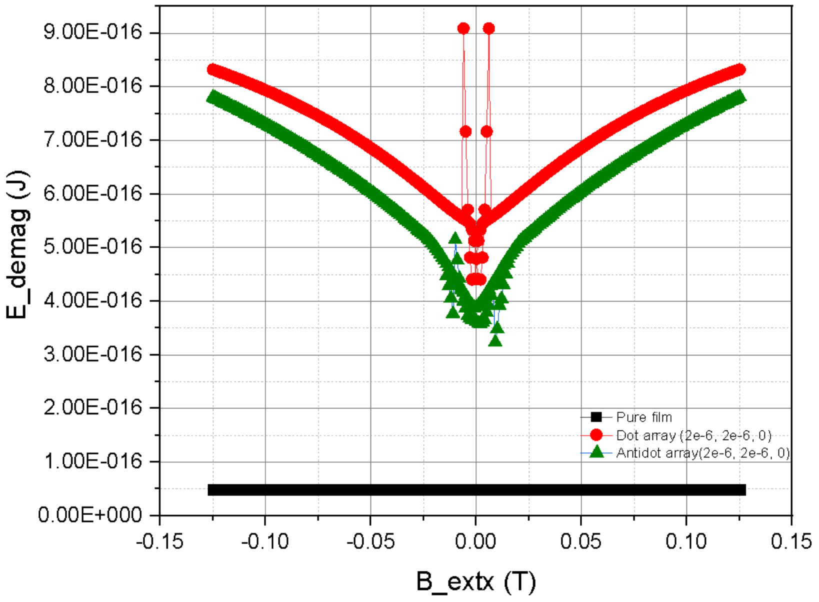

Figure 6.15. The demagnetization energies of 20 nm pure NiFe thin film, an array of circular dots (radius, r=2 μm), and an array of circular antidots (r=2 μm).

The exchange energy of the pure film, circular dot array, and circular antidot array are shown in Figure 6.15. The exchange energies of the pure thin film, circular dot array, and circular antidot array with the same radius size of 2 μm at the saturation field of 0.1 T are 1.7×10^{-32} J, 1.3×10^{-17} J, 1.7×10^{-17} J. When the applied field is zero, the exchange energies of the pure thin film, circular dot array, and circular antidot array with the same radius size of 2 μm are 9.6×10^{-29}, 1.68×10^{-17}, 4.23×10^{-17} J.

The Zeeman energy of the pure film, circular dot array, and circular antidot array are shown in Figure 6.17. The Zeeman energy of the pure film, circular dot array, and circular antidot array are shown in Figure 6.15. The Zeeman energies of the pure thin film, circular dot array, and circular antidot array with the same radius size of 2 μm at the saturation field of 0.1 T are -2.7×10^{-14} J, -2.1×10^{-14} J, -5.7×10^{-15} J.

When the applied field is zero, the Zeeman energies of the pure thin film, circular dot array, and circular antidot array with the same radius size of 2 μm are -2.7×10^{-16} J, -1.98×10^{-16} J, -4.28×10^{-17} J.

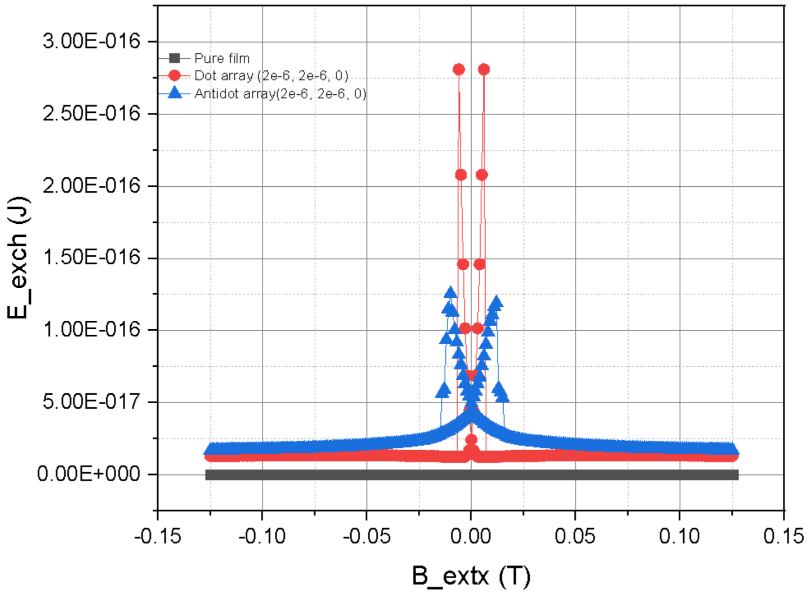

Figure 6.16. Exchange energy of 20 nm pure NiFe thin film, an array of circular dots (radius, r=2 μm), and an array of circular antidots (r=2 μm).

The total energy of the pure film, circular dot array, and circular antidot array are shown in Figure 6.18. The total energy of the pure film, circular dot array, and circular antidot array are shown in Figure 6.15. The total energies of the pure thin film, circular dot array, and circular antidot array with the same radius size of 2 μm at the saturation field of 0.1 T are -2.77×10^{-14} J, -2×10^{-14} J, -5×10^{-15} J. When the applied field is zero, the total energies of the pure thin film, circular dot array, and circular antidot array with the same radius size of 2 μm are -4.8×10^{-16} J, 1.6×10^{-16} J, 3.5×10^{-16} J.

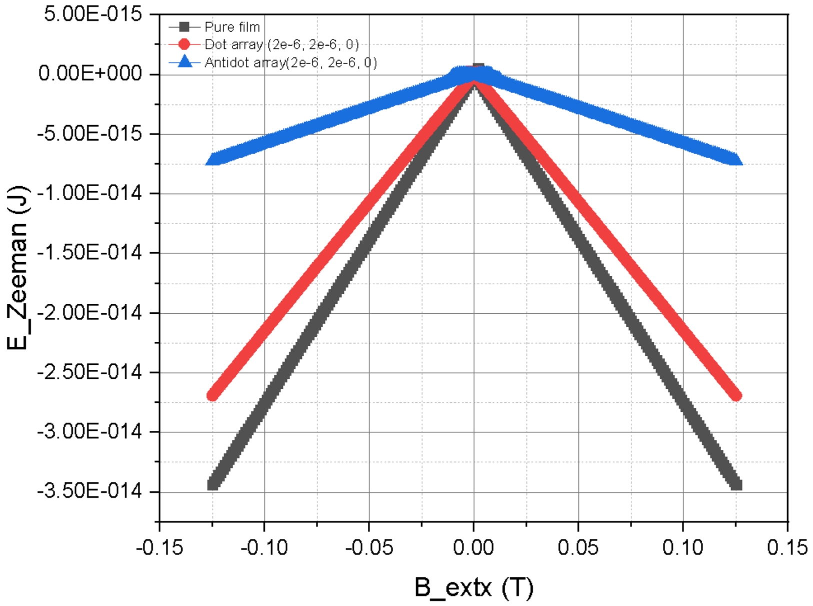

Figure 6.17. The Zeeman energies of 20 nm pure NiFe thin film, an array of circular dots (radius, r=2 μm), and an array of circular antidots (r=2 μm).

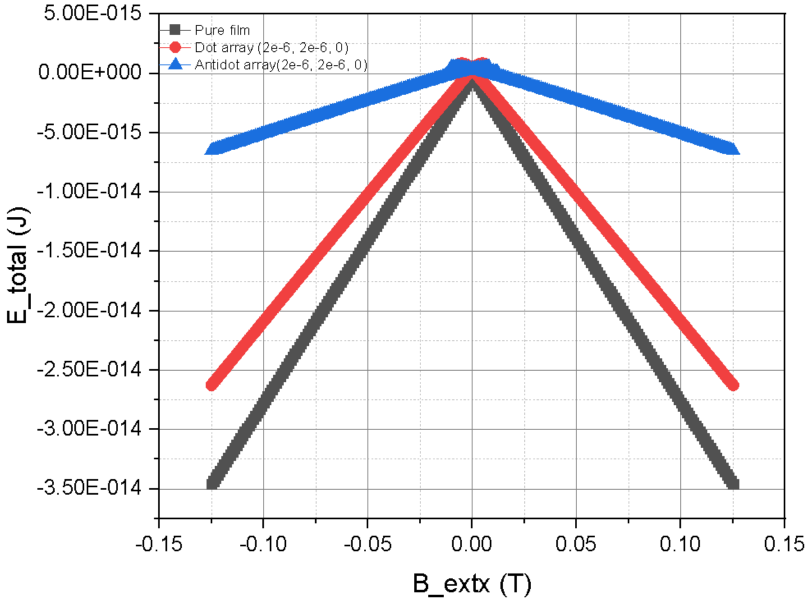

Figure 6.18. Total energy of pure NiFe thin film, the array of circular dots (radius, r=2 μm), and the array of circular antidots (r=2 μm).

6.2. Micromagnetic Simulations of NiFe Ring-Shaped Dot Arrays

Magnetic nanostructures raise a high interest for fundamental research and applications like nonvolatile magnetic random access memory (MRAM) [1], magnetic read heads [2], and ultrahigh-density data storage in which stable and reproducible switching is required. A homogenous magnetization takes place within the structure, but at the edges, the magnetization aligns according to the shape of the structure. Ferromagnetic ring structures enable small stray fields and there is no domain at the edge of the ring, therefore can be used in MRAM applications [5]. The film thickness, width, and diameter of the ring also have an effect on the formation of the domain types [6]–[10]. Two domain types occur in ferromagnetic rings, which are called the vortex state where the magnetization is circumferential, and the onion state with two domain walls oriented 180° with respect to each other. Different domain wall switching mechanisms occur from single onion to reverse onion, onion to a vortex, vortex to reverse onion, and triple vortex core switching [168–170] which include nucleation-free, nucleation of domains or vortex cores, etc. The switching from the vortex to the onion state occurs due to the nucleation and propagating magnetic domain at the half of the ring which is magnetized antiparallel to the applied magnetic field direction. The transition from the onion state to the vortex state is observed when one of the head-to-head or tail-to-tail domain walls in the onion state displaces and is annihilated with the opposite wall. Due to the Zeeman interaction, the spins in the ring dots align with the same direction of the external field so that the energy is minimum. When the field increases, the number of magnetic moments which are parallel to the external field increases. While so, the vortex core moves from the center to the border of the ring dot. The field that removes the vortex core is called the annihilation field. The new state becomes the collinear state. After the collinear state, the magnetic field is reduced and at a certain field which is named as nucleation field, the vortex state is observed again.

Figure 6.19 shows the vortex and the onion state, and the color codes represent the directions of spins. For example, the red and light blue colors refer to the spins pointing along the +x and -x directions, respectively.

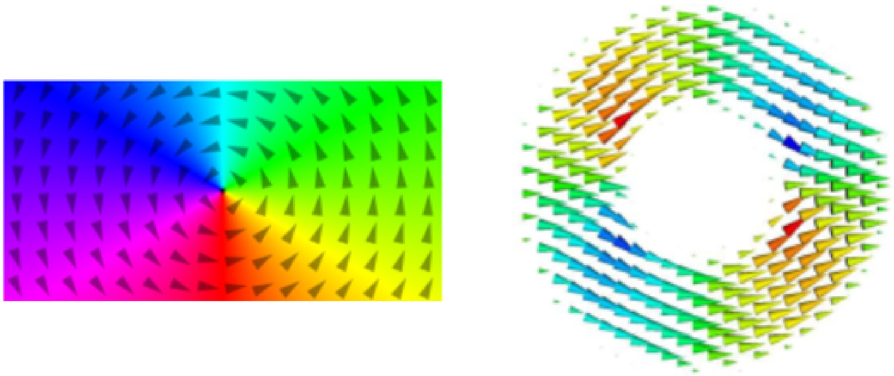

Figure 6.19. Vortex (left) and onion (right) magnetization states. [167].

To simulate the domain configurations, Mumax3 was employed on the defined ring dots with different widths and thicknesses. The parameters for Permalloy are such that the saturation magnetization is 800×10^3 A/m and the exchange stiffness constant is 13×10^{-12} J/m. The initial magnetization was set to random magnetization and relaxed to the minimum energy state. The applied maximum field was 100×10^{-3} T, with a step of 1×10^{-3} T along the +x direction. The magnetization curve of 30 nm thick 2 μm-width NiFe ring dot is shown in Figure 6.20.

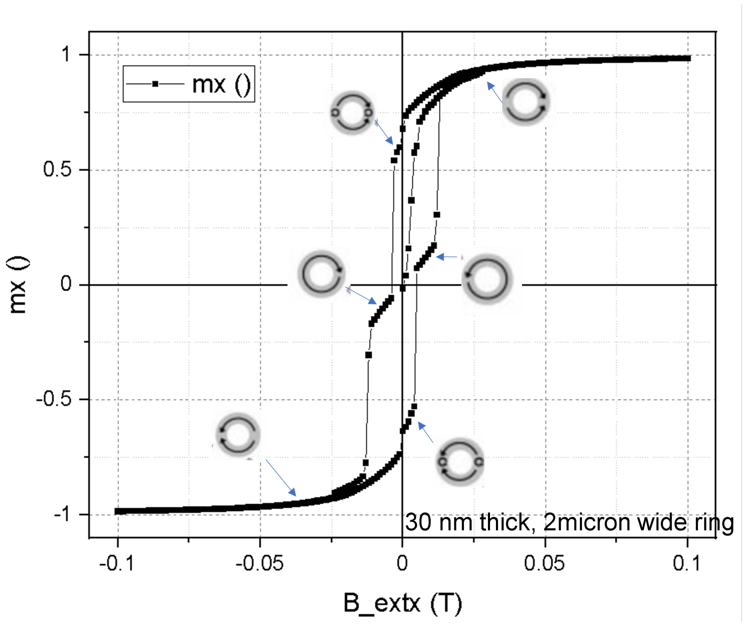

Figure 6.20. Magnetization curves and vortex, onion domains in 30 nm thick and 2 μm width NiFe ring-shaped dot.

Due to the shape effect, there are several domain states occurring with respect to the strength of the field and the direction of the field. At 0.1 T, all the spins within the ring orient in the +x directions like a single domain structure. In the reversed direction, while approaching the zero field value, a number of spins tend to deviate from the +x direction. At 0.007 T, an onion state is shown in Figure 6.21. Although the majority of the spins are still in the +x direction at remanence, two vortices appear at both sides of the onion state at 0.00 T. When the field increases in the reverse direction (-0.003 T), the vortex center begins to shift to the edges and spins start to switch to the -x direction. At -0.028 T, we see that the vortexes disappear and only the reverse onion state remains. The domain configurations of 30 nm and the 2-μm width-ring dot are shown in Figure 6.20.

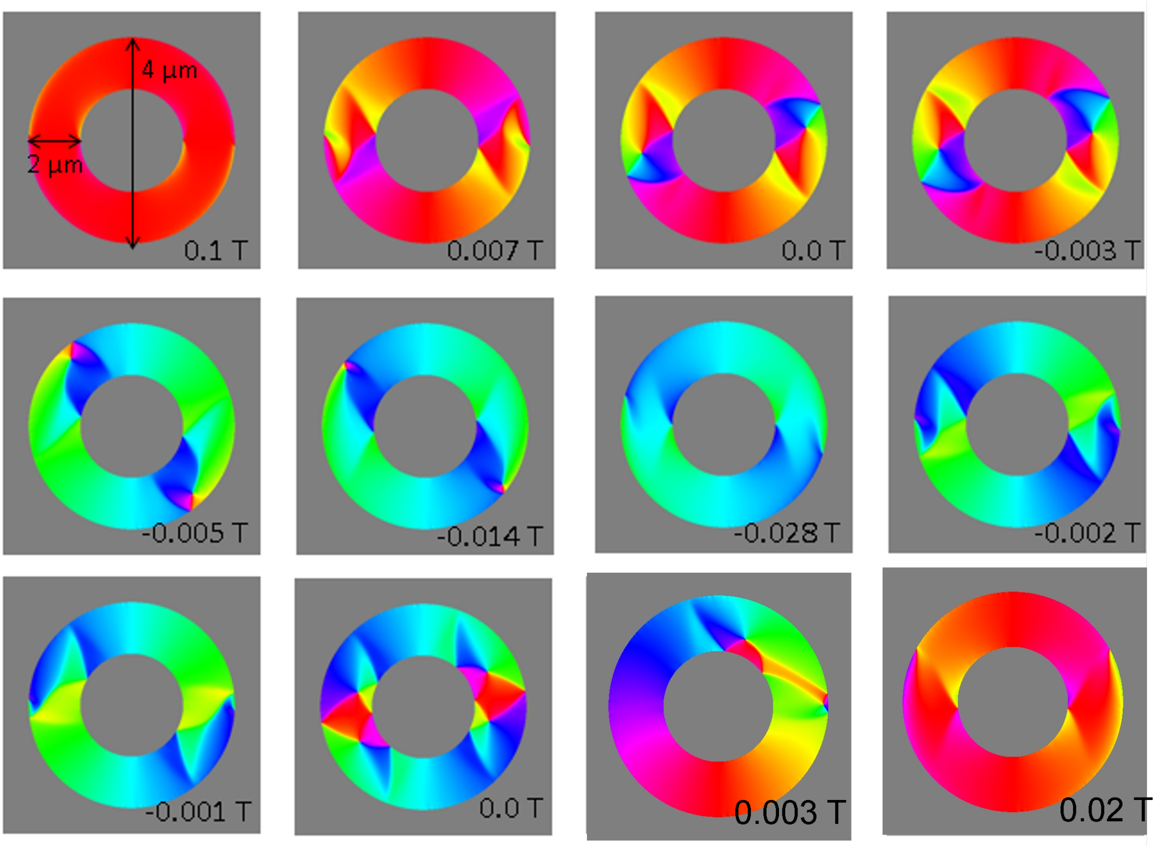

Figure 6.21. Domain configurations of 30 nm thick and 2 μm-width NiFe ring-shaped dot during the reversal of the field.

When the field goes from 0.1 T to -0.1 T, several plateaus emerge, which correspond to different spin configurations. The domain type in the ring dot, until the field is zero, is the onion state. At the remnant state, two vortices appear on both sides of the ring in Figure 6.21. One of the vortex structures on the left side is composed of spins curling around the center clockwise, and the other vortex has counterclockwise curling spins around the vortex center. During this process, a transition from the onion state to two vortex-onion states takes place and the two vortices do not have the same helicity. In the reverse field, the two vortex starts to move to the edge of the ring at -0.003 T and disappears at -0.0028 T leaving the place to another reverse onion state with the majority of the spins aligned in the -x direction. When the field is applied from -0.1 T to +0.1 T, the reverse onion state is still there, however, at the remnant state, two vortices reform on both sides of the ring with the same helicity.

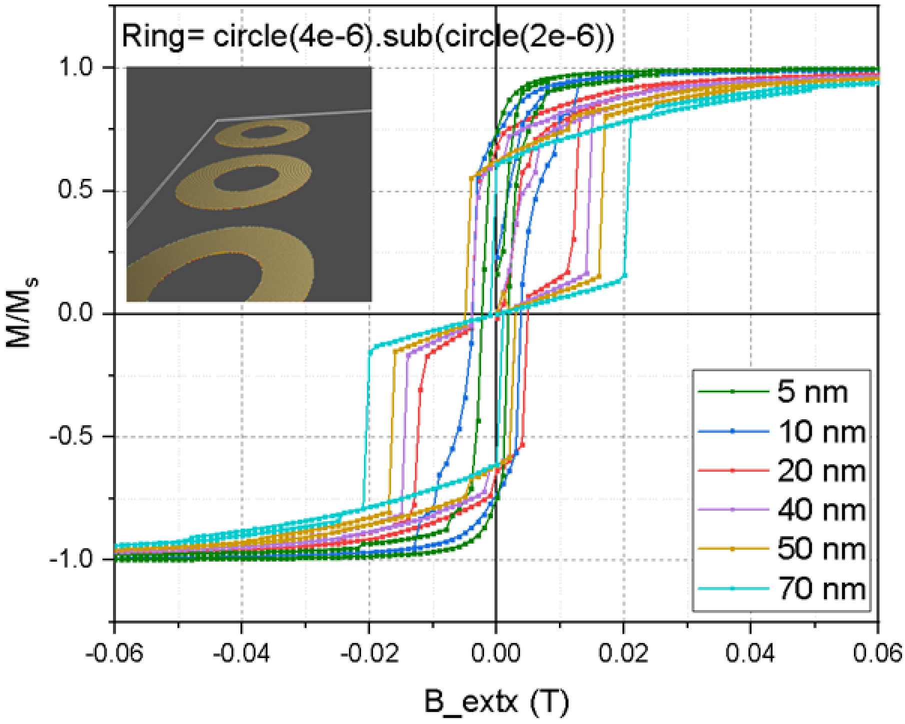

Figure 6.22. The hysteresis loops of the ring dot with a width of 2 μm with a range of thickness between 5 nm and 70 nm.

The left vortex has a counterclockwise curling of the spins, and the right vortex follows the same curling direction. Now this time, there is another state between the two vortices-onion states and the onion state, which is different from the first reversal path. A counterclockwise flux closure state occurs around 0.003 T. Then at 0.02 T, the flux-closure state transforms to the onion state again. In the first reversal path, the flux closure state does not occur due to the different helicities of the vortices. When the helicities are the same, the flux closure state is able to form. We can say that the helicity of the two vortices determines the formation of flux-closure states in the reversal process.

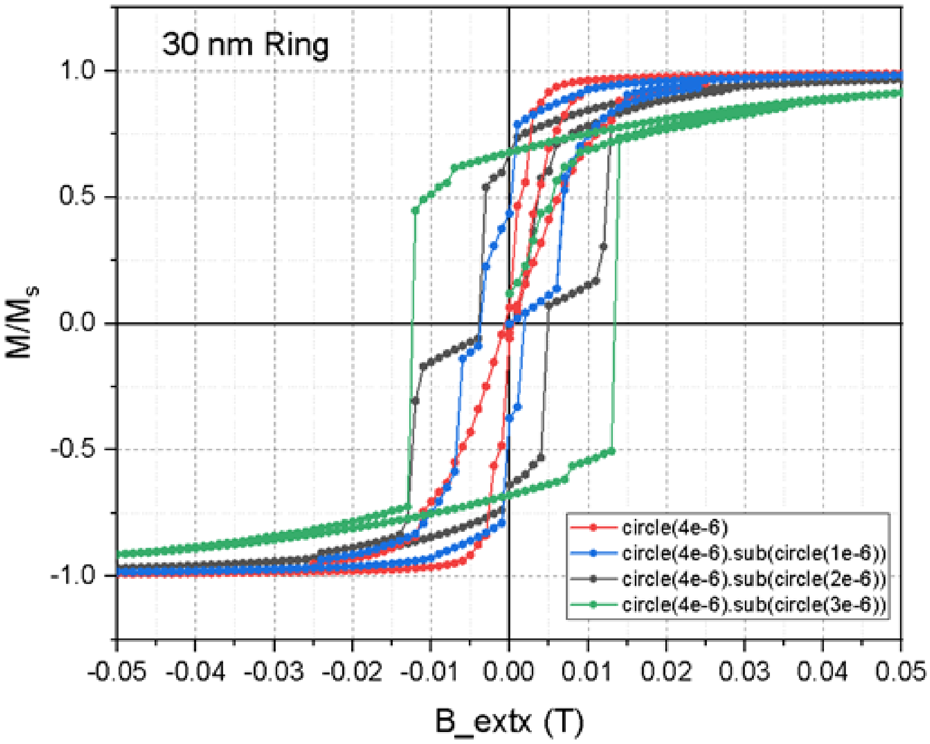

Figure 6.23. The hysteresis loop of 30 nm circular and ring dot structures with a width of 3 μm, 2 μm, and 1 μm.

To understand the effect of the thickness on the hysteresis loop profile of the ring dot, various thicknesses were simulated, keeping the size of the ring fixed at 2 μm. The thickness of the 2-μm width-ring structure ranges from 5 nm to 70 nm, and the magnetization curves of all the thicknesses are shown in Figure 6.22. The coercivity decreases with increasing thickness, and the remnant magnetization decreases, as well. The loops get wider from 5 nm to 70 nm. The transition between the domains gets slower and needs a large range of applied fields, for example, a 70 nm ring dot needs 0.002 T to shift to another domain type, while a 20 nm ring dot needs 0.001 T. In addition, larger fields are required to reach the magnetization saturation for the thicker dots.

The effect of the width of the ring in the magnetization reversal of the ring dots is studied by introducing different widths at the same thickness. The magnetization curves of a circle dot with a diameter of 4μm and ring dot structures with a width of 3 μm, 2 μm and 1 μm and with the same thickness of 30 nm are shown in Figure 6.23. From the circular to the 1 μm-width ring, the coercivity increases, and the remnant magnetization increases.

6.3. Micromagnetic Simulations of 3D NiFe Dot Array

Magnetic nanocaps (i.e. sphere, hemisphere) as a third dimension contribute additional magnetic interactions to a planar magnetic system. Exchange interaction and magnetization reversal exhibit modified characteristics with respect to a flat geometry. Curvature in magnetic surfaces induces a curvature-induced magnetic anisotropy and an effective Dzyaloshinskii–Morita interaction (DMI). The curved surface of a magnetic film possesses magnetic vortices, which are crucial for magnetic logic and memory applications. Curvature modifies the vortex structure in soft magnetic spherical shells. The individual and closely packed array of spherical magnetic caps show a vortex ground state. Similarly, the hemispherical magnetic caps have magnetic phase transitions such as onion and vortex states. Although 3D patterned bulk structures were used extensively in optic applications, arrays of nanoscale 3D structures need further research in magnetism since magnetic properties can be altered due to the curvature of the magnetic films. In this section, three-dimensional (3D) structures will be examined. The hemispherical shell dot array was produced by lithography and RF sputtering method. The diameter was determined to be 4 μm and the thickness was 20 nm. The dots did not touch each other with a separation distance of 4 μm. The magnetization of 20 nm pure thin film and hemisphere shell array film was measured by Vibrating Sample Measurement (VSM).

As shown in Figure 6.24, the magnetic easy axis for the pure and patterned film aligns in the film plane. The coercive field for pure NiFe thin film is 11 mT and the coercive field for NiFe hemisphere shell array is 21 mT. The hemispherical shell dot array shows a harder magnetic character than the pure thin film. The micromagnetic simulation of the hysteresis curve for the NiFe hemisphere array was employed by the micromagnetic simulation program, Mumax3. The diameter of hemisphere (D) is 1 μm; thickness (d) is 20 nm; the dimension of cell size is less than the exchange length for Permalloy which is 3.6 nm.

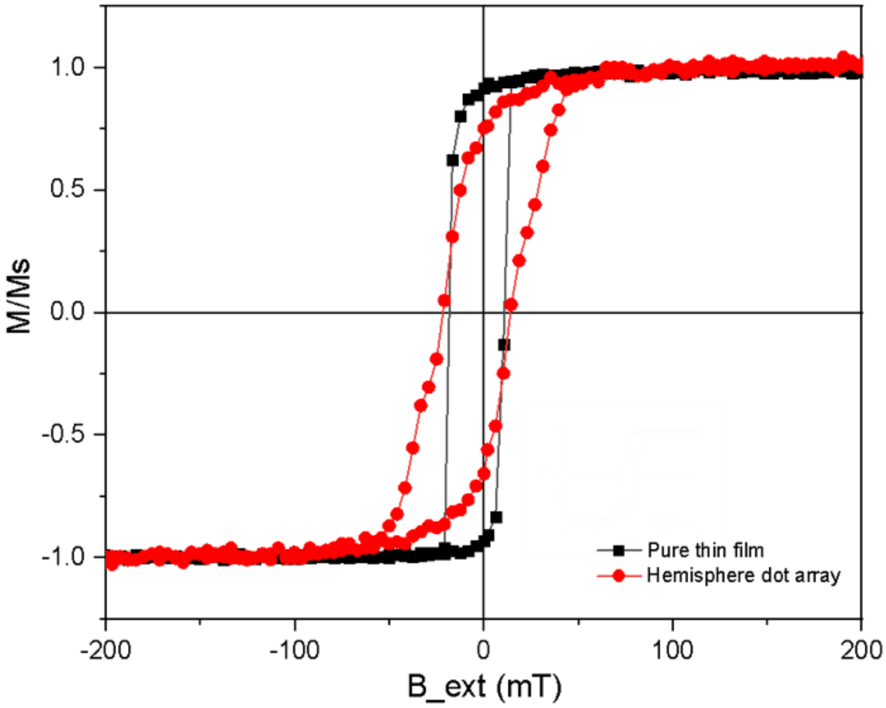

Figure 6.24. The experimental magnetization curves of an array of hemisphere dot array and pure NiFe thin film in the OOP measurement.

The simulations were performed using the Permalloy material parameters $M_{\text{sat}} = 8.6 \times 10^5$ A/m, exchange stiffness constant $A = 13 \times 10^{-12}$ J/m, and $K = 0$ J/m^3. The computations were done using the Landau–Lifshitz–Gilbert equation $d\mathbf{M}/dt = -|\gamma|\mathbf{M} \times \mathbf{H}_{eff} - \frac{|\gamma|}{M_s} M \times (M \times H_{eff})$. The simulation started with a random magnetization and minimized the total energy of the system. Then, an external field was applied to the defined geometry from 0.15 T to -0.15 T by 0.001 T step fields and the magnetization was recorded. Again, from -0.15 T to 0.15 T, the magnetization was saved. In addition, the same parameters were employed for the pure thin film. The simulated magnetization reversal mechanism for the pure and patterned thin film was shown in Figure 6.25. The hysteresis curves obtained from the simulation program have similar characteristics to the experimental magnetization curves. The magnetization profile across the curved hemisphere surface was shown in the subsets of Figure 6.25.

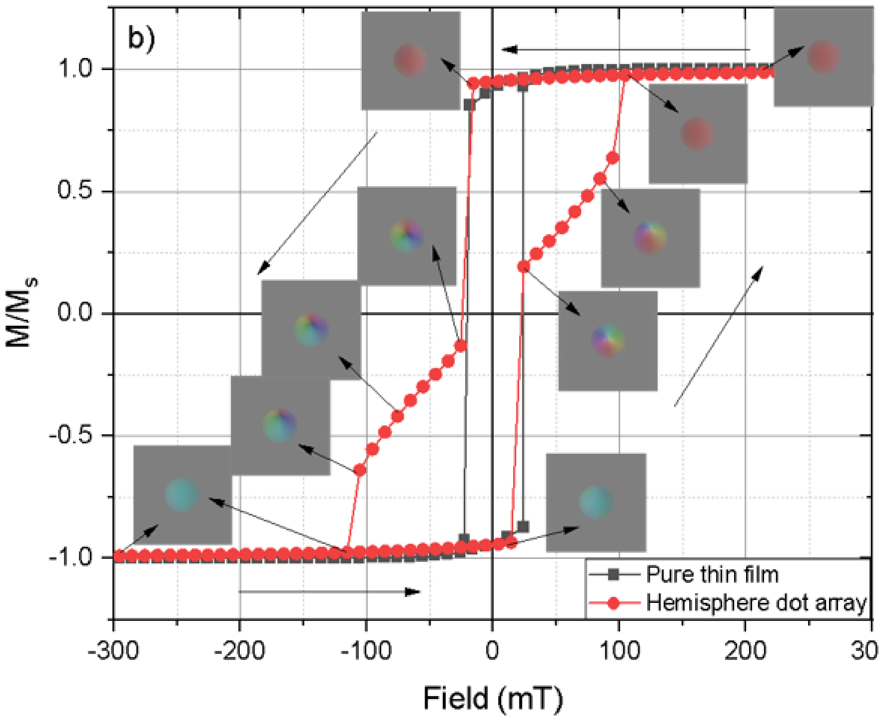

Figure 6.25. The simulated magnetization curves of a hemisphere dot array and pure NiFe thin film in the OOP measurement.

The simulation result has similar characteristics to the experimental magnetization measurements. The simulated coercivity is 19 mT and 25 mT for the pure thin film and hemisphere dot array, respectively. The hemispheres have the magnetic configuration of the vortex state which is defined by two characteristics, chirality, and polarity. Chirality is for the magnetic moments circling clockwise or anti-clockwise in the dot plane, and polarity represents the magnetic moments at the dot center pointing up or down [13]. At 300 mT, all the magnetic moments align along the applied field at the +x direction (red), forming a saturation state. When the field decreases to zero, the magnetic moments begin to deviate from the saturation and transform to the vortex state at- 25 mT. In the vortex configuration, the spin moments circle around the dot center clockwise, with a negative chirality, and spins at the dot center force each other to orient down with a negative polarity due to the exchange interaction. When the field increases in the reverse direction, the center of the vortex state shifts to the edge of the hemisphere (-105 mT) and returns to the negative saturation with all the spin moments antiparallel to the applied field (- 115 mT). When the field is reversed, the vortex magnetization reemerges with a positive chirality and a positive polarity at 25 mT. The vortex core moves to the edge when the field goes to 94 mT and further increase of the field gives the saturation magnetization at 104 mT. In the FMR spectrum of the 20 nm NiFe hemisphere array at the angle of 0 °, the spin wave mode at the shoulder of the main mode can correspond to the vortex magnetization.

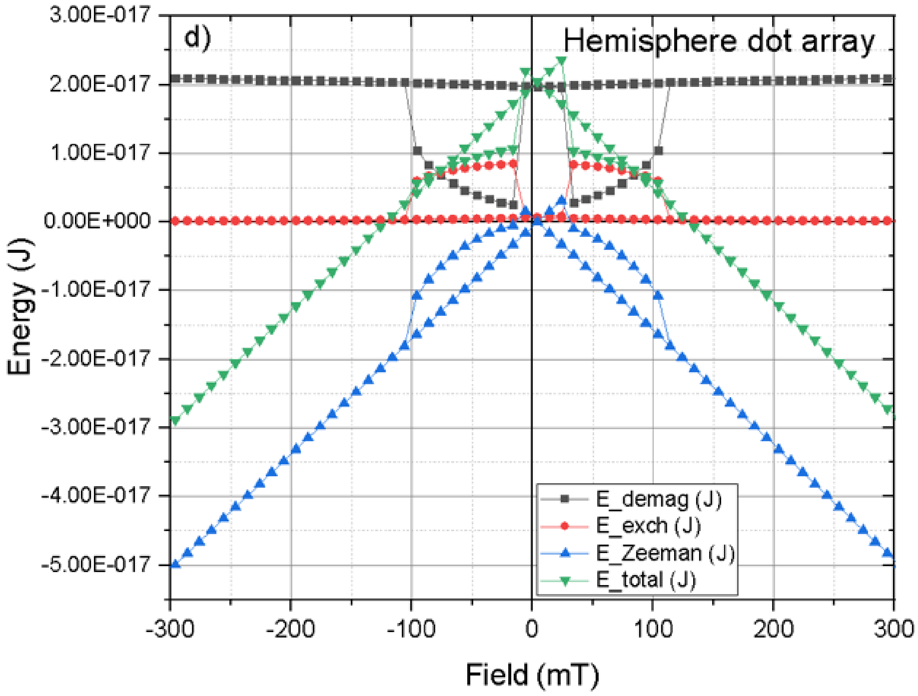

Figure 6.26. The calculated energy terms of a hemisphere dot array.

The total energy of the system used in the simulation program is described as

$$E(m) = \int \{A(\nabla m)^2 - \mu_0 M \cdot H_{ext} - \mu_0/2M \cdot H_{demag} + \text{crystal anisotropy}\} \quad d^3r, \quad (6.1)$$

where E is the total energy, m is the magnetization, the first term is the Exchange, the second term is the Zeeman, the third term is the demagnetization energy, and the last term is the crystalline anisotropy. The last term was neglected. The variation of demagnetization, exchange, Zeeman, and total energy regarding the change in the external field applied in the x direction from 0.3 T to -0.3 T and vice versa was represented in Figure 6.26. Demagnetization is the governing energy term among the other energies at the saturation state. When reaching the remanence, demagnetization energy decreases while the Zeeman and exchange energies increase. The energy values of the pure thin film are larger than the hemisphere array due to the less amount of magnetic film on the dot array. The total energy in pure thin film at saturation is around -4 × 10^{-16} J while it is -3 × 10^{-17} J for the hemisphere dot array. For the hemisphere dot array, demagnetization energy is 2.09 *times* 10^{-17} J at the saturation magnetization and decreases when the field goes to zero. Meanwhile, the exchange energy is less than the demagnetization energy for a magnitude of order two but increases from 1.6 × 10^{-19} J to 7.07 × 10^{-19} J. In addition, the Zeeman energy increases gradually when approaching the zero field. At the vortex configuration (-25 mT), while the demagnetization energy gets the minimum value (2.9 × 10^{-18} J), the exchange energy value becomes the maximum (8.51 × 10^{-18} J). As the core of the vortex shifts to the edge, demagnetization energy increases while the exchange energy decreases. At -76 mT, these two energy becomes equivalent (6.86 × 10^{-18} J) and after this point, demagnetization energy exceeds the exchange energy. At -106 mT, the core reaches the edge and completely vanishes after -115 mT. Then the spins all orient along the inverse field direction, resulting in the negative saturation (-300 mT). The demagnetization energy reaches 2.09 × 10^{-17} J which is larger than the other energies. When the field is zero, the total energy is maximum. After the vortex forms at 25 mT, the demagnetization energy decreases and the exchange energy increases with the shift of the core to the edge. At 83 mT, the exchange energy and demagnetization energy are equivalent. After that, demagnetization energy increases while the others decrease.

6.3.1. NiFe Sphere, Half Sphere, and Half Sphere Shell Dot Arrays

In this section, the magnetization and domain configurations of arrays of a sphere, half-sphere, and half-spherical shell dot will be under investigation. Initially, the magnetization was set to a random magnetization. By using the relax function, the magnetization state at the minimum energy was determined, and the magnetization was saved as a function of the applied field. The maximum applied field was 0.15 T with a step field of 0.001 T.

The hysteresis curves of the spherical dot, half-sphere dot, and half-sphere shell arrays with a separation distance of 64 nm along the x and y direction, when no PBC is applied, are given in Figure 6.27. The coercivity increases from the spherical dot array to the half-spherical shell array such that the coercive field for the spherical dot array is less than 0.02 T, the coercive field for the half-sphere dot is 0.05 T, and the coercive field for the half-spherical shell dot is 0.004 T. The remnant magnetization is the least in the spherical dot array. The shape of the hysteresis loops of the spherical dots is very different from the others.

The domain images of the spherical dot structures are shown in Figure 6.28. At 0.25 T, all the spheres are saturated. When the field decreased to 0.1 T, due to the reconfiguration of the spins in the dots at the edges, the dot array in the middle of the lattice was influenced by the surrounding dots. At 0.001 T, individual spin orientations occur within the dots. At -0.025 T, the total spins in each dot tend to align along the reversed field direction. At -0.250 T, all the dots experience saturation magnetization in the -x direction.

The domain images of the half-sphere dot structures are shown in Figure 6.29. After 0.012 T, the half-spherical dots show individual spin orientations, at -0.009 T, deviations from the +x direction are observed. At -0.034 T, a row of dots aligns in the -x direction, and the other dots are affected and switch to the -x direction at -0.135 T. The domain images of the half-sphere shell array are shown in Figure 6.30.

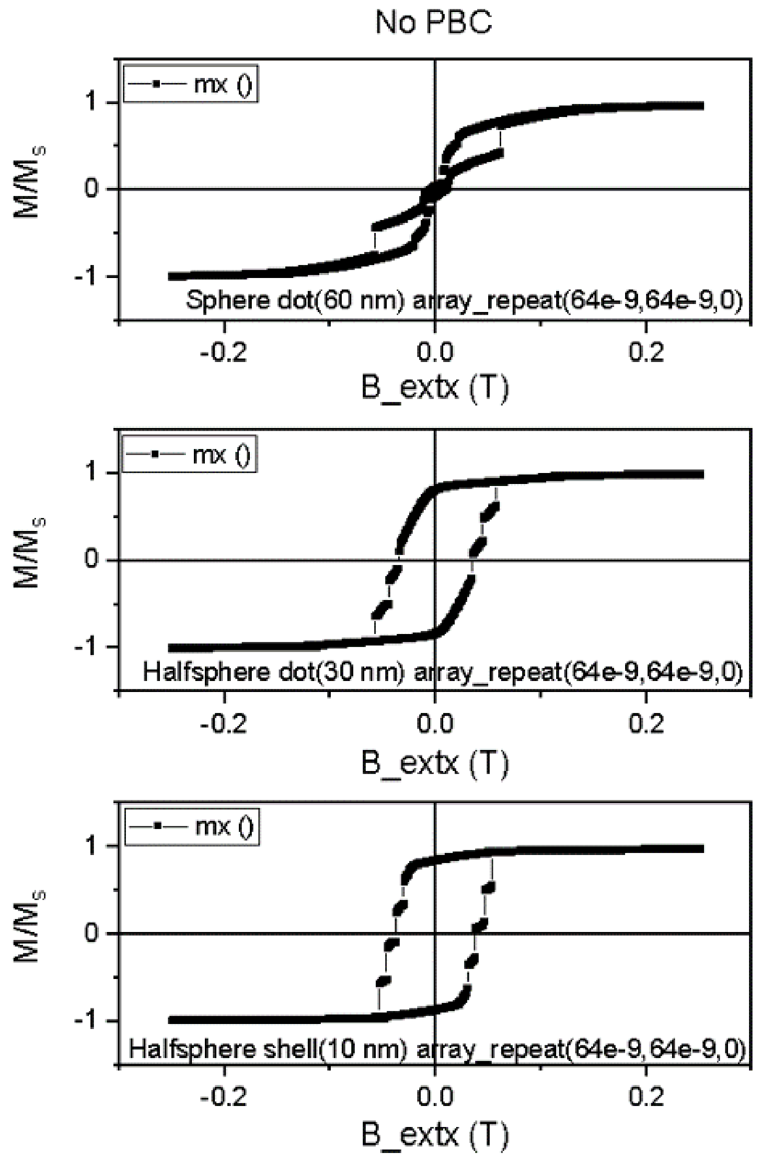

Figure 6.27. The magnetization curves of an array of sphere dots (60 nm), half-sphere dots (30 nm), half half-sphere shells (10 nm) with a separation distance of 64 nm along the x and y directions.

As a next step, the separation distance was increased to 80 nm along the x and y directions. The hysteresis curve of the spherical dot, half sphere dot, and half sphere shell arrays with a separation distance of 80 nm when no PBC is applied is given in Figure 6.31. The separation distance of 80 nm causes the hysteresis curve of the half-sphere dot and half-sphere shell array to change sharply when the field is inverted. The spherical dot array has a different hysteresis profile.

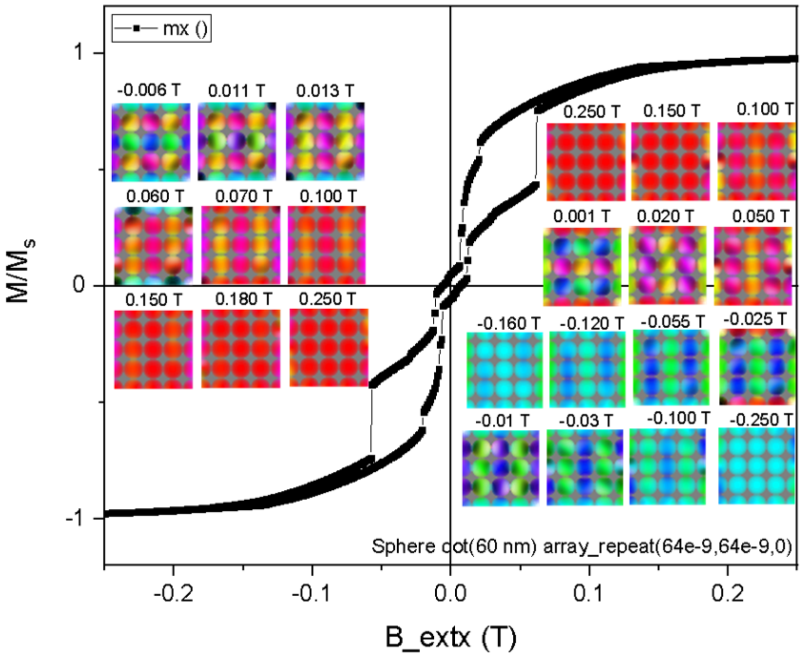

Figure 6.28. The magnetization curves and domain configurations of sphere dot (60 nm) array with a separation distance of 64 nm along the x and y directions.

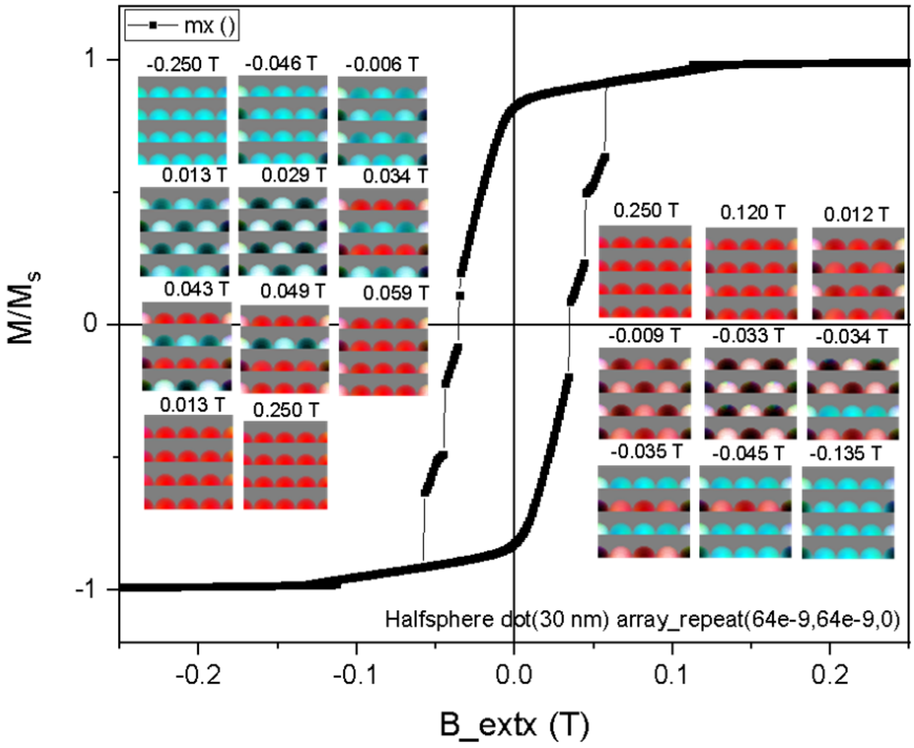

Figure 6.29. The magnetization curves and domain configurations of half sphere dot (30 nm) array with a separation distance of 64 nm along the x and y directions.

The domain configurations of the sphere array are given in Figure 6.32. Between 0.025 T and -0.025 T, the domain configurations are different in the majority of the dots, giving the two sharp loops. We can say that the remnant magnetization increased, and the coercivity decreased with respect to the one with a 64 nm separation distance. When PBC $(10, 10, 0)$ is applied, the hysteresis curves of the single sphere dot, sphere dot array with a separation distance of (60 nm, 60 nm, 0), (64 nm, 64 nm, 0) and (80 nm, 80 nm, 0) are shown in Figure 6.33. The PBC changed the hysteresis profile significantly for the spherical dot array with separation distances of 64 and 80 nm. The coercivity increased and the number of transitions between the domains was reduced with the addition of the PBC.

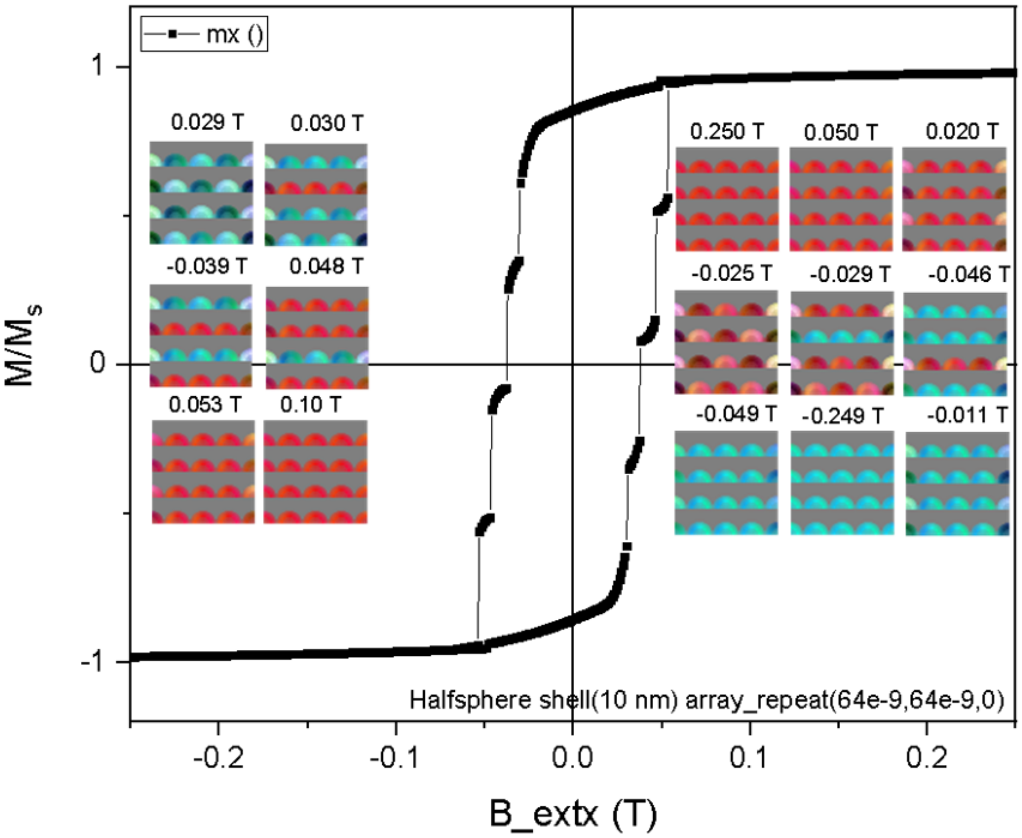

Figure 6.30. The magnetization curves and domain configurations of an array of half sphere shell (10 nm) with a separation distance of 64 nm along the x and y directions.

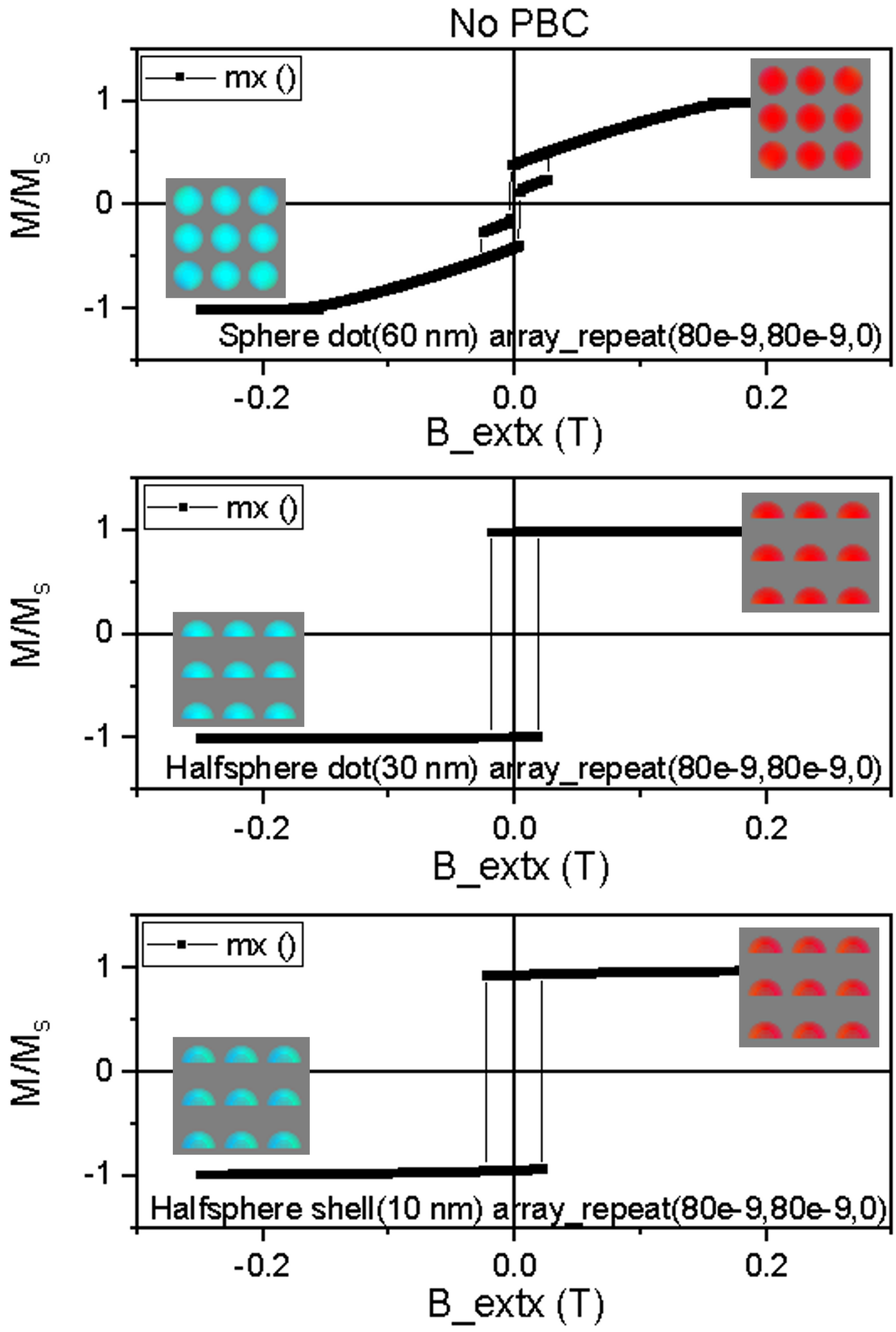

Figure 6.31. The magnetization curves and domain configurations of an array of sphere dots of 60, 30, and 10 nm thickness with a separation distance of 80 nm along the x and y directions.

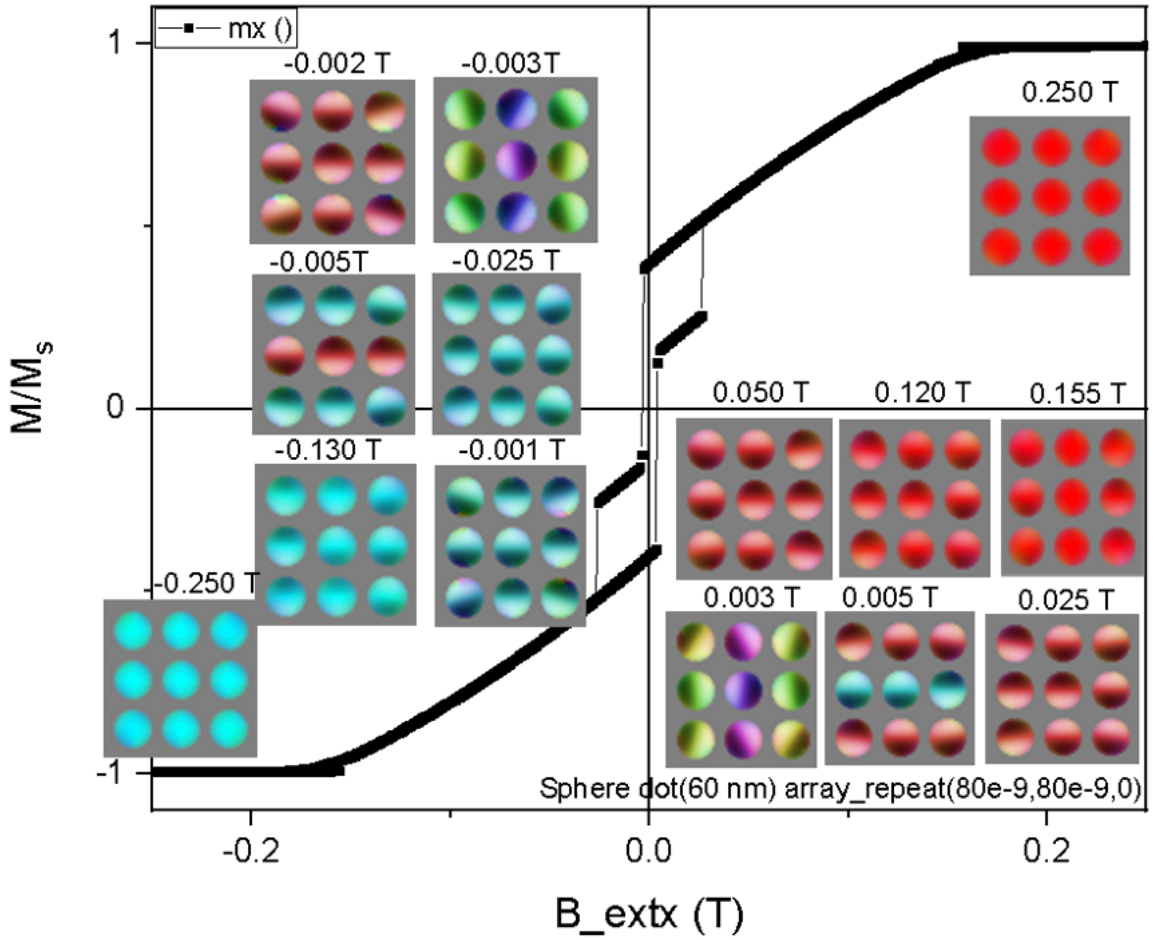

Figure 6.32. The magnetization curves and domain configurations of an array of sphere dots of 60 nm with a separation distance of 80 nm along the x and y directions.

The next study is about the effect of the size and the separation distance between the half-spherical structures on the hysteresis loops. To analyze the half-spherical structures, simulations were performed within a range of the diameter, d, from 45 to 360 nm by applying the magnetic field along the x direction. Initially, a random magnetization was assigned and the magnetization in the ground state was calculated. A high magnetic field was applied to align all the spins in the directions of the magnetic field, and the field was decreased in steps of 0.001 T until the magnetization was reversed. The hysteresis curves and domain configurations of the single NiFe hemisphere dot with various diameters with a PBC $(10, 10, 0)$ were given in Figure 6.34 for a diameter of 90 nm, Figure 6.35 for a diameter of 135 nm, Figure 6.36 for a diameter of 180 nm, Figure 6.37 for a diameter of 360 nm.

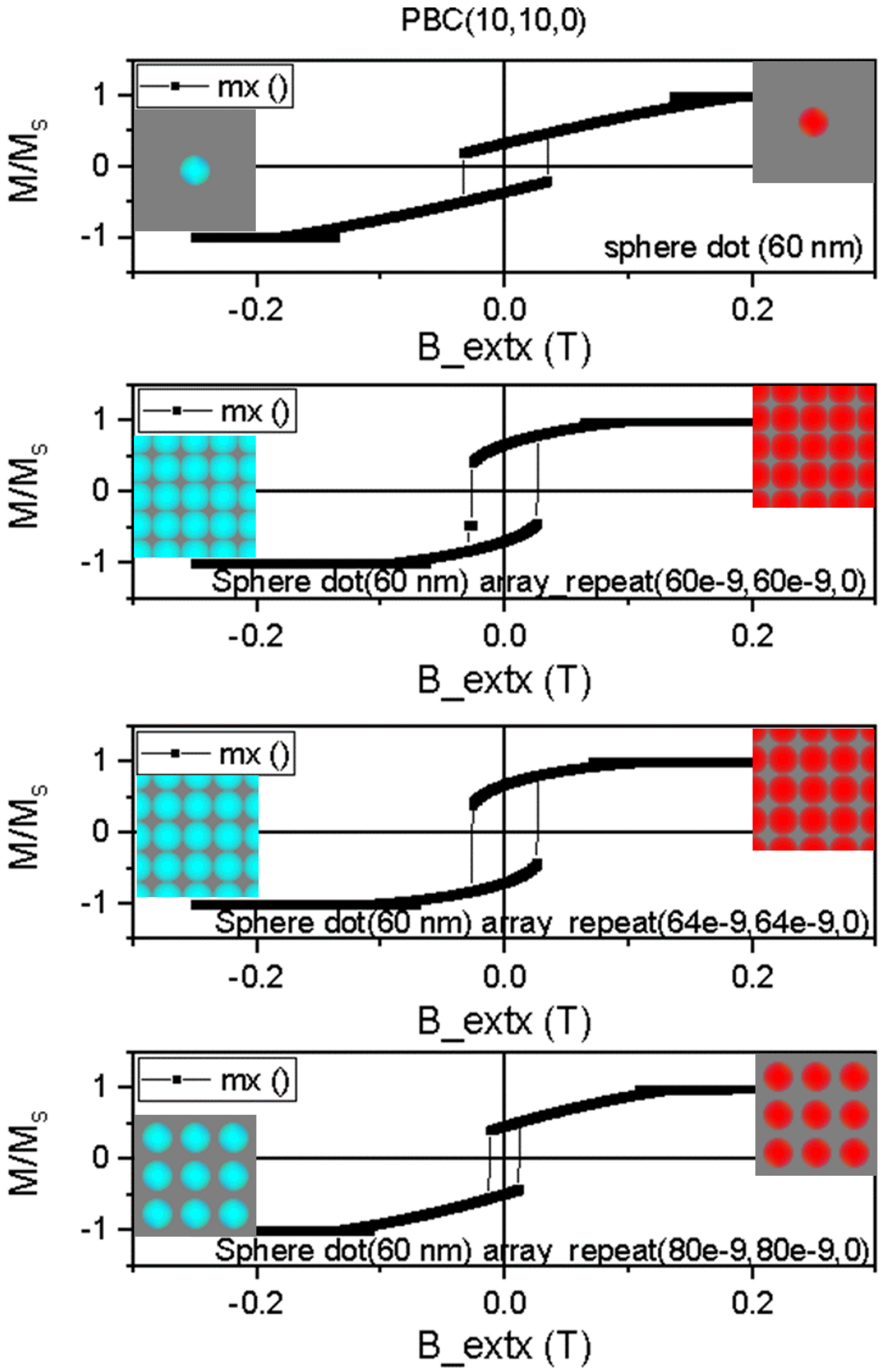

Figure 6.33. The magnetization curves and domain configurations of an array of sphere dots of 60 nm with a separation distance of 60, 64, and 80 nm along the x and y directions.

The hysteresis loop does not have a remnant magnetization and coercive field. In the domain images of the half-spherical dot structures, the single domain state is the state where the magnetic structure acts as a giant spin due to the large exchange of energy, as in the case of red and blue colored dots. The dot structure shows a spin-vortex configuration at the remnant state, which is a type of magnetic topological soliton. The vortex spin configuration finds a wide application in magnetic data storage due to the small thermal and quantum fluctuations [171] and is also used in the spin-torque nano-oscillators [172]. In the vortex state, the magnetic moments are curled in the plane of the dot structure in order to make the magnetostatic energy minimum. The core of the vortex is at the center of the dot in the remnant state.

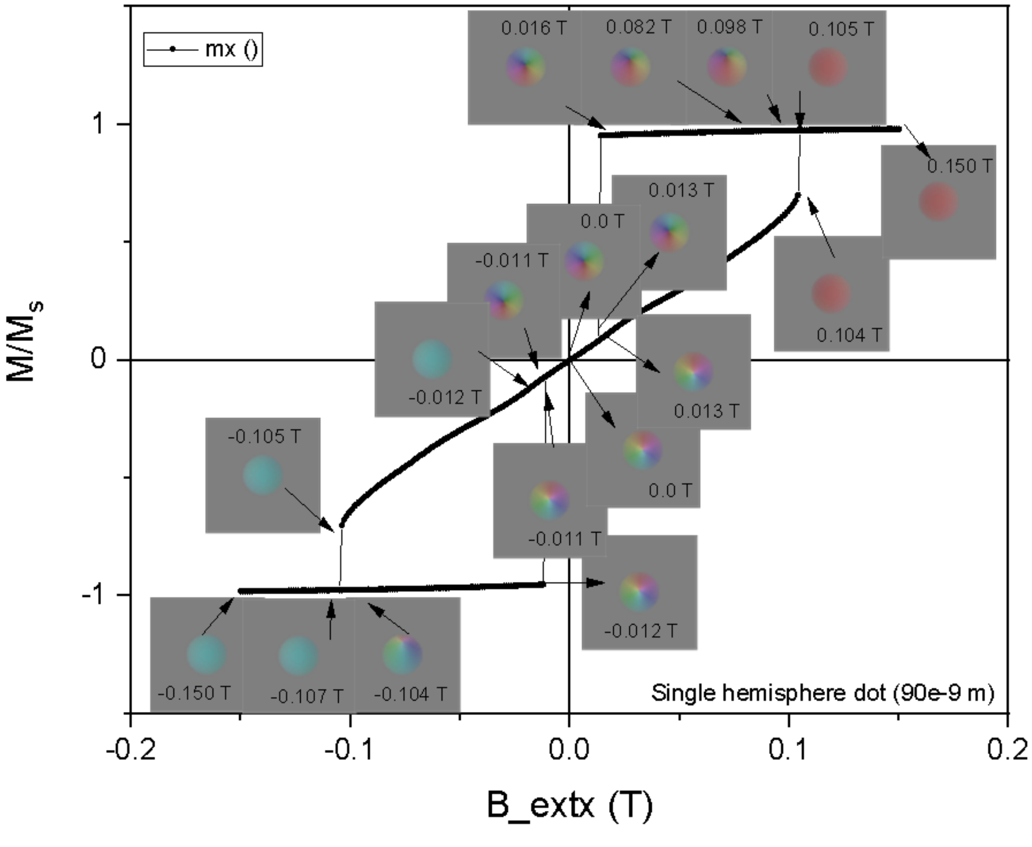

Figure 6.34. The hysteresis curves of a hemisphere dot with a 90 nm diameter.

At the core, magnetic moments align perpendicular to the plane of the dot. Therefore, this orientation prevents the singularity. From low fields to high fields, the vortex core moves towards the edge of the half-sphere dot. When the vortex is annihilated, the sample reaches saturation magnetization. After decreasing the applied field, the vortex nucleates again and follows a reversible loop. The hysteresis loop is affected by the size of the structure. When the size increases, the vortex nucleation increases, and expulsion fields are larger since the shape anisotropy decreases. Figure 6.38 shows that the loops shift towards larger fields and the loop elongates, which results in a smaller area. Saturation is reached at very large fields, higher than 0.20 T.

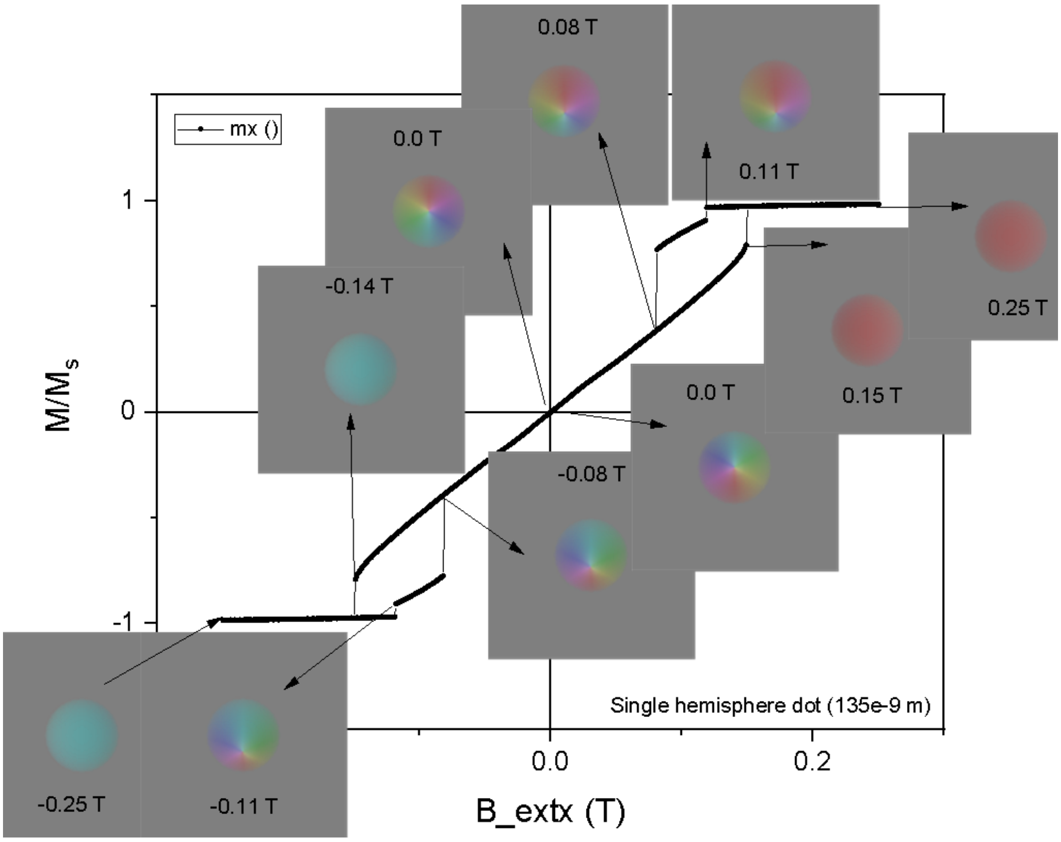

Figure 6.35. The hysteresis curve of a hemisphere dot with a 135 nm diameter.

Another study for the half-spherical dots is about the separation distance between the dots. The diameter of the half-sphere hemisphere was determined as 90 nm. The hysteresis curves and domain configurations of the hemisphere dot arrays with various separation distances with a PBC $(10, 10, 0)$ were given in Figure 6.42 for a separation distance of 64 nm along the x and y directions, in Figure 6.43 for a separation distance of 90 nm along the x and y directions, in Figure 6.44 for a separation distance of 100 nm along the x and y directions, in Figure 6.45 for a separation distance of 128 nm along the x and y directions, in Figure 6.46 for a separation distance of 140 nm along the x and y directions, in Figure 6.48 for a separation distance of 150 nm along the x and y directions, in Figure 6.49 for a separation distance of 200 nm.

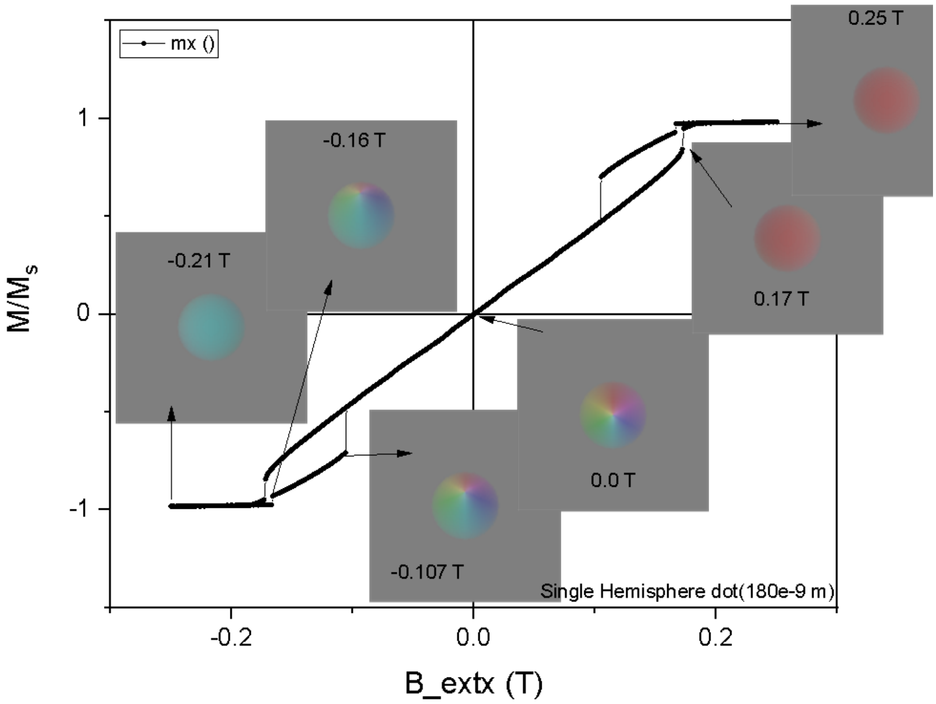

Figure 6.36. The hysteresis curves of a hemisphere dot with a 180 nm diameter.

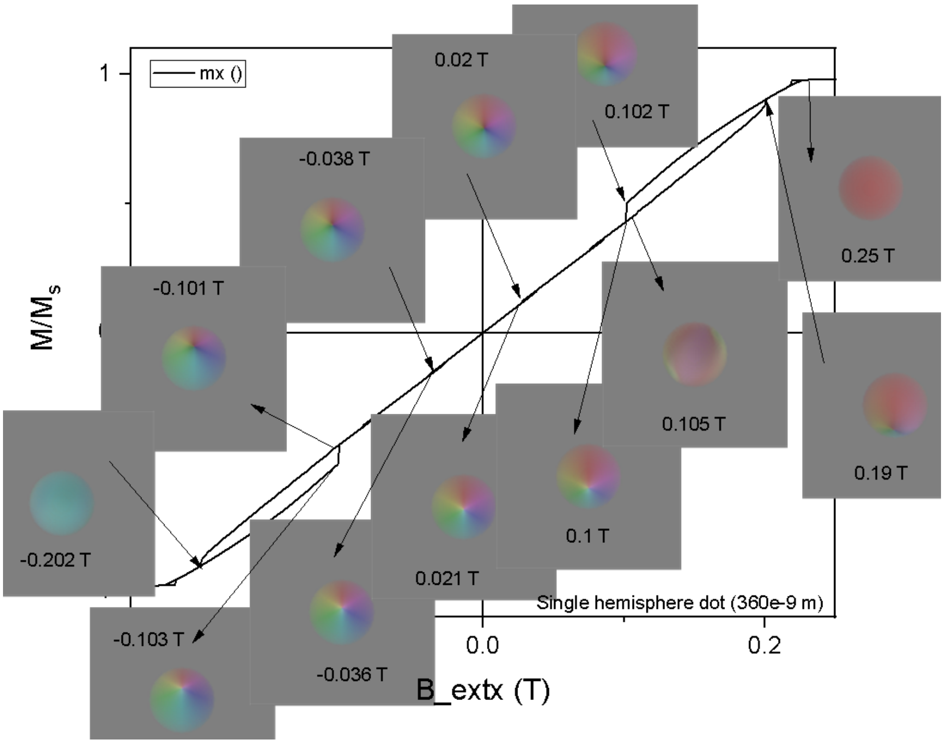

Figure 6.37. The hysteresis curves of a hemisphere dot with a 360 nm diameter.

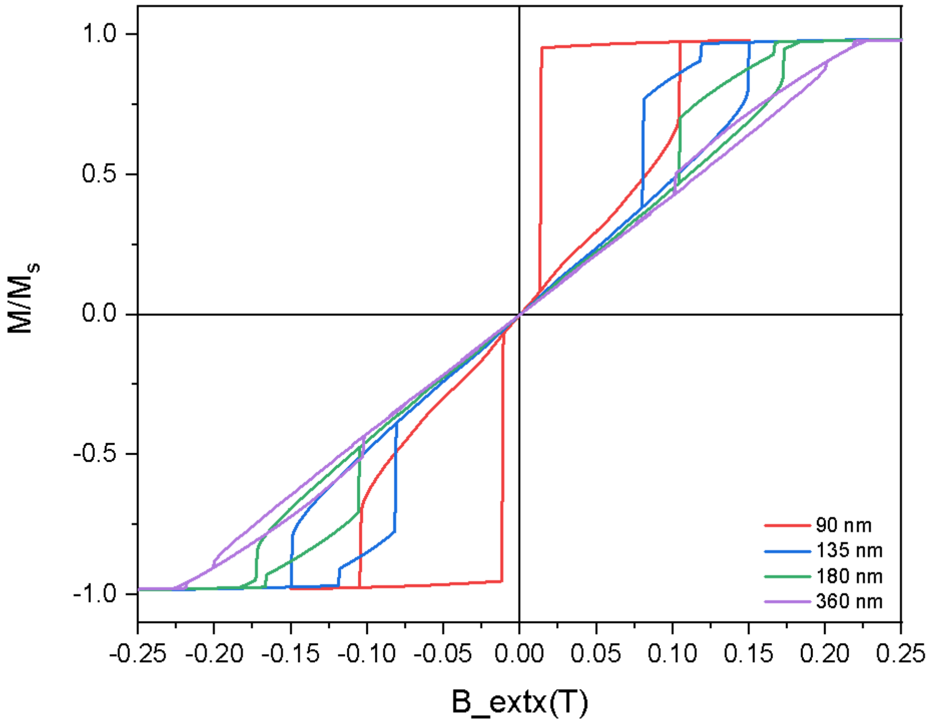

Figure 6.38. The hysteresis curves of a single hemisphere dot with a 90, 135, 180, and 360 nm diameter.

The magnetization saturation in the +x direction and -x direction in a half-spherical dot array is shown in Figures 6.39 and 6.40, respectively. The vortex state in the dot array is shown in Figure 6.41. When the separation distance is 64 nm, the array behaves like a continuous film, and sharp hysteresis loops are obtained. When the distance between the dots increases from 90 nm to 128 nm, different plateaus occur in the loop, which corresponds to different domain configurations. The change from 90 nm to 100 nm decreases the coercivity significantly. When the distance is 128 nm, the dots are arranged well in the grid size with the 10 times repetition along the x and y directions. Therefore, it gives a similar hysteresis loop with a distance of 64 nm. When the distance is 140 nm, the coercivity increases, and the number of domain transitions increases. The coercivity and the remnant magnetization become zero when the separation distance is 200 nm. Figure 6.50 shows all hysteresis loops of the separation distances from 64 nm to 200 nm.

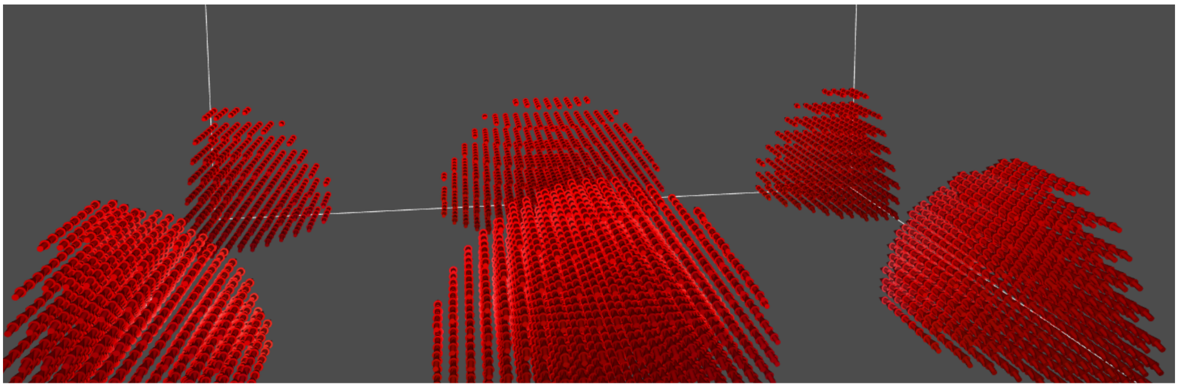

Figure 6.39. The hysteresis curve of a hemisphere dot with a 135 nm diameter.

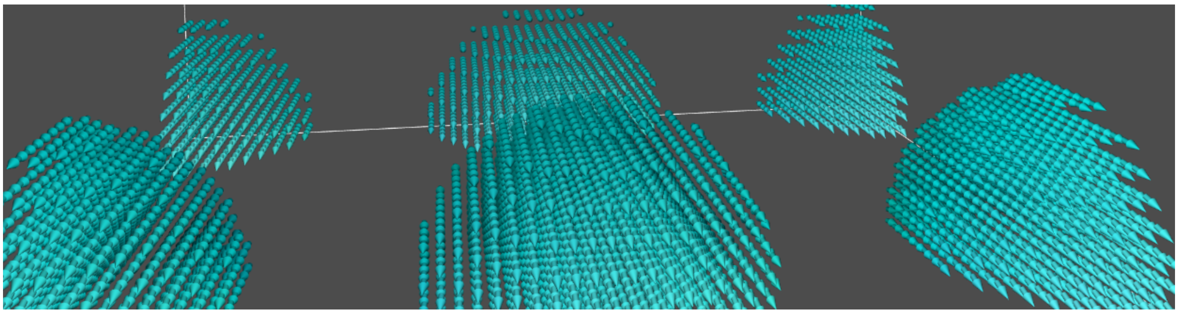

Figure 6.40. The view of the hemisphere dot array with spins pointing at the -x direction.

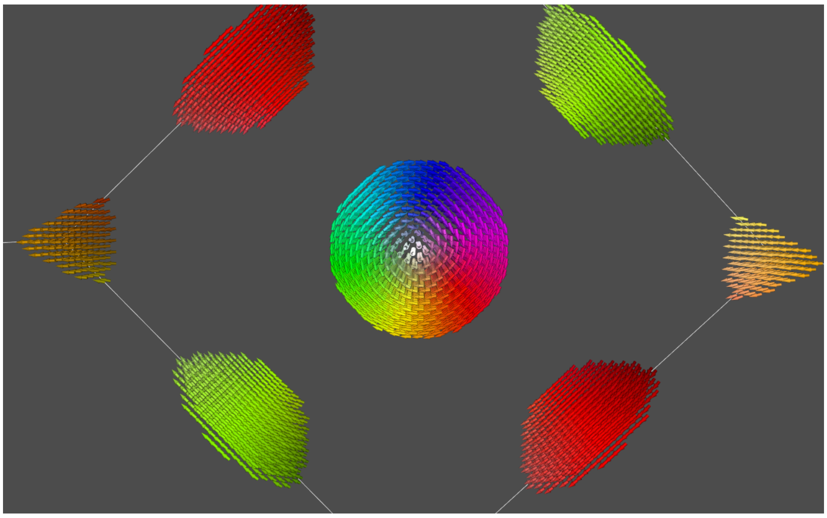

Figure 6.41. The view of the vortex configuration in the hemisphere dot array.

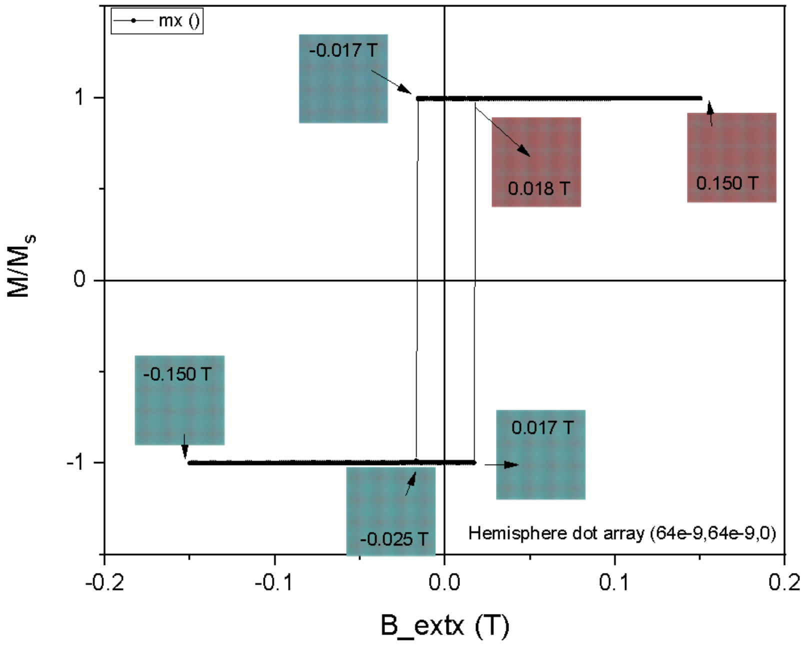

Figure 6.42. The hysteresis curves of hemisphere dot (90 nm) array with a separation distance of 64 nm along the x and y directions.

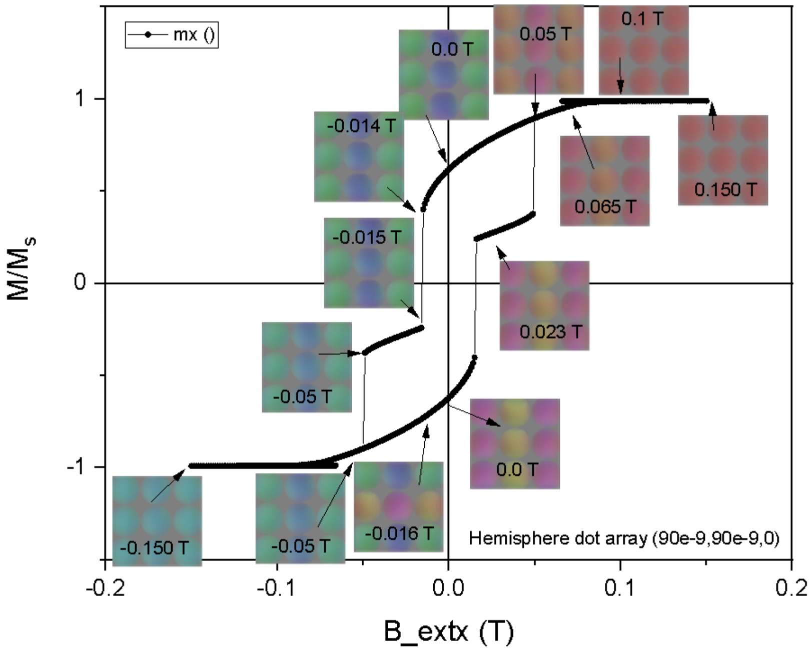

Figure 6.43. The hysteresis curves of a hemisphere dot with a 90 nm diameter and separation distance of 90 nm at the x and y directions.

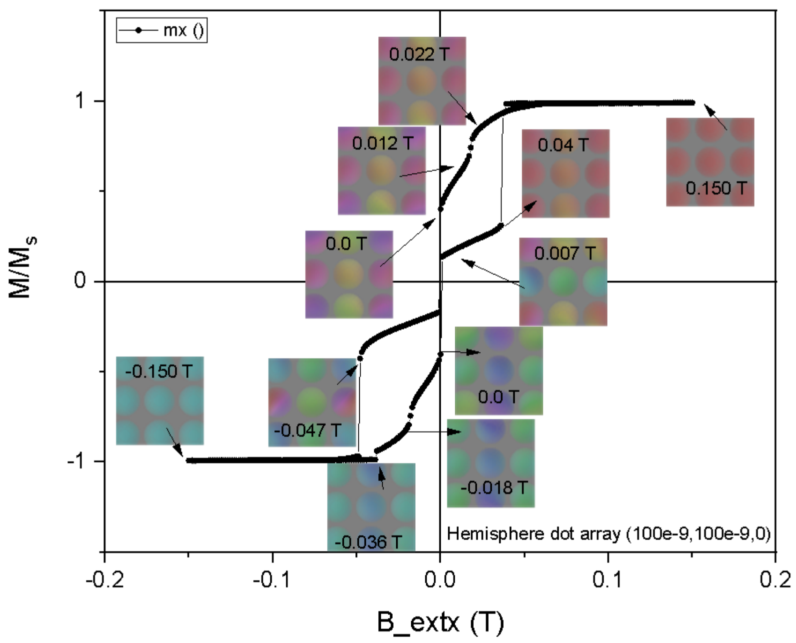

Figure 6.44. The hysteresis curves of a hemisphere dot with a 90 nm diameter and separation distance of 100 nm at the x and y directions.

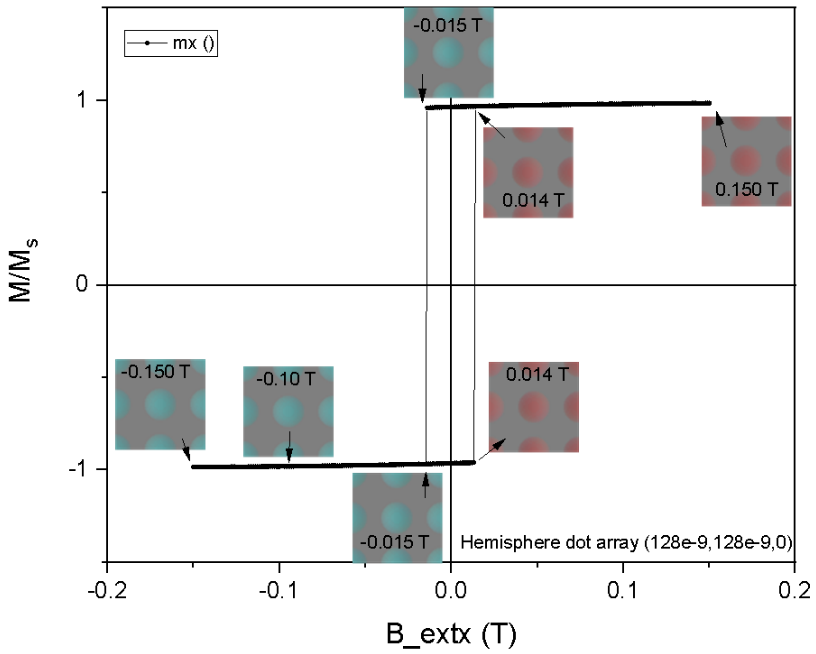

Figure 6.45. The hysteresis curves of a hemisphere dot with a 90 nm diameter and separation distance of 128 nm at the x and y directions.

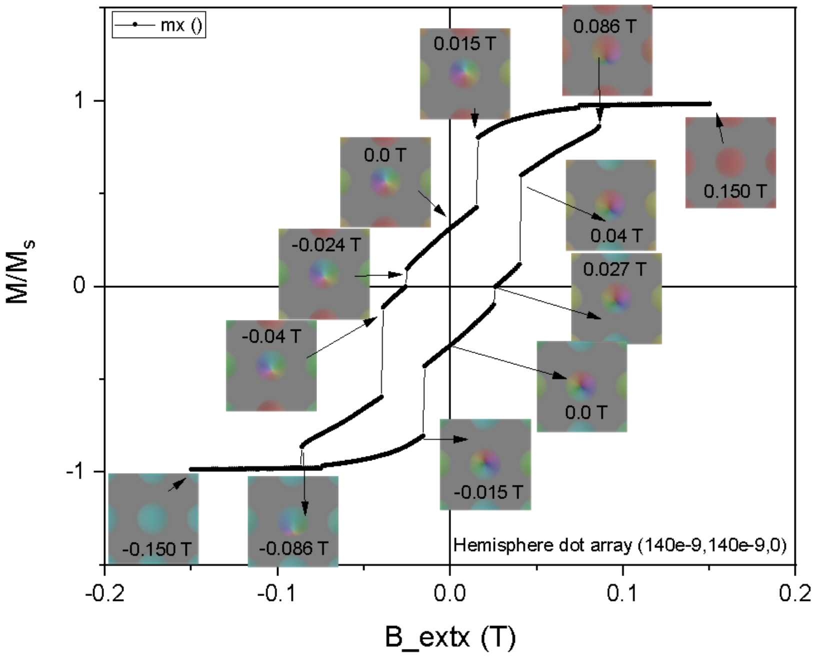

Figure 6.46. The hysteresis curves of a hemisphere dot with a 90 nm diameter and separation distance of 140 nm at the x and y directions.

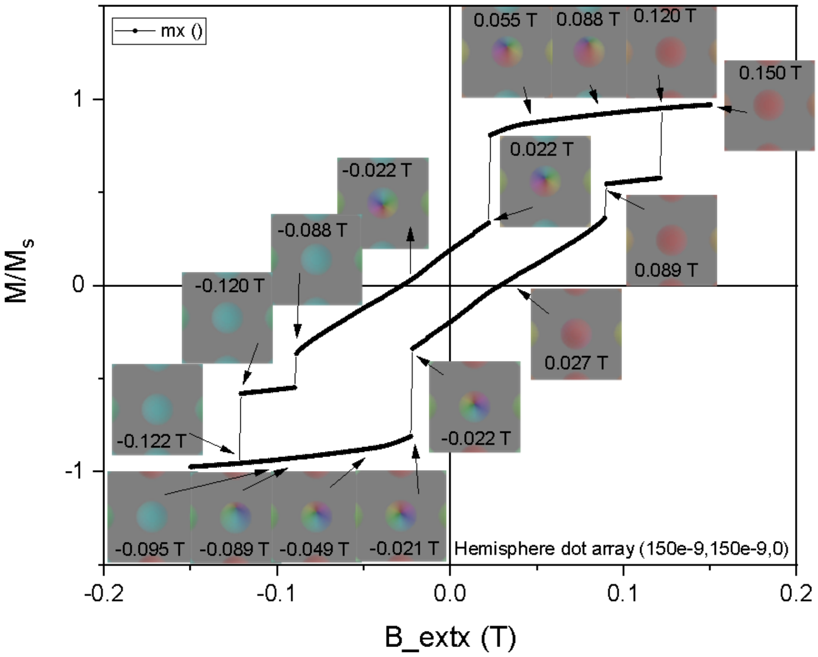

Figure 6.47. The hysteresis curves of a hemisphere dot with a 90 nm diameter and separation distance of 150 nm at the x and y directions.

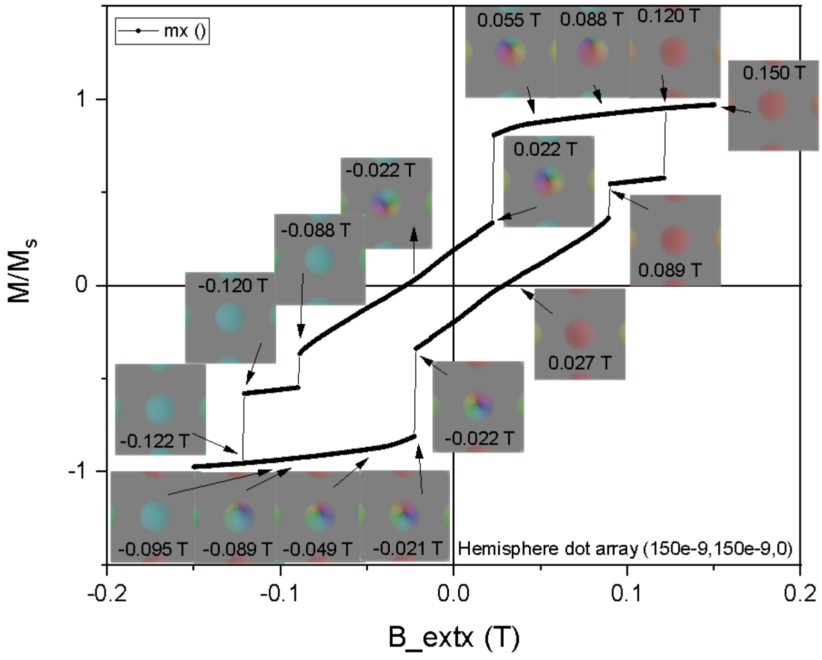

Figure 6.48. The hysteresis curves of a hemisphere dot with a 90 nm diameter and separation distance of 150 nm at the x and y directions.

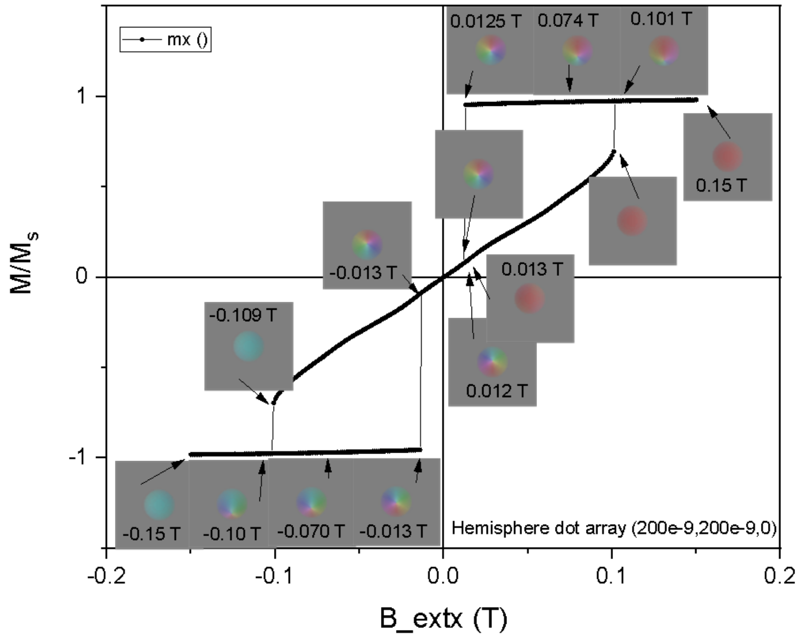

Figure 6.49. The hysteresis curves of a hemisphere dot with a 90 nm diameter and separation distance of 200 nm at the x and y directions.

Figure 6.51 shows the simulated demagnetization, exchange, Zeeman, and total energy variation as a function of the field for the hemisphere dots with a diameter of 90 and 360 nm. At the saturation state of the hemisphere dot with a diameter of 90 nm, the demagnetization energy is 2.05×10^{-17} J, exchange energy is 2.65×10^{-19} J, Zeeman energy is -2.47×10^{-17} J, and total energy is -3.95×10^{-18} J. At the remnant state of the hemisphere dot with a diameter of 90 nm, the demagnetization energy is 2.1×10^{-18} J, exchange energy is 8.6×10^{-18} J, Zeeman energy is 1.57×10^{-37} J, and total energy is 1.08×10^{-17} J. At the saturation state of the hemisphere dot with a diameter of 360 nm, the demagnetization energy is 1.25×10^{-15} J, exchange energy is 4×10^{-18} J, Zeeman energy is -2.6×10^{-15} J, and total energy is -1.35×10^{-15} J.

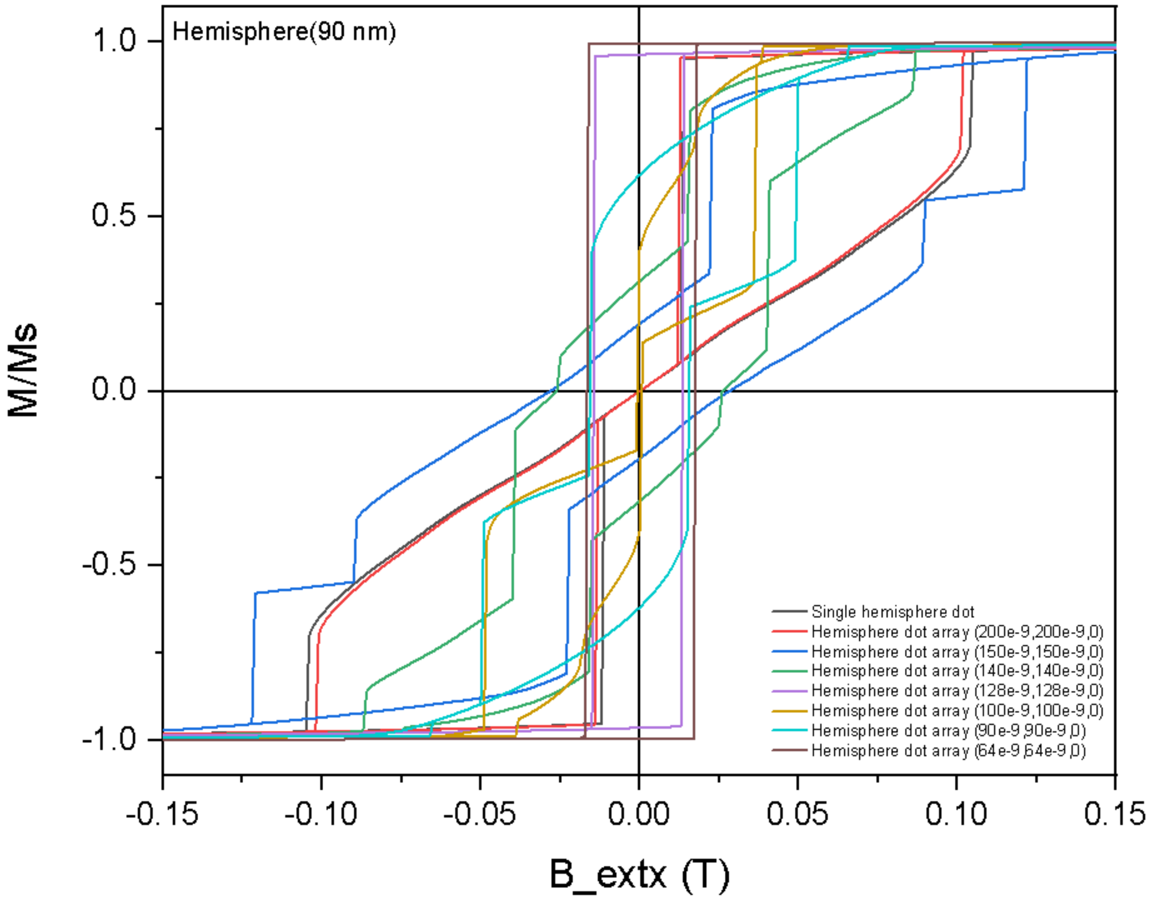

Figure 6.50. The hysteresis curves of an array of hemisphere dots with a 90 nm diameter and separation distance between 64 nm and 200 nm at the x and y directions.

At the remnant state of the hemisphere dot with a diameter of 360 nm, the demagnetization energy is 3.53×10^{-17} J, exchange energy is 4.57×10^{-17} J, Zeeman energy is 6.24×10^{-37} J, and total energy is 8.11×10^{-17} J. Figure 6.52 shows the simulated demagnetization, exchange, Zeeman and total energy variation as a function of the field for the hemisphere dot array with a diameter of 90 nm and inter-distance of 200 nm at the x and y directions. At the saturation state of the hemisphere dot array, the demagnetization energy is 2×10^{-17} J, exchange energy is 2.6×10^{-19} J, Zeeman energy is -2.47×10^{-17} J, and total energy is -4.27×10^{-18} J.At the remanence of the hemisphere dot array, the demagnetization energy is 2.14×10^{-18} J, exchange energy is 8.67×10^{-18} J, Zeeman energy is 1.55×10^{-37} J, and total energy is 1.08×10^{-17} J.

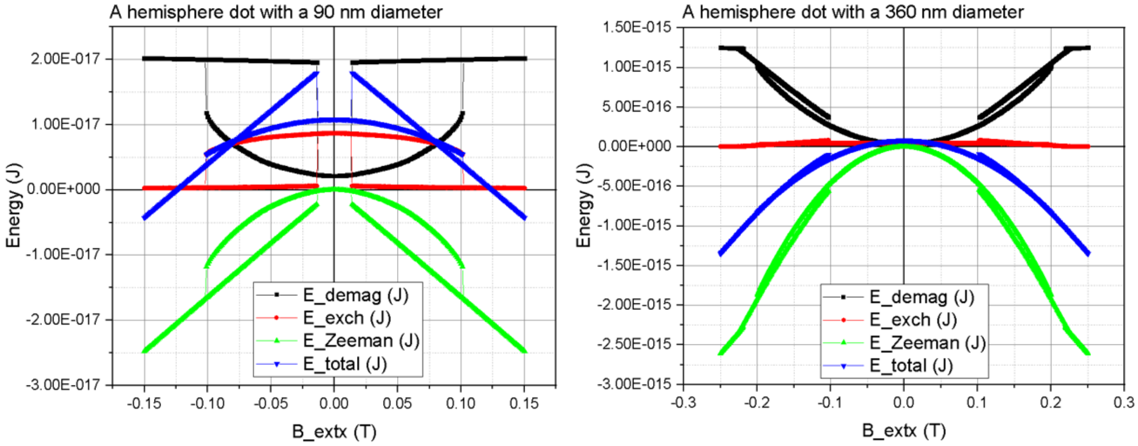

Figure 6.51. The simulated demagnetization, exchange, Zeeman and total energy variation as a function of the field for the hemisphere dots with a diameter of 90 and 360 nm.

6.4. Micromagnetic Simulations of NiFe Antidot Arrays

The antidot array structure in a continuous magnetic medium can form regions in which the remanence can be controlled so that can alter the magnetization dynamics and be used for data storage. The simulation parameters for the 20 nm NiFe thin film with circular, pacman, and half-circular antidot array are: Gridsize (512, 512, 1), Cellsize $(4 \times 10^{-9}\text{m}, 4 \times 10^{-9}\text{m}, 20 \times 10^{-9}\text{m})$, Edge smoothing factor of 8. Circular antidot array with 1μm diameter and center-to-center separation distance of $(1000e-9\text{m}, 1000e-9\text{m}, 0)$ along the x, y, and z direction with periodic boundary condition of PBC $(20, 20, 0)$ repetition along x, y, and z direction. The initial magnetization was uniform and set to the x direction $(1, 0, 0)$. The saturation magnetization was 8.6×10^5 A/m and the exchange stiffness was 13×10^{-12} J/m. The value of the uniaxial anisotropy was determined to be 8×10^2 J/m^2 along the x direction. The maximum applied magnetic field was 200×10^{-3} T with a step field of 1.0×10^{-3} T.

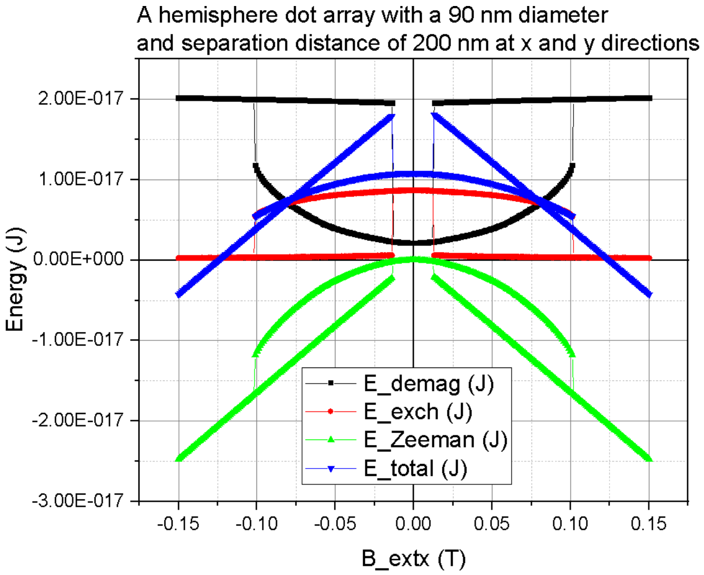

Figure 6.52. The simulated demagnetization, exchange, Zeeman and total energy variation as a function of the field for the hemisphere dot array with a diameter of 90 nm and inter-distance of 200 nm at x and y directions.

The hysteresis loops of the 20 nm NiFe pure thin film and the circular antidot array are given in Figure 6.53. The coercivity increases with the introduction of the holes in the film, and the remnant magnetization decreases. The coercive field for the pure thin film is 0.005 T and the remnant magnetization is 0.62. The coercive field for the antidot array is 0.02 T and the remnant is 0.62.

When the separation distance increases both in the x and y directions, the coercivity of the circular antidot array decreases, as shown in Figure 6.54. However, when the separation distance along the y direction increases from 1 to 4 μm in Figure 6.55, the coercivity is less than that with 1 μm separation distance between holes. When the separation distance increases from 1 to 4 μm along the x direction, the coercivity decreases more. Again, when the separation distance along the y direction decreases from 4 to 1 μm, the coercivity decreases while the remnant magnetization gets the smallest value, and the loop profile changes drastically.

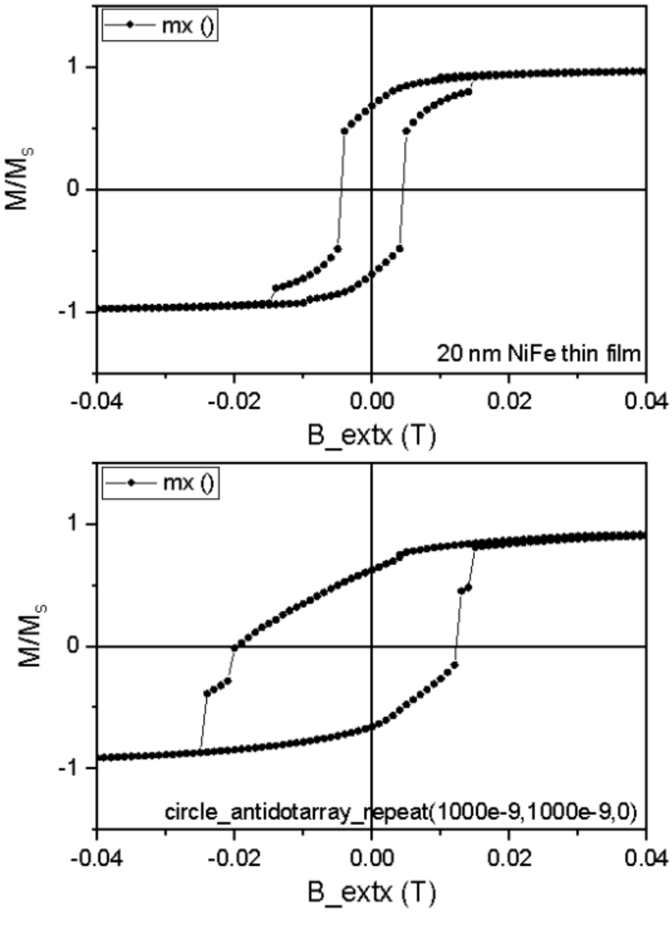

Figure 6.53. Hysteresis curves of a 20 nm NiFe thin film and circular antidot array with a diameter of 1 μm and edge-to-edge separation distances of 1 μm at both x and y directions.

In Figure 6.55, the coercive fields for the separation distance of $(1\mu\text{m}, 1\mu\text{m}, 0)$ is 0.02 T and the remnant magnetization is 0.62. The coercive fields for the separation distance of $(1\mu\text{m}, 4\mu\text{m}, 0)$ is 0.012 T and the remnant magnetization is 0.93. The coercive fields for the separation distance of $(4\mu\text{m}, 4\mu\text{m}, 0)$ is 0.002 T and the remnant magnetization is 0.79. The coercive fields for the separation distance of $(4\mu\text{m}, 1\mu\text{m}, 0)$ is 0.0005 T and the remnant magnetization is 0.15.

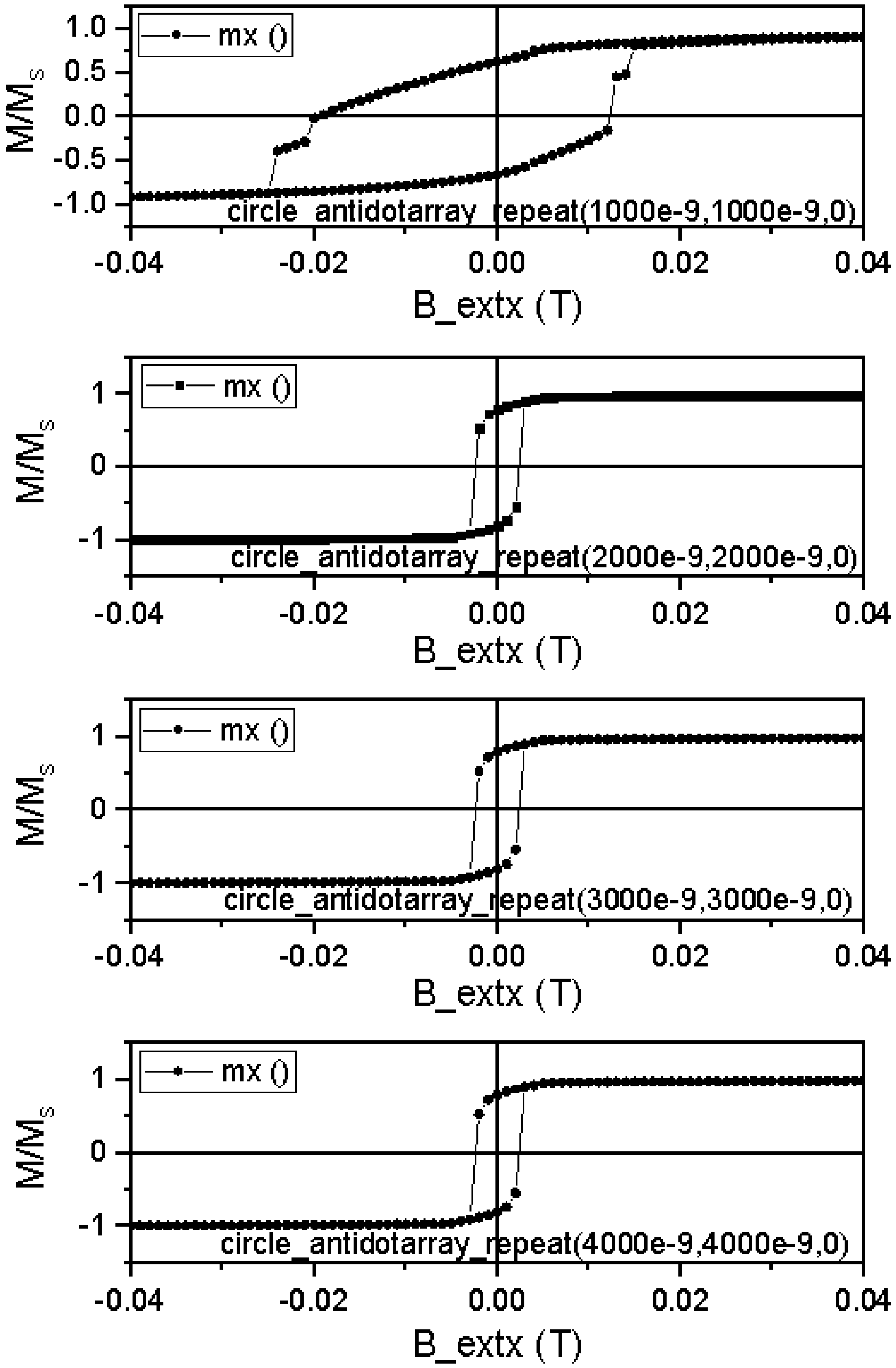

Figure 6.54. Hysteresis curves of the circular antidot array with a diameter of 1 μm and edge-to-edge separation distances of 1, 2, 3, and 4 μm at both x and y directions.

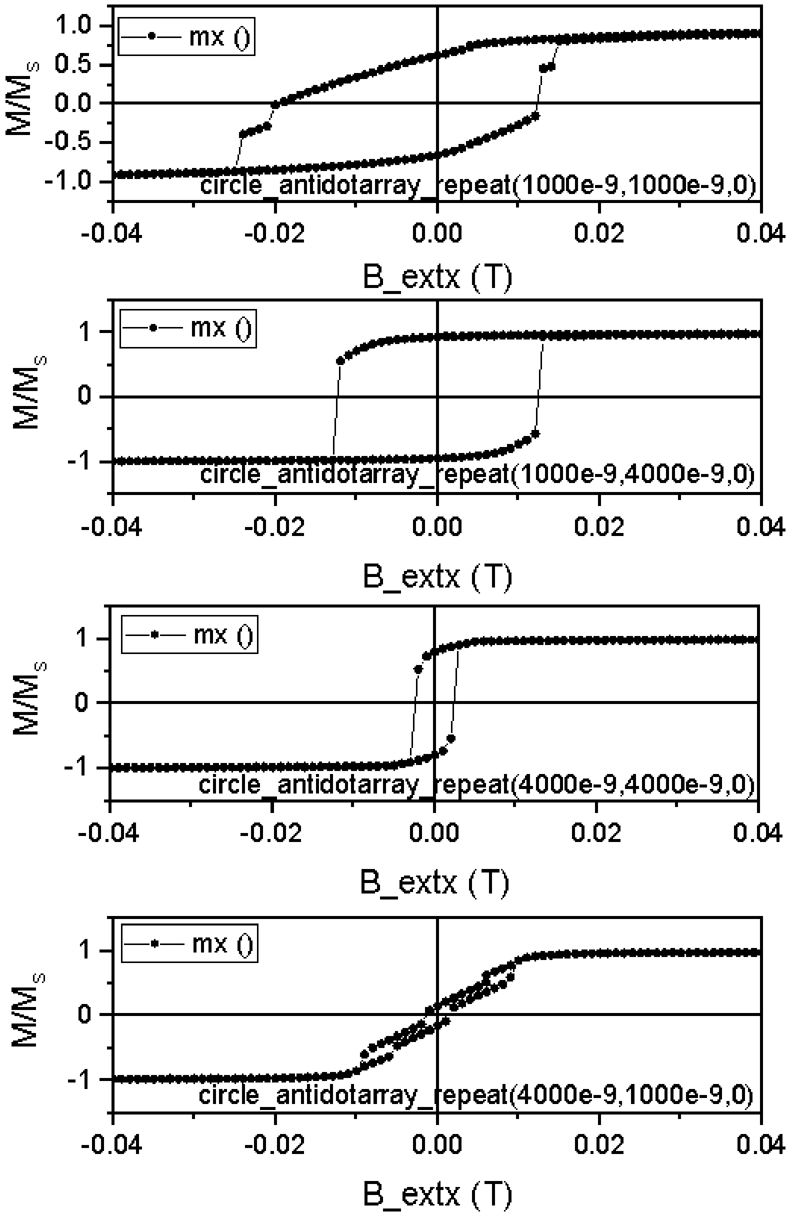

Figure 6.55. Hysteresis curves of the circular antidot array with a diameter of 1 μm and various edge-to-edge separation distances at x and y directions.

The effect of the antidot shape on the hysteresis loops of the films is shown in Figure 6.56. The pacman shape antidot has a larger coercivity and more domain structures. The coercivity of the circle, half-circle, and pacman antidot array is 0.012 T, 0.014 T, and 0.023 T, respectively. The effect of the separation distance on the half-circular antidot array is shown in Figure 6.57. When the distance between the holes increases, the coercivity and the number of domains decrease. The coercivity is

0.014 T for the separation distance of 1 μm and 0.007 T for the separation distance of 1.5 μm. The same situation goes with the pacman antidot array in Figure 6.58. The coercivity is 0.023 T for the separation distance of 1 μm and 0.008 T for the separation distance of 1.5 μm. The effect of the pacman size variation on the hysteresis loops is illustrated in Figure 6.59. From the large size of the pacman to the half-circle antidot, the coercivity decreases. The coercivity is 0.023 T for the large pacman antidot and 0.018 T for the narrow pacman antidot, and 0.014 T for the half-circle pacman antidot.

The simulated energies of the uniform thin film during the magnetization reversal are shown in Figure 6.60. At the saturation state of the pure thin film, the anisotropy energy is -6.5×10^{-17} J, demagnetization energy is 4.6×10^{-16} J, exchange energy is 1.08×10^{-17} J, Zeeman energy is -5.69×10^{-15} J, and total energy is -5.28×10^{-15} J. At the remnant state of the pure thin film, the anisotropy energy is -3.77×10^{-17} J, demagnetization energy is 2.11×10^{-16} J, exchange energy is 2.15×10^{-17} J, Zeeman energy is 3.79×10^{-30} J, and total energy is 1.95×10^{-16} J.

The simulated energies of circular antidot array film are shown in Figure 6.61. At the saturation state of the circle antidot array with a separation distance of 1 μm along the x and y directions, the anisotropy energy is -1.25×10^{-17} J, demagnetization energy is 2.63×10^{-16} J, exchange energy is 9.75×10^{-18} J, Zeeman energy is -1.12×10^{-15} J, and total energy is -8.5×10^{-16} J.

At the remnant state of the circle antidot array with a separation distance of 1 μm along the x and y directions, the anisotropy energy is -8.11×10^{-18} J, demagnetization energy is 1.69×10^{-16} J, exchange energy is 2.66×10^{-17} J, Zeeman energy is 1.48×10^{-30} J, and total energy is 1.87×10^{-16} J. The simulated energies of half-circular antidot array film with a separation distance of 1 μm are shown in Figure 6.62.

At the saturation state of the half-circle antidot array with a separation distance of 1 μm along the x and y directions, the anisotropy energy is -3.75×10^{-17} J, demagnetization energy is 6.73×10^{-16} J, exchange energy is 1.75×10^{-17} J, Zeeman energy is -3.3×10^{-15} J, and total energy is -2.65×10^{-15} J. At the remnant state of the half-circle antidot array with a separation distance of 1 μm along the x and y directions, the anisotropy energy is -1.64×10^{-17} J, demagnetization energy is 2.95×10^{-16} J, exchange energy is 6.50×10^{-17} J, Zeeman energy is 3.85×10^{-30} J, and total energy is 3.44×10^{-16} J.

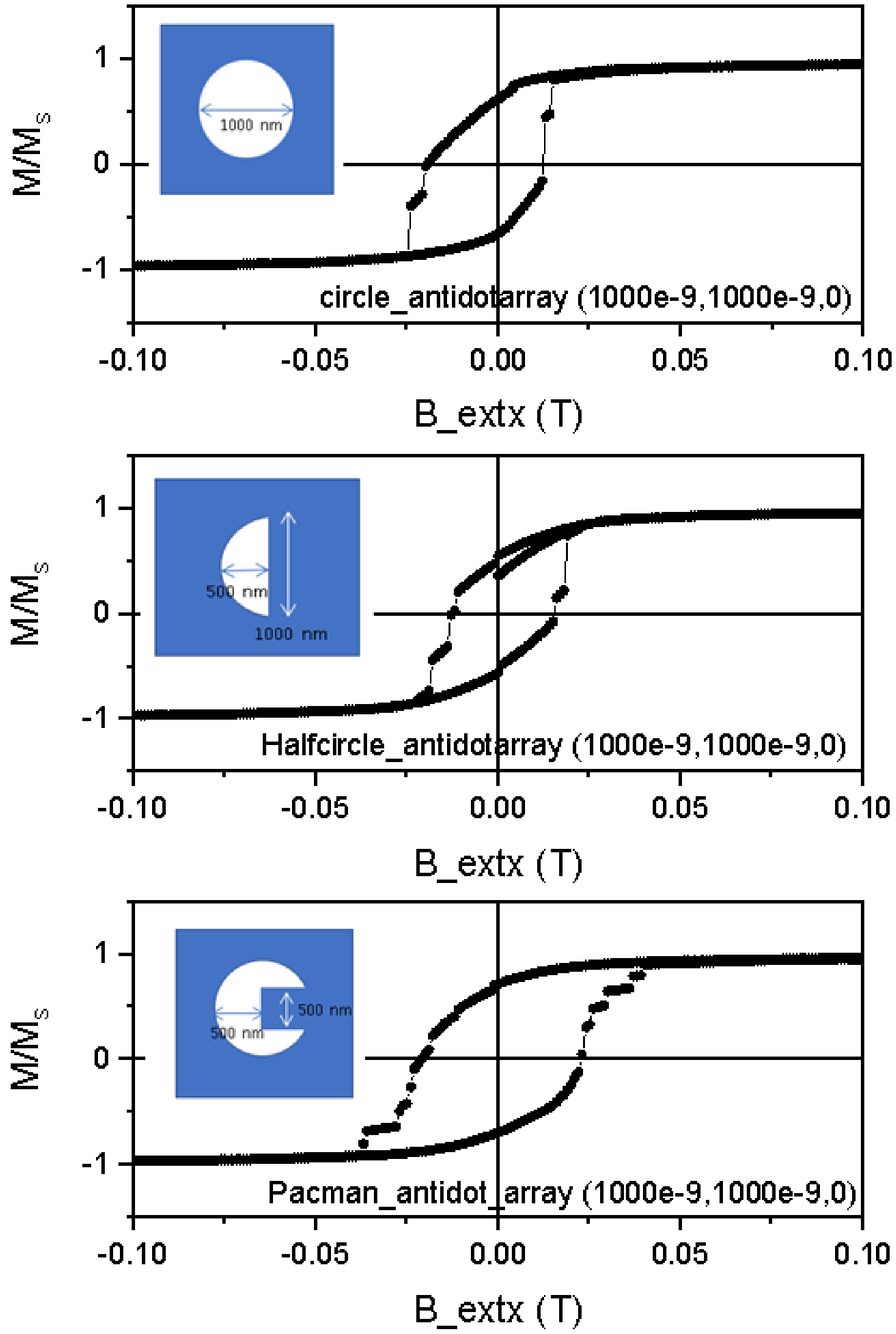

Figure 6.56. Hysteresis curves of the circle, half-circle, and pacman antidot structures.

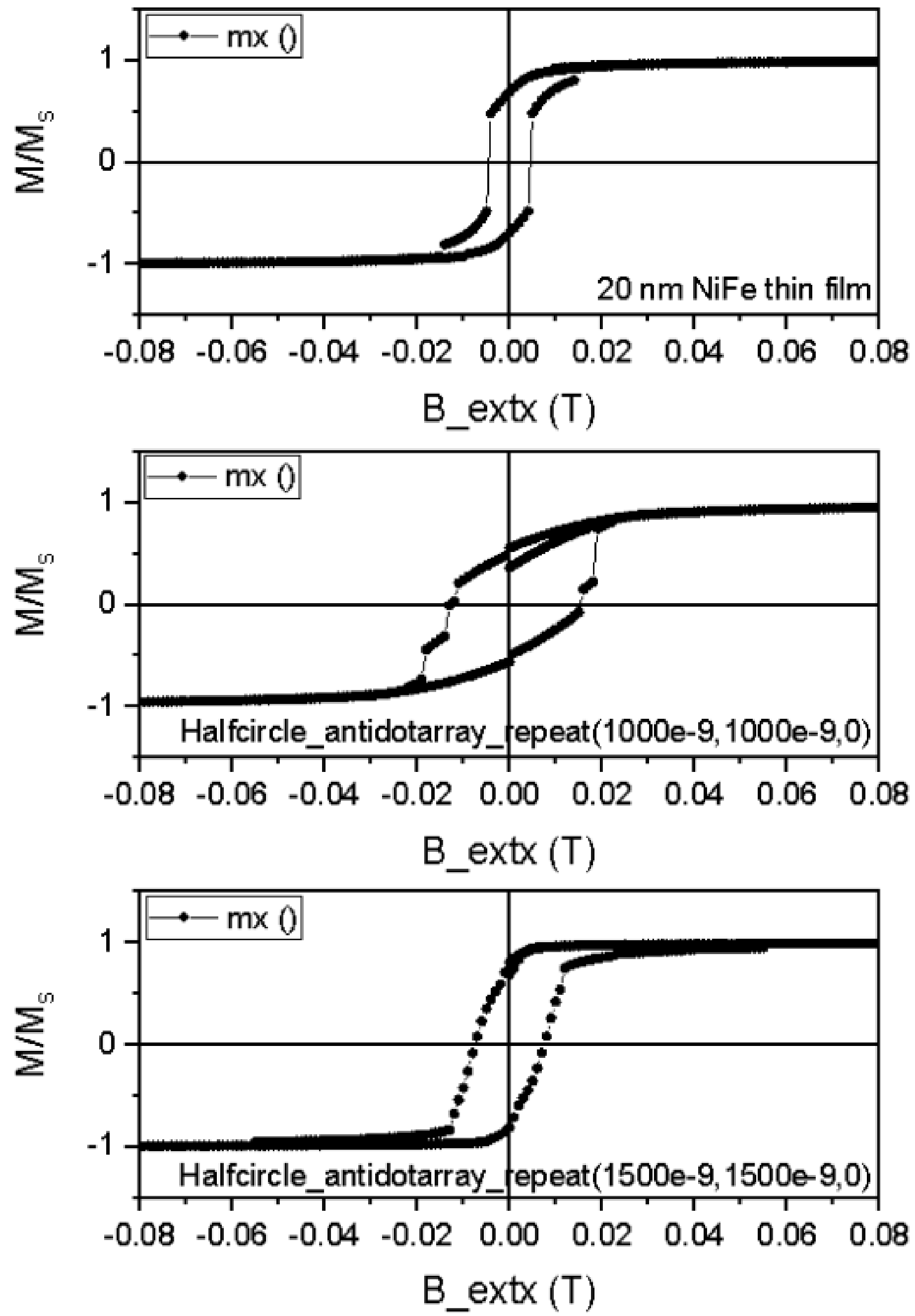

Figure 6.57. Hysteresis curves of pure thin film and half-circle antidot array structures with various separation distances along the x and y directions.

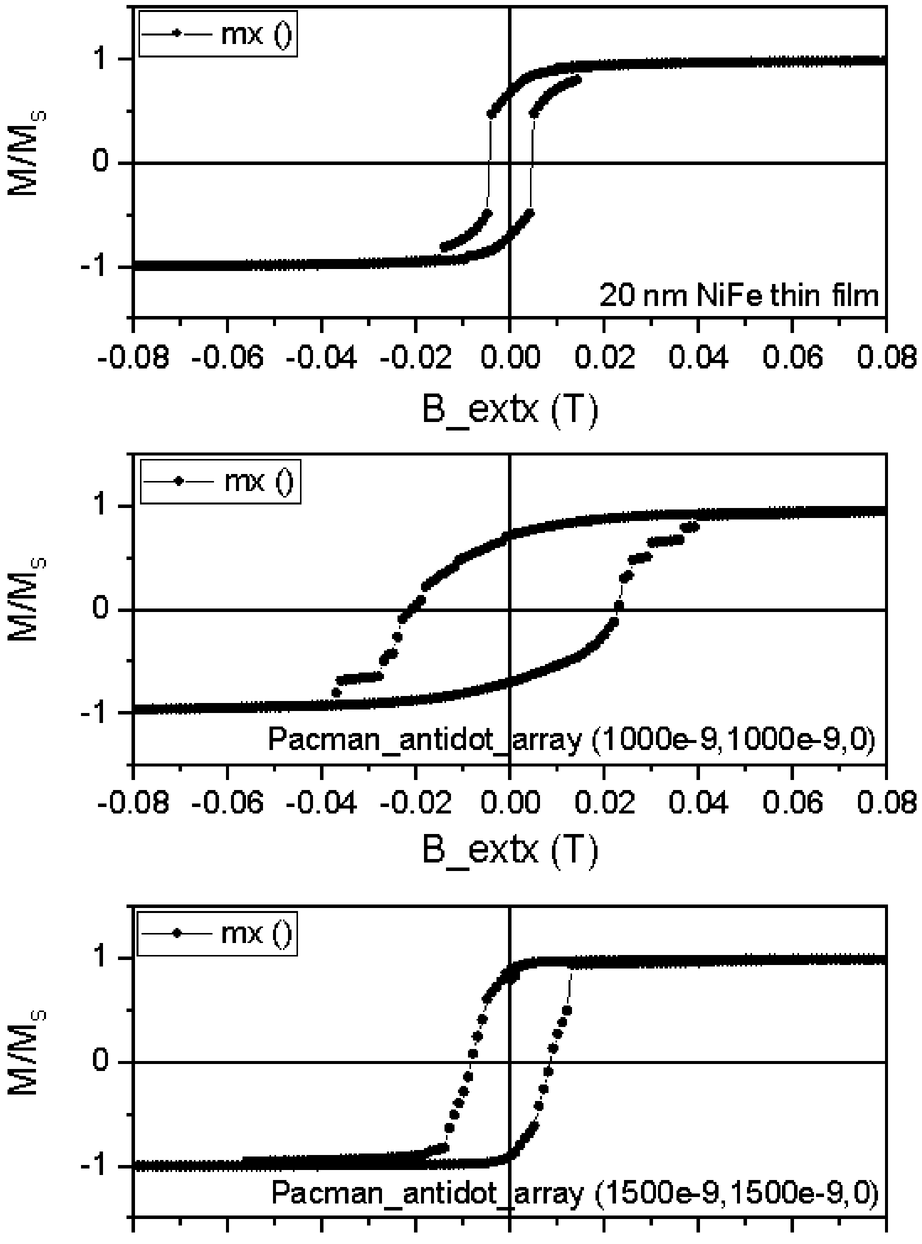

Figure 6.58. Hysteresis curves of pure thin film and Pacman antidot arrays with various separation distances along the x and y directions.

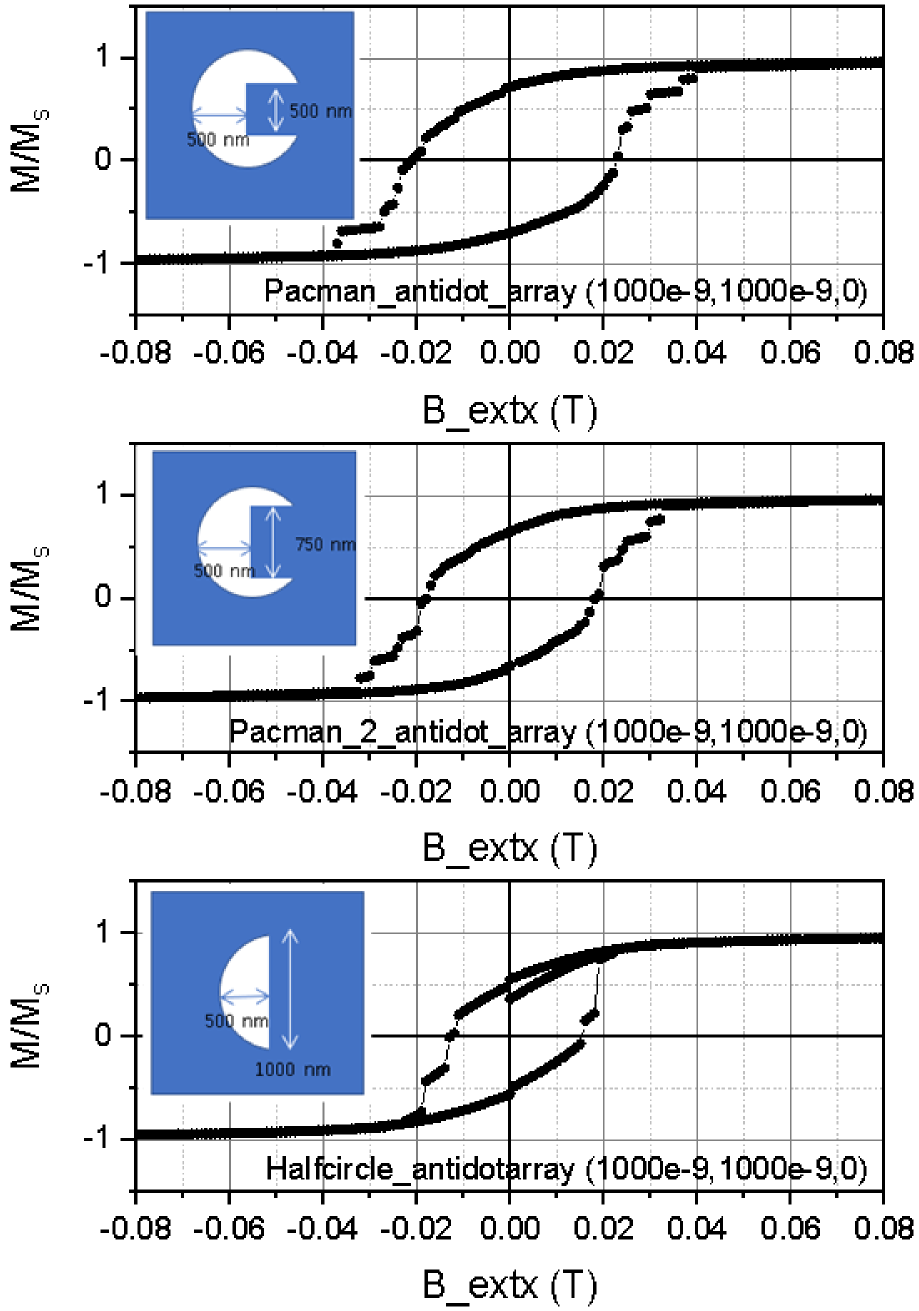

Figure 6.59. Hysteresis curves of Pacman with different sizes and half-circle antidot array structures with the same separation distances of 1 μm along the x and y directions.

The simulated energies of half-circular antidot array film with a separation distance of 1.5 μm are shown in Figure 6.63. At the saturation state of the half-circle antidot array with a separation distance of 1.5 μm along the x and y directions, the anisotropy energy is -5.99×10^{-17} J, demagnetization energy is 1.22×10^{-16} J, exchange energy is 5.21×10^{-18} J, Zeeman energy is -5.18×10^{-15} J, and total energy is -5.11×10^{-15} J. At the remnant state of the half-circle antidot array with a separation distance of 1.5 μm along the x and y directions, the anisotropy energy is -4.21×10^{-17} J, demagnetization energy is 1.08×10^{-17} J, exchange energy is 1.29×10^{-17} J, Zeeman energy is 3.28×10^{-30} J, and total energy is -1.83×10^{-17} J.

The simulated energies of pacman antidot array film with a separation distance of 1 μm are shown in Figure 6.64. At the saturation state of the pacman antidot array with a separation distance of 1 μm along the x and y directions, the anisotropy energy is -2.8×10^{-17} J, demagnetization energy is 5.19×10^{-16} J, exchange energy is 1.56×10^{-17} J, Zeeman energy is -2.48×10^{-15} J, and total energy is -1.98×10^{-15} J.

At the remnant state of the pacman antidot array with a separation distance of 1 μm along the x and y directions, the anisotropy energy is -2.04×10^{-17} J, demagnetization energy is 3.30×10^{-16} J, exchange energy is 4.96×10^{-17} J, Zeeman energy is 3.75×10^{-30} J, and total energy is 3.59×10^{-16} J. The simulated energies of pacman antidot array film with a separation distance of 1.5 μm are shown in Figure 6.65. At the saturation state of the pacman antidot array with a separation distance of 1.5 μm along the x and y directions, the anisotropy energy is -5.75×10^{-17} J, demagnetization energy is 1.09×10^{-16} J, exchange energy is 4×10^{-18} J, Zeeman energy is -4.97×10^{-15} J, and total energy is -4.91×10^{-15} J. At the remnant state of the pacman antidot array with a separation distance of 1.5 μm along the x and y directions, the anisotropy energy is -4.77×10^{-17} J, demagnetization energy is 3.77×10^{-17} J, exchange energy is 1.25×10^{-17} J, Zeeman energy is 3.49×10^{-30} J, and total energy is 2.56×10^{-18} J.

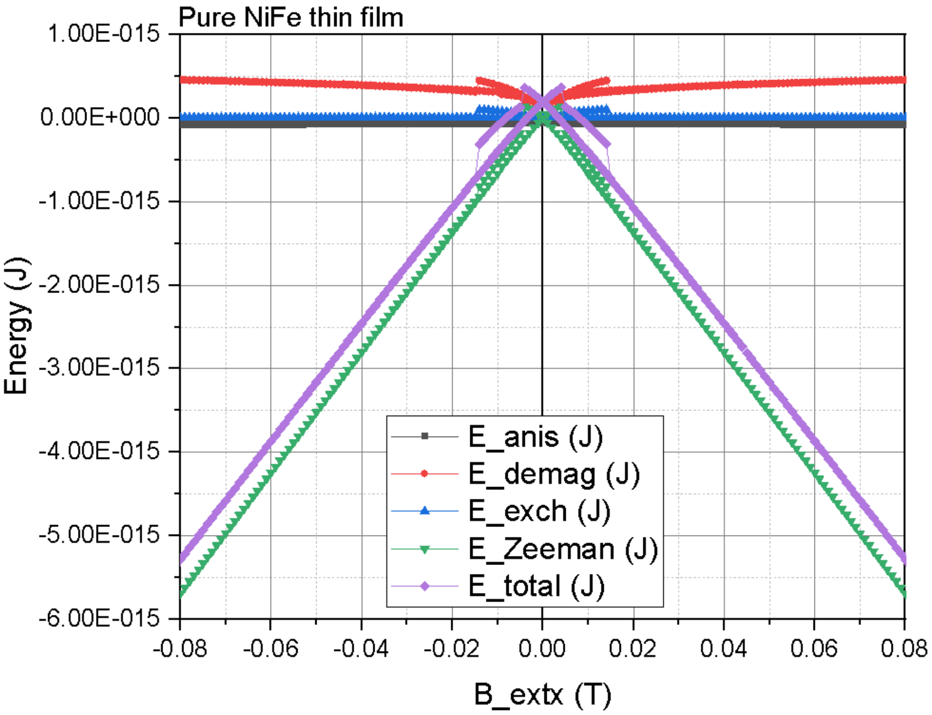

Figure 6.60. The simulated energies of a 20 nm NiFe thin film.

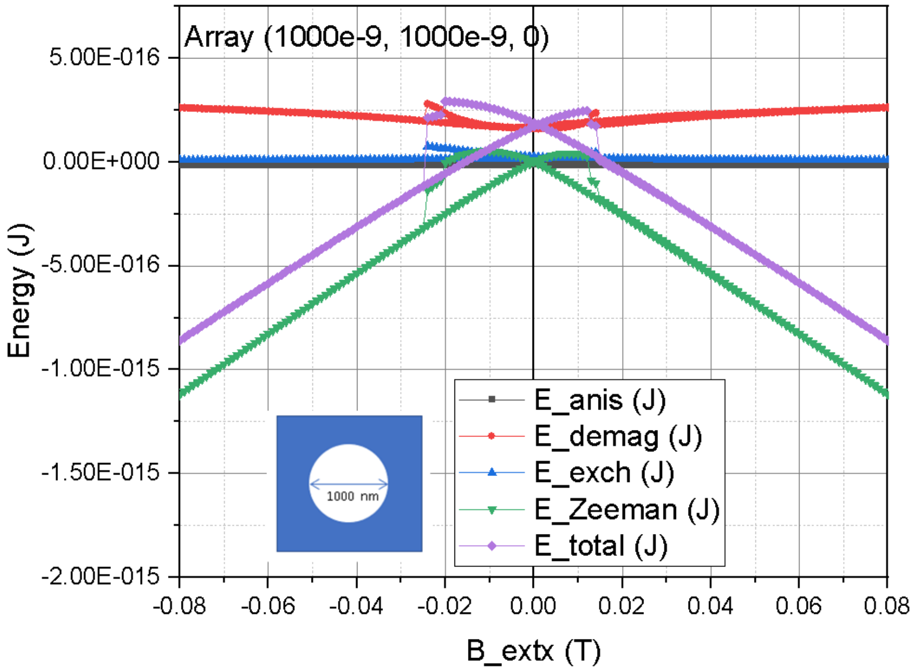

Figure 6.61. The simulated energies of a circular antidot array with a diameter of 1 μm and 1μm edge-to-edge separation distances at x and y directions.

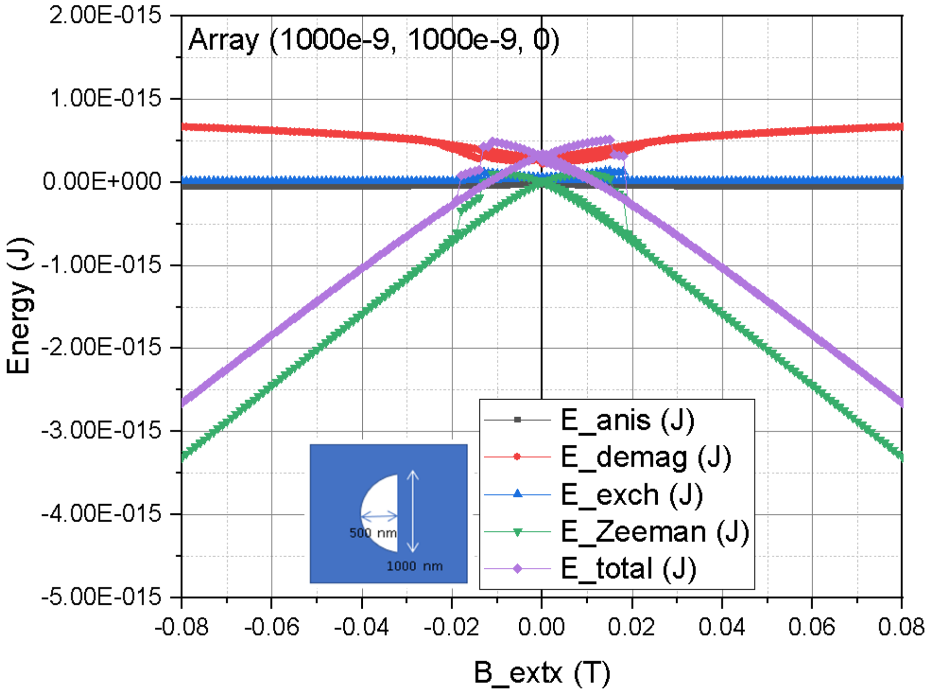

Figure 6.62. The simulated energies of half-circle antidot array structures with a separation distance of 1 μm along the x and y directions.

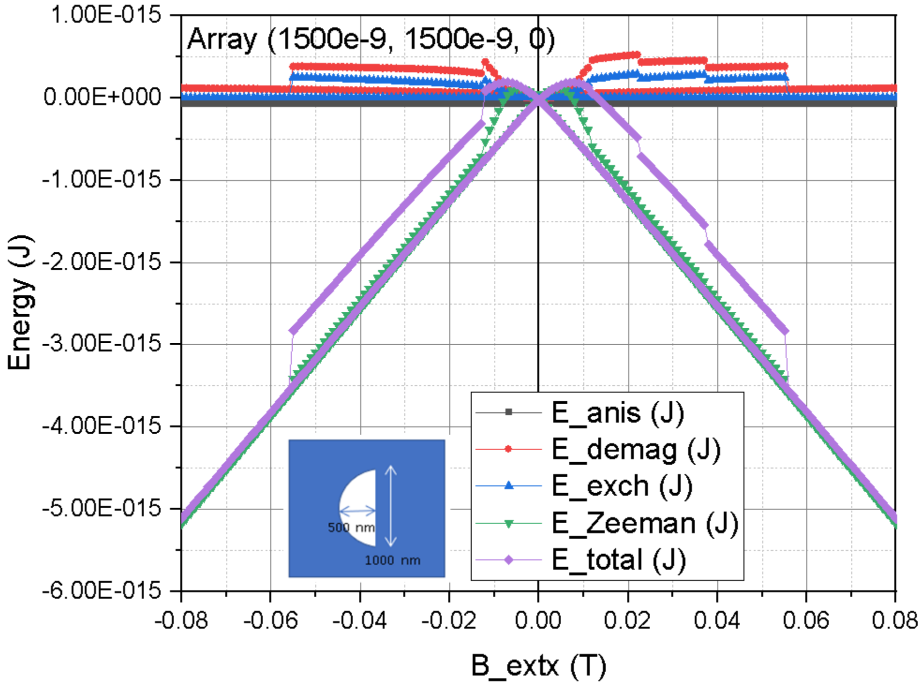

Figure 6.63. The simulated energies of a half-circular antidot array structure with a separation distance of 1.5 μm along the x and y directions.

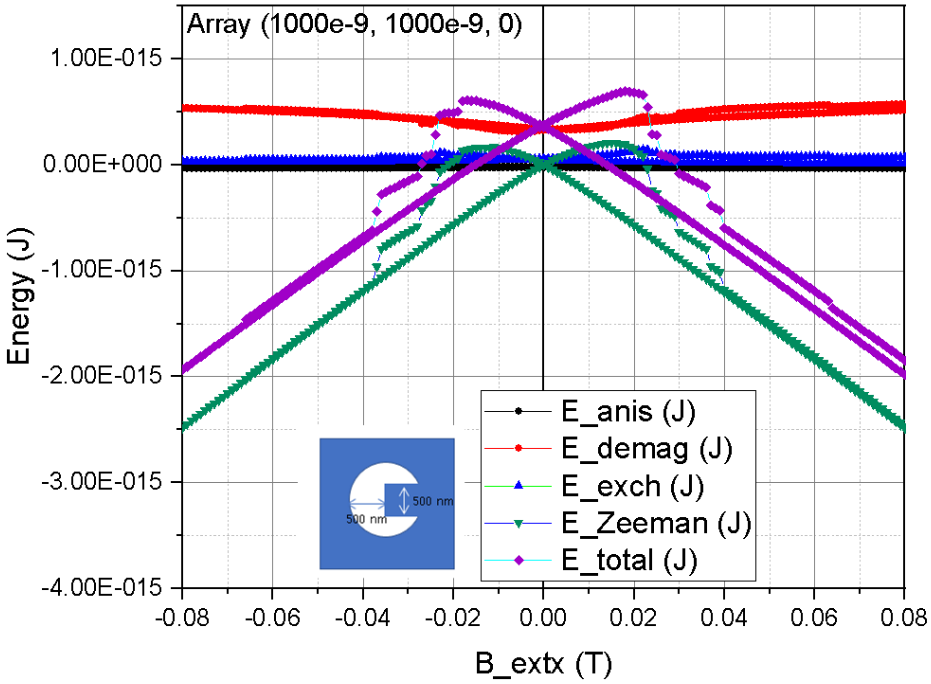

Figure 6.64. The simulated energies of Pacman with a separation distance of 1 μm along the x and y directions.

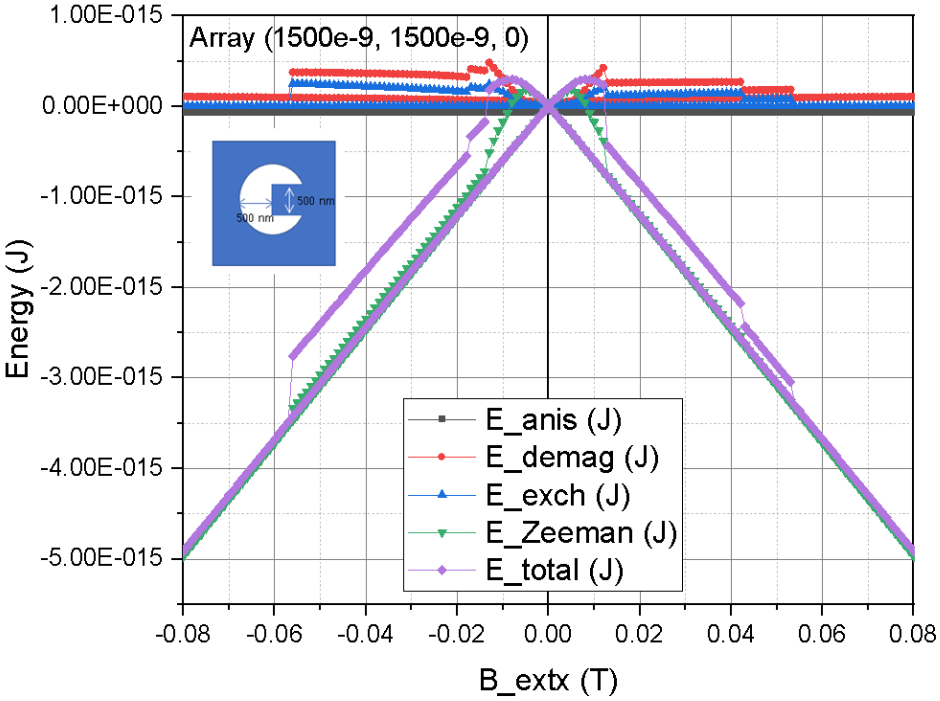

Figure 6.65. The simulated energies of Pacman with a separation distance of 1.5 μm along the x and y directions.

7. RESULTS

The growth of qualitative YIG films with magnetic anisotropy engineering is indeed a very important topic in light of recent developments in magnonics, magneto-optics, and spin-torque transfer properties. YIG thin films with a wide range of thickness were deposited on Si (100) substrate by the PLD technique. The substrate temperature, oxygen pressure, laser parameters, and post-annealing affect the crystallization of the produced YIG thin films. The X-ray diffraction pattern showed that as-grown YIG films were amorphous. From the FMR measurement, there was no microwave absorption signal, so the as-grown films were understood to be not magnetic. We had to anneal the films to create the YIG form. After annealing the film in the air at different temperatures from 750 °C to 850 °C, we gathered the proper crystallization of the films. We realized that XRD peaks became sharp and strong with annealing. Heating the substrate and keeping the temperature at 400 °C did not work for the formation of the YIG phase, but the annealing after deposition helped the improvement of the crystallization. During deposition, the system does not have an equilibrium state, the laser hits the target rapidly with a frequency of 10 Hz and power of 220 mJ and the ablated particles eject from the target and move to the substrate continuously. Because of this rapid process, the atoms did not have enough time to rearrange themselves on the substrate. However, atoms have a long time to arrange and diffuse between layers of the as-grown YIG film during annealing, which explains the crystallization formation due to the post-annealing.

The crystallite size was estimated from the full-width at half maximum (FWHM) of the (420) peaks of the annealed films by implementing the Scherrer's formula which is $D = k\lambda/\beta\cos\theta$ where $k = 0.94$ is a constant, $\lambda = 1.54178A^0$, β is the FWHM of the peak which is interested in. For the films with thicknesses more than 200 nm, the XRD spectrum reveals the polycrystalline structure of YIG film with three characteristic diffraction peaks from the garnet phase which is located at $2\theta = 28.9°$, $32.4°$ and $35.6°$, corresponding to (400), (420) and (422) crystal plane diffraction. The crystallite sizes of 300 and 400 nm YIG films are 2.9 and 15.6 nm, respectively. The crystallite sizes of 15, 20, 35, and 50 nm YIG films are calculated as 344.8, 279.6, 83.9, and 102.7 nm, respectively.

The lattice constants were calculated from indexing of the crystalline planes from the XRD measurement and given in Table 7.1. When the thickness increases, the OOP lattice constant and IP lattice constant approach each other, forming the YIG cubic crystalline structure as in 400 nm YIG film. This can be explained by the tetragonal distortion of the lattice. The OOP lattice constant shrinks, while the IP lattice constant expands from 15 nm to 400 nm. In the XRD profile Figure 4.17, one can observe that (420) peak shifts to a higher angle, which refers to the compression of the crystalline lattice. Since the unit cell volume of YIG is preserved during growth, the c lattice constant elongates out of the film plane, while the in-plane lattice constant a, is compressed because of the smaller lattice parameter of the substrate. The expansion of the c-axis causes a strong tetragonal lattice distortion in all the films. The degree of distortion indicates a tendency to decrease as the thickness increases from 15 to 50 nm. As seen in Figure 4.18, the lattice constants, a and c, approach each other, which refers to the relaxation of the films by increasing the film thickness.

Table 7.1. The in-plane and out-of-plane lattice constants.

	OOP lattice constant (nm)	**IP lattice constant (nm)**
15 nm	12.514	12.103
20 nm	12.507	12.116
35 nm	12.495	12.142
50 nm	12.412	12.305
300 nm	12.386	12.356
400 nm	12.377	12.377

The films in the thickness range of 15 nm -50 nm show only the (420) peak, which we get after annealing at 850^0 C. If we increase the thickness, the films are polycrystalline or have a textured structure. Magnetic easy axis changes when YIG films are polycrystalline or amorphous. From the VSM measurement of the hysteresis curves of

200 nm, 300 nm, and 400 nm YIG films, one can understand that the magnetic easy axis is in the film plane for all the thicknesses due to the shape/dipolar anisotropy. The saturation magnetization is determined as 122 emu/cm^3. The value of the saturation magnetization for bulk YIG is 140 emu/cm^3. The coercivity of both in-plane and out-of-plane hysteresis loops The coercive fields of both in-plane and out-of-plane hysteresis loops for 200 nm YIG film is 47 Oe and 100 Oe, the coercivity of both in-plane and out-of-plane hysteresis loops for 300 nm YIG film is 26 Oe and 45 Oe, and the coercivity of both in-plane and out-of-plane hysteresis loops for 400 nm YIG film is 17 Oe and 35 Oe, respectively. This shows that the coercivity decreases with increasing thicknesses from 200 to 400 nm.

There must be a factor to overcome the shape anisotropy to switch the direction of the magnetic easy axis from the film plane to the film normal. In most cases, crystalline or surface anisotropy or textured structures can trigger perpendicular magnetic anisotropy, which is the case in YIG films between 15 nm and 50 nm. Perpendicular magnetization was observed for all the films, since magneto crystalline anisotropy got stronger than shape anisotropy and forced the easy axis to align perpendicular to the film. Thinner films experienced the lattice distortion strongly. Due to the compressive lattice strain of the film/substrate interface, the expansion along the c-axis caused the easy axis to extend perpendicular to the plane of the film, which resulted in a possession of PMA. Although the OOP FMR spectrum shows perpendicular magnetic anisotropy, there is no in-plane anisotropy in the IP FMR spectrum. OOP FMR spectrum shows that the uniaxial perpendicular magnetic anisotropy decreases when the thickness increases. The large FMR linewidth is due to the defects, roughness, oxygen vacancies, and magnetic inhomogeneities within the film.

Another setup of the experiments consists of 40, 90, and 120 nm YIG films grown on Si (100) by PLD. The difference in this setup with respect to the previous one comes from the observation of spin-wave modes assisting the uniform resonance mode in addition to the PMA feature of the mentioned films. The strain at the Si substrate / YIG film interface due to the lattice mismatch gives rise to a perpendicular magnetic easy axis. During the annealing process, the temperature increased up to 850 °C in 30 minutes and the films were annealed at the fixed temperature of 850 °C for 3 hours and then were cooled to room temperature for a long time. After annealing, inhomogenous cracks were randomly distributed on the film surface, which can be explained by the different thermal expansion coefficients of the film and substrate and the compression of the film lattice during annealing. This leads to the emergence of non-uniform strain regions within the film volume. The distortion of the crystalline lattice is responsible for the perpendicular anisotropy in even 120 nm YIG film. The FMR spectrum of the films shows that the lattice strain did not relax completely, since the spin wave modes which were created in the inhomogeneous magnetic regions still exist in 120 nm film. Magnetization pinning at the surface and interface of the film determines the allowed quantum number of the spin wave modes. Unpinned spins at the free surface and pinned spins at the film/substrate interface were estimated. The exchange stiffness constant (D) is determined by analyzing the FMR spectrum. The linear relation between the resonance field and the square of the mode number implies that the modes are standing spin wave modes and surface modes. We suggest that the spin wave modes around the uniform mode at lower and higher fields are surface spin waves and standing spin waves, respectively. Exchange stiffness was found to be between 1.02×10^9 and 5.12×10^9 Oe cm^2.

Next, the results of the study of magnetic properties of dot/antidot arrays in NiFe thin films will be discussed. The patterns have been obtained using the photolithography method. Ferromagnetic NiFe thin films have been deposited on an array of dot/antidot arrays by using RF sputtering. FMR analysis demonstrates that the angular dependence of the resonance field of the patterned films is quite different compared to the un-patterned film due to the induced shape anisotropy. The FMR spectra of NiFe thin films with dot/antidot array show differences with respect to the pure thin film with the same thickness. Spin wave modes appear near the main resonance mode, which originates from the shape anisotropy. Geometrical parameters of dot/antidot structures affect the resonance spectrum due to the competition between shape and intrinsic anisotropies. FMR measurements were employed to examine the response of a patterned array of NiFe dot/antidot structures to the microwave at 9.1 GHz at RT. The angular variation of FMR spectra was analyzed in IP and OOP geometries by rotating the sample inside the cavity. During the IP measurement, the microwave magnetic field was perpendicular to the film plane and an external DC magnetic field was applied in the film plane. In the OOP geometry, the microwave field was in the film plane, and the applied field was swept from the film plane towards the film normal. The main FMR peak shifted to a lower field value as the dot size increased. Several spin wave modes were observed in the spectrum. Since the dots do not touch each other, the exchange interaction is negligible, so we estimate that the additional modes arise from the dipolar interactions between the dots. Figure 5.4 shows the angle-dependent resonance field graphs obtained from FMR measurements for the 40 nm film with a dot array. The resonance field of the 40 nm pure NiFe thin film in OOP FMR geometry is around 1000 mT, The resonance field of 40 nm NiFe thin film with dot array in OOP FMR geometry is more than 1000 mT, the resonance field of 40 nm pure NiFe thin film with half-circular dot array in OOP FMR geometry is less than 1000 mT. The anisotropy decreased with respect to the pure film. We can call it the effect of shape anisotropy. When the size of the dot decreases, the resonance field also decreases. There are similar values of the anisotropy in IP FMR geometry for pure thin film and dot arrays, but the pure film has two additional spin-wave resonances, and the circular dot array has one additional spin-wave resonance which does not follow the same angular behavior where there is a phase difference between the main uniform mode and the spin wave resonance mode. The half-circular dot array has only the uniform resonance mode. Both in IP and OOP measurement geometry, there is a clear magnetic anisotropy for all the films.

The effect of the dot shape has an influence on the resonance field and excitation of the spin waves apart from the uniform resonance mode. In the IP FMR spectrum of the 40 nm NiFe dot array, we see the creation of spin-wave modes at the 90°. Also, the resonance peak was observed even at very low fields such as 10 mT. Figure 5.3 shows the angular variation of the resonance field for the 20 nm NiFe thin films. There are many spin wave modes at each angle accompanying the main resonance. The number of spin-wave modes decreases, especially in the 4μm diameter dot array, and accumulates around the angle of 90°. For the 6μm diameter dot array, the excited spin wave modes have different phases from the main resonance mode. In the IP FMR geometry, there is anisotropy for all the films. The pure film has two more spin wave modes in IP geometry, the dot arrays do not have additional spin wave modes. For the antidot array with the same diameter, spin wave modes were observed at the field of around 100 mT in Figure 5.10. In the case of the ring dot array, the width of the ring dot has led to the spin wave mode resonance with a different phase from the main resonance mode as shown in Figure 5.7. However, the effect of the separation distance between the ring dots did not alter the angular resonance profile significantly. In the IP FMR geometry, the smallest width-ring dot has less anisotropy than the other ring dot arrays. All the ring dot arrays do not have additional spin wave mode excitation in the IP geometry as shown in Figure 5.8.

After the analysis of the dot array structures, the dynamic response of the antidot arrays to the microwave absorption will be given in the following. Antidot arrays have gathered a lot of interest due to their potential applications such as ultrahigh-density data storage, magnonic crystals, and magnetic metamaterials. For this reason, it is important to study their magnetization dynamics well. Antidot arrays with different shapes, different sizes, and inter-antidot spacing in the micron range have been fabricated by lithography. The effect of the shape of the antidot structure on the FMR spectrum is investigated for the pure thin film, antidot arrays of the circle (Z2), large pacman (Z8), and narrow pacman (Z6) structures in Figure 5.14. Taking into account the OOP FMR geometry, while the resonance field of the pure thin film is about 1000 mT, introducing the circular antidots with a diameter of 3 μm causes a decrease of the resonance field down to 850 mT. When we compare the resonance fields of the circular and pacman antidots with the same diameter and separation distance of 3μm, we see that the pacman antidot array needs a much larger field ($\approx$ 1100 mT) to bring the system to the resonance. For the narrow pacman (Z6), we could not obtain a well-defined angular variation of the resonance fields like the others due to technical problems during the measurement and reading of the data. In the IP measurement geometry, all the aforementioned films have a pronounced magnetic anisotropy. The difference between the minimum and maximum values of the resonance films in the circular antidot array is 18 mT while the pure film has a less resonance variation of 7 mT. When we compare the anisotropy between the circular and pacman antidot structures, the circular one possesses a higher value of the in-plane anisotropy. When the total pacman antidot size decreases, the anisotropy tends to increase, as seen in the case where the variation of the resonance field in the narrow pacman antidot array is 18 mT, while it is 4 mT for the large one.

For the half-circular antidot array, Figure 5.15 demonstrates that the resonance field of half-circular antidot structure with larger size (7 μm) is more than 1500 mT, and decreases to 1400 mT which is the resonance field of the pure thin film for the 5 μm size of the half-circular antidot. We observe a smaller resonance field that is less than 1200 mT for the size of 3 μm. The shape effect is seen clearly in the angular behavior of the resonance field of spin-wave modes in the 3μm-size half-circular antidot array. The IP FMR measurement in Figure 5.16 shows that the pure thin film has a 25 mT variation of the resonance field while the antidot arrays have a smaller change in the resonance field. 7 μm-size antidot structure has larger IP anisotropy than 5 μm and 3 μm-size antidot structures. Especially, the angular variation of the spin wave resonance fields is more strength than the main resonance in 3 μm-size antidot array.

The effect of the distance between the pacman-shaped antidot structures and their size has been studied, as well. Figure 5.17 shows the effect of the different distances between the antidots at the y direction on the angular resonance fields for OOP and IP measurement geometry while keeping the other parameters constant. When the distance is larger, the number of the spin wave modes increases since the region with the film coating is larger. Unfortunately, for this experimental setup, the maximum value of the resonance fields at around 90 ° are missing for both antidot arrays since the angle step is not well assigned to follow the shift of the resonance peak around the angle of 90 °. But we can say that more spin wave modes are in resonance at the larger distance between the antidots. In the IP measurement geometry, the anisotropy decreases compared to the pure thin film. The effect of the pacman antidot size is shown in Figure 5.18. The angular variation of the resonance field in IP and OOP FMR measurement of the pacman antidots with sizes of 4 μm and 5.5 μm, the resonance field is less than that of the pure thin film. The larger antidots exhibit smaller IP anisotropy, as expected.

By employing a micromagnetic simulation program, Mumax3, the magnetization reversal mechanism of different dot/antidot structures and arrays were investigated. One can tailor the coercivity and the remanence by changing the size and the separation distance between dots/antidots and also the film thickness. The results of the simulations show that the coercivity increases with decreasing dot size in the case of circular, pacman, and half-circular dots. When the separation distance between the dots (2 μm) in an array increases, the coercivity decreases. For the array of dots and antidots, the coercivity of the antidot array is larger than the dot array with the same diameter and thickness, and separation distance (2 μm, 2 μm).

Next, the domain structures were studied in the ring-type dots. The competition between the magnetostatic and exchange energies determines the magnetic states. In the ring dot study, vortex and onion states were obtained, and the transitions between vortex and onion states were studied. Plateaus in the hysteresis loops correspond to different magnetization configurations in the magnetization reversal process. Ring structures show magnetic vortex configuration and a small remnant magnetization at zero applied fields. One of the conclusions of the ring dot magnetization reversal process is that in the onion state, the helicity of the two vortices determines the formation of flux-closure states in the reversal process. If the two vortices have opposite helicity, the onion state transforms to the reverse onion state without the flux-closure state between. The thickness and width affect the coercive field and the remnant magnetization of the rings. Further, the magnetization reversal of the 3D nanostructures was studied. The experimental and simulation results of the magnetization curves showed the vortex magnetic state formation during the field reversal process. The energy values were calculated from the simulations. From saturation to the vortex state, the exchange and total energy of the hemisphere array increase, while demagnetization and Zeeman energies decrease. There is no remnant magnetization and coercive field for the single-hemisphere dot structures. When the hemisphere size increases, the magnetization loops are displayed at higher fields. The energy values increase, as well. The separation distance influences the hysteresis profile in a hemispherical dot array. For example, the magnetization reversal of the hemispherical dots with a separation distance of 200 nm is similar to the hysteresis loop of a single hemispherical dot. The simulated energies of both the single dot and the dot array are very close to each other. However, it completely changes when the separation distance is 128 nm. In addition to the dot structures, the antidot arrays were also analyzed by the Mumax3 program. When the antidot size increases, since the area between the antidots reduces, the magnetization reversal is not easy. The pacman-shaped antidot has a larger coercive field, while the half-circle-shaped antidot has less coercivity. When the distance between the holes increases, the coercivity decreases. The energies for the antidot arrays and pure thin film were plotted as a function of the field.

8. CONCLUSION

This thesis reports on the results of experimental studies of the structural and magnetic properties of yttrium iron garnet (YIG) thin films grown by pulsed laser deposition technique. YIG thin films with perpendicular magnetic anisotropy represent a requirement for novel magnonic and spin-related applications, i.e. for fast response in magnetic memory devices, logic devices, spin-transfer torque, and magneto-optical device applications. Observing the presence of PMA in insulating materials is a rare magnetic phenomenon. In this work, we have achieved to obtained perpendicularly magnetized YIG thin films on a Si (100) substrate. We have investigated the phase formation, crystallization, and magnetic properties of the YIG thin films prepared on Si (100) substrates by PLD. The effect of post-deposition annealing temperature and thickness on the crystal structure and magnetic anisotropy were explored. XRD analysis revealed that post-annealing provides a high-quality crystallization of YIG films. The lattice mismatch and the thickness factor result in a tetragonal distorted lattice structure that affects the magnetocrystalline anisotropy. The crystalline structure and magnetic properties are related to each other to the extent that tetragonally distorted lattices exhibit PMA. Strong magneto crystalline anisotropy and the resultant PMA emerge due to the compressive strain caused by lattice mismatch between the Si substrate and the YIG thin film. In conclusion, as far as our best knowledge we, for the first time, report PMA-oriented YIG thin films grown on the Si substrate. Unlike the literature, it is an original study with a non-garnet substrate without the use of any additional layer or doping material. We showed that a compressive strain induced by the lattice mismatch of the YIG/Si structure is the main reason for perpendicular magnetization. Our study revealed that the structural and magnetic properties of YIG thin/ultra-thin films on the silicon substrate can be adjusted by controlling the thickness and annealing process. For the films with thicknesses of 40 nm, 90 nm, and 120 nm, in addition to PMA, an even and odd number of spin-wave modes were obtained from the FMR spectra. The spin wave modes were explained as the standing spin wave modes and surface spin wave modes. The presented study has some superior properties with respect to the YIG-related literature such that the use of standard PLD technology, no further complications, the use of cheap substrate which does not contain magnetic ions (in an amount causing interference with the film magnetism) and the films reveal PMA in the 15-120 nm range of thickness are remarkable for the YIG magnetic insulator to be widely used in many areas where garnet substrates are not suitable. Perpendicularly magnetized YIG thin films on the Si substrate will allow the modification of spin wave propagation and fabrication of advanced spin wave devices.

The other experimental study of this thesis is about the investigation of the magnetic properties of dot/antidot arrays in NiFe thin films. The array of dot/antidot has been produced by the lithography technique. Ferromagnetic NiFe thin films were deposited on the array structure by using RF sputtering and, following the lift-off process, the photoresist was removed from the film surface completely. FMR analysis of the array patterns demonstrates that the angular dependence of the magnetic anisotropy field of the patterned films is quite different compared to the film grown on an unpatterned film due to the induced shape anisotropy. The size and shape have an effect on the magnetization dynamics and determine the value of the induced anisotropies. The value of the resonance field changes with the size of the dots. The IP magnetic anisotropy of dot arrays decreases compared with the pure thin film. While several spin wave modes appeared next to the uniform resonance peak in the OOP geometry, the number of excited spin waves decreases or vanishes for the IP geometry. The 0.5μm width-ring dot array shows the effect of shape anisotropy in OOP measurement geometry. The half-circular antidot array is another example that has a clear shape anisotropy effect in the OOP geometry. The broadening of the resonance linewidth is due to the spin waves combined with the uniform resonance peak. In addition, microwave absorption takes place in the patterned films by applying very small field values.

The simulation of the patterned films shows that the magnetization reversal mechanism is strongly influenced by the shape, size, and distance between the dot/antidot structures. The hysteresis loops show different characteristics compared to the unpatterned film depending on the shape, size, and separation distance. Demagnetization is related to the shape effect. These defects in thin films can be used in microwave and spintronic applications such as waveguides, filters, and high-density data storage. In conclusion, dot/antidot arrays in magnetic thin films have the ability to control magnetization reversal and domain configurations.

8.1. Summary

Magnetic garnet films have been considered a good alternative material to ferromagnetic conductors in spintronics applications since the beginning of the 1980s. Since garnets are mainly composed of oxides that make them insulators, information losses due to Eddy currents are very low. Insulating garnets are applied in high-frequency applications and are used for fast switching of magnetic properties since their magnetization is very low. Being able to control magnetic anisotropy in garnets is currently an important and popular subject. Particularly, perpendicularly magnetized garnet films are implemented for spin-orbit switching, spin transfer torque, and reliable and fast response. Yttrium iron garnet (YIG) is an excellent magnetic insulator with a very low damping constant. Bulk crystal or thick YIG films in the micron range are very suitable for applications like microwave filtering, tuning, insulators, and phase shifters. When the thickness scale of YIG reduces down to the thin/ultrathin regime, it is much easier to manipulate magnetic properties, which is crucial for spintronic and magneto-optical applications. Thus, it is important to have an accurate structural and magnetic characterization of YIG thin films. In this thesis, YIG films were prepared by Pulsed Laser Deposition (PLD) which is a technique to obtain high-quality ferrite films for microwave device applications on naturally oxidized Si (100) substrates. The growth conditions were optimized by adjusting laser power, oxygen partial pressure, and thermal treatment parameters. The chemical composition and stoichiometry ratio of the samples were analyzed by X-ray Photoelectron Spectroscopy (XPS) technique and the YIG phase formation was confirmed. The crystal structure of the YIG films was also characterized by XRD analysis. XRD analysis shows that the annealing helps the crystallization of YIG films. XRD measurement revealed that the (400), (420), and (421) characteristic peaks of the YIG phase were obtained for the 200, 300, and 400 nm YIG films and only the (420) peaks were observed for thinner films. From the VSM measurements, the polycrystalline films have an IP magnetic easy axis, while thinner films have OOP magnetic easy axis. The effect of annealing temperature and thickness on magnetic properties was investigated by Ferromagnetic Resonance (FMR) technique at 9.5 GHz. FMR is one of the most sensitive and precise methods to determine magnetization, magnetic anisotropy, dynamic change/dipolar energies, and relaxation and damping in magnetization dynamics. The FMR spectra from all samples have been recorded at room temperature for different angles between the applied dc magnetic field and the film normal in OOP and IP geometry. There is no magnetic anisotropy in IP geometry. The FMR spectrum in OOP geometry shows the PMA behavior of the films between 40 nm and 120 nm. The reason is basically the compressive strain induced by the lattice mismatch between YIG and Si. In this thesis, for the first time, spin wave modes were observed in addition to PMA achievement in YIG on a non-garnet substrate. Multiple spin wave modes were enhanced in 40, 90, and 120 nm films. Standing spin wave modes were excited and the spin wave modes along the lateral of the film originated from the inhomogeneous confined magnetic regions on the surface. Different from the literature, no additional layer or doping material was used in the fabrication of YIG films, and with the use of Si as a common and available substrate, a cheaper fabrication process is possible for a wide range of applications like the electronic industry. These findings provide a platform for the next-generation Yttrium Iron Garnet-based electronic devices, advanced magnonics, and spintronics applications.

In addition to YIG-related studies, we studied the effect of the dot/antidot array on the magnetic properties of NiFe thin films by means of both experimental and micromagnetic simulations. Antidot structure is a periodic arrangement of nano/microscale holes in the continuous film and controls magnetic properties such as tuning the magnetization reversal, magnetic domain structure, and magnetic anisotropy. Antidots introduce locally distributed shape anisotropy fields and behave as pinning centers for domain wall propagation and modify intrinsic magnetic anisotropy locally. These defects provide applications such as magnonic crystal waveguides, spin wave emitters, microwave filters, and high-density magnetic data storage. Arrays of NiFe dots/antidots with diameters in the μm range were fabricated by the lithography and RF sputtering technique. Magnetization configuration of the NiFe dot/antidot array was obtained by using a finite difference discretization modeling based micromagnetic simulation program, Mumax3, which uses Landau Lifshitz Gilbert Equation. The magnetization curves for the single circle, half-circle, and pacman shape dots were obtained. Then, dot arrays with different separation distances were simulated. The hysteresis loop of a dot array and an antidot array with the same size and separation distance was plotted. Different shape dots were studied. The domain configurations were investigated. In addition, we have also prepared antidot arrays with varying sizes and shapes. The magnetization reversal of NiFe antidot arrays has been systematically studied. The hysteresis loop profile is modified due to the demagnetizing fields between the antidots. We also observed that the domains can be controlled by altering the antidot diameter. The results show an increase in the coercivity and a decrease in the remanence of the films with the antidot array compared to the continuous film.

The size and the inter-pattern spacing of the antidots in the NiFe thin film influence the magnetization reversal. The size and shape determine the value of the induced anisotropies in square antidot arrays. FMR spectrum changes with the size of the dots/antidots. The IP magnetic anisotropy of arrays decreases compared to the pure thin film. While several spin wave modes appeared around the uniform resonance mode in the OOP geometry, the number of spin waves decreases or vanishes in the IP geometry. In the OOP FMR spectrum, magnetostatic spin wave modes originated from the confinement along the film lateral, change with respect to the dot size. In IP FMR measurement, spin reorientation with respect to the size of the dot/antidot structures was observed. The simulation of the patterned films shows that the magnetization reversal mechanism is strongly influenced by the shape, size, and distance between the dot/antidot structures. The domain configurations and the coercive field are related to the shape and distance between the structures. Below the saturated regime, each domain has a different switching mechanism and a different resonance mode. Therefore, in the FMR spectrum, depending on the shape, in the saturated regime, we still observe additional resonance modes that imply the existence of different domains rather than a single domain.

8.2. Future Work

The experimental studies of the simulated microstructures will be performed, and VSM, FMR measurements, and SW excitations at different microwave frequencies will be done. In quantum magnonics, YIG material is a converter in hybrid systems. At low temperature in the mK range, YIG films with PMA is not studied. The next step is to study the quantum states of YIG with PMA at mK low temperatures. Antidots/dots array structures can be used as microwave filters and converters at some specific frequency. Depending on the shape, unique array structures will be used for information coding and encoding applications by microwave absorption. The variance in shape alters the domains, spin wave modes, spin wave absorption, and transmission, which is highly important for cryptologic applications. Within the thesis, the magnetization curves and the energy of the 3D patterned dot arrays were determined by running the Mumax3 program. The magnetization states of the cone and pyramid shape array structures were visualized between Figure 8.1 and Figure 8.5, and Figure 8.6, respectively. Figure 8.7 shows the energy variations of a pyramid dot during the magnetic field reversal process. In future work, experimental studies of the simulated structures will be done, which cover the fabrication of the dot structures by lithography and Permalloy deposition, and VSM and MOKE measurements of the patterned films. By changing the dot size and the interspace distance between dots, the variation of the magnetization configuration will be determined. The FMR measurements will give the spin wave spectrum depending on the shape effect, the anisotropy energies will be calculated.

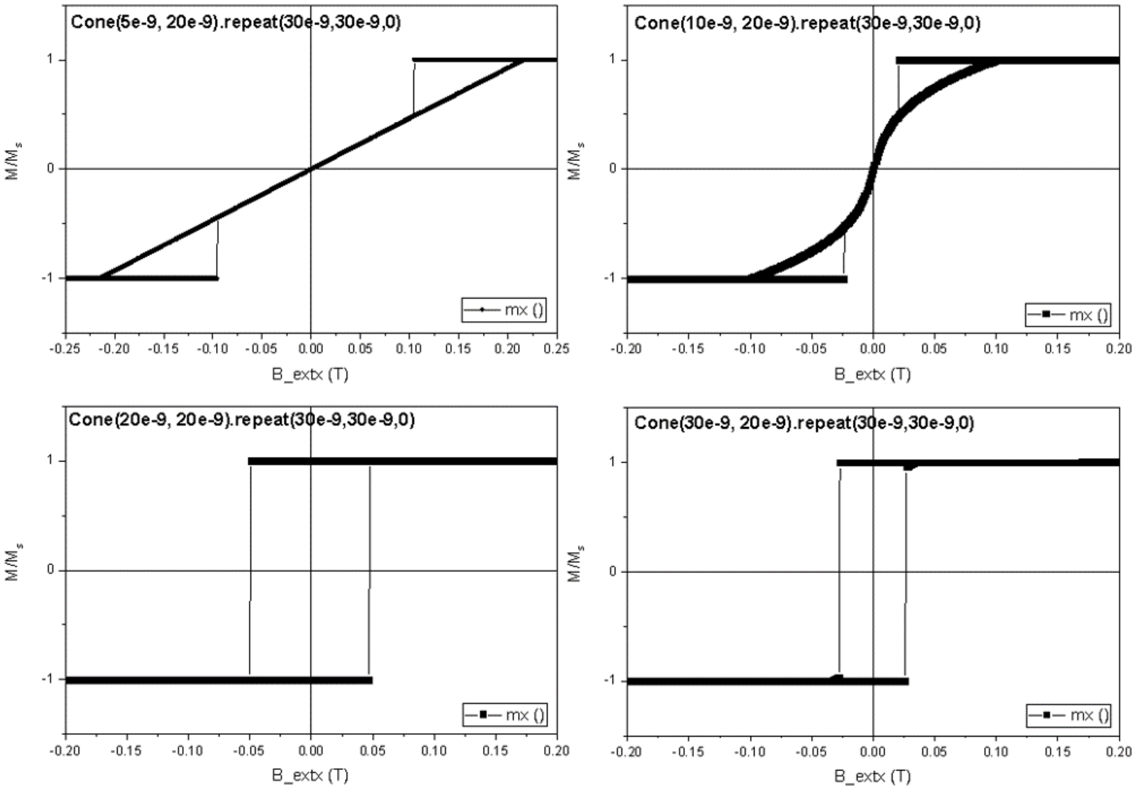

Figure 8.1. A cone array with a diameter of 5, 10, 20, and 30 nm, a height of 20 nm, and a separation distance of 30 nm at x and y directions.

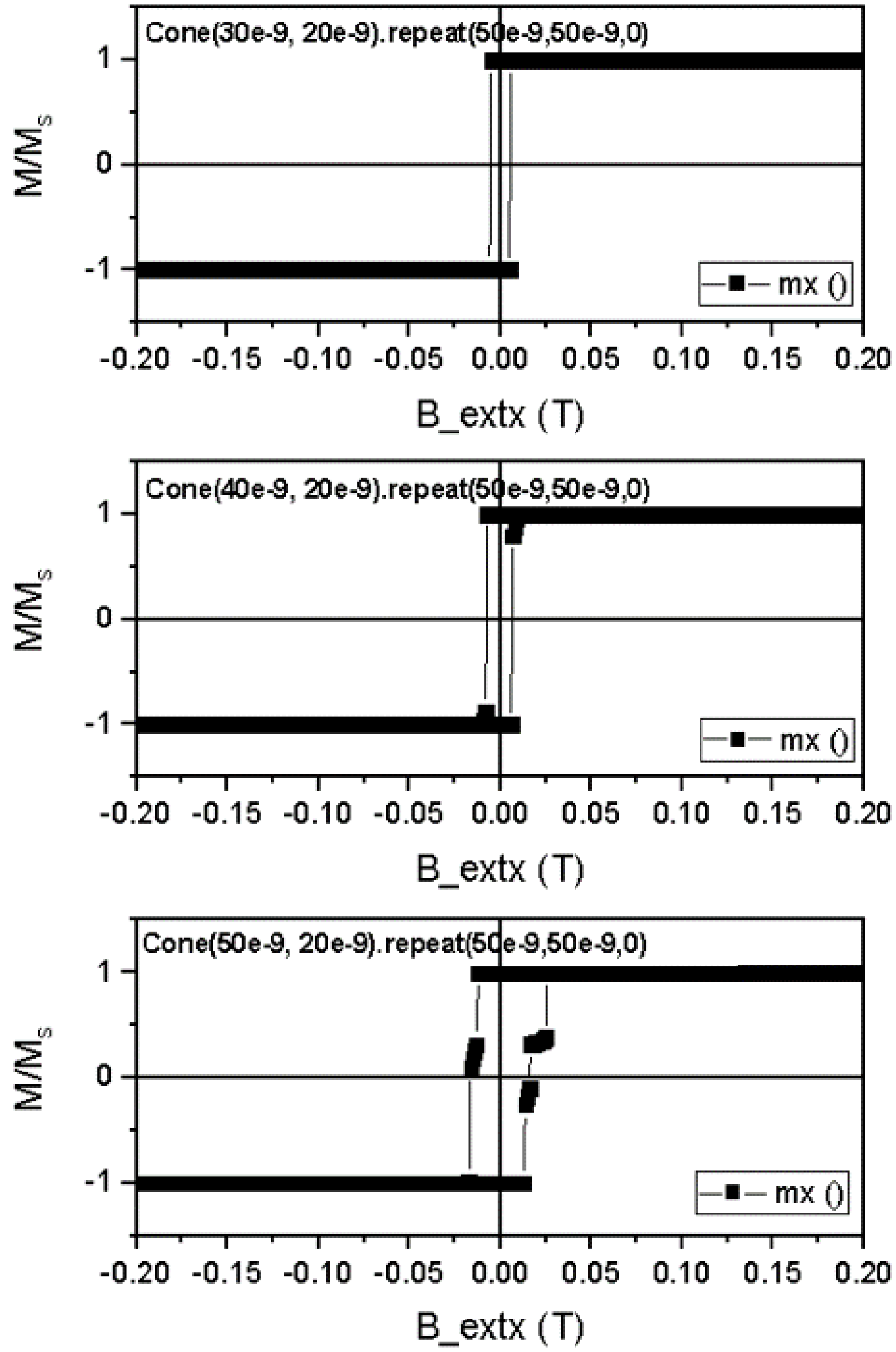

Figure 8.2. A cone array with a diameter of 30, 40, and 50 nm and a height of 20 nm and separation distance of 50 nm at x and y directions.

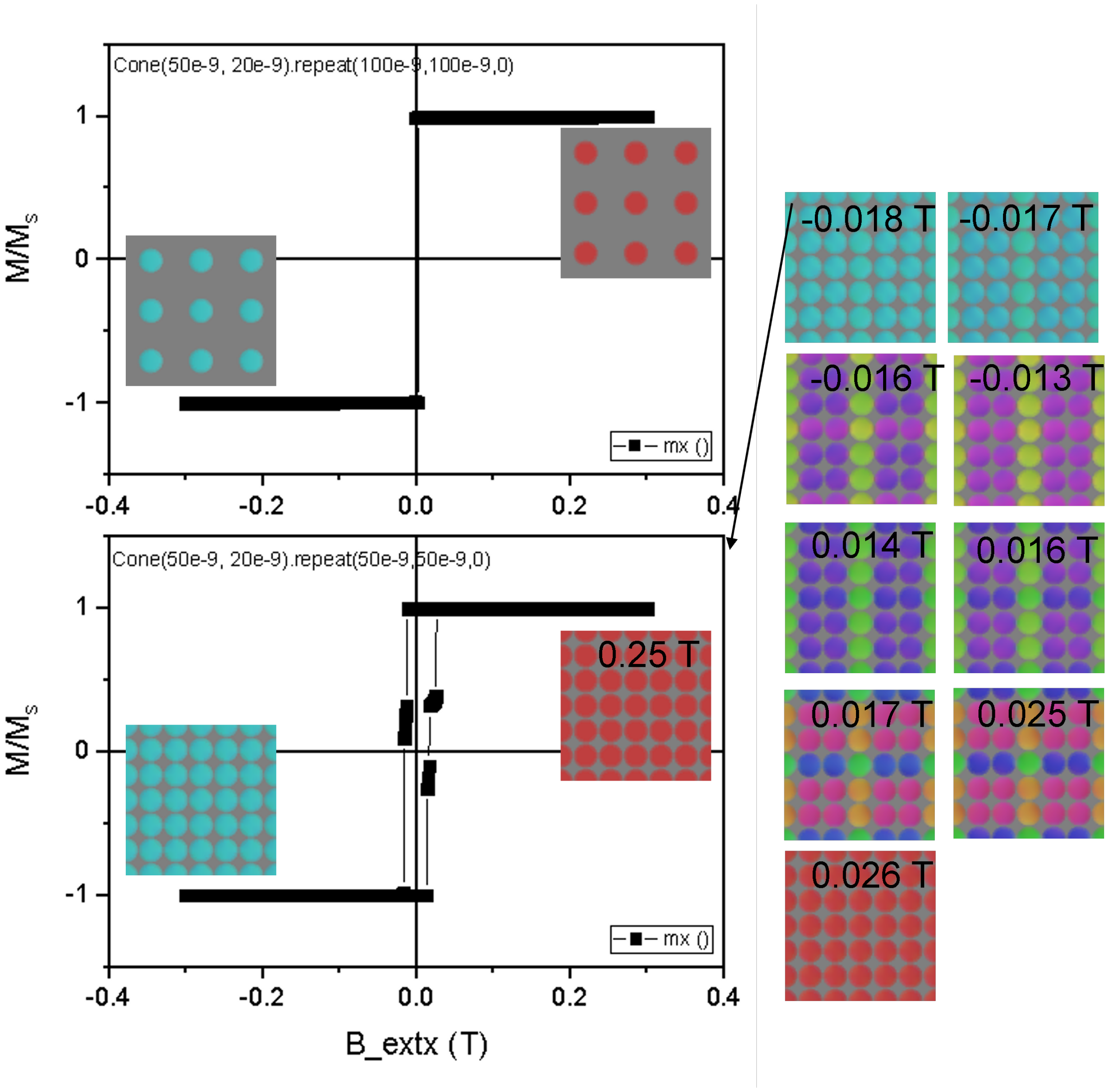

Figure 8.3. A cone array with a diameter of 50 nm a, a height of 20 nm, and a separation distance of 50 and 100 nm at x and y directions.

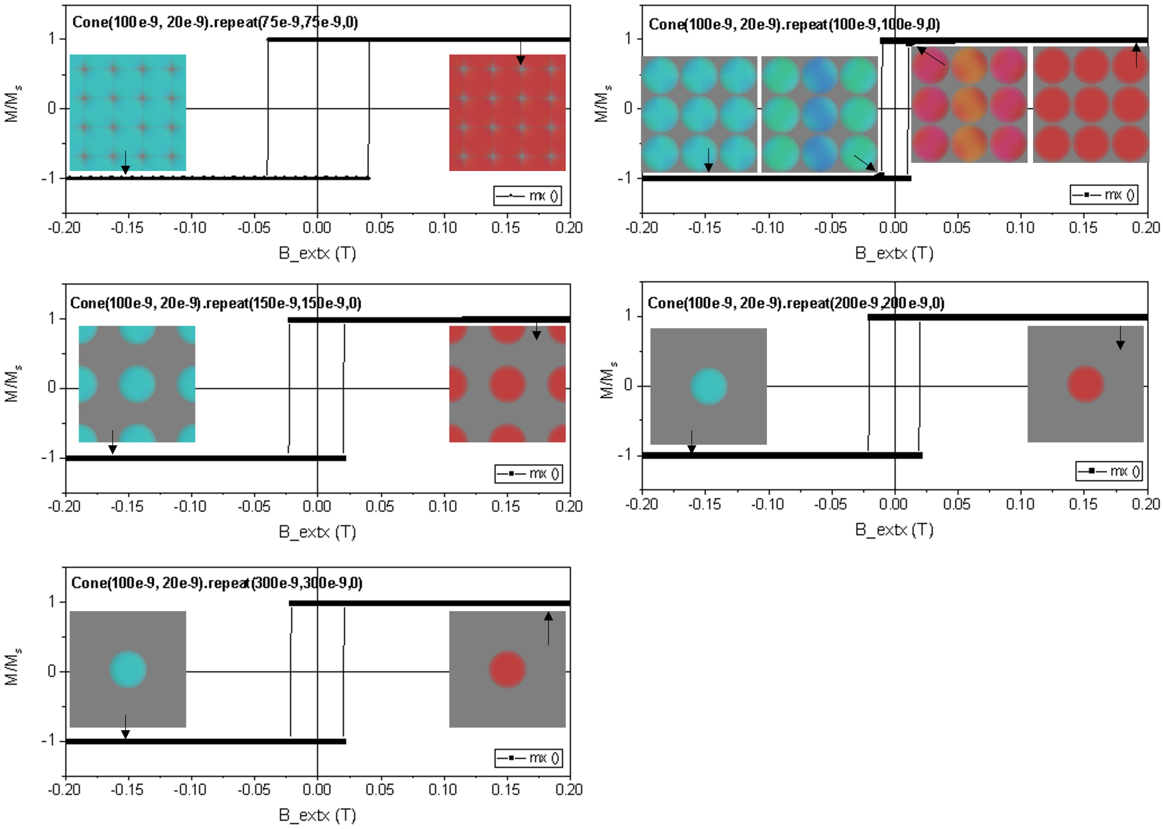

Figure 8.4. A cone array with a diameter of 100 nm and a height of 20 nm and various separation distances at x and y directions.

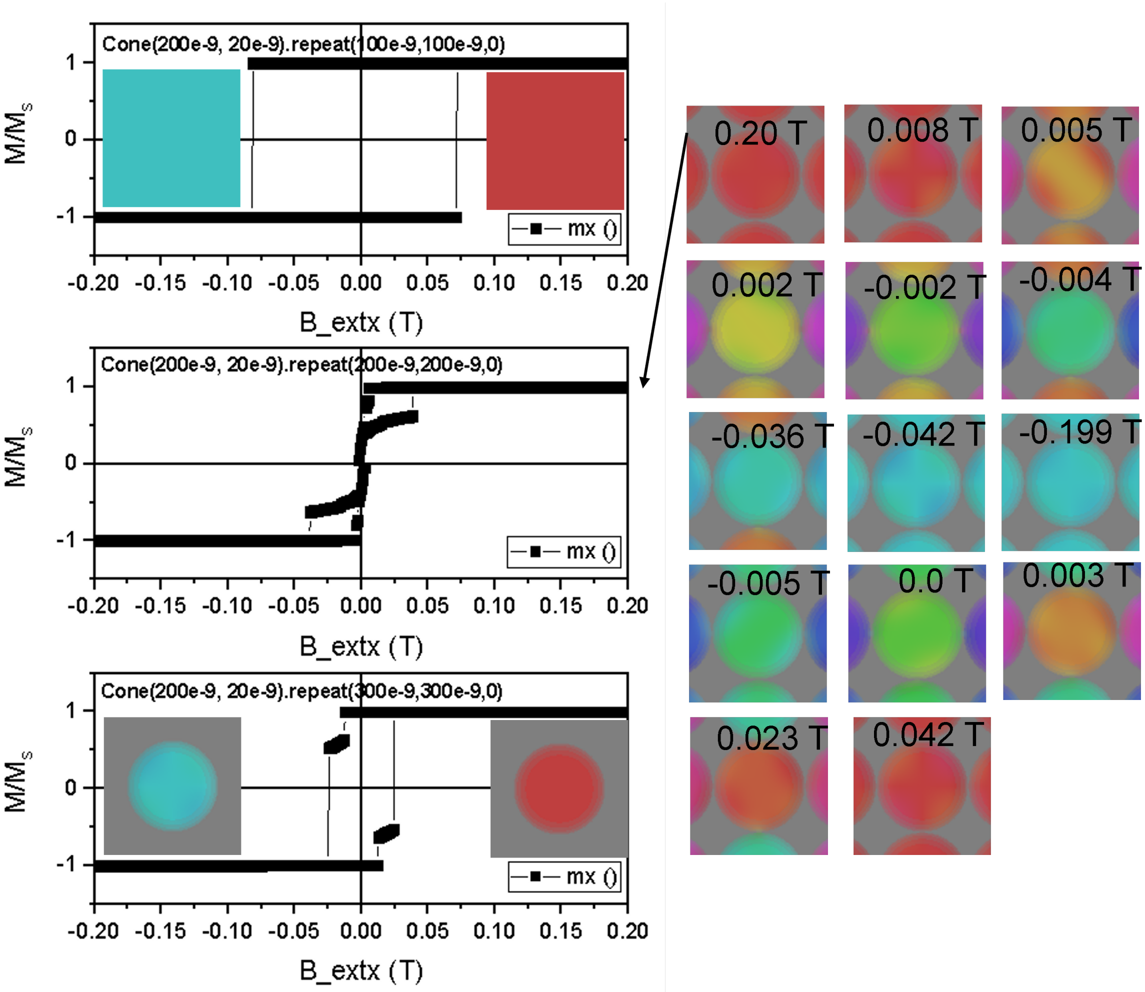

Figure 8.5. A cone array with a diameter of 200 nm, a height of 20 nm, and various separation distances at x and y directions.

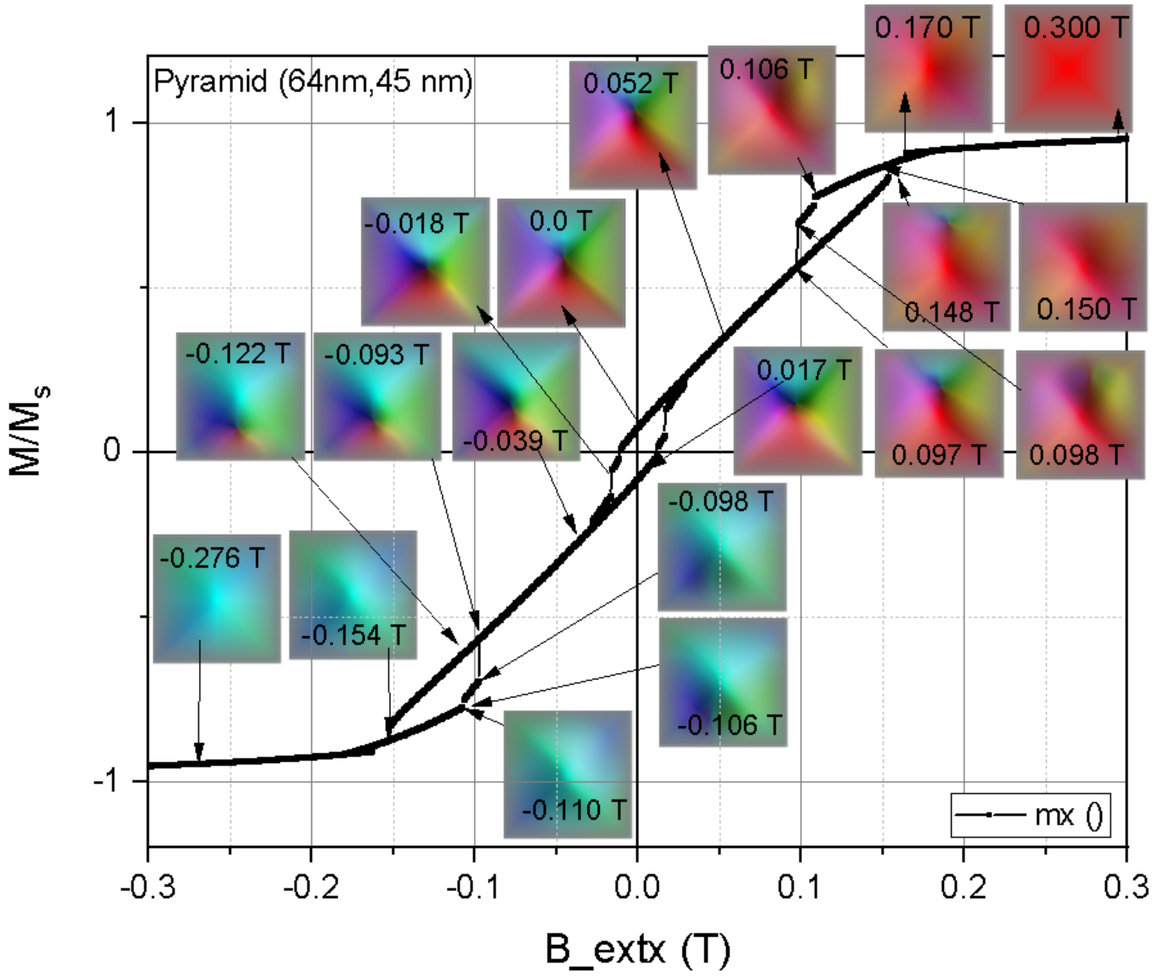

Figure 8.6. The hysteresis curve of a pyramid dot with a size of 64 × 64 nm^2 in the x-y plane and 45 nm height in the z-direction.

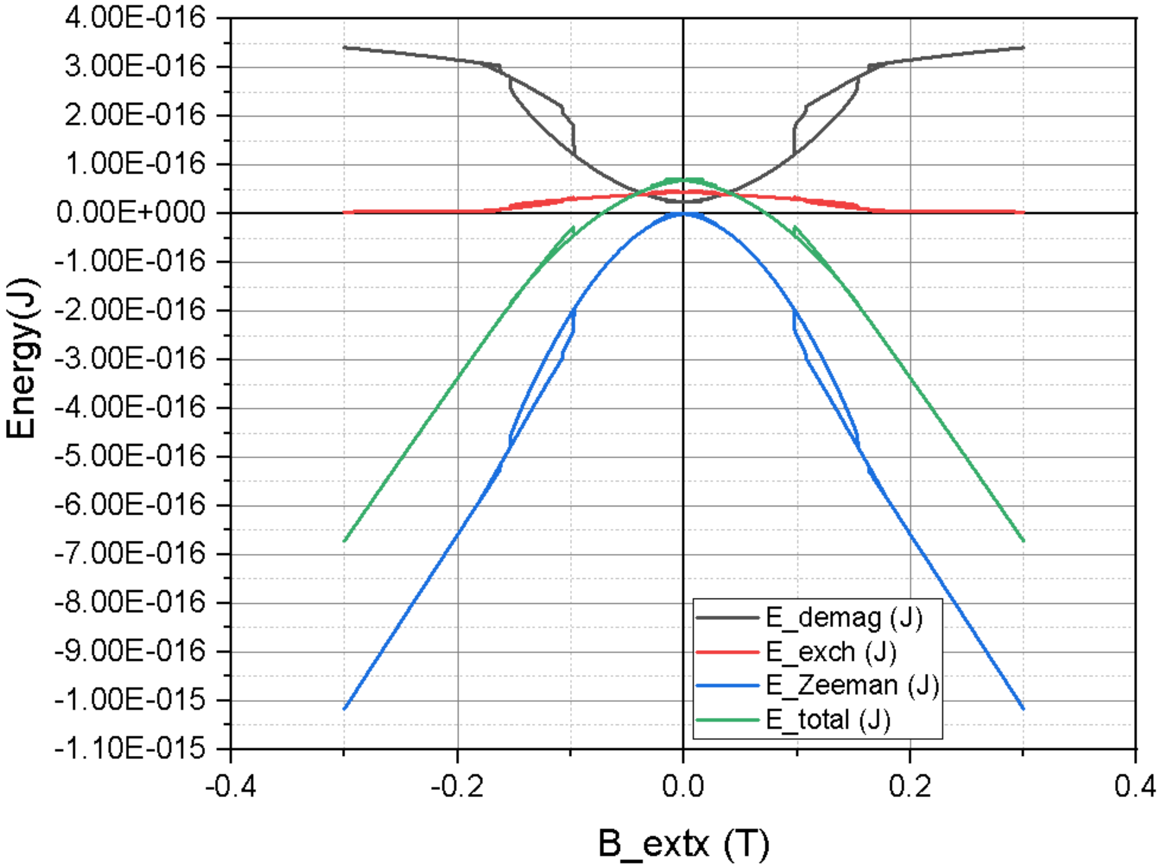

Figure 8.7. The calculated energies of a pyramid dot with a size of 64 × 64 nm^2 in the x-y plane and 45 nm height in the z-direction when the field is swept from 0.3 T to -0.3 T and vice versa.

REFERENCES

1. Liu, L., O. Lee, T. Gudmundsen, D. Ralph and R. Buhrman, “Current-Induced Switching of Perpendicularly Magnetized Magnetic Layers Using Spin Torque From The Spin Hall Effect”, *Physical Review Letters*, Vol. 109, No. 9, p. 096602, 2012.

2. Everschor-Sitte, K., J. Masell, R. M. Reeve and M. Kläui, “Perspective: Magnetic Skyrmions—Overview of Recent Progress in an Active Research Field”, *Journal of Applied Physics*, Vol. 124, No. 24, p. 240901, 2018.

3. Montazeri, M., P. Upadhyaya, M. C. Onbasli, G. Yu, K. L. Wong, M. Lang, Y. Fan, X. Li, P. Khalili Amiri, R. N. Schwartz *et al.*, “Magneto-Optical Investigation of Spin–Orbit Torques in Metallic and Insulating Magnetic Heterostructures”, *Nature Communications*, Vol. 6, No. 1, p. 8958, 2015.

4. Chappert, C., A. Fert and F. N. Van Dau, “The Emergence of Spin Electronics in Data Storage”, *Nature Materials*, Vol. 6, No. 11, pp. 813–823, 2007.

5. Princep, A. J., R. A. Ewings, S. Ward, S. Tóth, C. Dubs, D. Prabhakaran and A. T. Boothroyd, “The full Magnon Spectrum of Yttrium Iron Garnet”, *Nature Portfolio Journal Quantum Materials*, Vol. 2, No. 1, p. 63, 2017.

6. Serga, A. A., A. V. Chumak and B. Hillebrands, “YIG Magnonics”, *Journal of Physics D: Applied Physics*, Vol. 43, No. 26, p. 264002, 2010.

7. Kajiwara, Y., K. Harii, S. Takahashi, J. Ohe, K. Uchida, M. Mizuguchi, H. Umezawa, H. Kawai, K. Ando, K. Takanashi, S. Maekawa and E. Saitoh,

"Transmission of Electrical Signals by Spin-wave Interconversion in a Magnetic Insulator", *Nature*, Vol. 464, No. 7286, pp. 262–266, 2010.

8. Chumak, A. V., A. A. Serga and B. Hillebrands, "Magnon Transistor for All-Magnon Data Processing", *Nature Communications*, Vol. 5, No. 1, p. 4700, 2014.

9. Serga, A. A., V. S. Tiberkevich, C. W. Sandweg, V. I. Vasyuchka, D. A. Bozhko, A. V. Chumak, T. Neumann, B. Obry, G. A. Melkov, A. N. Slavin and B. Hillebrands, "Bose–Einstein Condensation in an Ultra-Hot Gas of Pumped Magnons", *Nature Communications*, Vol. 5, No. 1, p. 3452, 2014.

10. Geller, S. and M. A. Gilleo, "Structure and Ferrimagnetism of Yttrium and Rare-earth–Iron Garnets", *Acta Crystallographica*, Vol. 10, No. 3, pp. 239–239, 1957.

11. Pardavi-Horvath, M., "Microwave Applications of Soft Ferrites", *Journal of Magnetism and Magnetic Materials*, Vol. 215-216, pp. 171–183, 2000.

12. Yang, H., G. Zhang, Y. Lin, T. Ye and P. Kang, "Electrical, Magnetic and Magnetoelectric Properties of BaTiO3/BiY2Fe5O12 Particulate Composites", *Ceramics International*, Vol. 41, No. 5, pp. 7227–7232, 2015.

13. Kirischuk, V., V. Ageev, L. Sadovnikov, N. Strilchuk, V. Zheltonozhsky, Y. V. Koblyanskiy, G. Melkov and O. Puzik, "Long-term Stability of Yttrium–Iron Garnet Films Under Irradiation by Neutrons, Protons, Deuterons and Electrons", *Nuclear Instruments and Methods in Physics Research Section A: Accelerators, Spectrometers, Detectors and Associated Equipment*, Vol. 580, No. 1, pp. 419–422, 2007.

14. Harris, V. G., A. Geiler, Y. Chen, S. D. Yoon, M. Wu, A. Yang, Z. Chen, P. He,

P. V. Parimi, X. Zuo, C. E. Patton, M. Abe, O. Acher and C. Vittoria, "Recent Advances in Processing and Applications of Microwave Ferrites", *Journal of Magnetism and Magnetic Materials*, Vol. 321, No. 14, pp. 2035–2047, 2009.

15. Ravi, B., X. Guo, Q. Yan, R. Gambino, S. Sampath and J. Parise, "Phase Evolution and Magnetic Properties of Al Substituted Yttrium Iron Garnet Nanopowders and Plasma-sprayed Coatings", *Surface and Coatings Technology*, Vol. 201, No. 16-17, pp. 7597–7605, 2007.

16. Zhang, D., X.-M. Wang, T.-F. Li, X.-Q. Luo, W. Wu, F. Nori and J. You, "Cavity Quantum Electrodynamics with Ferromagnetic Magnons in a Small Yttrium-Iron-Garnet Sphere", *Nature Portfolio Journal Quantum Information*, Vol. 1, No. 1, pp. 1–6, 2015.

17. Tabuchi, Y., S. Ishino, A. Noguchi, T. Ishikawa, R. Yamazaki, K. Usami and Y. Nakamura, "Coherent Coupling Between a Ferromagnetic Magnon and a Superconducting Qubit", *Science*, Vol. 349, No. 6246, pp. 405–408, 2015.

18. Patton, C. E., "Linewidth and Relaxation Processes for the Main Resonance in The Spin-Wave Spectra of Ni-Fe Alloy Films", *Journal of Applied Physics*, Vol. 39, No. 7, pp. 3060–3068, 1968.

19. Chumak, A. V., P. Pirro, A. A. Serga, M. Kostylev, R. Stamps, H. Schultheiss, K. Vogt, S. Hermsdoerfer, B. Laegel, P. Beck *et al.*, "Spin-Wave Propagation in a Microstructured Magnonic Crystal", *Applied Physics Letters*, Vol. 95, No. 26, p. 262508, 2009.

20. Nicolas, J., "Microwave Ferrites", *Handbook of Ferromagnetic Materials*, Vol. 2, pp. 243–296, 1980.

21. Adam, J. D., L. E. Davis, G. F. Dionne, E. F. Schloemann and S. N. Stitzer, “Ferrite Devices and Materials”, *Institute of Electrical and Electronics Engineers Transactions on Microwave Theory and Techniques*, Vol. 50, No. 3, pp. 721–737, 2002.

22. Geller, S., “Crystal Chemistry of the Garnets”, *Zeitschrift für Kristallographie-Crystalline Materials*, Vol. 125, No. 1-6, pp. 1–47, 1967.

23. Levinstein, R. L., HJ S. Licht and L. Blank, “The growth of High Quality Garnet Films from Supercooled Melts”, *Applied Physics Letters*, Vol. 19, No. 11, pp. 486–488, 1971.

24. Gurevich, A. G. and G. A. Melkov, *Magnetization Oscillations and Waves*, Chemical Rubber Company Press, Florida, 1996.

25. Uchida, K., T. Kikkawa, A. Miura, J. Shiomi and E. Saitoh, “Quantitative Temperature Dependence of Longitudinal Spin Seebeck Effect at High Temperatures”, *Physical Review X*, Vol. 4, No. 4, p. 041023, 2014.

26. Rohde, U. L., A. K. Poddar and G. Böck, *The Design of Modern Microwave Oscillators for Wireless Applications: Theory and Optimization*, John Wiley Sons, New Jersey, 2005.

27. Capku, Z., C. Deger, P. Aksu and F. Yildiz, “Origin of Perpendicular Magnetic Anisotropy in Yttrium Iron Garnet Thin Films Grown On Si (100)”, *Institute of Electrical and Electronics Engineers Transactions on Magnetics*, Vol. 56, No. 11, pp. 1–6, 2020.

28. Capku, Z. and F. Yildiz, “Spin Wave Modes Observation in YIG Thin Films

with Perpendicular Magnetic Anisotropy", *Journal of Magnetism and Magnetic Materials*, Vol. 538, p. 168290, 2021.

29. Coey, J. M., *Magnetism and Magnetic Materials*, Cambridge University Press, Cambridge, 2010.

30. Getzlaff, M., *Fundamentals of Magnetism*, Springer, Heidelberg, 2007.

31. Spaldin, N. A., *Magnetic materials: Fundamentals and Applications*, Second edition, Cambridge University Press, Cambridge, 2010.

32. Wikipedia, "Curie temperature Wikipedia, The Free Encyclopedia", `https://en.wikipedia.org/wiki/Curie-temperature`, accessed on August 2023.

33. Wikipedia, "Paramagnetism Wikipedia, The Free Encyclopedia", `https://en.wikipedia.org/wiki/Paramagnetism`, accessed on June 2023.

34. Wikipedia, "Magnetic hysteresis Wikipedia, The Free Encyclopedia", `https://en.wikipedia.org/wiki/Magnetic-hysteresis`, accessed on August 2023.

35. Wikipedia, "Zeeman effect Wikipedia, The Free Encyclopedia", `https://en.wikipedia.org/wiki/Zeeman-effect`, accessed on September 2023.

36. Weiss, P., "L'hypothèse du champ moléculaire et la propriété ferromagnétique", *Journal of Physics: Theories and Applications*, Vol. 6, No. 1, pp. 661–690, 1907.

37. Wikipedia, "Magnetic domain Wikipedia, The Free Encyclopedia", `https://en.wikipedia.org/wiki/Magnetic-domain`, accessed on May 2023.

38. Chikazumi, S. and C. D. Graham, *Physics of Ferromagnetism*, 94, Oxford University Press, New York, 1997.

39. Kawakami, M., T. Hihara, Y. Kōi and T. Wakiyama, "The Co59 Nuclear Magnetic Resonance in Hexagonal Cobalt", *Journal of the Physical Society of Japan*, Vol. 33, No. 6, pp. 1591–1598, 1972.

40. Gengnagel, H. and U. Hofmann, "Temperature Dependence of the Magnetocrystalline Energy Constants K1, K2, and K3 of Iron", *Physica Status Solidi (b)*, Vol. 29, No. 1, pp. 91–97, 1968.

41. Franse, J. and G. De Vries, "The Magnetocrystalline Anisotropy Energy of Nickel", *Physica*, Vol. 39, No. 4, pp. 477–498, 1968.

42. Wikipedia, "Magnetocrystalline anisotropy Wikipedia, The Free Encyclopedia", `https://en.wikipedia.org/wiki/Magnetocrystalline-anisotropy`, accessed on August 2023.

43. Chikazumi, S., "Ferromagnetic Properties and Superlattice Formation of Iron Nickel Alloys (I)", *Journal of the Physical Society of Japan*, Vol. 5, No. 5, pp. 327–333, 1950.

44. Skomski, R., *Simple Models of Magnetism*, Oxford University Press, New York, 2008.

45. Blundell, S., *Magnetism in condensed matter*, Oxford University Press, New York, 2001.

46. Den Broeder, F., W. Hoving and P. Bloemen, "Magnetic Anisotropy of Multilayers", *Journal of Magnetism and Magnetic Materials*, Vol. 93, pp. 562–570, 1991.

47. Bozorth, R. M., *Ferromagnetism*, John Wiley Sons, New Jersey, 2003.

48. Bloch, F., "Zur Theorie des Ferromagnetismus", *Zeitschrift für Physik*, Vol. 61, No. 3-4, pp. 206–219, 1930.

49. Sáenz, A. W., "Spin Waves in Exchange-Coupled Complex Magnetic Structures and Neutron Scattering", *Physical Review*, Vol. 125, No. 6, p. 1940, 1962.

50. Harris, A. B., "Spin-wave Spectra of Yttrium and Gadolinium Iron Garnet", *Physical Review*, Vol. 132, No. 6, p. 2398, 1963.

51. Damon, R. W. and J. Eshbach, "Magnetostatic Modes of a Ferromagnet Slab", *Journal of Physics and Chemistry of Solids*, Vol. 19, No. 3-4, pp. 308–320, 1961.

52. Puszkarski, H., "Surface Spin Waves in Hexagonal Cobalt Thin Films", *Physica Status Solidi (b)*, Vol. 22, No. 2, pp. 355–359, 1967.

53. Brown, S., R. Henry, P. Wigen and P. Besser, "Observation of an Exchange Dominated Surface Spin Wave in Yttrium Iron Garnet Films", *Solid State Communications*, Vol. 11, No. 9, pp. 1179–1182, 1972.

54. Yu, J., R. Turk and P. Wigen, "Exchange-Dominated Surface Spin Waves in Thin

Yttrium-Iron-Garnet Films", *Physical Review B*, Vol. 11, No. 1, p. 420, 1975.

55. Wigen, P. and H. Puszkarski, "Microscopic Model for the Tensorial Surface Anisotropy Field Observed in Thin Yitrium-Iron Garnet Film Spin-Wave Resonance", *Solid State Communications*, Vol. 18, No. 3, pp. 363–365, 1976.

56. Stakelon, T., "Spin Wave Propagation Near the Surface of a Ferromagnet with Surface Anisotropy", *Journal of Applied Physics*, Vol. 49, No. 3, pp. 1592–1594, 1978.

57. Farle, M., "Ferromagnetic Resonance of Ultrathin Metallic Layers", *Reports on Progress in Physics*, Vol. 61, No. 7, p. 755, 1998.

58. He, Y. and P. Wigen, "Determination of Magnetic Anisotropy Constants for Garnet Films From Angular Dependence of FMR", *Journal of Magnetism and Magnetic Materials*, Vol. 53, No. 1-2, pp. 115–120, 1985.

59. Heinrich, B., "Radio Frequency Techniques", *Ultrathin Magnetic Structures II: Measurement Techniques and Novel Magnetic Properties*, pp. 195–296, 1994.

60. Beljers, H. and J. Smit, "Ferromagnetic Resonance Absorption in BaFe12O19 a Highly Anisotropic Crystal", *Philips Research Reports*, Vol. 10, No. 113, pp. 113–130, 1955.

61. Teale, R. and F. Pelegrini, "Magnetic Surface Anisotropy and Ferromagnetic Resonance in Single-Crystal GdAl2", *Journal of Physics F: Metal Physics*, Vol. 16, No. 5, p. 621, 1986.

62. Rado, G. T., “Theory of Ferromagnetic Resonance and Static Magnetization in Ultrathin Crystals”, *Physical Review B*, Vol. 26, No. 1, p. 295, 1982.

63. Frait, Z. and D. Fraitova, *Spin Waves and Magnetic Excitations*, North-Holland, Amsterdam, 1988.

64. Suhl, H., “Ferromagnetic Resonance in Nickel Ferrite Between One and Two Kilomegacycles”, *Physical Review*, Vol. 97, No. 2, p. 555, 1955.

65. Soohoo, R., *Ferromagnetic and Spin-wave Resonance in Multilayer Films*, Ph.D. Thesis, American Institute of Physics, 1988.

66. Soohoo, R., “General Spin-wave Dispersion Relations”, *Physical Review*, Vol. 120, No. 6, p. 1978, 1960.

67. Sparks, M., “Ferromagnetic Resonance in Thin Films. II. Theory of Linewidths”, *Physical Review B*, Vol. 1, No. 9, p. 3856, 1970.

68. Eshbach, J. and R. Damon, “Surface Magnetostatic Modes and Surface Spin Waves”, *Physical Review*, Vol. 118, No. 5, p. 1208, 1960.

69. Stancil, D. D. and D. D. Stancil, “Propagation Characteristics and Excitation of Magnetostatic Waves”, *Theory of Magnetostatic Waves*, pp. 119–153, 1993.

70. Kalinikos, B., “Excitation of Propagating Spin Waves in Ferromagnetic lms”, *Institution of Electrical Engineers Proceedings H: Microwave Optics Antennas*, Vol. 127, p. 1, 1980.

71. Kalinikos, B. and A. Slavin, “Theory Of Dipole-Exchange Spin Wave Spectrum for Ferromagnetic Films with Mixed Exchange Boundary Conditions”, *Journal of Physics C: Solid State Physics*, Vol. 19, No. 35, p. 7013, 1986.

72. Damon, R. and H. Van De Vaart, “Propagation of Magnetostatic Spin Waves at Microwave Frequencies in a Normally-Magnetized Disk”, *Journal of Applied Physics*, Vol. 36, No. 11, pp. 3453–3459, 1965.

73. Bhattacharya, P., R. Fornari and H. Kamimura, *Comprehensive Semiconductor Science and Technology*, Elsevier, Amsterdam, 2011.

74. Marc, G. and L. Palmisano, *Heterogeneous Photocatalysis: Relationships with Heterogeneous Catalysis and Perspectives*, Elsevier, Amsterdam, 2019.

75. Smentkowski, V. S., “Trends in Sputtering”, *Progress in Surface Science*, Vol. 64, No. 1-2, pp. 1–58, 2000.

76. Wasa, K., M. Kitabatake and H. Adachi, *Thin Film Materials Technology: Sputtering of Control Compound Materials*, Springer, Heidelberg, 2004.

77. Wikipedia, “Sputter Deposition Wikipedia, The Free Encyclopedia”, `https://en.wikipedia.org/wiki/Sputter-deposition`, accessed on April 2023.

78. Cullity, B. D., *Elements of X-ray Diffraction*, Addison-Wesley, Boston, 1956.

79. Wikipedia, “X-Ray Crystallography Wikipedia, The Free Encyclopedia”, `https://en.wikipedia.org/wiki/X-ray-crystallography`, accessed on

September 2023.

80. Stevie, F. A. and C. L. Donley, “Introduction to X-Ray Photoelectron Spectroscopy”, *Journal of Vacuum Science & Technology A*, Vol. 38, No. 6, p. 063204, 2020.

81. Wikipedia, “X-Ray Photoelectron Spectroscopy Wikipedia, The Free Encyclopedia”, `https://en.wikipedia.org/wiki/X-ray-photoelectron-spectroscopy`, accessed on February 2023.

82. Wikipedia, “Photolithography Wikipedia, The Free Encyclopedia”, `https://en.wikipedia.org/wiki/Photolithography`, accessed on August 2023.

83. Wikipedia, “Photoresist Wikipedia, The Free Encyclopedia”, `https://en.wikipedia.org/wiki/Photoresist`, accessed on August 2023.

84. Cullity, B. D. and C. D. Graham, *Introduction to Magnetic Materials*, Second edition, John Wiley Sons, New Jersey, 2011.

85. Wikipedia, “Vibrating-Sample Magnetometer Wikipedia, The Free Encyclopedia”, `https://en.wikipedia.org/wiki/Vibrating-sample-magnetometer`, accessed on August 2023.

86. Yalçın, O., *Ferromagnetic Resonance: Theory and Applications*, InTech, Croatia, 2013.

87. Vansteenkiste, A., J. Leliaert, M. Dvornik, M. Helsen, F. Garcia-Sanchez and

B. V. Waeyenberge, “The Design and Verification of MuMax3”, *American Institute of Physics Advances*, Vol. 4, No. 10, p. 107133, 2014.

88. Donahue, M., D. Porter, J. Lau and R. McMichael, “Interagency report NISTIR 6376. National Institute of Standards and Technology, Gaithersburg”, *Journal of Research of the National Institute of Standards and Technology*, Vol. 114, pp. 57–67, 1999.

89. Lopez-Diaz, L., D. Aurelio, L. Torres, E. Martinez, M. A. Hernandez-Lopez, J. Gomez, O. Alejos, M. Carpentieri, G. Finocchio and G. Consolo, “Micromagnetic Simulations Using Graphics Processing Units”, *Journal of Physics D: Applied Physics*, Vol. 45, No. 32, p. 323001, 2012.

90. Wang, H., C. Du, P. C. Hammel and F. Yang, “Strain-Tunable Magnetocrystalline Anisotropy in Epitaxial Y3Fe5O12 Thin Films”, *Physical Review B*, Vol. 89, No. 13, p. 134404, 2014.

91. Quindeau, A., C. O. Avci, W. Liu, C. Sun, M. Mann, A. S. Tang, M. C. Onbasli, D. Bono, P. M. Voyles, Y. Xu *et al.*, “Tm3Fe5O12/Pt Heterostructures with Perpendicular Magnetic Anisotropy For Spintronic Applications”, *Advanced Electronic Materials*, Vol. 3, No. 1, p. 1600376, 2017.

92. Garello, K., C. O. Avci, I. M. Miron, M. Baumgartner, A. Ghosh, S. Auffret, O. Boulle, G. Gaudin and P. Gambardella, “Ultrafast Magnetization Switching By Spin-Orbit Torques”, *Applied Physics Letters*, Vol. 105, No. 21, p. 212402, 2014.

93. Linares, R., R. McGraw and J. Schroeder, “Growth and Properties of Yttrium Iron Garnet Single-Crystal Films”, *Journal of Applied Physics*, Vol. 36, No. 9,

pp. 2884–2886, 1965.

94. Robertson, J., "Liquid Phase Epitaxy of Garnets", *Journal of Crystal Growth*, Vol. 45, pp. 233–242, 1978.

95. Jungfleisch, M., V. Lauer, R. Neb, A. Chumak and B. Hillebrands, "Improvement of the Yttrium Iron Garnet/Platinum Interface for Spin Pumping-Based Applications", *Applied Physics Letters*, Vol. 103, No. 2, p. 022411, 2013.

96. Onbasli, M., A. Kehlberger, D. H. Kim, G. Jakob, M. Kläui, A. V. Chumak, B. Hillebrands and C. A. Ross, "Pulsed Laser Deposition Of Epitaxial Yttrium Iron Garnet Films with Low Gilbert Damping and Bulk-Like Magnetization", *Applied Physics Letters Materials*, Vol. 2, No. 10, p. 106102, 2014.

97. Sun, Y., Y.-Y. Song, H. Chang, M. Kabatek, M. Jantz, W. Schneider, M. Wu, H. Schultheiss and A. Hoffmann, "Growth and Ferromagnetic Resonance Properties of Nanometer-Thick Yttrium Iron Garnet Films", *Applied Physics Letters*, Vol. 101, No. 15, p. 152405, 2012.

98. Galstyan, O., H. Lee, A. Babajanyan, A. Hakhoumian, B. Friedman and K. Lee, "Magneto-Optical Visualization by Bi: YIG Thin Films Prepared at Low Temperatures", *Journal of Applied Physics*, Vol. 117, No. 16, p. 163914, 2015.

99. Nur-E-Alam, M., M. Vasiliev, V. A. Kotov and K. Alameh, "Highly Bismuth-Substituted, Record-Performance Magneto-Optic Garnet Materials with Low Coercivity For Applications in Integrated Optics, Photonic Crystals, Imaging And Sensing", *Optical Materials Express*, Vol. 1, No. 3, pp. 413–427, 2011.

100. Shone, M., "The Technology of YIG Film Growth", *Circuits, Systems and Signal*

Processing, Vol. 4, pp. 89–103, 1985.

101. Sander, D., “The Magnetic Anisotropy and Spin Reorientation of Nanostructures and Nanoscale Films”, *Journal of Physics: Condensed Matter*, Vol. 16, No. 20, p. R603, 2004.

102. Tudu, B. and A. Tiwari, “Recent Developments in Perpendicular Magnetic Anisotropy Thin Films for Data Storage Applications”, *Vacuum*, Vol. 146, pp. 329–341, 2017.

103. Chumak, A. V., A. A. Serga and B. Hillebrands, “Magnon Transistor for All-Magnon Data Processing”, *Nature Communications*, Vol. 5, No. 1, p. 4700, 2014.

104. Yildiz, F., M. Przybylski and J. Kirschner, “Perpendicular Anisotropy and Oscillatory Interlayer Coupling in Fe 0.5 Co 0.5/Rh/Fe 0.5 Co 0.5 Bilayers On Rh (001)”, *Journal of Applied Physics*, Vol. 105, No. 7, p. 07C312, 2009.

105. Yildiz, F., M. Przybylski and J. Kirschner, “Direct Evidence of a Nonorthogonal Magnetization Configuration in Single Crystalline Fe 1- X Co X/Rh/Fe/Rh (001) System”, *Physical Review Letters*, Vol. 103, No. 14, p. 147203, 2009.

106. Guo, C., C. Wan, M. Zhao, H. Wu, C. Fang, Z. Yan, J. Feng, H. Liu and X. Han, “Spin-Orbit Torque Switching İn Perpendicular Y3Fe5O12/Pt Bilayer”, *Applied Physics Letters*, Vol. 114, No. 19, p. 192409, 2019.

107. Maier-Flaig, H., S. Geprägs, Z. Qiu, E. Saitoh, R. Gross, M. Weiler, H. Huebl and S. Goennenwein, “Perpendicular Magnetic Anisotropy in İnsulating Ferrimagnetic Gadolinium Iron Garnet Thin Films”, *arXiv preprint arXiv:1706.08488*, 2017.

108. Popova, E., N. Keller, F. Gendron, L. Thomas, M.-C. Brianso, M. Guyot, M. Tessier and S. Parkin, “Perpendicular Magnetic Anisotropy in Ultrathin Yttrium Iron Garnet Films Prepared By Pulsed Laser Deposition Technique”, *Journal of Vacuum Science & Technology A: Vacuum, Surfaces, and Films*, Vol. 19, No. 5, pp. 2567–2570, 2001.

109. Calhoun, B., J. Overmeyer and W. Smith, “Ferrimagnetic Resonance in Gadolinium Iron Garnet”, *Physical Review*, Vol. 107, No. 4, p. 993, 1957.

110. Kigami, Y., T. Namikawa and Y. Yamazaki, “Stress Induced Magnetic Anisotropy of YBi 2 Fe 5-x Ga x O 12 Sputtered Films”, *Institute of Electrical and Electronics Engineers Translation Journal on Magnetics in Japan*, Vol. 5, No. 4, pp. 319–324, 1990.

111. Kubota, M., A. Tsukazaki, F. Kagawa, K. Shibuya, Y. Tokunaga, M. Kawasaki and Y. Tokura, “Stress-induced Perpendicular Magnetization in Epitaxial Iron Garnet Thin Films”, *Applied Physics Express*, Vol. 5, No. 10, p. 103002, 2012.

112. Bhoi, B., N. Venkataramani, R. Aiyar and S. Prasad, “FMR and Magnetic Studies on Polycrystalline YIG Thin Films Deposited Using Pulsed Laser”, *Institute of Electrical and Electronics Engineers Transactions on Magnetics*, Vol. 49, No. 3, pp. 990–994, 2013.

113. Zhang, Y., J. Xie, L. Deng and L. Bi, “Growth of Phase Pure Yttrium Iron Garnet Thin Films on Silicon: The Effect of Substrate and Postdeposition Annealing Temperatures”, *Institute of Electrical and Electronics Engineers Transactions on Magnetics*, Vol. 51, No. 11, pp. 1–4, 2015.

114. Tang, C., M. Aldosary, Z. Jiang, H. Chang, B. Madon, K. Chan, M. Wu, J. E.

Garay and J. Shi, “Exquisite Growth Control and Magnetic Properties of Yttrium Iron Garnet Thin Films”, *Applied Physics Letters*, Vol. 108, No. 10, p. 102403, 2016.

115. Schultrich, B., *Tetrahedrally Bonded Amorphous Carbon Films I: Basics, Structure and Preparation*, Vol. 263, Springer, Heidelberg, 2018.

116. Geller, S. and M. Gilleo, “The Crystal Structure and Ferrimagnetism of Yttrium-Iron Garnet, Y3Fe2 (Feo4) 3”, *Journal of Physics and Chemistry of solids*, Vol. 3, No. 1-2, pp. 30–36, 1957.

117. Popova, E., N. Keller, F. Gendron, M. Guyot, M.-C. Brianso, Y. Dumond and M. Tessier, “Structure and Magnetic Properties of Yttrium–İron–Garnet Thin Films Prepared by Laser Deposition”, *Journal of Applied Physics*, Vol. 90, No. 3, pp. 1422–1428, 2001.

118. Yildiz, F., M. Przybylski, X.-D. Ma and J. Kirschner, “Strong Perpendicular Anisotropy in Fe 1- X Co X Alloy Films Epitaxially Grown on Mismatching Pd (001), Ir (001), and Rh (001) Substrates”, *Physical Review B*, Vol. 80, No. 6, p. 064415, 2009.

119. Kalaycı, T., C. Deger, S. Akbulut and F. Yildiz, “Tuning Magnetic Properties of Non-Collinear Magnetization Configuration in Pt/[Pt/Co] 6/Pt/Co/Pt Multilayer Structure”, *Journal of Magnetism and Magnetic Materials*, Vol. 436, pp. 11–16, 2017.

120. Siegel, G., M. C. Prestgard, S. Teng and A. Tiwari, “Robust Longitudinal Spin-Seebeck Effect in Bi-YIG Thin Films”, *Scientific Reports*, Vol. 4, No. 1, p. 4429, 2014.

121. Abidov, A., B. Allabergenov, J. Lee, H.-W. Jeon, S.-W. Jeong and S. Kim, “X-Ray Photoelectron Spectroscopy Characterization Of Fe Doped Tio2 Photocatalyst”, *International Journal of Materials, Mechanics and Manufacturing*, Vol. 1, No. 3, p. 294, 2013.

122. Jin, L., K. Jia, Y. He, G. Wang, Z. Zhong and H. Zhang, “Pulsed Laser Deposition Grown Yttrium-Iron-Garnet Thin Films: Effect of Composition and Iron Ion Valences on Microstructure and Magnetic Properties”, *Applied Surface Science*, Vol. 483, pp. 947–952, 2019.

123. Hauser, C., T. Richter, N. Homonnay, C. Eisenschmidt, M. Qaid, H. Deniz, D. Hesse, M. Sawicki, S. G. Ebbinghaus and G. Schmidt, “Yttrium Iron Garnet Thin Films with Very Low Damping Obtained by Recrystallization of Amorphous Material”, *Scientific Reports*, Vol. 6, No. 1, p. 20827, 2016.

124. Sun, Y., Y.-Y. Song, H. Chang, M. Kabatek, M. Jantz, W. Schneider, M. Wu, H. Schultheiss and A. Hoffmann, “Growth and Ferromagnetic Resonance Properties of Nanometer-Thick Yttrium Iron Garnet Films”, *Applied Physics Letters*, Vol. 101, No. 15, p. 152405, 2012.

125. Onbasli, M. C., A. Kehlberger, D. H. Kim, G. Jakob, M. Kläui, A. V. Chumak, B. Hillebrands and C. A. Ross, “Pulsed Laser Deposition of Epitaxial Yttrium Iron Garnet Films with Low Gilbert Damping and Bulk-Like Magnetization”, *Applied Physics Letters Materials*, Vol. 2, No. 10, p. 106102, 2014.

126. Sellappan, P., C. Tang, J. Shi and J. E. Garay, “An Integrated Approach to Doped Thin Films With Strain-Tunable Magnetic Anisotropy: Powder Synthesis, Target Preparation and Pulsed Laser Deposition of Bi: YIG”, *Materials Research Letters*, Vol. 5, No. 1, pp. 41–47, 2017.

127. Henry, R., P. Besser, D. Heinz and J. Mee, “Ferromagnetic Resonance Properties of LPE YIG Films”, *Institute of Electrical and Electronics Engineers Transactions on Magnetics*, Vol. 9, No. 3, pp. 535–537, 1973.

128. Mee, J. and J. Archer, “RH Meade u. TN Hamilton”, *Applied Physics Letters*, Vol. 10, p. 289, 1967.

129. d'Allivy Kelly, O., A. Anane, R. Bernard, J. B. Youssef, C. Hahn, A. H. Molpeceres, C. Carrétéro, E. Jacquet, C. Deranlot, P. Bortolotti, R. Lebourgeois, J.-C. Mage, G. de Loubens, O. Klein, V. Cros and A. Fert, “Inverse Spin Hall Effect in Nanometer-Thick Yttrium Iron Garnet/Pt System”, *Applied Physics Letters*, Vol. 103, No. 8, p. 082408, 2013.

130. Heinrich, B., C. Burrowes, E. Montoya, B. Kardasz, E. Girt, Y.-Y. Song, Y. Sun and M. Wu, “Spin Pumping at the Magnetic Insulator (YIG)/Normal Metal (Au) Interfaces”, *Physical Review Letters*, Vol. 107, No. 6, p. 066604, 2011.

131. Kang, Y.-M., S.-H. Wee, S.-I. Baik, S.-G. Min, S.-C. Yu, S.-H. Moon, Y.-W. Kim and S.-I. Yoo, “Magnetic Properties of YIG (Y3Fe5O12) Thin Films Prepared by the Post Annealing of Amorphous Films Deposited by RF-Magnetron Sputtering”, *Journal of Applied Physics*, Vol. 97, No. 10, p. 10A319, 2005.

132. Liu, T., H. Chang, V. Vlaminck, Y. Sun, M. Kabatek, A. Hoffmann, L. Deng and M. Wu, “Ferromagnetic Resonance Of Sputtered Yttrium Iron Garnet Nanometer Films”, *Journal of Applied Physics*, Vol. 115, No. 17, p. 17A501, 2014.

133. Marmion, S. R., M. Ali, M. McLaren, D. A. Williams and B. J. Hickey, “Temperature Dependence Of Spin Hall Magnetoresistance in Thin YIG/Pt Films”, *Physical Review B*, Vol. 89, No. 22, 2014.

134. Chen, J., F. Heimbach, T. Liu, H. Yu, C. Liu, H. Chang, T. Stückler, J. Hu, L. Zeng, Y. Zhang, Z. Liao, D. Yu, W. Zhao and M. Wu, “Spin Wave Propagation in Perpendicularly Magnetized nm-Thick Yttrium Iron Garnet Films”, *Journal of Magnetism and Magnetic Materials*, Vol. 450, pp. 3–6, 2018.

135. Ustinov, A. B., B. A. Kalinikos and E. Lähderanta, “Nonlinear Phase Shifters Based on Forward Volume Spin Waves”, *Journal of Applied Physics*, Vol. 113, No. 11, p. 113904, 2013.

136. Kanazawa, N., T. Goto, K. Sekiguchi, A. B. Granovsky, C. A. Ross, H. Takagi, Y. Nakamura and M. Inoue, “Demonstration of a Robust Magnonic Spin Wave Interferometer”, *Scientific Reports*, Vol. 6, No. 1, p. 30268, 2016.

137. Kanazawa, N., T. Goto, K. Sekiguchi, A. B. Granovsky, C. A. Ross, H. Takagi, Y. Nakamura, H. Uchida and M. Inoue, “The Role of Snell’s Law for a Magnonic Majority Gate”, *Scientific Reports*, Vol. 7, No. 1, p. 7898, 2017.

138. Zhu, Y., K. H. Chi and C. S. Tsai, “Magnonic Crystals-Based Tunable Microwave Phase Shifters”, *Applied Physics Letters*, Vol. 105, No. 2, p. 022411, 2014.

139. Haldar, A., C. Tian and A. O. Adeyeye, “Isotropic Transmission of Magnon Spin Information without a Magnetic Field”, *Science Advances*, Vol. 3, No. 7, p. e1700638, 2017.

140. Chumak, A. V., A. A. Serga and B. Hillebrands, “Magnonic Crystals for Data Processing”, *Journal of Physics D: Applied Physics*, Vol. 50, No. 24, p. 244001, 2017.

141. Kosen, S., A. F. van Loo, D. A. Bozhko, L. Mihalceanu and A. D. Karenowska,

"Microwave Magnon Damping in YIG Films at Millikelvin Temperatures", *Applied Physics Letters Materials*, Vol. 7, No. 10, p. 101120, 2019.

142. Morris, R. G. E., A. F. van Loo, S. Kosen and A. D. Karenowska, "Strong Coupling Of Magnons in A YIG Sphere to Photons in A Planar Superconducting Resonator in The Quantum Limit", *Scientific Reports*, Vol. 7, No. 1, 2017.

143. Andrich, P., C. F. Casas, X. Liu, H. L. Bretscher, J. R. Berman, F. J. Heremans, P. F. Nealey and D. D. Awschalom, "Hybrid Nanodiamond-YIG Systems for Efficient Quantum İnformation Processing and Nanoscale Sensing", *arXiv preprint arXiv:1701.07401*, 2017.

144. Chumak, A. V., "Magnon Spintronics: Fundamentals of Magnon-Based Computing", *Spintronics Handbook: Spin Transport and Magnetism*, pp. 247–302, Second Edition, Chemical Rubber Company Press, Florida, 2019.

145. Serga, A., A. Chumak and B. Hillebrands, "YIG Magnonics", *Journal of Physics D: Applied Physics*, Vol. 43, No. 26, p. 264002, 2010.

146. Fischer, T., M. Kewenig, D. A. Bozhko, A. A. Serga, I. I. Syvorotka, F. Ciubotaru, C. Adelmann, B. Hillebrands and A. V. Chumak, "Experimental Prototype of a Spin-Wave Majority Gate", *Applied Physics Letters*, Vol. 110, No. 15, p. 152401, 2017.

147. Klingler, S., P. Pirro, T. Brächer, B. Leven, B. Hillebrands and A. V. Chumak, "Spin-Wave Logic Devices Based on Isotropic Forward Volume Magnetostatic Waves", *Applied Physics Letters*, Vol. 106, No. 21, p. 212406, 2015.

148. Wigen, P., "Microwave Properties of Magnetic Garnet Thin Films", *Thin Solid*

Films, Vol. 114, No. 1-2, pp. 135–186, 1984.

149. Jia, X., K. Liu, K. Xia and G. E. Bauer, “Spin Transfer Torque on Magnetic Insulators”, *Europhysics Letters*, Vol. 96, No. 1, p. 17005, 2011.

150. Soumah, L., N. Beaulieu, L. Qassym, C. Carrétéro, E. Jacquet, R. Lebourgeois, J. B. Youssef, P. Bortolotti, V. Cros and A. Anane, “Ultra-Low Damping Insulating Magnetic Thin Films Get Perpendicular”, *Nature Communications*, Vol. 9, No. 1, p. 3355, 2018.

151. Deorani, P., J. H. Kwon and H. Yang, “Nonreciprocity Engineering in Magnetostatic Spin Waves”, *Current Applied Physics*, Vol. 14, pp. S129–S135, 2014.

152. Tacchi, S., R. Silvani, G. Carlotti, M. Marangolo, M. Eddrief, A. Rettori and M. G. Pini, “Strongly Hybridized Dipole-Exchange Spin Waves in Thin Fe-N Ferromagnetic Films”, *Physical Review B*, Vol. 100, No. 10, p. 104406, 2019.

153. Rameev, B., F. Yildiz, S. Kazan, B. Aktas, A. Gupta, L. Tagirov, D. Rata, D. Buergler, P. Gruenberg, C. Schneider *et al.*, “FMR Investigations of Half-Metallic Ferromagnets”, *Physica Status Solidi (a)*, Vol. 203, No. 7, pp. 1503–1512, 2006.

154. Collet, M., O. Gladii, M. Evelt, V. Bessonov, L. Soumah, P. Bortolotti, S. Demokritov, Y. Henry, V. Cros, M. Bailleul *et al.*, “Spin-Wave Propagation in Ultra-Thin YIG Based Waveguides”, *Applied Physics Letters*, Vol. 110, No. 9, p. 092408, 2017.

155. Krysztofik, A., H. Głowinski, P. Kuświk, S. Zietek, L. E. Coy, J. N. Rychły, S. Jurga, T. W. Stobiecki and J. Dubowik, “Characterization of Spin Wave Prop-

agation in (1 1 1) YIG Thin Films with Large Anisotropy", *Journal of Physics D: Applied Physics*, Vol. 50, No. 23, p. 235004, 2017.

156. Sheng, L., Y. Liu, J. Chen, H. Wang, J. Zhang, M. Chen, J. Ma, C. Liu, S. Tu, C.-W. Nan *et al.*, "Spin Wave Propagation in a Ferrimagnetic Thin Film with Perpendicular Magnetic Anisotropy", *Applied Physics Letters*, Vol. 117, No. 23, p. 232407, 2020.

157. Chen, J., C. Wang, C. Liu, S. Tu, L. Bi and H. Yu, "Spin Wave Propagation in Ultrathin Magnetic Insulators with Perpendicular Magnetic Anisotropy", *Applied Physics Letters*, Vol. 114, No. 21, p. 212401, 2019.

158. Chen, J., F. Heimbach, T. Liu, H. Yu, C. Liu, H. Chang, T. Stückler, J. Hu, L. Zeng, Y. Zhang *et al.*, "Spin Wave Propagation in Perpendicularly Magnetized nm-Thick Yttrium Iron Garnet Films", *Journal of Magnetism and Magnetic Materials*, Vol. 450, pp. 3–6, 2018.

159. Guo, X., Y. Chen, G. Wang, J. Ge, Y. Zhang, X. Tang, F. Ponchel, D. Remiens and X. Dong, "Improved Performance of YIG (Y3Fe5O12) Films Grown on Pt-Buffered Si Substrates by Chemical Solution Deposition Technique", *Journal of the American Ceramic Society*, Vol. 99, No. 7, pp. 2217–2220, 2016.

160. Hao, L., M. Lin, D. Xu, N. Li and W. Zhang, "Cogging Torque Reduction of Axial-Field Flux-Switching Permanent Magnet Machine by Rotor Tooth Notching", *Institute of Electrical and Electronics Engineers Transactions on Magnetics*, Vol. 51, No. 11, pp. 1–4, 2015.

161. Mendil, J., M. Trassin, Q. Bu, J. Schaab, M. Baumgartner, C. Murer, P. T. Dao, J. Vijayakumar, D. Bracher, C. Bouillet *et al.*, "Magnetic Properties and Do-

main Structure of Ultrathin Yttrium Iron Garnet/Pt Bilayers", *Physical Review Materials*, Vol. 3, No. 3, p. 034403, 2019.

162. Hansen, P., P. Röschmann and W. Tolksdorf, "Saturation Magnetization of Gallium-Substituted Yttrium Iron Garnet", *Journal of Applied Physics*, Vol. 45, No. 6, pp. 2728–2732, 1974.

163. Kittel, C., "On the Theory of Ferromagnetic Resonance Absorption", *Physical Review*, Vol. 73, No. 2, p. 155, 1948.

164. Schreiber, F. and Z. Frait, "Spin-Wave Resonance in High-Conductivity Films: The Fe-Co Alloy System", *Physical Review B*, Vol. 54, No. 9, p. 6473, 1996.

165. Klingler, S., A. V. Chumak, T. Mewes, B. Khodadadi, C. Mewes, C. Dubs, O. Surzhenko, B. Hillebrands and A. Conca, "Measurements of the Exchange Stiffness of YIG Films Using Broadband Ferromagnetic Resonance Techniques", *Journal of Physics D: Applied Physics*, Vol. 48, No. 1, p. 015001, 2014.

166. Portis, A., "Low-Lying Spın Wave Modes in Ferromagnetic Films", *Applied Physics Letters*, Vol. 2, No. 4, pp. 69–71, 1963.

167. Vansteenkiste, A., J. Leliaert, M. Dvornik, M. Helsen, F. Garcia-Sanchez and B. Van Waeyenberge, "The Design and Verification of MuMax3", *American Institute of Physics advances*, Vol. 4, No. 10, p. 107133, 2014.

168. Rothman, J., M. Kläui, L. Lopez-Diaz, C. Vaz, A. Bleloch, J. Bland, Z. Cui and R. Speaks, "Observation of a Bi-Domain State and Nucleation Free Switching in Mesoscopic Ring Magnets", *Physical Review Letters*, Vol. 86, No. 6, p. 1098, 2001.

169. Kläui, M., C. Vaz, L. Lopez-Diaz and J. Bland, “Vortex Formation in Narrow Ferromagnetic Rings”, *Journal of Physics: Condensed Matter*, Vol. 15, No. 21, p. R985, 2003.

170. Mani, A. S., *New Hard Layer Design of MRAM Based on Ring Elements*, University of Illinois, Chicago, 2006.

171. Pigeau, B., G. De Loubens, O. Klein and A. Riegler, “A Frequency-Controlled Magnetic Vortex Memory”, *Applied Physics Letters*, Vol. 96, p. 132506, 2010.

172. Tsunegi, S., K. Yakushiji, A. Fukushima, S. Yuasa and H. Kubota, “Microwave Emission Power Exceeding 10 W in Spin Torque Vortex Oscillator”, *Applied Physics Letters*, Vol. 109, No. 25, p. 252402, 2016.

APPENDIX A:

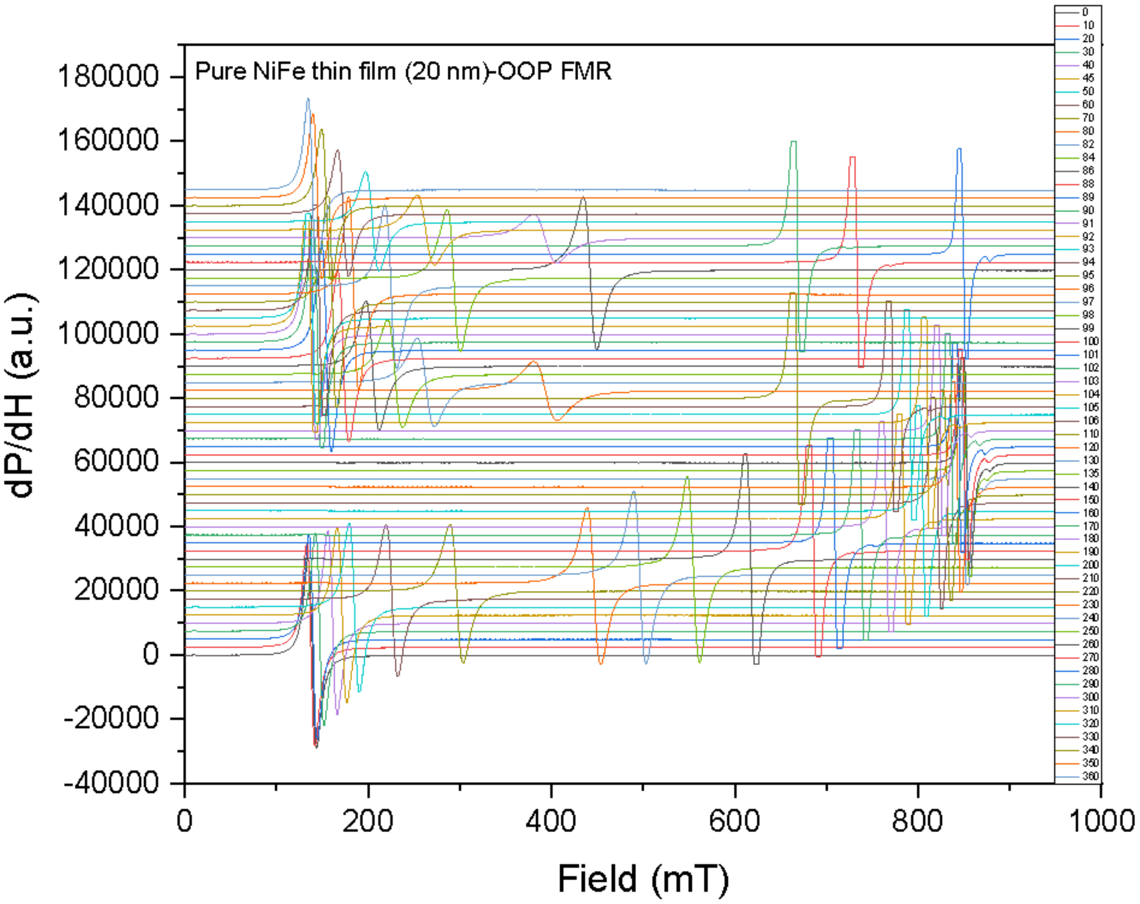

Figure A.1. The full FMR spectrum of a pure NiFe thin film in the OOP measurement geometry.

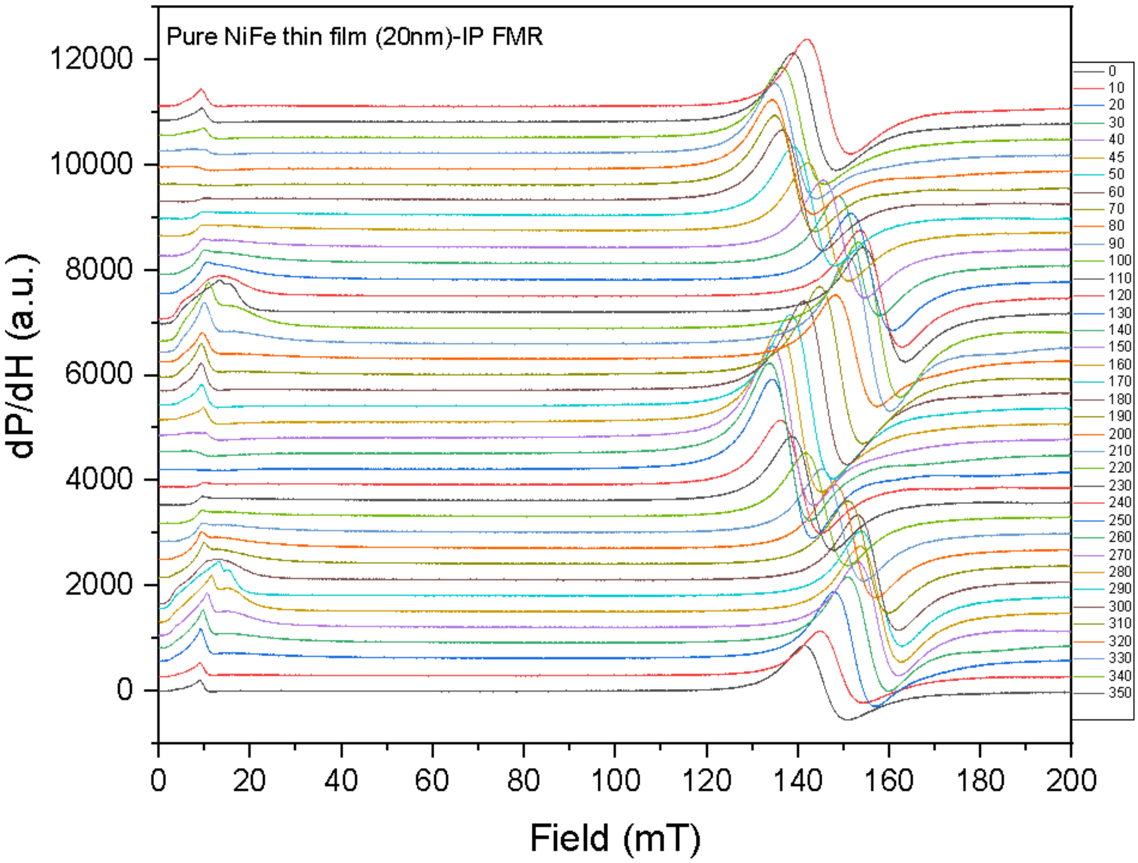

Figure A.2. The full FMR spectrum of a pure NiFe thin film in the IP measurement geometry.

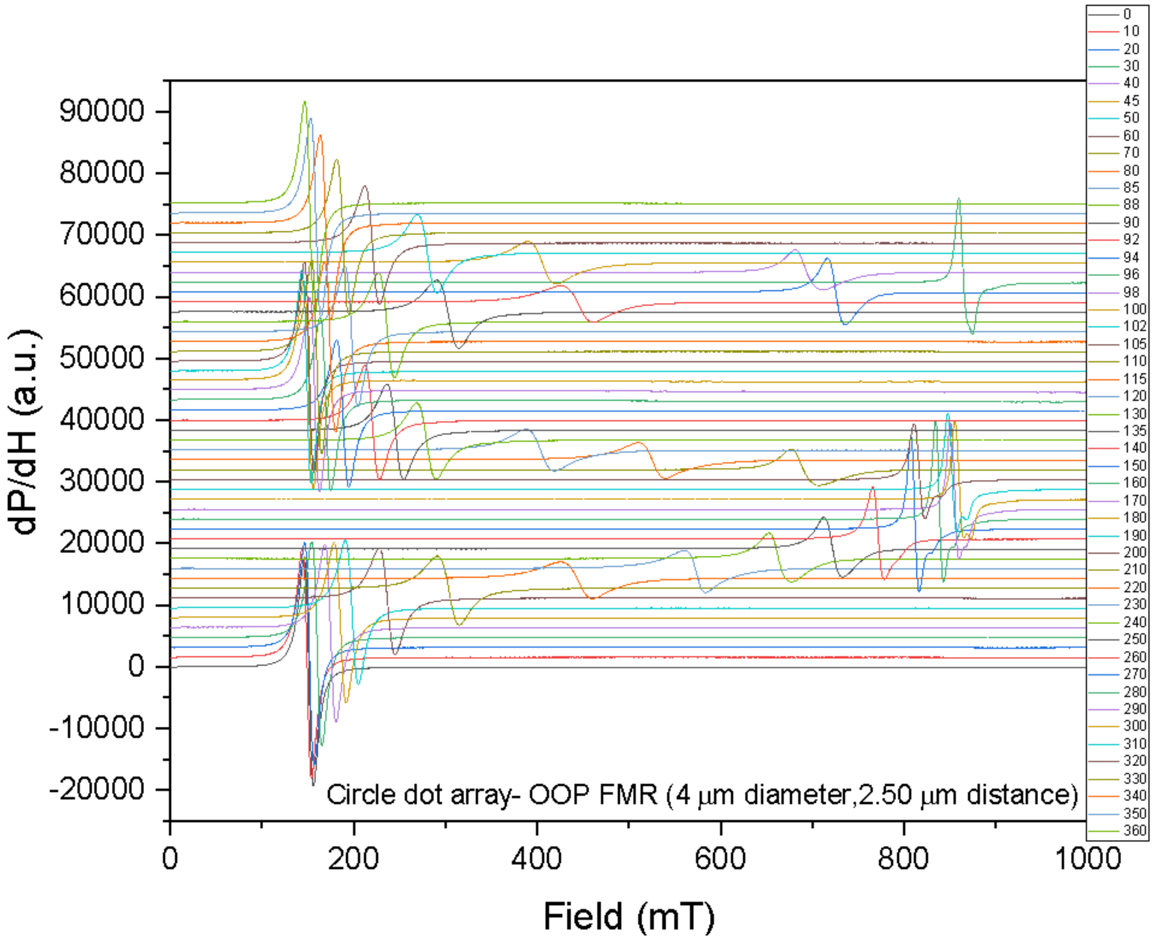

Figure A.3. The full FMR spectrum of a circular dot array with a diameter of 4 μm and separation distance of 2.50 μm in OOP measurement geometry.

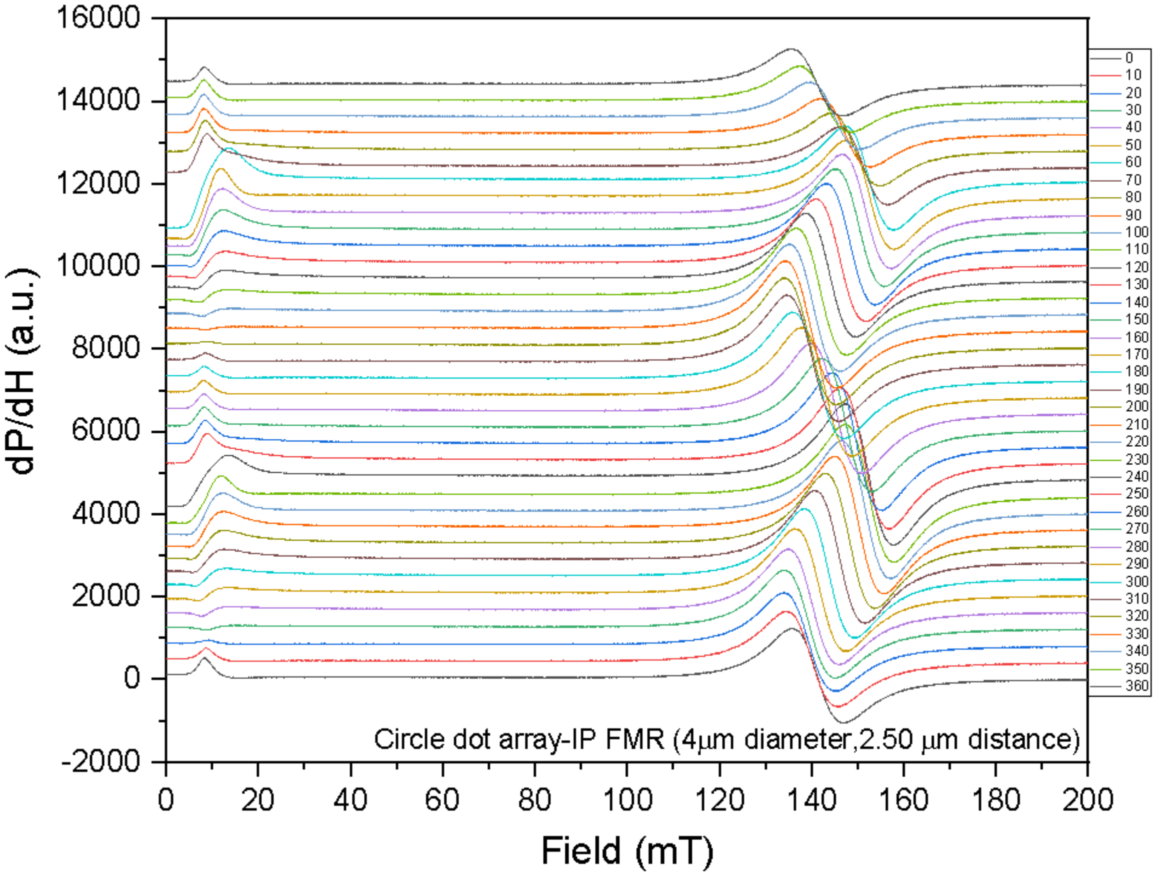

Figure A.4. The full FMR spectrum of a circular dot array with a diameter of 4 μm and separation distance of 2.50 μm in IP geometry.

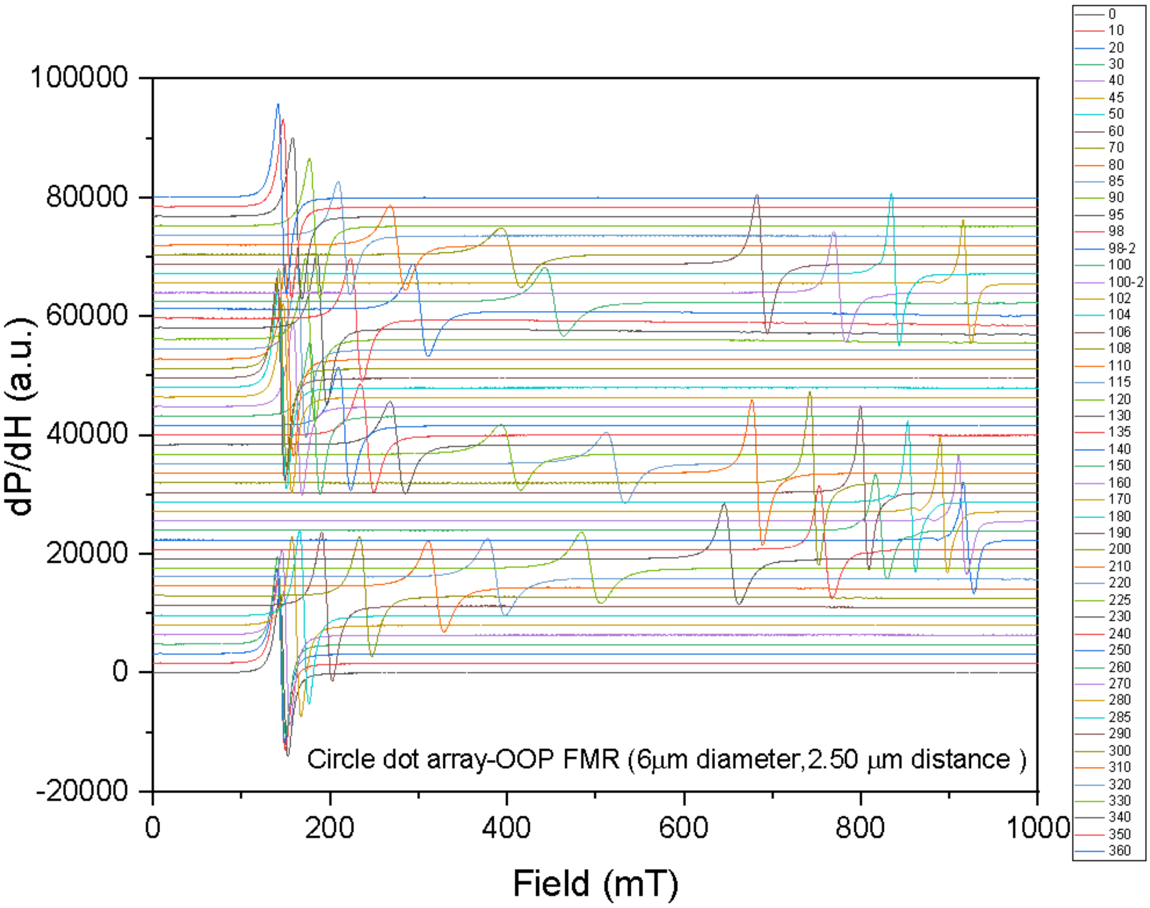

Figure A.5. The full FMR spectrum of a circular antidot array with a diameter of 6 μm and separation distance of 2.50 μm in OOP measurement geometry.

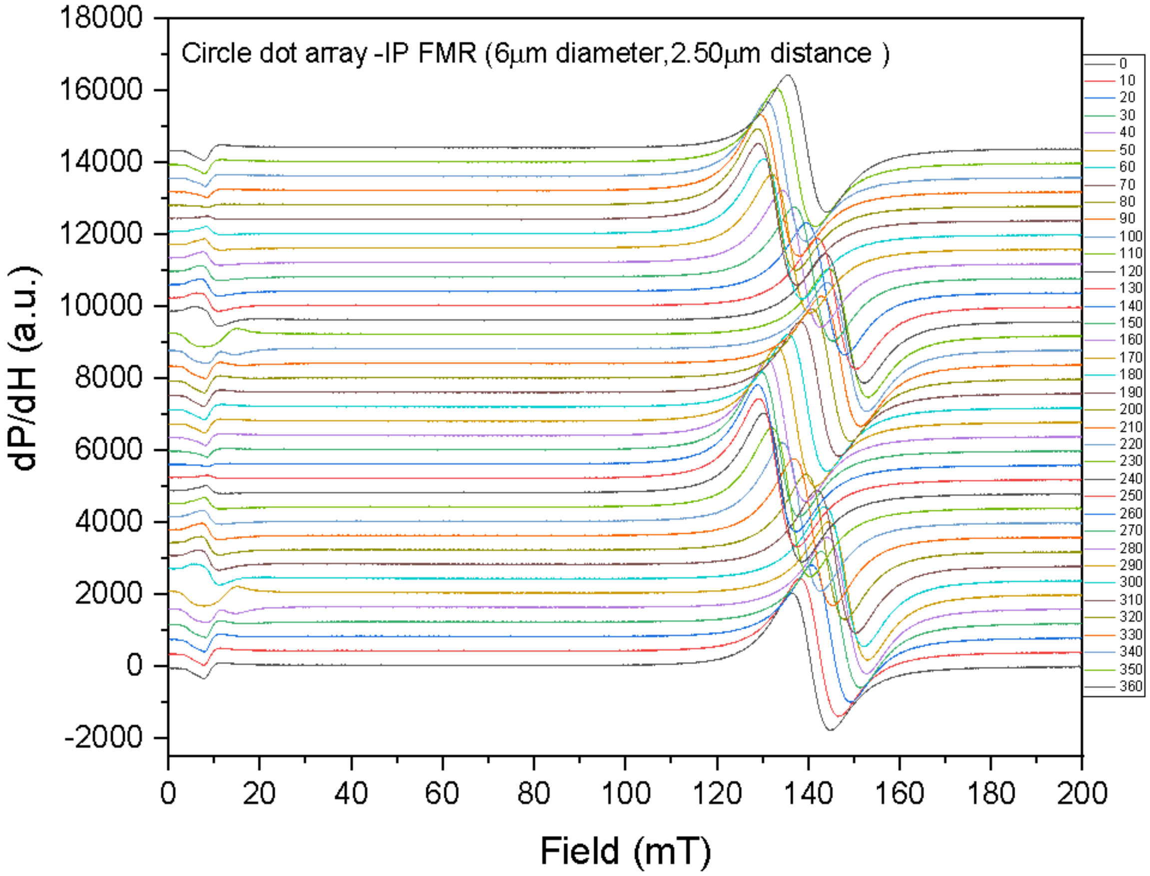

Figure A.6. The full FMR spectrum of a circular antidot array with a diameter of 6 μm and separation distance of 2.50 μm in IP measurement geometry.

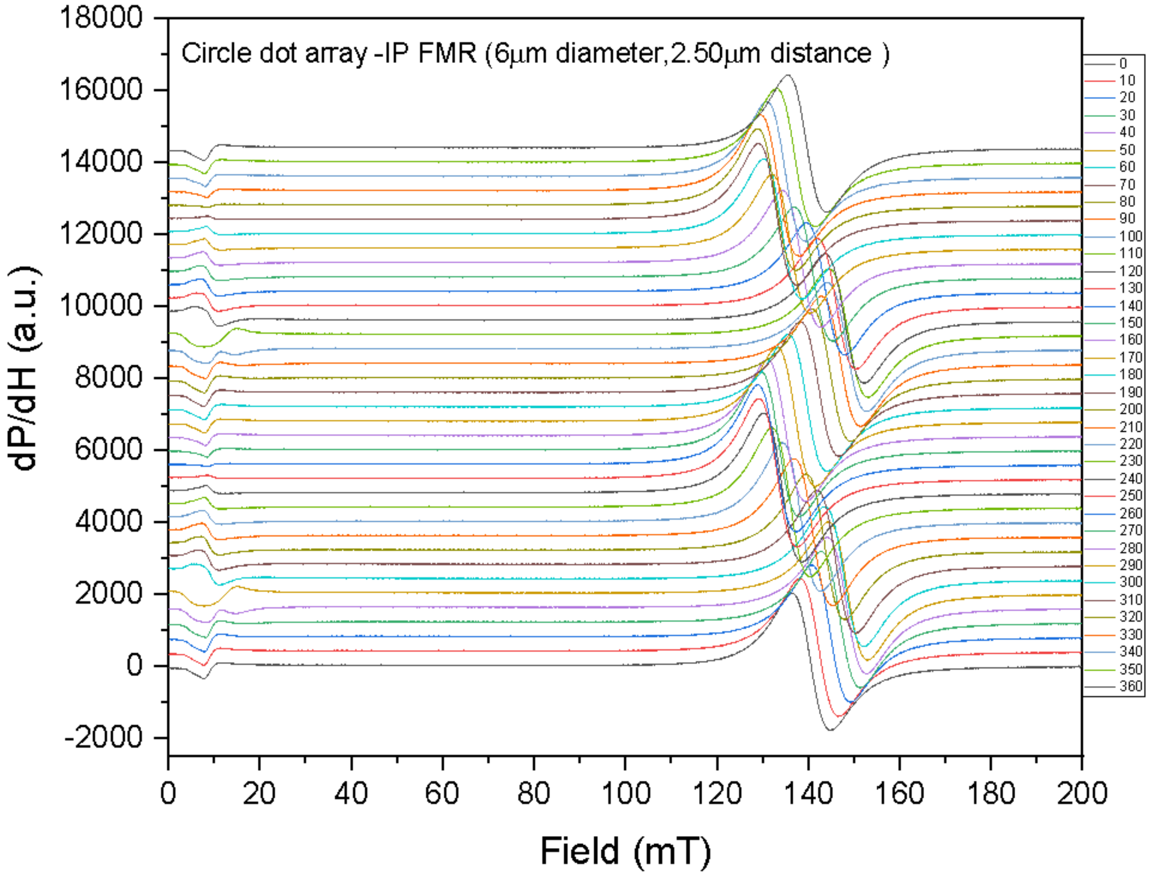

Figure A.7. The full FMR spectrum of a circular antidot array with a diameter of 6 μm and separation distance of 2.50 μm in IP measurement geometry.

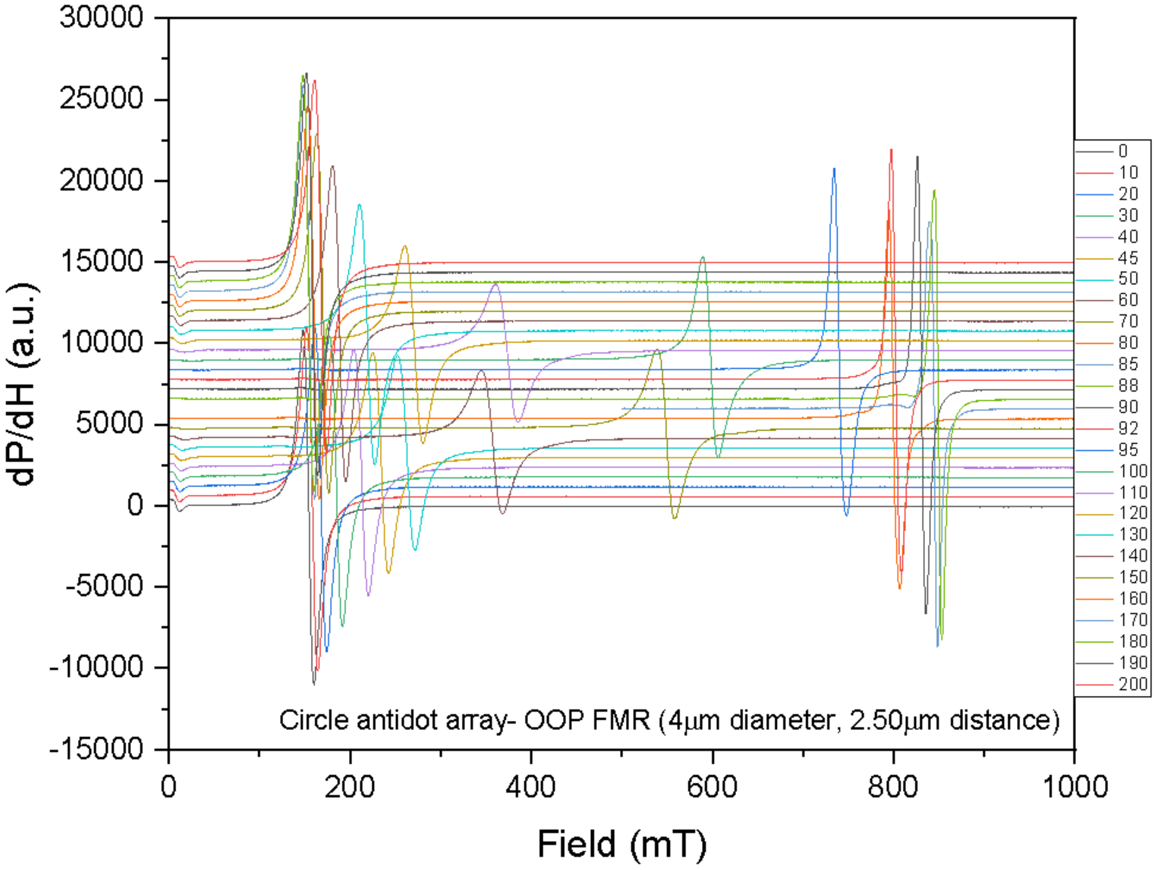

Figure A.8. The full FMR spectrum of a circular antidot array with a diameter of 4 μm and separation distance of 2.50 μm in OOP measurement geometry.

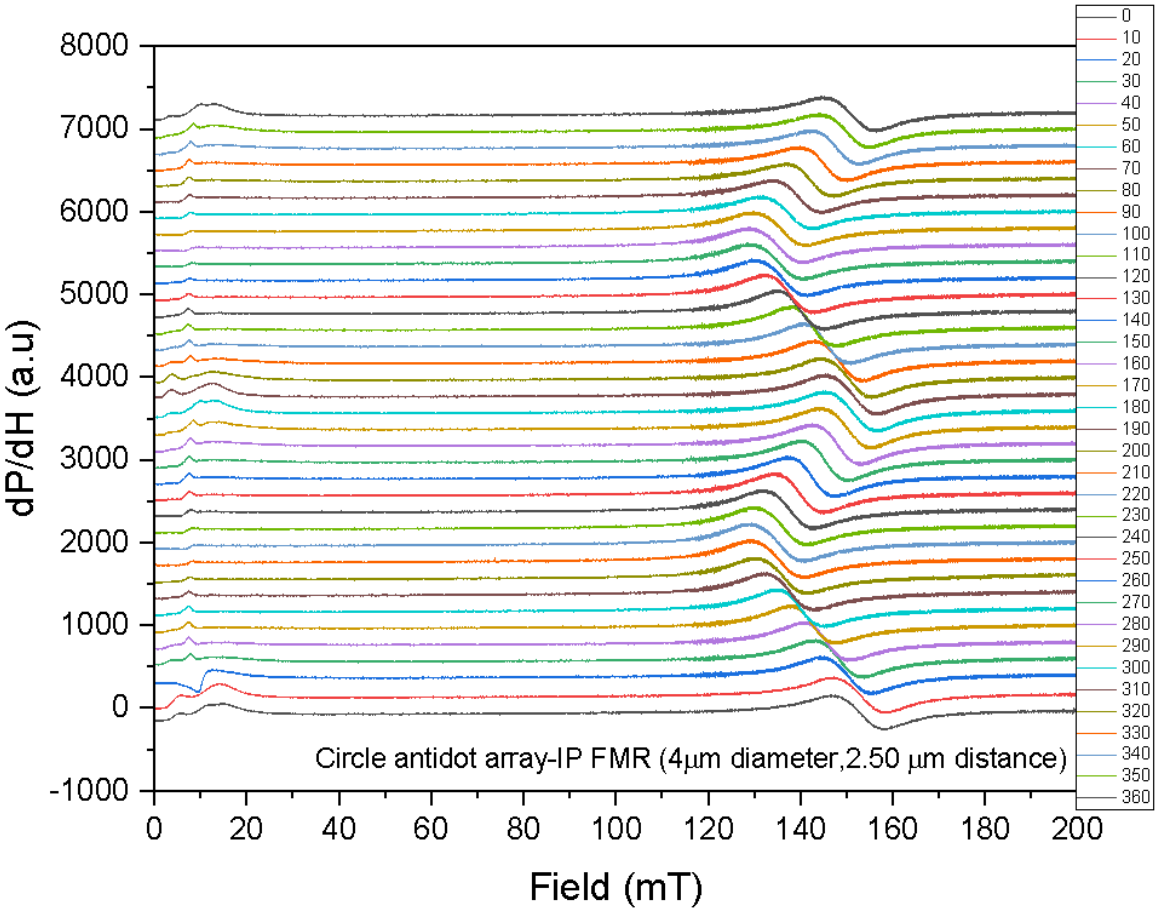

Figure A.9. The full FMR spectrum of a circular antidot array with a diameter of 4 μm and separation distance of 2.50 μm in IP measurement geometry.